



University
of Glasgow

Naeem, Muhammad Azhar (2013) *Monolithically integrated polarisation mode convertor with a semiconductor laser*. PhD thesis.

<http://theses.gla.ac.uk/4419/>

Copyright and moral rights for this thesis are retained by the author

A copy can be downloaded for personal non-commercial research or study

This thesis cannot be reproduced or quoted extensively from without first obtaining permission in writing from the Author

The content must not be changed in any way or sold commercially in any format or medium without the formal permission of the Author

When referring to this work, full bibliographic details including the author, title, awarding institution and date of the thesis must be given



University of Glasgow | School of Engineering

Monolithically integrated polarisation mode convertor with a semiconductor laser

Muhammad Azhar Naeem

February 2013

A thesis submitted for the degree of

Doctor of Philosophy (Ph.D.)

in the

College of Science & Engineering

School of Engineering

© Muhammad Azhar Naeem 2013

Declaration of Authorship

I, **Muhammad Azhar Naeem**, declare that this thesis titled “**Monolithically integrated polarisation mode convertor with a semiconductor laser**” and the contributions presented in it are my own. I confirm that:

- This work was done wholly or mainly while in candidature for a research degree at this University.
- Where any part of this thesis has previously been submitted for a degree or any other qualification at this University or any other institution, this has been clearly stated.
- Where I have consulted the published work of others, this is always clearly attributed.
- Where I have quoted from the work of others, the source is always given. With the exception of such quotations, this thesis is entirely my own work.
- I have acknowledged all main sources of help.
- Where the thesis is based on work done by myself jointly with others, I have made clear exactly what was done by others and what I have contributed myself.

Signed: Muhammad Azhar Naeem

Date: February 13, 2013

In the name of Allah,
the most Beneficent and the most Merciful

Abstract

In this thesis, the design, optimisation, fabrication and operation of waveguide based semiconductor lasers, integrated with polarisation mode convertors (PMCs), is described. Devices are fabricated in the GaAs/AlGaAs and InP/AlGaInAs material systems, using two types of structures; single PMC and back-to-back PMCs. The convertor designs are based upon air trenches, of sub-wavelength dimensions, being introduced into waveguide structures in order to achieve an asymmetric cross-sectional profile, resulting in wave-pate functionality.

The GaAs/AlGaAs PMCs are fabricated using reactive ion etching (RIE), and the phenomena of RIE lag technique is also exploited for obtaining the required asymmetric waveguide profile in a single etch step. These are then integrated with semiconductor lasers. The InP/AlGaInAs PMCs are fabricated using a combination of RIE and inductively coupled plasma (ICP) etching and are integrated with semiconductor lasers and also differential phase shifter (DPS) sections to realise devices with active polarisation control.

Integrated devices fabricated on InP/AlGaInAs material system with a semiconductor laser, a PMC followed by a DPS section yields ~40 % polarisation mode conversion whilst the DPS section is held at the transparency condition. Greater than 85 % polarisation mode conversion was also obtained with back to back PMCs, which was complement to the devices fabricated with a single PMC.

Furthermore, a first active polarisation controller, monolithically integrated with a semiconductor laser is reported. High speed modulation of the integrated device with 300 Mbps is also demonstrated via current injection to the phase shifter section of the device.

Acknowledgement

First of all, I would like to offer my profound thanks to my project supervisors Dr. Barry M. Holmes and Dr. Anthony Kelly, for having made this research work into possibility. Their enthusiastic support, technical guidance and never ending encouragement throughout my PhD studies have been invaluable, and are truly appreciated. They really did a lot for me. Thanks very much.

I am very thankful to all the individuals who have helped me from the very start, especially Dr. Usman Younas and Dr. kamran Abid. Thanks to my office mates Shahid Mahmood, Jehan Akbar, Olesya Ignatova, Maria Carla Camasta, Dr. Wout Jansen, Dr. Mohsin Haji, Vincenzo Pusino and Saima for their constructive discussions and suggestions. I pray for their bright careers.

Special thanks to Dr. Marc Sorel, Dr. Corrie Farmer, Dr. Michael Strain, Dr. Lianping Hou, Dr. Antonio, Dr. Piotr Stolarz, Dr. Affar Shahid, Muhammad Mirza, Devnath for their help and support during times of difficulty throughout the course of this research work. I would like to thank Bill Ward for provision of the laser facilities in Rankine building, and to JWNC technical staff, Dougi Lang, Mark, Ronnie, Eve, Hellen, Donald, Linda, Mary and Dr. Hiaping.

I would like to thank all my sincere friends from Pakistan especially Nasir Aziz, Muhammad Amin, Rana Fiaz ul Hasan, Ghazi Balal and Afzal Nadeem, who prayed for me throughout my PhD course. I am very thankful to Sania Zahra Malik and Shehbaz Hijazi for their friendship and their enjoyable company in Glasgow.

I am particularly thankful to my parents especially my mother, who died during my studies, and father who always prayed for my success. They did a lot for me from my childhood to date. I never give them reward. Allah bless them. Thanks to my brothers Waqar Naeem, Azam Naeem and sisters for their exceptional love, help and support throughout my life. It would be unjustified, not to thanks my wife Adeela Azhar and sons Ali Haziq Naeem and Muhammad

Mahad Naeem who gave me lot of love and encourages me always during their stay with me in Glasgow.

List of Publications

1. **Naeem, M. A.**, Holmes, B. M., Kelly, A. E., Marsh, J. H. and Hutchings, D. C., “*Passive polarization mode convertor monolithically integrated within a semiconductor laser*”, in *IEEE Photonics Conference, 2012*, San Francisco, USA.
2. Holmes, B. M., **Naeem, M. A.**, Hutchings, D. C., Marsh, J. H. and Kelly, A. E., “*A Semiconductor Laser with Monolithically Integrated Dynamic Polarization Control*”, *Optics Express*, Vol. 20, Issue 18, pp. 20545-20550 (2012).
3. **Naeem, M. A.**, Haji, M., Holmes, B. M., Hutchings, D. C., Marsh, J. H. and Kelly, A. E., “*A Semiconductor Laser with Monolithically Integrated Polarization modulator*”, (Ready for submission to *Optics Letters*)

To my parents, especially to my mother who
died during my PhD studies

Table of Contents

Declaration of Authorship.....	ii
Abstract	iv
Acknowledgement.....	v
List of Publications.....	vii
Table of Contents	ix
List of Figures	xiv
Acronyms	xxiv
Chapter 1	1
1.1. Introduction	1
1.2. Polarisation mode dispersion.....	4
1.3. Applications of polarisation mode convertors.....	5
1.4. Thesis outline.....	9
1.5. References	13
Chapter 2	19
2.1. Introduction	19
2.2. Material aspects	19
2.2.1. Semiconductor materials	20
2.2.2. Bulk material properties	24
2.2.3. Quantum well material	26
2.2.4. Strained quantum well materials	29

2.3.	Semiconductor optical amplifiers	31
2.4.	Polarisation mode convertors theory	33
2.4.1.	Maxwell's Equations	33
2.4.2.	Wave Equations	34
2.4.3.	Plane waves	36
2.4.4.	Polarisation	38
2.4.5.	Birefringence	41
2.4.6.	Retardation.....	43
2.4.7.	Electro-optic effects.....	45
2.4.8.	Carrier induced effects.....	46
2.5.	Review of the major contributions to polarisation mode convertors.....	47
2.6.	Conclusions	54
2.7.	References	56
Chapter 3	65
3.1.	Introduction	65
3.2.	Lithography	66
3.3.	Electron-beam lithography resists	68
3.3.1.	Proximity correction	71
3.4.	Dry etching	72
3.4.1.	Principle.....	73
3.5.	Overview of the fabrication process	77
3.5.1.	Sample preparation and cleaning.....	78
3.5.2.	Registration markers.....	78
3.5.3.	Waveguide definition	79

3.5.4. Cap layer removal.....	80
3.5.5. Planarization	80
3.5.6. Current injection window	82
3.5.7. Contact metallisation	82
3.5.8. Mechanical thinning	83
3.5.9. N-contact metallisation and annealing	83
3.5.10. Cleaving and mounting	84
3.6. Conclusions	84
3.7. References	86
Chapter 4	88
4.1. Introduction	88
4.2. Material structure.....	88
4.3. Basic material testing.....	91
4.3.1. Transmission line measurement	91
4.3.2. Ridge waveguide lasers	94
4.3.2.1. Design and optimisation.....	94
4.3.2.2. Device fabrication	97
4.3.2.3. Device characterisation	97
4.3.2.4. Calculation of material parameters	98
4.3.2.5. Temperature characteristics.....	101
4.3.2.6. Spectrum analysis.....	103
4.3.2.7. Far field pattern analysis	104
4.4. Conclusions	106
4.5. References	108

Chapter 5	109
5.1. Introduction	109
5.2. Principle of the etched slot polarisation mode convertor	110
5.3. Modelling and design of the polarisation mode convertor	111
5.4. Optimisation of the trench depth in realised devices.....	116
5.5. Device structure with a single PMC.....	117
5.5.1. Device fabrication.....	118
5.5.2. Passive device measurements.....	119
5.6. Device structure with back to back PMCs.....	121
5.6.1. Modelling and design of devices with back to back PMCs.....	122
5.6.2. Fabricated device.....	123
5.6.3. Passive measurements with back to back PMCs	124
5.6.4. Active PMC measurements	125
5.6.5. Voltage-Current characteristics	126
5.7. Device structure with deep to shallow etching.....	128
5.7.1. Fabricated device.....	130
5.7.2. Active PMC measurements	131
5.7.3. Power-current characteristics	132
5.8. Conclusions	132
5.9. References	134
Chapter 6	136
6.1. Introduction	136
6.2. Material structure.....	137
6.3. Waveguide design.....	139

6.4.	Modelling and design of the device with a single PMC.....	141
6.4.1.	Device structure with a single PMC.....	145
6.4.2.	PMC fabrication analysis.....	146
6.4.3.	Realised device with a single PMC.....	150
6.4.4.	Light current characteristics.....	151
6.4.5.	Optical spectrum measurements.....	153
6.4.6.	Transparency current measurements.....	154
6.4.7.	Active PMC measurements.....	156
6.4.8.	Active polarisation control.....	158
6.4.9.	Polarisation modulation measurements with data injection.....	163
6.4.10.	High speed polarisation modulation measurements.....	165
6.5.	Integrated devices with back to back PMCs.....	173
6.5.1.	Modelling and design of device.....	174
6.5.2.	Device measurements.....	176
6.6.	Conclusions.....	178
6.7.	References.....	179
Chapter 7	181
7.1.	Conclusions.....	181
7.2.	Future recommendations.....	182
Annex I	184
Annex II	186
Annex III	191
Annex IV	193

List of Figures

Figure 1.1: A schematic picture of the dense wavelength division multiplexing system.....	2
Figure 1.2: A schematic diagram of the principle of the polarisation division multiplexer technique.....	2
Figure 1.3: A schematic diagram of integrated semiconductor laser with PMC to establish a TM polarised output signal.....	5
Figure 1.4: Schematic diagrams of two possible configurations of integrated polarisation independent amplifier circuit structures: (a) parallel and (b) series....	6
Figure 1.5: Integrated polarisation diversity scheme [41].....	7
Figure 1.6: A schematic diagram of the functionality of an integrated optical isolator fabricated monolithically.....	8
Figure 2.1: A schematic diagram of a GaAs zinc-blende structure.	20
Figure 2.2: (a) A planar bond structure of GaAs lattice showing the two valance electrons shared by a Ga and an As atom and (b) a bond structure showing a broken bond due to the absorption of a photon with energy above the band-gap.	21
Figure 2.3: Energy-band diagram in real space.....	21
Figure 2.4: The energy-band diagram showing the energy levels of the electron and the hole when an incident photon having optical energy, equal to or greater than the band-gap energy strikes the semiconductor material.	22
Figure 2.5: Energy-momentum diagram of (a) direct band-gap material and (b) indirect band-gap material.....	23
Figure 2.6: Energy-band structure of a direct band-gap semiconductor material.	24
Figure 2.7: Energy-density of states for quantum well and bulk semiconductors.	27

Figure 2.8: Energy band model for a single quantum well.	28
Figure 2.9: A schematic multi quantum well energy band diagram.	28
Figure 2.10: Band-edge profile for the compressive strained, un-strained and tensile strained quantum wells.	30
Figure 2.11: The geometry of a plane wave travelling in +z direction.	37
Figure 2.12: Construction of the polarisation vector.....	40
Figure 2.13: Schematic representations of polarised lights (a) linear (b) right circular (c) left circular (d) right elliptical and (e) left elliptical.	41
Figure 2.14: A retarder plate.	43
Figure 2.15: Input and output polarisations of light through (a) a half wave-plate and (b) a quarter wave-plate.....	44
Figure 2.16: Different approaches to the realization of PMCs.	48
Figure 2.17: A schematic diagram of the periodic asymmetric rib waveguide.....	49
Figure 2.18: (a) A schematic diagram of top view of the passive 45° PMC based on tilted rib waveguides (b) cross section of the feeding waveguide (A-B) and (c) cross section of the convertor section (C-D).....	50
Figure 2.19: A schematic diagram of a deep etched bended waveguide structure used for the polarisation conversion.....	50
Figure 2.20: (a) A schematic diagram of a single section passive PMC with angled facet waveguide structure and (b) the cross-sectional profile of the device.	51
Figure 2.21: A schematic diagram of cross-section profile of RIE Lag structure.	52
Figure 2.22: A schematic diagram of cross-sectional profile of tilted waveguide facet in both directions.	53
Figure 3.1: A schematic illustration of e-beam writing procedure.	67
Figure 3.2: Schematic diagrams of exposure (a) before development (b) after development (positive resist) and (c) negative resist.	68

Figure 3.3: A schematic diagram of lift off process.....	69
Figure 3.4: A schematic diagram for definition of wave-guiding structure using PMMA (on left) and HSQ (on right) process steps.....	70
Figure 3.5: Simulated trajectories of one hundred (100KeV energy) electrons through 1 μ m HSQ and 40 μ m InP [3].....	72
Figure 3.6: A schematic diagram of a parallel plate type RIE machine.....	73
Figure 3.7: Simulation results by Matlab software for etch depth.	75
Figure 3.8: Real time etch depth obtained by laser reflectometry method.....	76
Figure 3.9: An un-etched area due to residual SiO ₂	76
Figure 3.10: Cross markers (a) before e-beam job submission (b) after e-beam job written.....	79
Figure 3.11: Global markers of 20 μ m x 20 μ m dimensions after alignment.	79
Figure 3.12: A real time trace obtained during the cap layer removal by laser reflectometer.....	80
Figure 3.13: SEM pictures showing the broken metal contacts.....	81
Figure 3.14: SEM picture of planarization.....	82
Figure 3.15: Fabrication of semiconductor lasers process flow diagram.....	85
Figure 4.1: A schematic diagram of the mask used for the contact pads.....	91
Figure 4.2: A schematic diagram of the four probe measurement setup.....	92
Figure 4.3: The measured resistances as a function of contact pads separations..	93
Figure 4.4: Schematic diagrams of (a) deep etched and (b) shallow etched devices.	95
Figure 4.5: Simulated waveguide modal effective index of fundamental, 1 st and 2 nd order TE polarised modes as a function of the waveguide width for (a) deep etched and (b) shallow etched ridge waveguide structures.	96

Figure 4.6: Simulated modal profiles of a fundamental mode of (a) deep and (b) shallow etched ridge waveguide structures with 3 μm wide ridge waveguides....	96
Figure 4.7: Power as a function of applied current for 3 μm wide and various cavity length ridge waveguide lasers.	97
Figure 4.8: A plot of inverse differential quantum efficiency as a function of the cavity length.	99
Figure 4.9: A plot of $\ln J_{th}$ as a function of $1/L$	100
Figure 4.10: A plot of emitted power as a function of current at various temperatures.	102
Figure 4.11: A graph of natural log of threshold current as a function of temperature.....	102
Figure 4.12: A schematic diagram of optical spectrum measurement setup.....	103
Figure 4.13: Spectrum showing the excitation wavelength of 870 nm for 0.5 mm long and 3 μm wide ridge waveguide laser at 80 mA.....	104
Figure 4.14: A plot of observed peak wavelength with increase in the current..	104
Figure 4.15: Far field simulation of a 3 μm wide shallow etched waveguide structure.	105
Figure 4.16: A schematic picture of far field patterns measurement setup.....	105
Figure 4.17: The measured far field patterns in (a) horizontal and (b) vertical directions.	106
Figure 5.1: (a) A schematic design of a single trench PMC and (b) the symmetric and asymmetric waveguide sections.	110
Figure 5.2: A plot of % polarisation mode conversion as a function of the trench depth for different trench widths at constant trench position (140 nm) from the waveguide edge.	113

Figure 5.3: A plot of % polarisation mode conversion as a function of the propagation direction at various trench positions from the waveguide edge, at constant trench width (230 nm) and trench depth (1.25 μm).	114
Figure 5.4: The TE to TM mode conversion as a function of the propagation direction for 45° (50 %) rotation.	115
Figure 5.5: The TE to TM mode conversion as a function of the propagation direction for 90° (100 %) rotation.	116
Figure 5.6: SEMs of trench widths relative to the trench depths.	117
Figure 5.7: A schematic diagram of the device with a single PMC.	117
Figure 5.8: SEM picture of the cross section of the passive PMC.	119
Figure 5.9: A schematic diagram of the device measurement setup with Nd:YAG solid state laser, emitting at 1064 nm.	120
Figure 5.10: The % TM purity as a function of the PMC length (experimentally measured and re-simulated).	121
Figure 5.11: A schematic diagram of the device, with back to back PMCs.	122
Figure 5.12: The TE to TM mode conversion as a function of the propagation direction for PMCs, attached back to back.	123
Figure 5.13: SEM picture of cross-section profile of the PMC.	124
Figure 5.14: A plot showing experimentally measured and re-simulated results of the % TM purity as a function of the convertor length (attached back to back).	125
Figure 5.15: A schematic of the device measurement setup with Ti-Sapphire and GaAs laser.	126
Figure 5.16: Voltage-current curves for three sections of an integrated device.	127
Figure 5.17: A plot of output power as a function of the current on the output gain section of an integrated device.	128
Figure 5.18: A schematic diagram of the deep and shallow etched sections.	128

Figure 5.19: (a) An optical microscope image of the fabricated device with a pumped laser section, tapers, cap removal region and PMC sections (b) magnified view of PMC (c) magnified view of tapers used for coupling the two PMCs (d) magnified view of cap removal region and tapers and (e) magnified view of a pumped laser section.	129
Figure 5.20: (a) SEM picture of cross section of the integrated device including a pumped laser section (b) magnified view of cross section of the pumped laser section and (c) magnified top view of the pumped laser section.	130
Figure 5.21: Comparison of CW and pulsed current performance of the shallow to deep etched devices.	131
Figure 5.22: Hysteresis of the emitted power as a function of the current.	132
Figure 6.1: Energy band diagram (conduction band only) of InP/AlGaInAs material system.	139
Figure 6.2: Schematic diagrams of (a) deep etched and (b) shallow etched ridge waveguide structures.	139
Figure 6.3: Simulated waveguide modal effective refractive index of fundamental, 1 st and 2 nd order TE polarised modes as a function of the waveguide width for (a) deep etched and (b) shallow etched ridge waveguide structures.	141
Figure 6.4: Simulated modal profile of a fundamental mode of deep and shallow etched ridge waveguide structures.	141
Figure 6.5: Simulated % polarisation mode conversion as a function of the trench depth.	142
Figure 6.6: A plot of % polarisation mode conversion as a function of the propagation direction at various trench widths.	143
Figure 6.7: The TE to TM mode conversion as a function of the propagation direction.	144
Figure 6.8: Modal profiles at (a) the launched position (b) at start of the PMC and (c) at the length of 174 μm of the PMC.	144

Figure 6.9: A schematic diagram of the integrated device with a single PMC...	146
Figure 6.10: Various fabrication stages (a) as fabricated (b) after removal of HSQ (c) after HSQ planarization and (d) after metallisation.....	146
Figure 6.11: A schematic diagram of the device measurement setup with a 1555 nm tuneable laser.....	147
Figure 6.12: A plot of % TM purity as a function of the convertor length at different fabrication stages.....	148
Figure 6.13: The % TM purity as a function of the convertor length (experimentally measured, initially simulated and re-simulated).	149
Figure 6.14: SEM image of cross section profile of the PMC used with a semiconductor laser (a magnified view is given in the inset).	150
Figure 6.15: L-I curves of the TE and TM polarised light at the laser facet of the integrated device.	152
Figure 6.16: L-I curves of the TE and TM polarised light at the DPS angled facet of the integrated device.	152
Figure 6.17: Optical spectrums measured at constant currents on the input laser sections, ranging from 40 to 140 mA, with varying currents from 0 to 20 mA on the output gain section.....	153
Figure 6.18: A plot of peak wavelength as a function of the current on a laser section, with constant current on the DPS section.	154
Figure 6.19: A schematic diagram of the transparency current measurement setup.	155
Figure 6.20: Measured transparency current as a function of the wavelength for various fabricated devices.	155
Figure 6.21: A setup used for active PMC measurements.	156

Figure 6.22: The TM purity as a function of the DPS current for a range of laser bias currents in mA. The transparency point for each laser bias is indicated on the graph.....	158
Figure 6.23: The % TM purity as a function of the convertor length for different laser currents.	159
Figure 6.24: Output power as a function of the DPS current for polarisation angles of 45° and -45°.....	160
Figure 6.25: Output power as a function of the DPS current with addition of a QWP, with a fast axis aligned in plane of the wafer (TE aligned).....	161
Figure 6.26: A schematic diagram of the measurement setup of temporal response of the polarisation state.	162
Figure 6.27: Polarisation modulated output measured with 8 ns input driving pulse to the DPS section.	162
Figure 6.28: A plot of output voltage (response) versus frequency measured with low speed DC probes.....	163
Figure 6.29: A schematic diagram of the measurement setup for measurements of response of polarisation state after inducing binary input data.	163
Figure 6.30: Polarisation switched optical output pulse (measured), and induced electrical input binary data.	164
Figure 6.31: Optical output pulses measured for polarisation angles of 45° and -45° (with injection of electrical input binary data).....	165
Figure 6.32: A schematic of the wire bonded arrangement of the device to use with RF probes.	166
Figure 6.33: Optical output power as a function of the voltage on the DPS section using RF probes for polarisation angles of +45° and -45°.....	167
Figure 6.34: Eye diagrams obtained at 45° (b) and -45°, and optical output signals measured for polarisation angles of (c) 45°, (d) -45°, (e) 0° (TE) and (f) 90° (TM) at 100 Mbps.....	168

Figure 6.35: Eye diagrams obtained at 45° (b) and -45°, and optical output signals measured for polarisation angles of (c) 45°, (d) -45°, (e) 0° (TE) and (f) 90° (TM) at 200 Mbps.....	169
Figure 6.36: Eye diagrams obtained at 45° (b) and -45°, and optical output signals measured for polarisation angles of (c) 45°, (d) -45°, (e) 0° (TE) and (f) 90° (TM) at 300 Mbps.....	170
Figure 6.37: Eye diagrams obtained at 45° (b) and -45°, and optical output signals measured for polarisation angles of (c) 45°, (d) -45°, (e) 0° (TE) and (f) 90° (TM) at 400 Mbps.....	171
Figure 6.38: Eye diagrams obtained at 45° (b) and -45°, and optical output signals measured for polarisation angles of (c) 45°, (d) -45°, (e) 0° (TE) and (f) 90° (TM) at 500 Mbps.....	172
Figure 6.39: Optical output signals measured for polarisation angles of (a) 45°, (b) -45°, (c) 0° (TE) and 90° (TM) at 300 Mbps (on the same scale).....	173
Figure 6.40: A schematic diagram of the integrated device with two back to back PMCs, followed by a DPS section, with change in the optical axis at A, B and C.	174
Figure 6.41: The TE to TM mode conversion as a function of the propagation direction for the integrated devices (with back to back PMCs and a DPS section).	175
Figure 6.42: Modal profiles (a) at the start of the 1 st PMC (b) at the termination point of 1 st PMC (188 μm) and (c) at the termination point of 2 nd PMC (366 μm).	176
Figure 6.43: A plot of % TM purity (experimentally measured and re-simulated) as a function of the PMC length at three laser drive currents.	176
Figure 6.44: Comparison of polarisation mode conversion with single (and back to back) PMCs at 100 mA current on a semiconductor laser section.....	177

Figure 7.1: A schematic diagram of the integrated device with two single PMCs, and two DPS sections with a semiconductor laser section..... 183

Acronyms

Symbol	Description	Symbol	Description
BPM	Beam propagation method	BSS	Beam step size
CAD	Computer aided design	CAIBE	Chemically assisted ion beam etching
CATS	Computer aided transcription system	CW	Continuous wave
DPS	Differential phase shifter	DQW	Double quantum well
DUT	Device under test	DWDM	Dense wavelength division multiplexer
EBL	Electron beam lithography	EDFA	Erbium doped fibre amplifier
FEM	Finite element method	FPL	Fabry-Parot laser
FWHM	Full width half maximum	GRINCH	Graded index separate confinement hetero-structure
hh	Heavy hole	HSQ	Hydrogen Silsesquioxane
ICP	Inductively coupled plasma	IPA	Isopropanol
JWNC	James Watt Nano Fabrication Centre	LED	Light emitting diode
lh	Light hole	L-I	Light-Current
MBE	Molecular beam epitaxy	MFS	Minimum feature size
MOCVD	Metal organic chemical vapour deposition	MQW	Multi quantum well

Symbol	Description	Symbol	Description
OEIC	Optoelectronic integrated circuit	OSA	Optical spectrum analyser
PDM	Polarisation division multiplexer	PECVD	Plasma enhanced chemical vapour deposition
P-I	Power-Current	PIC	Photonic integrated circuit
PL/EL	Photo-luminous/electro-luminous	PMC	Polarisation mode convertor
PMMA	Poly-Methyl Methacrylate	QW	Quantum well
QWP	Quarter wave plate	RF	Radio frequency
R-I	Resistance-Current	RIE	Reactive ion etch
RO	Reverse osmosis	RTA	Rapid thermal annealer
SCH	Separate confinement hetero-structure	SEM	Scanning electron microscope
SOA	Semiconductor optical amplifier	SOI	Silicon on insulator
SOP	State of polarisation	SQW	Single quantum well
TE	Transverse electric	TEC	Thermo electric cooler
TLM	Transmission line measurement	TM	Transverse magnetic
TMAH	Tetra-Methyl Ammonium Hydroxide	VB6	Vector beam 6
V-I	Voltage-Current	VRU	Variable resolution unit

Chapter 1

Introduction

1.1. Introduction

During the last thirty years, there has been an exponential growth in the exploitation of optical fibre based technologies and networks [1]. Global communications is now heavily reliant upon optical based technologies. Further developments in optical communications technologies aim to provide the basis for all-optical networking capabilities with the goal of hosting 1300 nm to 1600 nm bandwidth and carrying information with very low losses and flexible routing channels [2, 3]. Optical fibres are the preferred medium for carrying data, but can suffer from limitations like dispersion and attenuation which reduces the transmission length, thus limiting the available bandwidth. This dispersion in optical fibres can be material, polarisation dependant or geometrical. The impact of these factors becomes prominent as the length of optical fibre is increased and the signal weakens. This weakened signal can be regenerated using several techniques which involve signal detection, electrical amplification of the signal, re-timing, pulse shaping and re-transmission. The advent of erbium doped fibre amplifiers (EDFAs) [4] have advanced the optical data networks. Initially reported by both Desurvire et al. [5] and Mears et al. [6] in 1987 the EDFA is designed to operate at the crucial 1550 nm telecommunications wavelength, and provides the

means for cost effective amplification, and enhanced performance, in current fibre optic based communication systems. The development of dense wavelength division multiplexed (DWDM) [7] systems resulted in the ability to transmit multiple signals, each at different modulation format and data rates, and each with a slightly different wavelength, on a single transmission fibre. This also resulted in the enhanced performance and efficiency of fibre optic based communication networks. A schematic picture of a DWDM system is shown in Figure 1.1.

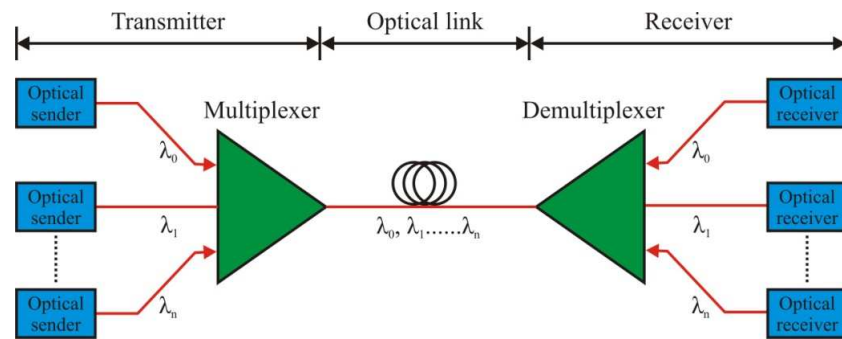


Figure 1.1: A schematic picture of the dense wavelength division multiplexing system.

Additionally, by coupling a DWDM system with a polarisation division multiplexer (PDM) [8], two orthogonally polarised optical signals of the same wavelength, with different modulation formats and data rates, can be merged to travel along a single transmission line, effectively doubling the fibre's capacity. The transmitted signal is split at the receiver and two orthogonally orientated polarised filters are used to recover the original orthogonally polarised signals. A schematic diagram of the principle of the PDM technique is shown in Figure 1.2.

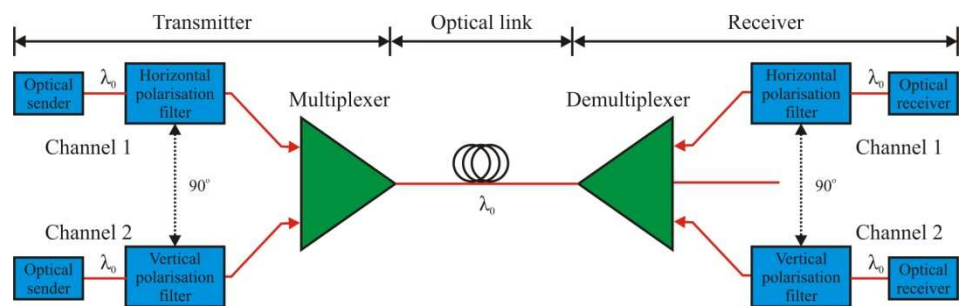


Figure 1.2: A schematic diagram of the principle of the polarisation division multiplexer technique.

High transmission rates and processing capabilities in optical communication systems necessitate high performance, high reliability and cost effective [3] electrical and optical components. These requirements become ever more stringent for enhanced next generation network services [9, 10], therefore, a successive migration of discrete active and passive components to an integrated level is desirable. In the electronic domain, various functionalities based on the discrete components have been realised in low cost, very large scale, integrated (VLSI) circuits [11]. This trend overlaps to their optoelectronic counterparts such as large scale optoelectronic integrated circuits (OEICs) [12, 13] and photonic integrated circuits (PICs) [14, 15]. Integrated circuits realised with lithography not only reduces size but also minimises the number of packaging stages and eliminates costly and time consuming assembly, which further helps in reducing the coupling losses to optical fibres. Additionally, the reduction of manual alignment and the compactness of the integrated circuits decreases the impact of mechanical vibration or temperature change on the device performance [16].

Generally, PICs are polarisation sensitive. Therefore, potential PICs must be independent from variation in the state of polarisation (SOP) of the input light. This variation is due to the two principle state of polarisations (PSPs) in PICs, which are commonly referred as transverse electric (TE) and transverse magnetic (TM) polarisations. TE is referred to light polarised in the plane of the wafer, whereas, TM is referred to light polarised perpendicular to the wafer. The problem of varying SOP of the signal, received at the output of a fibre span needs to be overcome in both the optical fibres and at the fibre-OEIC/PIC interfaces. This random effect of SOP in the optical fibres can be minimised using a costly installation of polarisation maintaining (PM) fibres [17], and receivers in PICs can be designed to operate independent of the incoming SOP. Therefore, the importance of polarisation control and manipulation is becoming ever-more critical as optical fibre systems progress towards data rates at Gigabit or higher rates with greater data processing capabilities.

Polarisation states can be manipulated by using bulk optics, or, more effectively through the use of integrated polarisation control techniques. These are

based upon the careful design of the semiconductor planar waveguide materials or through integration schemes based upon the incorporation of compact waveguide-based polarisation mode convertors (PMCs). PMCs are used to convert the SOP of the incoming signal into another state. These are realised as both active and passive devices. Active PMCs have been realised by applying magneto-optic [18], electro-optic [19, 20] and photo-elastic [21, 22] effects and require an external power supply and a control unit. Therefore, integrated passive PMCs are preferred. The subsequent section gives an overview of potential applications of integrated PMCs.

1.2. Polarisation mode dispersion

The SOP of the signal at the sender output and receiver input usually do not correspond to each other. This is due to the transmission characteristics of the optical data link, and caused by the polarisation mode dispersion (PMD) [23-25]. The PMD effects are linear electromagnetic propagation phenomenon, which occurs in single mode fibres. Despite of the name, this single mode fibre actually supports two modes of propagation which are orthogonally polarised to each other. These two orthogonal modes are referred to as the principle state of polarisations (PSPs) [26]. In an ideal fibre, due to the symmetry of the refractive indices, the two orthogonal modes are degenerate, whereas, in a real fibre, small imperfections results in a non symmetrical refractive indices distribution, which leads to a random birefringence along the fibre length. This non-symmetrical distribution of refractive indices is due to the internal stress on the fibre core and the geometry, such as elliptical cross sections, micro-bends or micro-twists [27], and also on external factors such as temperature, electric or magnetic fields. Because of optical birefringence in the fibre, the two orthogonal modes experience different refractive indices, resulting in different propagation constants, and therefore, with different group velocities, referred to as differential group delay. This random change of birefringence along the fibre length results in random coupling of modes, and leads to pulse distortion and system impairments that limit the transmission capacity of the fibre [27]. A single mode fibre can be

modelled as a concatenation of short fibre sections, which are assumed to be short enough that any perturbations acting on them are constant over their entire individual lengths [28]. In the frequency domain, PMD manifests itself as the frequency dependant variation of the SOP at the fibre section output for a fixed input polarisation [29], whereas, in the time domain, there is a mean time delay of a pulse traversing the fibre which is a function of the polarisation of the input pulse. Furthermore, the amount of change in the polarisation is a function of the wavelength.

1.3. Applications of polarisation mode convertors

PMCs are used mainly for polarisation manipulation and control in a diverse range of applications including polarimetry [30], metrology [31], time of flight [32] and optical communication systems. PMCs are important for networks developed to transmit information with GHz rates. In applications such as the polarisation division multiplexer (PDM) [8], a transverse magnetic (TM) polarised signal (with the electrical vector normal to the plane of the wafer) is desired at the output. This can be obtained by fabricating a PMC monolithically integrated with a semiconductor laser all upon an active waveguide material. A schematic diagram of this arrangement is shown in Figure 1.3.

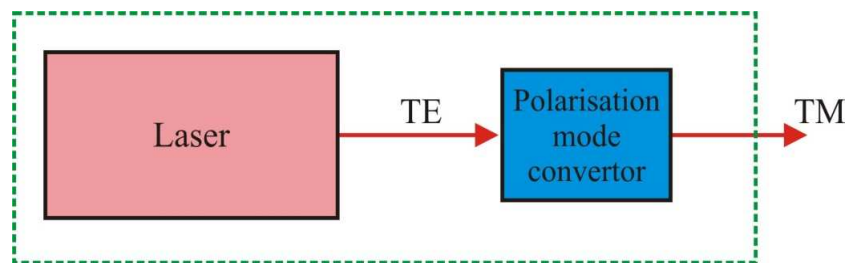


Figure 1.3: A schematic diagram of integrated semiconductor laser with PMC to establish a TM polarised output signal.

In the majority of semiconductor based lasers, there is a gain difference between the transverse electric (TE) mode, with its electrical vector orientated in the plane of the wafer, and the orthogonal TM mode. This difference is due to quantum mechanical selection rules linked to the energy levels of heavy holes

(hh) and light holes (lh) in the semiconductors valance band. This mechanism is explored more fully in subsequent sections. Furthermore, SOAs typically operate in the TE mode and there are various losses (e.g. coupling inter-faces) and additional noise in SOAs represents a power penalty for their operation. Several techniques to overcome the gain difference, including the use of waveguides with different cross-sectional designs [33, 34] and strained layer materials [35-38] have been reported. Other techniques, where semiconductor optical amplifiers (SOAs) are placed either in parallel or in series with PMCs to eliminate the gain difference have also been reported [39, 40] and schematic diagrams of these techniques are shown in Figure 1.4.

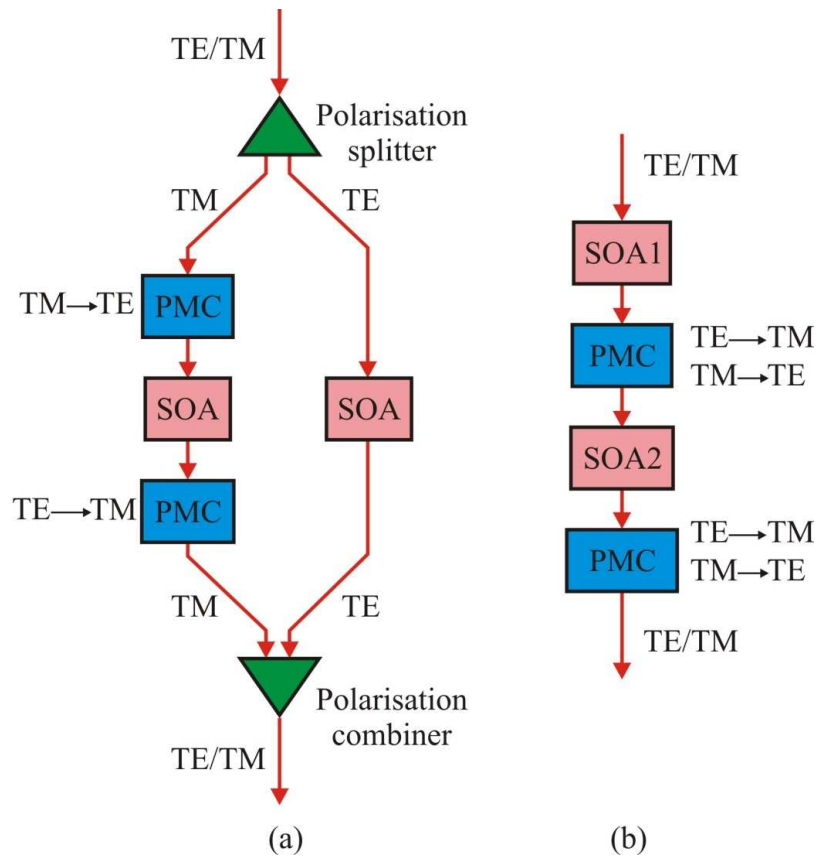


Figure 1.4: Schematic diagrams of two possible configurations of integrated polarisation independent amplifier circuit structures: (a) parallel and (b) series.

In the parallel structure arrangement (Figure 1.4 (a)), the incident signal first passes through the polarisation splitter and is split into TE and TM polarised components. The TE component is directly coupled with SOA for amplification,

whereas, in the other branch, the TM component first passes through a 90° PMC converting it to the TE polarisation. Thereon, that TE component passes through SOA for amplification and is again converted, back to TM via second 90° PMC. Both amplified components are then re-combined through a polarisation combiner to give the same SOP as at the input.

In the series structure arrangement (Figure 1.4 (b)), both TE and TM components pass through the structure. The TE component of the signal is amplified in the first SOA, whereas, the TM component remains unaffected. In order to obtain equal gain in both the TE and TM components, PMC is inserted, which rotates both the components by 90° . The second SOA now amplifies the TM rotated TE signal, whereas, the TE rotated to TM component passes through unaffected. A second 90° PMC then converts both the components back to their original SOP. Both techniques by using PMCs in parallel or in series with SOAs help to attain polarisation independence.

Polarisation dependent effects can also be controlled using the polarisation diversity scheme proposed by Barwicz et al. [41] for integrated devices (Figure 1.5). This scheme also helps to attain polarisation independence.

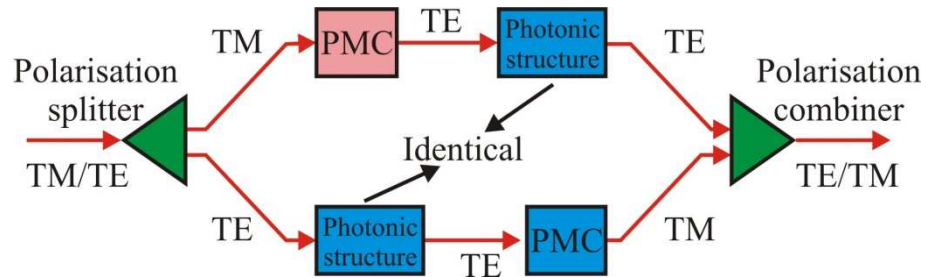


Figure 1.5: Integrated polarisation diversity scheme [41].

In this scheme, an incident signal is split into its two orthogonal TE and TM components via a polarisation splitter. The TM component is rotated into a TE state when it passes through the 90° PMC. The TE components travelling in each branch then pass through two identical photonic structures, which are TE polarisation sensitive. The original TE component in the lower branch is then converted to TM using a 90° PMC to avoid from any type of interference during

recombination of the signal through the polarisation combiner at the output of the device. This scheme is suggested to avoid any type of fabrication imperfections.

Integrated optical isolators are also a potential application of PMCs (or polarisation rotators). Optical sources which are stable with narrow linewidths are desired in integrated optical circuits. These sources must be free from the injection noise that arises as a result of emitted radiations that are reflected back into the laser cavity [42-49]. Bulk isolators [50] based on the magneto-optic Faraday effect [18] have been realised and are in general use today, however, they are bulky and add cost to systems due to intricate alignment requirements. Furthermore, the gyrotropic media are required in realising magneto optic isolator devices. Monolithically integrated isolators are, therefore, highly desirable, and initial demonstrations of such devices have been interesting [51-53]. The functionality of the isolators is illustrated in Figure 1.6.

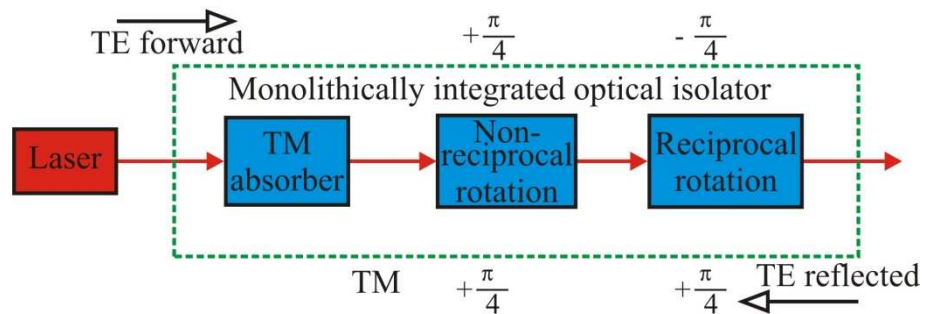


Figure 1.6: A schematic diagram of the functionality of an integrated optical isolator fabricated monolithically.

The device shown in Figure 1.6 is formed using a TM absorber [54] with non-reciprocal [55, 56] and reciprocal [57, 58] rotation sections. Here, each rotation section rotates the SOP of incoming signal by an angle of 45° .

Semiconductor hetero-structure lasers predominately emit TE polarised light. This emitted signal passes through the TM absorber, then the non-reciprocal and reciprocal rotation sections. The TE signal undergoes a non-reciprocal 45° rotation, followed by a -45° reciprocal rotation, thus cancelling the imparted polarisations, and returns the polarisation to its original state. Hence, in the forward propagation direction, a TE signal is emitted at the output facet of the

device. Any reflection of this signal back into the output facet of the device, undergoes a combined rotation (of 90°) from the two rotation sections and becomes a TM polarised signal. This TM signal is then absorbed by the TM absorber and no light travels back to the input laser.

PMCs are also used as wave plates or retardation plates. If the PMCs are fabricated such that the phase difference between the two orthogonal components TE and TM fields become π (or 180°), which corresponds to one half of the wavelength ($\lambda/2$) the PMC is referred to as a half wave plate. Alternatively, if the phase difference becomes $\pi/2$ (or 90°), corresponding to one quarter of the wavelength ($\lambda/4$) the PMC is referred to as a quarter wave plate. These concepts are explained further in the next chapter.

Due to the increasing requirement for the polarisation control, it is, therefore the intention of this study to design, fabricate and test various integrated polarisation control techniques/technologies.

1.4. Thesis outline

The remainder of this thesis is compiled as follows:

Chapter 2 explains the basic theory of semiconductor materials, lasers and semiconductor optical amplifiers (SOAs). An overview of semiconductor properties - including bulk, quantum well and strained quantum well materials -, is presented. The theory of direct and indirect band-gap transitions and the effects of heavy and light hole transitions upon resultant polarisation states, and polarisation insensitive devices, are presented and explained. The governing equations behind the functionality of PMCs based on structural birefringence are also reviewed. The chapter finishes with a detailed review of the major contributions towards the realisation of integrated PMCs.

Chapter 3 provides an overview of the fabrication technologies used throughout this investigation. This includes electron-beam and photo-lithographic techniques and dry etch processing. A complete overview of fabrication processes is

presented, which starts from cleaning of the wafer, through dry etching and metallisation lift off techniques.

Chapter 4 covers the characterisation of the GaAs/AlGaAs material based device used in this research. The methods for material characterisation including transmission line measurement (TLM) and characterisation of ridge waveguide based lasers are presented. Furthermore, Fabry-Perot Laser (FPL) design, optimisation, realisation and characterisation are explained. The active semiconductor material properties, such as, the internal quantum efficiency (η_i), internal loss (α_i), threshold current density (J_{th}) and the modal optical gain (g_m) of the devices, are presented. The optical spectrum and the far-field measurements are also discussed in this chapter.

Chapter 5 demonstrates the principle design and optimisation, fabrication and characterisation of a single trench and single etched passive PMC - obtained through the use of the reactive ion etch (RIE) lag technique. The characteristics of integrated devices fabricated in the GaAs/AlGaAs material system are also presented. Device structures designed with both deep and shallow etched regions for active device functionality are discussed. The results obtained through the characterisation of fabricated devices are presented.

Chapter 6 describes the structure of the InP/AlGaInAs material system with a brief description of the epitaxial layers and the band diagram. The structures devised for the realisation of the devices using a single PMC and back-to-back PMCs integrated with semiconductor lasers are presented, with discussion of their modelling and optimisation. The characterisation and measurement of these devices, including transparency current, optical spectrum and polarisation mode conversion efficiency, is reviewed. Furthermore, the dynamic polarisation control of incoming signals and the temporal response of the polarisation modulation using a function generator are presented. The response of these devices when applying electrical binary input data and the corresponding optical output pulse trains obtained are also presented, including the high speed modulation of the polarisation at 300 Mbps.

Finally, conclusions and the recommendations for the future work are given in **Chapter 7**.

Table 1.1: Resource distribution map.

Activities	Author's involvement
Ridge waveguide lasers	
Design and optimisation	Complete
Device fabrication	Complete
Characterisation	Complete
Polarisation mode convertors (GaAs/AlGaAs)	
Material design	-
Modelling and design	complete
Fabrication	complete
Characterisation	complete
Fabrication process optimisation	Complete
Active Polarisation mode convertors (InP/AlGaInAs)	
Material design	-
Modelling and design	complete
Fabrication	-
Characterisation	complete

In this research work, a design of PMC with single trench was made. This trench helps to rotate the optical axis of the PMC to attain 50 % (half) or 100 %

(full) polarisation mode conversion depending upon the trench depth. Additionally, a novel design by attaching two back to back PMCs to attain 100 % polarisation mode conversion was devised. The design was also made for integrated devices by incorporating a single and two PMCs with a semiconductor laser, and a differential phase shifter section. These integrated devices were fabricated for the first time on GaAs/AlGaAs and InP/AlInGaAs material systems. A dynamic polarisation control was achieved with single PMC devices and high speed polarisation modulation was attained at 300 Mbps, which is absolutely a novel aspect of the work in this thesis.

1.5. References

1. Connelly, M.J., *Semiconductor Optical Amplifiers*. 2002: Kluwer Academic Publishers, The Netherlands, ISBN 0-7923-7657-9.
2. Nguyen, T.H. and M.N.O. Sadiku, *Next generation networks*. Potentials, IEEE, 2002. **21**(2): p. 6-8.
3. O'Mahony, M.J., et al., *Future Optical Networks*. Lightwave Technology, Journal of, 2006. **24**(12): p. 4684-4696.
4. Miniscalco, W.J., *Erbium-doped glasses for fiber amplifiers at 1500 nm*. Lightwave Technology, Journal of, 1991. **9**(2): p. 234-250.
5. Desurvire, E., J.R. Simpson, and P.C. Becker, *High-gain erbium-doped traveling-wave fiber amplifier*. Opt. Lett., 1987. **12**(11): p. 888-890.
6. Mears, R.J., et al., *Low-noise erbium-doped fibre amplifier operating at 1.54 μm* . Electronics Letters, 1987. **23**(19): p. 1026-1028.
7. Kartalopoulos, S.V. and I.C. Society, *Introduction to DWDM technology: data in a rainbow*. 2000: SPIE Optical Engineering Press, ISBN 0-7803-5399-4.
8. Schönfelder, T., *Polarization division multiplexing in optical data transmission systems*. 2003, Telefonaktiebolaget LM Ericsson (publ) (Stockholm, SE): United States, Patent 6580535.
9. Chae-Sub, L. and D. Knight, *Realization of the next-generation network*. Communications Magazine, IEEE, 2005. **43**(10): p. 34-41.
10. Wilkinson, N., *Next Generation Network Services: Technologies & Strategies*. 2002: John Wiley & Sons, Ltd, Chichester, UK, ISBN 0-471-48667-1.
11. Moore, G.E., *Cramming More Components Onto Integrated Circuits*. Proceedings of the IEEE, 1998. **86**(1): p. 82-85.

12. Forrest, S.R., *Optoelectronic integrated circuits*. Proceedings of the IEEE, 1987. **75**(11): p. 1488-1497.
13. Wada, O., T. Sakurai, and T. Nakagami, *Recent progress in optoelectronic integrated circuits (OEIC's)*. Quantum Electronics, IEEE Journal of, 1986. **22**(6): p. 805-821.
14. Koch, T.L. and U. Koren, *Semiconductor photonic integrated circuits*. Quantum Electronics, IEEE Journal of, 1991. **27**(3): p. 641-653.
15. Nagarajan, R., et al., *Large-scale photonic integrated circuits*. Selected Topics in Quantum Electronics, IEEE Journal of, 2005. **11**(1): p. 50-65.
16. Waynant, R.W. and M.N. Ediger, *Electro-Optics Handbook*. 2000: McGraw-Hill, New York, ISBN 0-07-068716-1.
17. Li, M.J., et al., *Speciality fibers for optical communication systems in Kaminow I. P., Li T. Willner A. E. (Eds.), "Optical fiber telecommunications V. A: Components and Subsystems", ch. 15, pp. 523-592*. 2008: 1st Ed., Academic Press, Oxford, UK.
18. Zvezdin, A.K. and V.A. Kotov, *Modern magneto-optics and magneto-optical materials*. 1997: 1st Edition, Institute of Physics Publishing, Bristol, UK. ISBN 0-7503-0362-X.
19. Alferness, R.C. and L.L. Buhl, *Waveguide electro-optic polarization transformer*. Applied Physics Letters, 1981. **38**(9): p. 655-657.
20. Schlak, M., et al., *Tunable TE/TM-mode polarization convertor on (001)-InP-substrate*. Photonics Technology Letters, IEEE, 1991. **3**(1): p. 15-16.
21. Yamanouchi, K., K. Higuchi, and K. Shibayama, *TE-TM mode conversion by interaction between elastic surface waves and a laser beam on a metal-diffused optical waveguide*. Applied Physics Letters, 1976. **28**(2): p. 75-77.
22. Yamanouchi, K., K. Wakazono, and K. Shibayama, *Optical surface wave mode converters and modulators utilizing static strain-optic effects*. Quantum Electronics, IEEE Journal of, 1980. **16**(6): p. 628-634.

23. Damask, J.N., *Polarization optics in telecommunications*. 2005: 1st Ed., Springer, New York, USA.
24. Poole, C.D. and R.E. Wagner, *Phenomenological approach to polarisation dispersion in long single-mode fibres*. *Electronics Letters*, 1986. **22**(19): p. 1029-1030.
25. Poole, C.D., et al., *Fading in lightwave systems due to polarization-mode dispersion*. *Photonics Technology Letters, IEEE*, 1991. **3**(1): p. 68-70.
26. Kaminov, I.P., *Polarization in optical fibers*. *Quantum Electronics, IEEE Journal of*, 1981. **17**(1): p. 15-22.
27. Gordon, J.P. and H. Kogelnik, *PMD fundamentals: Polarization mode dispersion in optical fibers*. 2000. **97**(9): p. 4541-4550.
28. Derickson, D., *Fiber optic test and measurement*. 1997: 1st Ed., Prentice Hall, New Jersey, USA.
29. Eickhoff, W., Y. Yen, and R. Ulrich, *Wavelength dependence of birefringence in single-mode fiber*. *Appl. Opt.*, 1981. **20**(19): p. 3428-3435.
30. Azzam, R.M.A., *Principles and Applications of Optical Polarimetry*. 2009: John Wiley & Sons.
31. Yoshizawa, T., *Handbook of Optical metrology: Principles and Applications*. 2009: CRC Press.
32. Amann, M.-C., et al., *Laser ranging: a critical review of usual techniques for distance measurement*. *Optical Engineering*, 2001. **40**(1): p. 10-19.
33. Deguet, C., et al., *Homogeneous buried ridge stripe semiconductor optical amplifier with near polarization independence*. *Proceedings, European Conference on Optical Communication*, 1999: p. 26-30.
34. Holtmann, C., et al., *Polarization independent bulk active region semiconductor optical amplifiers for 1.3 μm wavelengths*. *Photonics Technology Letters, IEEE*, 1996. **8**(3): p. 343-345.

35. Magari, K., M. Okamoto, and Y. Noguchi, *1.55 μm polarization-insensitive high-gain tensile-strained-barrier MQW optical amplifier*. Photonics Technology Letters, IEEE, 1991. **3**(11): p. 998-1000.
36. Newkirk, M.A., et al., *1.5 μm multiquantum-well semiconductor optical amplifier with tensile and compressively strained wells for polarization-independent gain*. Photonics Technology Letters, IEEE, 1993. **5**(4): p. 406-408.
37. Godefroy, A., et al., *1.55- μm polarization-insensitive optical amplifier with strain-balanced superlattice active layer*. Photonics Technology Letters, IEEE, 1995. **7**(5): p. 473-475.
38. Joma, M., et al., *Polarization insensitive semiconductor laser amplifiers with tensile strained InGaAsP/InGaAsP multiple quantum well structure*. Applied Physics Letters, 1993. **62**(2): p. 121-122.
39. Grobkopf, G., et al., *Optical amplifier configurations with low polarisation sensitivity*. Electronics Letters, 1987. **23**(25): p. 1387-1388.
40. Koga, M. and T. Matsumoto, *Polarization insensitive optical amplifier consisting of two semiconductor laser amplifiers and a polarization insensitive isolator in series*. Photonics Technology Letters, IEEE, 1989. **1**(12): p. 431-433.
41. Barwicz, T., et al., *Polarization-transparent microphotonic devices in the strong confinement limit*. Nat Photon, 2007. **1**(1): p. 57-60.
42. Fujiwara, M., K. Kubota, and R. Lang, *Erratum: Low-frequency intensity fluctuation in laser diodes with external optical feedback*. Applied Physics Letters, 1981. **39**(2): p. 182-182.
43. Fujiwara, M., K. Kubota, and R. Lang, *Low-frequency intensity fluctuation in laser diodes with external optical feedback*. Applied Physics Letters, 1981. **38**(4): p. 217-220.

44. Hirota, O. and Y. Suematsu, *Noise properties of injection lasers due to reflected waves*. Quantum Electronics, IEEE Journal of, 1979. **15**(3): p. 142-149.
45. Hirota, O., Y. Suematsu, and K. Kin-Sing, *Properties of intensity noises of laser diodes due to reflected waves from single-mode optical fibers and its reduction*. Quantum Electronics, IEEE Journal of, 1981. **17**(6): p. 1014-1020.
46. Ikushima, I. and M. Maeda, *Self-coupled phenomena of semiconductor lasers caused by an optical fiber*. Quantum Electronics, IEEE Journal of, 1978. **14**(5): p. 331-332.
47. Ikushima, I. and M. Maeda, *Lasing spectra of semiconductor lasers coupled to an optical fiber*. Quantum Electronics, IEEE Journal of, 1979. **15**(9): p. 844-845.
48. Lang, R. and K. Kobayashi, *External optical feedback effects on semiconductor injection laser properties*. Quantum Electronics, IEEE Journal of, 1980. **16**(3): p. 347-355.
49. Stubkjaer, K. and M. Small, *Noise properties of semiconductor lasers due to optical feedback*. Quantum Electronics, IEEE Journal of, 1984. **20**(5): p. 472-478.
50. *IO-F-FFB-980-X Isolator, OFR Inc, <http://www.ofr.com>*.
51. Holmes, B.M., J.J. Bregenzler, and D.C. Hutchings. *Enabling Technologies for the Monolithic Integration of Semiconductor Lasers and Waveguide Optical Isolators*. in *Lasers and Electro-Optics, 2007. CLEO 2007. Conference on*. 2007.
52. Holmes, B.M. and D.C. Hutchings. *Towards the Monolithically Integrated Optical Isolator on a Semiconductor Laser Chip*. in *Lasers and Electro-Optics Society, 2006. LEOS 2006. 19th Annual Meeting of the IEEE*. 2006.

53. Hutchings, D.C., *Prospectus for the implementation of magneto-optic elements in optoelectronic integrated circuits: A personal perspective*. Journal of Physics D: Applied Physics, 2003. **36**(18): p. 2222-2229.
54. Izutsum, M. and Z.L. Wang, *Propagation losses of guided waves in metallized sidewall waveguides*. Japanese Journal of Applied Physics, 1998. **37**(6B): p. 3643-3646.
55. Holmes, B.M. and D.C. Hutchings. *Quasi-phase-matched polarisation rotation in III-IV waveguides incorporating magneto-optic claddings*. in *Lasers and Electro-Optics, 2006 and 2006 Quantum Electronics and Laser Science Conference. CLEO/QELS 2006*. 2006.
56. Holmes, B., D.C. Hutchings, and J.J. Bregenzler, *Experiments towards the realisation of a monolithically-integrated optical isolator incorporating quasi-phase matched magneto-optical effects*, in *MRS Fall Meeting : Materials research society*. 2004, Materials Research Society: Boston, USA.
57. Bregenzler, J.J., et al. *Realization of a single-section passive polarization converter using a single-step etch process*. in *Lasers and Electro-Optics Society, 2004. LEOS 2004. The 17th Annual Meeting of the IEEE*. 2004.
58. Holmes, B.M. and D.C. Hutchings. *High efficiency and low loss fully integrated passive waveguide mode converters*. in *Lasers and Electro-Optics, 2006 and 2006 Quantum Electronics and Laser Science Conference. CLEO/QELS 2006. Conference on*. 2006.

Chapter 2

Theoretical background and literature review

2.1. Introduction

In this chapter, a review of semiconductor materials used throughout the investigation including bulk, quantum well and strained quantum well materials, are discussed. Further, semiconductor optical amplifiers (SOAs), which most aptly demonstrate the requirement for polarisation control in integrated optical circuits and photonic integrated circuits (PICs), are presented. Thereon, polarisation mode convertor theory and a review of major contributions in realisation of PMCs, are provided.

2.2. Material aspects

The field of optoelectronics is based principally upon the interactions between light and electrons within the materials through which the light is propagating. To ascertain the behaviour of optoelectronic materials and their characteristics, the fundamental principles of semiconductor physics are of great significance. In the next sections, a review of semiconductor materials including bulk, quantum well (QW) and strained quantum well materials are presented.

2.2.1. Semiconductor materials

The study of semiconductor materials started in the early nineteenth century [1] and over the years many semiconductor materials have been investigated. The elemental semiconductors, which are composed of single species of atoms, are found to be in group IV of the periodic table like Silicon (Si) and Germanium (Ge) [2, 3]. However, compound semiconductors, which are composed of two or more elements, can be found from group III and group V of periodic table like GaAs, GaP, AlGaAs, InGaAsP etc. Other compound semiconductors belong to group II and group VI of the periodic table like ZnS, ZnTe, CdS etc [4].

For a III-V compound semiconductor such as GaAs, The Gallium (Ga) and Arsenic (As) atoms form a zincblende structure which consists of two interpenetrating face centred cubic lattices in which one belongs to group III atoms (Ga) and the other to group V atoms (As) as shown in Figure 2.1.

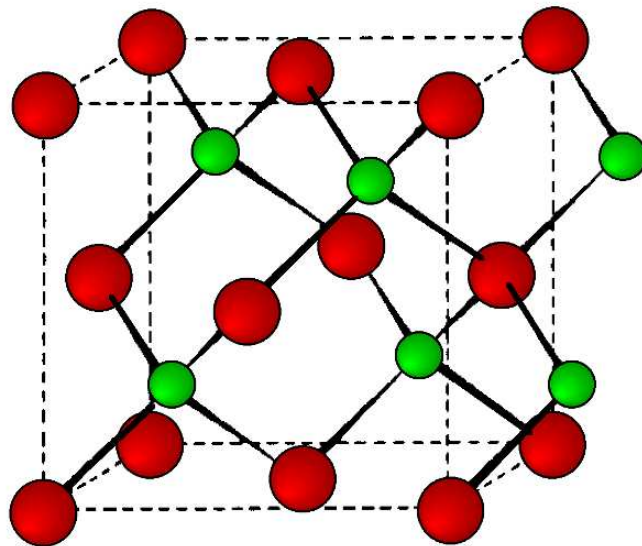


Figure 2.1: A schematic diagram of a GaAs zinc-blende structure.

The simplified planar bond structure [5, 6] of GaAs is shown in Figure 2.2 (a) and (b).

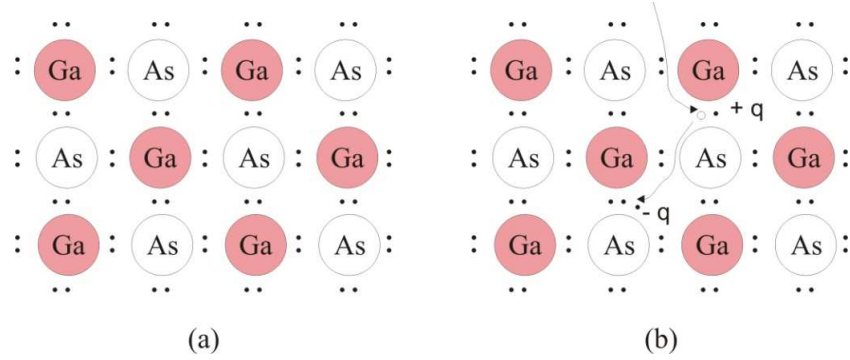


Figure 2.2: (a) A planar bond structure of GaAs lattice showing the two valance electrons shared by a Ga and an As atom and (b) a bond structure showing a broken bond due to the absorption of a photon with energy above the band-gap.

Here, each bond between adjacent atoms is indicated with two dots representing two valance electrons. These valance electrons are contributed by both Ga and As atoms. The bond structure shown in Figure 2.2 (a) clarifies that each Ga atom is connected to four nearby As atoms making four valance bonds. If there is no broken bond, this implies that there will be no free electrons available for conduction in the conduction band. The energy band diagram is shown in Figure 2.3. Here, E_c and E_v are the energies at the conduction and valance band edges respectively, whereas, the difference between the two is defined as the band gap energy E_g and is given by equation 2.1.

$$E_g = E_c - E_v$$

2.1

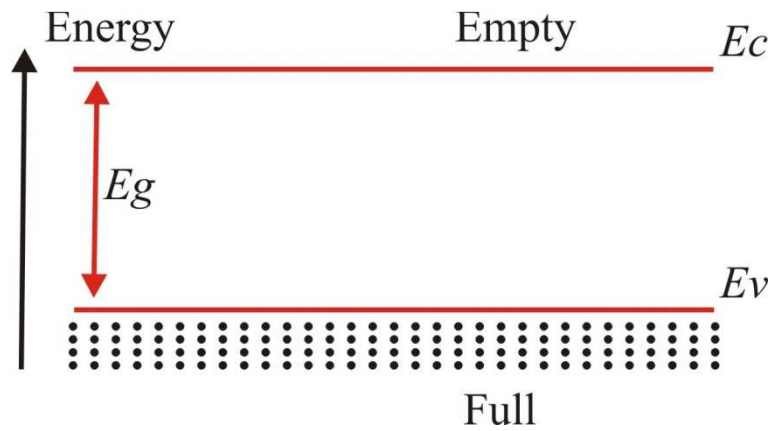


Figure 2.3: Energy-band diagram in real space.

When an incident photon with an optical energy $h\nu$, equal to or greater than the band-gap energy E_g , strikes the semiconductor material, optical absorption can occur. This absorption of the photon may break the valance bond and generate an electron-hole pair. This phenomenon is illustrated in Figure 2.4 where a dot represents a free electron propagating in the conduction band by leaving a hole in the valance band. Here, a hole is represented by the empty circle.

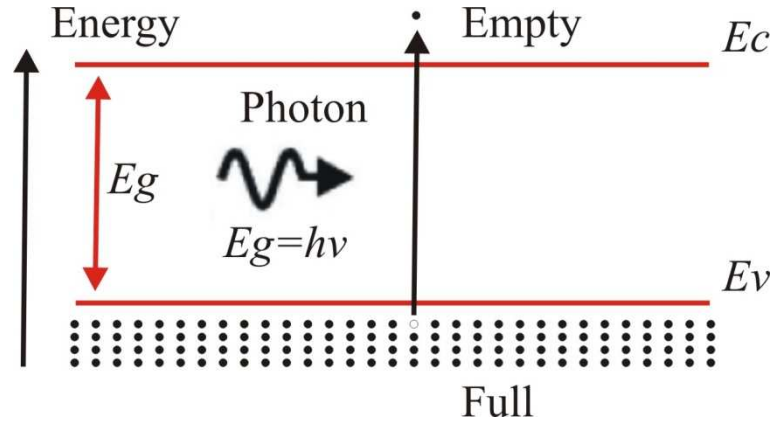


Figure 2.4: The energy-band diagram showing the energy levels of the electron and the hole when an incident photon having optical energy, equal to or greater than the band-gap energy strikes the semiconductor material.

If an electron in the conduction band recombines with the hole in the valance band, the excess energy emerges in the form of a photon. This process is referred to as spontaneous emission. Similarly if in the presence of a photon propagating in the semiconductor with the electrons in the conduction band and the holes in the valance band, the photon may stimulate the downward transition of the electron from the conduction band to the valance band and emit another photon, in phase with the incident photon and equal in energy in a process referred to as stimulated emission.

Semiconductor materials are generally characterised by their energy-band structures, such as direct band-gap or indirect band-gap as shown in Figure 2.5.

In direct band-gap materials (Figure 2.5 (a)), an electron-hole recombination occurs directly without the need of any phonon (or lattice

vibration) whereas in indirect band-gap materials (Figure 2.5 (b), phonons (or lattice vibrations) are needed for an electron-hole pair to recombine [4].

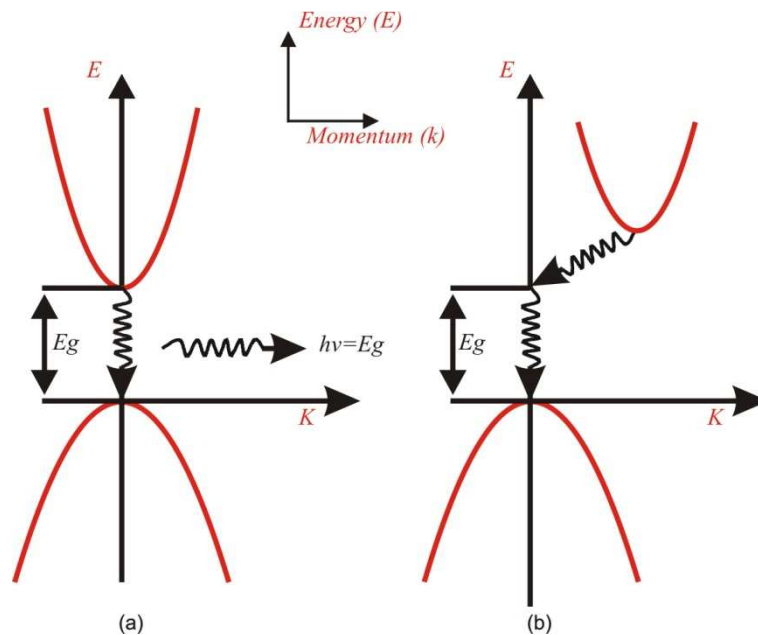


Figure 2.5: Energy-momentum diagram of (a) direct band-gap material and (b) indirect band-gap material.

Direct band-gap materials are the most suitable and efficient ones for optoelectronic device fabrication. As there is no need of momentum change for excited electrons to recombine, most of the injected carriers contribute for light (photon) generation in a direct recombination process. Therefore, the direct band-gap materials are preferred for making LEDs and LASERs. These materials are suitable light emitters through recombination process but also, as absorption of photons, causes electron-hole pairs generation, these can also be used as light detectors. The indirect band-gap materials (such as silicon) are used as detectors and in fabrication of solar cells, as they are less likely to re-emit the absorbed light.

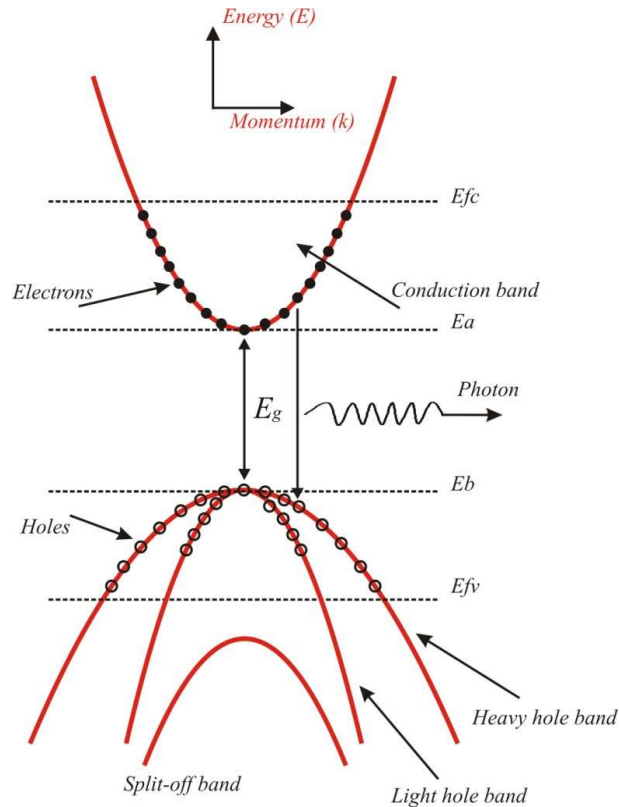


Figure 2.6: Energy-band structure of a direct band-gap semiconductor material.

2.2.2. Bulk material properties

The material used in the active region of any semiconductor material determines its gain, operational properties and characteristics. Semiconductor materials with an active region with dimensions significantly larger than the deBroglie wavelength ($\lambda_B = h / p$) are called bulk materials. This wavelength is associated to the momentum (p) of a particle and represents wave-particle duality. The active region of the bulk materials is grown using the direct band-gap materials where the top of the valance band and the bottom of the conduction band energies have the same momentum vector as shown in Figure 2.6. Here, the probability of radiative transitions from the conduction band to the valance band is much greater than the indirect band-gap materials. In Figure 2.6, there is one conduction band and three valance bands shown. Three valance bands represent heavy hole (hh), light hole (lh) and split off (so) bands.

The heavy and light hole bands are degenerate as the top of both bands have the same energy level and momentum. The energy of an electron at the bottom of the conduction band and the energy of the hole at the top of the valence band, is given by equations 2.2 and 2.3, respectively.

$$E_a = \frac{\hbar^2 k^2}{2m_c} \quad 2.2$$

$$E_b = \frac{\hbar^2 k^2}{2m_v} \quad 2.3$$

Where \hbar is the reduced Planck constant, which is equal to $h/2\pi$, k is the magnitude of the momentum vector and, m_c and m_v are the effective masses of the electron and the hole in the conduction and valence bands, respectively.

The concept of density of states plays an important role in optical absorption and gain processes in semiconductors. The density of allowed electron states (ρ_c) and occupation probability (f_c) of an electron, with energy E in the conduction band, is given by equations 2.4 and 2.5.

$$\rho_c(E) = \frac{1}{2\pi^2} \left[\frac{2m_c}{\hbar^2} \right]^{3/2} E^{1/2} \quad 2.4$$

$$f_c(E) = \frac{1}{1 + e^{\left[\frac{E - E_{fc}}{kT} \right]}} \quad 2.5$$

where E_{fc} is the quasi Fermi level of the conduction band with respect to the bottom of the band, k is the Boltzmann constant and T is the temperature.

The Fermi level is a reference energy level at which the probability of occupation by an electron is one half. Its position/placement on the semiconductor energy-band diagram depends upon the doping concentrations of the material.

The total electron density (n) can be calculated by taking the integral over all the allowable energies, of the product of density of states and the occupation probability of those states, given by equation 2.6.

$$n = \frac{1}{2\pi^2} \left[\frac{2mc}{\hbar^2} \right]^{3/2} \int_0^{\infty} \frac{E^{1/2}}{1 + e^{[(E - E_{fc})/kT]}} dE$$

2.6

Similarly the hole density in the valance band (p) can be given by equation 2.7.

$$p = \frac{1}{2\pi^2} \left[\frac{2mv}{\hbar^2} \right]^{3/2} \int_0^{\infty} \frac{E^{1/2}}{1 + e^{[(E_{fv} - E)/kT]}} dE$$

2.7

The electron and hole densities may then be used to calculate the optical gain of the material.

2.2.3. Quantum well material

Herbert Kroemer [7] was the first to propose in 1963, that population inversion could be remarkably enhanced in lasers, based on hetero-junctions. By incorporating a smaller layer of direct band-gap material like GaAs into the two larger band-gap layers of a material like AlAs, carriers can be confined in the lower band-gap area and lasing can occur with low threshold currents at the room temperature [8].

Later, it was further investigated and discovered that the band-gap can be controlled by making very thin layers in the active region. These thin layers are called quantum wells and are generally between 2 to 10 nm of thickness.

Electrons or holes can be confined in the direction perpendicular to the layer surface, although their movement cannot be completely blocked in the other directions. This confinement is a quantum effect and has deep effect on the density of states which becomes constant within certain energy levels in the quantum wells. A typical energy-density of states diagram for the quantum well and the bulk material is shown in Figure 2.7.

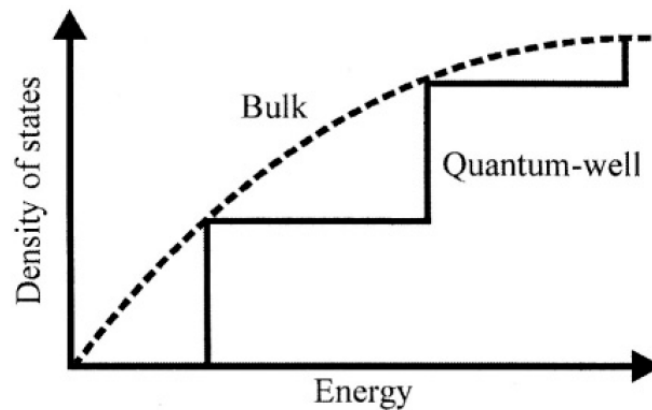


Figure 2.7: Energy-density of states for quantum well and bulk semiconductors.

The band-gap energy between the conduction band and the valence band can be controlled by the thickness of the well. It can be increased by narrowing the well, resultantly the wavelength is reduced. Therefore, by changing the thickness of the quantum well, the emitted wavelength can be altered in quantum well materials.

Quantum wells structures can be grown using modern crystal growth techniques [9], such as molecular beam epitaxy (MBE) or metal organic chemical vapor deposition (MOCVD). The details of these growth techniques are not explained in detail due to being beyond the scope of this work. Electrons and holes can both be confined in these wells, and once an electron or a hole is captured in the well, the probability that it can escape from this well becomes very low leading to more likelihood of recombination.

The energy band model for a single quantum well (SQW) is shown in Figure 2.8. Here, two type of holes, hh and lh are present in the valence band.

During recombination process, the electrons in the conduction band, and the holes in the valence band, recombine, resulting in the emission of a photon. This emission of a photon occurs, when the condition of degeneracy is satisfied, which is defined as a state at which the energy and the momentum of a heavy and light hole are the same. When the holes are not at degenerate state, they will emit more TE or TM depending upon their position in the valance band. If hh is closer to the conduction band, then TE will be more dominant than TM and vice versa.

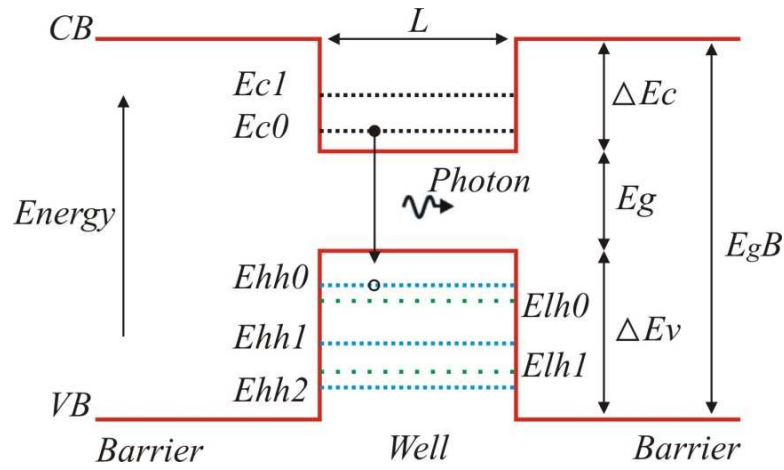


Figure 2.8: Energy band model for a single quantum well.

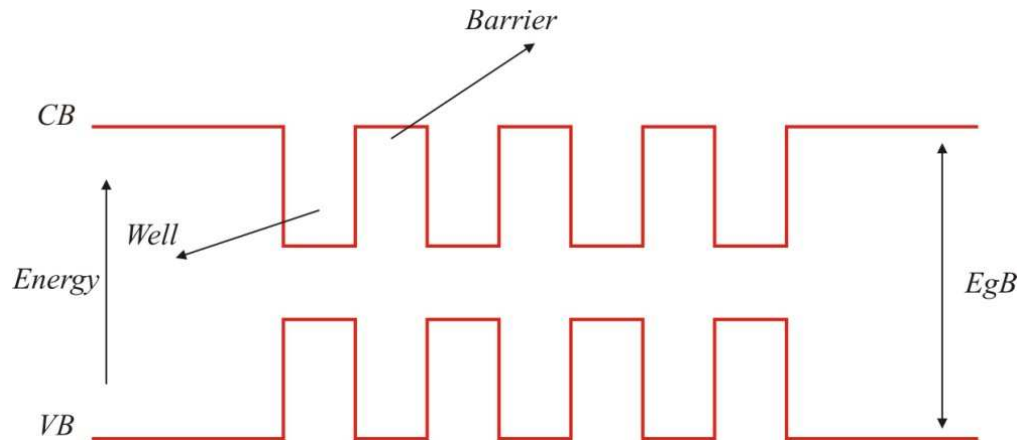


Figure 2.9: A schematic multi quantum well energy band diagram.

A multi quantum well (MQW) material can also be fabricated by stacking well and barrier layers (as shown in Figure 2.9). They have higher optical and carrier confinement due to the multi quantum wells as compared to the SQW material. The optical confinement factor of SQW depends upon the thickness of

the well and the refractive indices of the well and the barrier regions. Therefore, using multi-quantum wells, more confinement can be obtained. The confinement factor of MQW can be given as $\Gamma_{MQW} = N_w \Gamma_{SQW}$, where N_w is the number of wells and Γ_{SQW} is a SQW confinement factor. Furthermore, quantum well materials have wider optical bandwidth and higher saturation output powers compared to bulk material devices.

2.2.4. Strained quantum well materials

Quantum well materials can be classified un-strained or strained depending upon their growth. The gain coefficient for the un-strained quantum well is very polarisation dependent. This is due to the fact that the optically induced transitions from the conduction band to the heavy hole valance band are more favourable, i.e. more TE polarised light than the TM polarised light, whereas the transitions from the conduction band to the light hole valance band, which are more favourable to the TM polarised light, are less significant. Induced strain in the quantum well materials can control the polarisation sensitivity to some extent.

Strained layer super lattices [10, 11] have been of great interest since the early 1980s. It has been demonstrated that the material properties like lattice constant, band-gap and perpendicular transport effective mass can be altered by inducing strain within the semiconductor materials. Strain is induced in quantum well structures when the lattice parameter of the substrate does not match with the lattice parameter of the deposited layer, which must therefore deform in order for the two lattices to match with each other. Many applications of strained super lattices including long wavelength detectors [11] and semiconductor lasers [12] have been demonstrated. It has been shown that strained lattice material devices have superior performance in terms of polarisation sensitivity as compared to un-strained or conventional devices [13, 14]. Two types of strains, compressive and tensile can be induced in the semiconductor materials. The effect upon the band diagram of the un-strained, compressive and tensile strain quantum well materials is shown in Figure 2.10.

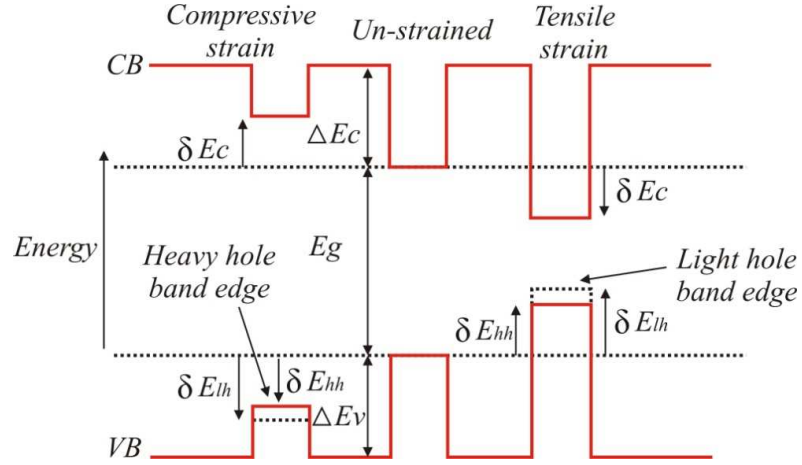


Figure 2.10: Band-edge profile for the compressive strained, un-strained and tensile strained quantum wells.

Strain induces a shift of δE_c in the conduction band edge and δE_{hh} and δE_{lh} in the heavy and light hole band edges respectively, which are given by [15].

$$\delta E_c = -a_c(2\varepsilon_{xx} + \varepsilon_{zz}) \quad 2.8$$

$$\delta E_{hh} = a_v(2\varepsilon_{xx} + \varepsilon_{zz}) + b(\varepsilon_{xx} - \varepsilon_{zz}) \quad 2.9$$

$$\delta E_{lh} = a_v(2\varepsilon_{xx} + \varepsilon_{zz}) - b(\varepsilon_{xx} - \varepsilon_{zz}) \quad 2.10$$

where

$$\varepsilon_{xx} = \frac{a_0 - a}{a} \quad \text{and} \quad \varepsilon_{zz} = -2 \frac{C_{12}}{C_{11}} \varepsilon_{xx}$$

In the above equations, a_c , a_v and b are the conduction band, valance band and shear deformation potentials respectively, a and a_0 are the well and the barrier lattice constants respectively. C_{11} and C_{12} are the shear elastic coefficients, respectively.

The value of these parameters and the effective masses of the electron and the hole depends upon the composition of the well and the barrier materials.

In compressive strained quantum wells, the heavy hole band edge is closer to the conduction band edge than the light hole band edge, which leads to the more TE gain than TM gain. Conversely, in tensile strained quantum wells, the situation is reversed and the light hole band is found to be closer to the conduction band edge than the heavy hole band, which leads to more TM gain than TE gain in the material. In these materials, TE and TM gains are difficult to equalise, so it is hard to get polarisation insensitive gain. Polarisation insensitive devices can also be fabricated by inducing compressive and tensile strains in a single layer or by using the strain effects in the barrier layers of the quantum well materials. However, it is very difficult to achieve in practice [16-18].

When strain is induced in the material (either compressive or tensile), the cubic symmetry of the lattice is disturbed, which results in the removal of the degeneracy of the heavy and light hole bands. Due to large strain, hole effective mass is significantly reduced [18-22] along with the density of states [22, 23]. In this research work, InP/AlGaInAs material, which predominantly emits TE light, is used. This is a strained material, and described in detail in chapter 6.

2.3. Semiconductor optical amplifiers

Semiconductor optical amplifiers (SOAs), most aptly demonstrate the requirement for polarisation control in integrated optical circuits and photonic integrated circuits. These are fabricated in active media; the structures include a waveguide within a semiconductor gain medium. In an SOA, the injected signal propagates in the waveguide and is amplified through stimulated emission. This amplification process is referred to as a gain, which is achieved by inducing a population inversion in the active region of the waveguide using electrical pumping. As to the author's knowledge, the highest gain obtained in quantum dot SOAs is 18 dB at 1300 nm wavelength [24]. The different SOA structures available today are based on the semiconductor p-n double hetero-structures, providing carrier confinement and optical guiding.

Early studies on SOAs were carried out in the 1960's at the time when semiconductor lasers were first introduced. Later, several different types of SOA were demonstrated, in 1970's and 1980's [25-28], which operated at 830 nm, 1300 nm and 1550 nm wavelengths [29]. Initially, SOAs were fabricated with asymmetrical waveguide structures having large polarisation sensitive gains. However, later (in 1989) SOAs with much reduced polarisation sensitivities [30] were fabricated with symmetrical waveguide structures. Onwards development in SOA design and fabrication progressed with advances in materials, fabrication technologies and devices (photonic integrated circuits), to a point where reliable and cost effective devices became available for use in optical communication systems.

In SOAs, optical feedback and polarisation insensitivity are the two main challenges to accept them as practical amplifiers. The former is due to reflections at the cleaved facets, resulting in high gain reduction in the cavity resonance of the SOA. Therefore it is desirable to design SOAs to suppress the reflections from the end facets, and the facet reflectivities should satisfy the condition given in equation 2.11 [31].

$$G\sqrt{R_1R_2} < 0.17$$

2.11

Where G is the single pass amplification factor, and R_1 and R_2 are the power reflection coefficients at the input and output facets, respectively.

Polarisation sensitivity is another un-desirable feature of early SOAs, as the state of polarisation of the input signal varies randomly with time. Due to this, different amplifier gains appear for the transverse electric (TE) and the transverse magnetic (TM) modes of the semiconductor waveguide structures. Different techniques are employed to realise polarisation independent SOAs. These techniques include square cross section [32-35] or ridge waveguides [36] or strained layer super-lattice materials [16, 37-39]. The strain induced in the layers of the active region of the waveguide has a strong effect, and this is used to control the polarisation. TE and TM confinement factors are equalised by the

effects of compressive and tensile strains either in the quantum well layers or barrier layers (as described in previous sections). In this research work, SOAs are used in integrated devices which act as differential phase shifter (DPS), and are further described in chapter 6.

2.4. Polarisation mode convertors theory

2.4.1. Maxwell's Equations

In optics, classical and quantum theories are benchmarks. In classical theory, the behaviour of light is considered in terms of electromagnetic fields and waves. Here, absorption and emissions have no importance and, therefore, it is suitable for use, in modelling passive components. Quantum theory describes that the light is composed of photons and exchange of energy occurs when photons interact with electrons. This theory is largely applied to active components [40].

The laws of electricity and magnetism, in classical theory, are described by Maxwell's equations. These equations are the experimental verification of the existing theories of current and magnetism and provide the relations of different quantities describing the electric and magnetic fields. These quantities are electric displacement vector \mathbf{D} , electric field strength \mathbf{E} , magnetic flux density \mathbf{B} , magnetic field strength \mathbf{H} and current density \mathbf{J} .

Maxwell's equations in differential form and in free space are given in equations 2.12 to 2.15.

$$\nabla \cdot \mathbf{D} = \rho_f \tag{2.12}$$

$$\nabla \cdot \mathbf{B} = 0 \tag{2.13}$$

$$\nabla \times \mathbf{E} = -\frac{\partial \mathbf{B}}{\partial t} \tag{2.14}$$

$$\nabla \times \mathbf{H} = \mathbf{J}_f + \frac{\partial \mathbf{D}}{\partial t}$$

2.15

In the above equations, ρ_f is the volume density of free charges and \mathbf{J}_f is the current density. These equations 2.12, 2.13, 2.14 and 2.15 are also called Gauss's law, Gauss's law for magnetism, Faraday's law of induction and Ampere's law (with Maxwell's correction), respectively [40].

2.4.2. Wave Equations

A prominent feature of Maxwell's equations is to predict the presence of harmonically varying electric and magnetic fields, which are also known as electromagnetic waves. Wave equations can be derived by the assumptions that neither any current \mathbf{J} nor any charges ρ are present, and assuming non magnetic material ($\mu = \mu_0$) where μ_0 is the permeability of the free space, which is $4\pi \times 10^{-7}$ V·s/(A·m).

If we put $\mathbf{D} = \epsilon \mathbf{E}$ and $\mathbf{B} = \mu_0 \mathbf{H}$ in equations 2.14 and 2.15 then there will be only two variables \mathbf{E} and \mathbf{H} . Here, ϵ is the permittivity of the material and is equal to $\epsilon_0 \epsilon_r$, where ϵ_0 is the permittivity of free space (8.85×10^{-12} F/m) and ϵ_r is relative permittivity of the material, which is unity for free space. By taking the curl (vectorial operator) of equation 2.14, it yields

$$\begin{aligned} \nabla \times (\nabla \times \mathbf{E}) &= \nabla \times \left(-\frac{\partial \mathbf{B}}{\partial t} \right) \\ &= \nabla \times \left(-\frac{\partial (\mu_0 \mathbf{H})}{\partial t} \right) \\ &= -\mu_0 \frac{\partial}{\partial t} (\nabla \times \mathbf{H}) \\ &= -\mu_0 \frac{\partial}{\partial t} \left(\frac{\partial \mathbf{D}}{\partial t} \right) \end{aligned}$$

$$= -\mu_0 \frac{\partial^2 \mathbf{D}}{\partial t^2}$$

2.16

By using the following standard vector quantity to simplify equation 2.16

$$\nabla \times (\nabla \times \mathbf{F}) = \nabla(\nabla \cdot \mathbf{F}) - \nabla^2 \mathbf{F}$$

2.17

Here, the operator ∇ is a gradient of the scalar function ϕ , and ∇^2 is a Laplacian and both are defined in Cartesian coordinates given in equations 2.18 and 2.19.

$$\nabla \phi = \frac{\partial \phi}{\partial x} \mathbf{i} + \frac{\partial \phi}{\partial y} \mathbf{j} + \frac{\partial \phi}{\partial z} \mathbf{k}$$

2.18

$$\nabla^2 = \frac{\partial^2}{\partial x^2} + \frac{\partial^2}{\partial y^2} + \frac{\partial^2}{\partial z^2}$$

2.19

Using equations 2.18 and 2.19, equation 2.16 can be reduced to

$$\nabla(\nabla \cdot \mathbf{E}) - \nabla^2 \mathbf{E} = -\mu_0 \partial^2 (\boldsymbol{\varepsilon} \mathbf{E}) / \partial t^2$$

2.20

This equation 2.20 is known as the wave equation for the electric field \mathbf{E} .

If the medium is homogeneous and isotropic, there is no charge and assuming that $\boldsymbol{\varepsilon}$ is not time dependent then equation 2.20 can be given as

$$\nabla^2 \mathbf{E} = \mu_0 \boldsymbol{\varepsilon} \frac{\partial^2 \mathbf{E}}{\partial t^2}$$

2.21

This equation 2.21 is called the vector wave equation for the electric field \mathbf{E} .

Similarly the vector wave equation for the magnetic field \mathbf{H} can be derived which is given as

$$\nabla^2 \mathbf{H} = \mu_0 \epsilon \frac{\partial^2 \mathbf{H}}{\partial t^2}$$

2.22

The time independent wave equations for the electric field \mathbf{E} and the magnetic fields \mathbf{H} can also be derived from the aforementioned wave equations, which are given in equations 2.23 and 2.24.

$$\nabla^2 \mathbf{E} + \omega^2 \mu_0 \epsilon \mathbf{E} = 0$$

2.23

$$\nabla^2 \mathbf{H} + \omega^2 \mu_0 \epsilon \mathbf{H} = 0$$

2.24

These equations 2.23 and 2.24 are also applicable for the electric and magnetic fields oscillating with a single angular frequency ω [40].

2.4.3. Plane waves

The simplest solution to the wave equation (Helmholtz equation) is represented by a plane wave. A plane wave is a wave, whose surfaces of constant phase are infinite planes, perpendicular to the direction of propagation. Figure 2.11 shows the geometry of the plane wave travelling in the +z direction.

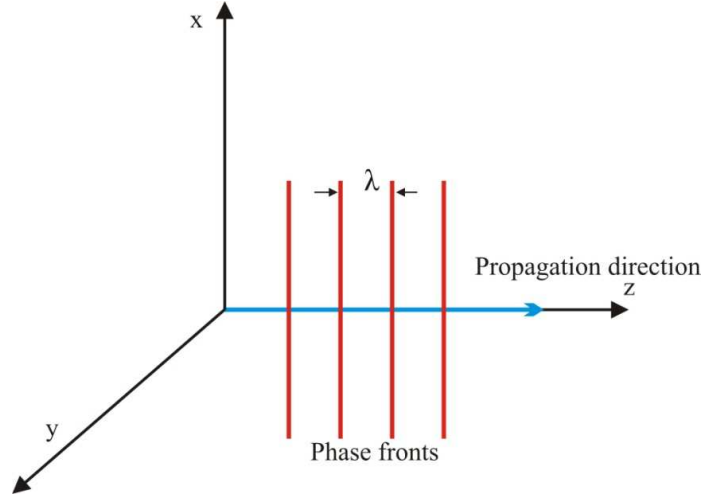


Figure 2.11: The geometry of a plane wave travelling in +z direction.

From Figure 2.11, it can be observed that the field variation is in the z direction, and there are no field quantities varying in x and y directions. i.e. $\partial/\partial x = \partial/\partial y = 0$. For simplicity, it is possible to consider the electric field to have only a single component, i.e. in the x direction. Then equation 2.23 can be written in a scalar equation, which is

$$\frac{d^2 E_x}{dz^2} + \omega^2 \mu_0 \epsilon = 0$$

2.25

After derivation, this equation has a solution in the form, which is given as

$$E_x = \hat{E}_x e^{(-jkz)}$$

2.26

where \hat{E}_x is a constant. By directly substituting this, in equation 2.25, this is valid for wave number (k), provided

$$k = \omega(\mu_0 \epsilon)^{1/2}$$

2.27

Therefore, the full solution in the time variation for forward propagating waves can be given as

$$E_x = \hat{E}_x e^{j(\omega t - kz)} \quad 2.28$$

The wave number (k) can be expressed as

$$k = 2\pi/\lambda \quad 2.29$$

Here, λ is a wavelength, representing the distance separating planes of equal phase as shown in Figure 2.11.

The velocity of the wave, which is referred to as its phase velocity, is given by

$$V_p = \omega/k \quad 2.30$$

From equation 2.27, the phase velocity can be calculated using equation 2.30, thus

$$V_p = 1/(\mu_0 \epsilon)^{1/2} \quad 2.31$$

After putting values of μ_0 and ϵ_0 in equation 2.31, phase velocity is obtained 3×10^8 m/s, which is equivalent to the velocity of light (c). This is a major success of Maxwell's equations.

2.4.4. Polarisation

Light is a transverse electromagnetic wave where the electric and magnetic field vectors oscillate at right angles to each other. By virtue of its transverse character, light can be polarised, such that the field vectors assume an ordered

arrangement in space and time. For linear polarisation, the electric field vectors all lie in a well-defined plane called the plane of polarisation. The magnetic field vectors then lie in an orthogonal plane. The process of transforming un-polarised light into polarised light is known as polarisation. If the electric field of a plane wave in vacuum propagates in the z direction then the most general form of the electromagnetic wave is given in equation 2.32 [40].

$$\mathbf{E} = E_x e^{j(\omega t - kz + \phi_x)} \mathbf{i} + E_y e^{j(\omega t - kz + \phi_y)} \mathbf{j}$$

2.32

where ϕ_x and ϕ_y are constant arbitrary phase factors. The polarisation of the resulting wave mainly depends upon the values of E_x , E_y , ϕ_x , and ϕ_y .

If the magnitude of the electric field vector is constant in the x and y directions and there is no change in the phases, i.e. $\phi_x = \phi_y$, then the polarisation is linear polarisation and can be expressed mathematically as

$$\mathbf{E} = E_0 e^{j(\omega t - kz + \phi)}$$

2.33

$$\text{where } E_0 = [E_x \mathbf{i} + E_y \mathbf{j}]$$

In equation 2.33, the direction of the electric field vector is independent of time and space, therefore it is defined by a new vector, E_0 . E_0 is the vectorial sum of $E_x \mathbf{i}$ and $E_y \mathbf{j}$ as shown in Figure 2.12. In linear polarisation, the direction of the electric field vector E_0 gives the direction of polarisation.

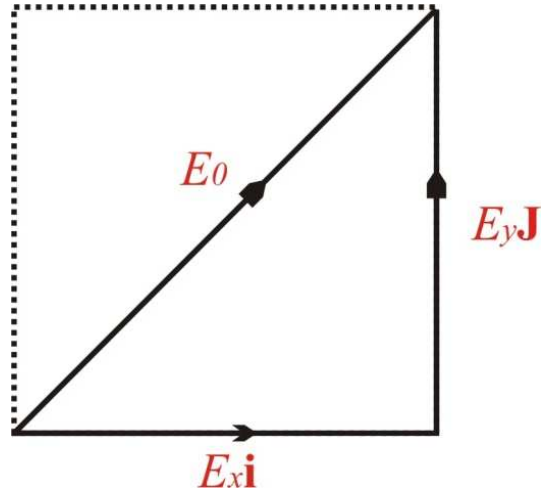


Figure 2.12: Construction of the polarisation vector.

But if there is a change in the phases such as $\phi_x = \phi_y \pm \pi / 2$ and no change in the magnitude of the electric field vectors, then the polarisation is said to be circular polarised (left hand or right hand) and mathematically expressed as

$$\mathbf{E} = E_0 e^{j(\omega t - kz + \phi)} \mathbf{i} + E_0 e^{j(\omega t - kz + \phi \pm \pi / 2)} \mathbf{j}$$

2.34

$$\text{where } E_0 = [E_x \mathbf{i} + E_y \mathbf{j}]$$

When both the phase and the magnitude of the electric field vectors are not equal then the polarisation described as elliptical polarisation.

Schematic representations of linear, right circular, left circular, right elliptical and left elliptical polarisations light are shown in Figure 2.13.

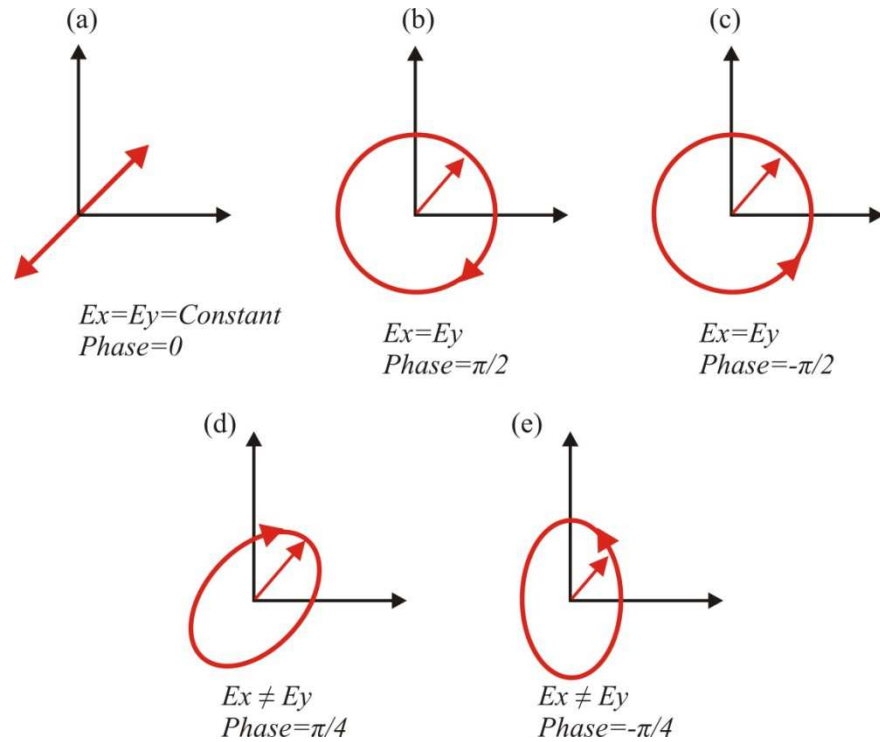


Figure 2.13: Schematic representations of polarised lights (a) linear (b) right circular (c) left circular (d) right elliptical and (e) left elliptical.

2.4.5. Birefringence

The relative permittivity (ϵ_r) of a crystal (material) mainly depends upon its electronic polarisability, which involves the displacement of electrons in various directions of the material. This change in ϵ_r in various crystal directions means that the refractive index of the material depends upon the direction of the electric field in the propagating light. Consequently, the velocity of light in the material depends upon the direction of propagation and the state of polarisation of the light.

Generally, the propagation of light through crystals can be described in terms of the materials refractive indices, which are referred to as principle refractive indices n_1 , n_2 and n_3 along three directions x, y and z, respectively. These directions are mutually orthogonal to each other. Depending upon the lattice structures of the crystallographic material, these structures can be categorized in terms of their optical properties [40]. These can be cubic, uniaxial

or biaxial structures. In cubic crystal structure, the atomic lengths of the three unit cell dimensions are equal. Therefore, ϵ_r is the same in all the three directions, resultantly the refractive indices are the same, i.e. $n_1 = n_2 = n_3$. These types of crystals are called isotropic crystals. In uniaxial crystal structures, there are two identical and one unique unit cell dimensions. Therefore, the relative permittivity components are the same in two directions, although, different in the third direction. This results in two identical refractive indices and one unique refractive index, i.e. $n_1 = n_2 \neq n_3$. In biaxial crystal structures, the unit cell dimensions are not the same in all three directions resulting in three different ϵ_r components. Resultantly, there are three different refractive indices, i.e. $n_1 \neq n_2 \neq n_3$. This phenomenon, in which changes in refractive indices occur, is referred to as birefringence.

When light passes through any uniaxial material, it decomposes into two orthogonally polarised rays, which travel with different phase velocities, as they experience different refractive indices. These two polarised rays are called ordinary ray and extraordinary ray. The ordinary ray has the same phase velocity in all directions and the field is perpendicular to the phase propagation direction, whereas, the extraordinary ray has a phase velocity which depends upon the direction of propagation and its state of polarisation.

In waveguides, these two different rays are known as TE and TM modes. This division of modes (Birefringence) is due to two dissimilar refractive indices for different polarisations to the material with single axis of anisotropy. Therefore, the birefringence magnitude is defined as

$$\Delta n = n_e - n_o$$

2.35

Where n_e and n_o are the refractive indices for polarisations perpendicular (ordinary) and parallel (extraordinary) to the axis of anisotropy respectively (in waveguides this becomes n_{TE} and n_{TM}).

Mainly, the materials used in integrated optics are based on isotropic materials like GaAs, InP or Si. These isotropic materials can be converted into anisotropic by applying electric or magnetic fields, mechanical stress or changing the waveguide cross-section geometry. Therefore for realisation of passive PMCs in integrated form, form birefringence [41], which is also known as a shape or geometrical birefringence, is introduced. This is achieved by different techniques including slanted side walls and sub-wavelength air trenches. The detail description of these techniques is given in the subsequent sections.

2.4.6. Retardation

The phase velocity in the material is given as c/n , where c is the velocity of light and n is the refractive index. The perpendicular (ordinary) and parallel (extraordinary) beams to the optical axis travel at different phase velocities in the waveguides, where relative to each other, one is slow and the other is fast, depending upon the refractive indices of the respective paths. The axis which has lower refractive index is referred to as the fast axis, whereas the other is referred to as the slow axis (in uniaxial material). When these two light components emanate from the waveguide, their relative phases have been shifted. This phenomenon is called retardation and is the basis for the construction of wave plates. A schematic diagram of a retarder plate is shown in Figure 2.14.

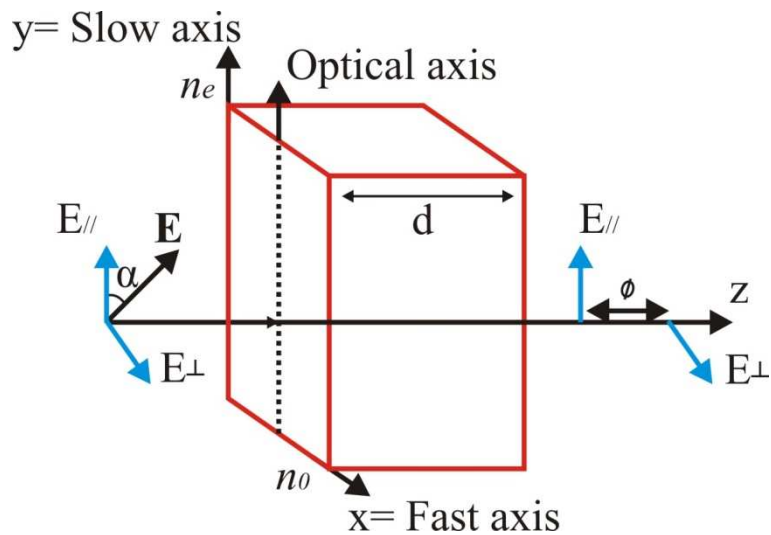


Figure 2.14: A retarder plate.

In Figure 2.14, the optical axis (y-axis) is parallel to the plate face. When linearly polarised light is incident on the plate face, the field parallel to the optical axis ($E_{//}$) travels as an extraordinary wave, whereas the field perpendicular (E_{\perp}) to the optical axis travels as an ordinary wave. Here, the extraordinary wave travels slower than the ordinary wave since $n_e > n_o$. Therefore, the optical axis is slower for waves polarised parallel, and faster for waves polarised perpendicular to it. When the beam comes out at the output side, these two wave components have been phase shifted by ϕ . This phase shifting depends upon the initial angle (α) of \mathbf{E} and the thickness of the crystal. Therefore, the initial linear polarisation light can be rotated or changed into circularly or elliptically polarised light at the output. This is summarized in Figure 2.15.

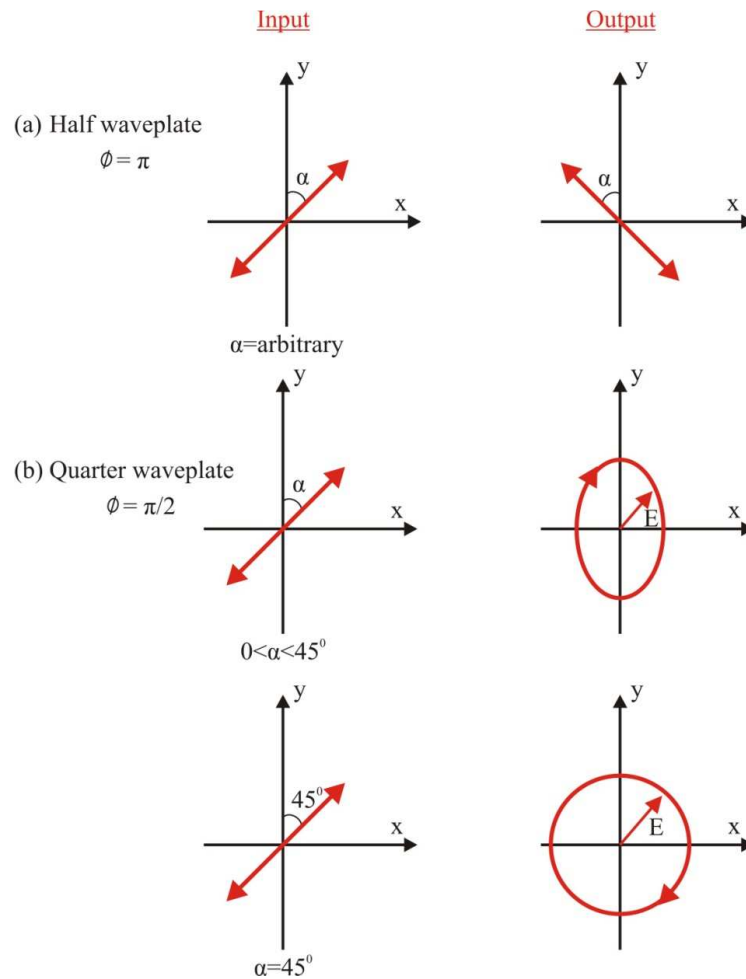


Figure 2.15: Input and output polarisations of light through (a) a half wave-plate and (b) a quarter wave-plate.

If the thickness of the plate (as shown in Figure 2.14) is d , then the perpendicular (ordinary) beam to the optical axis experiences a phase change $\phi_o = k_o d$ through the material where k_o is the wave-vector of the ordinary wave and is given as $k_o = kn_o = (2\pi / \lambda)n_o$. Here, λ is the wavelength of the free space. Similarly, the parallel (extraordinary) beam to the optical axis experiences a phase change of $\phi_e = (2\pi / \lambda)n_e d$ through the material. Therefore, the phase difference between these two components of the incident beam is given as

$$\phi = \frac{2\pi}{\lambda}(n_e - n_o)d$$

2.36

Equation 2.36 specifies that the resultant polarisation depends upon the type of the material and its thickness d . It should be noted that for actual magnitudes, the phase difference ϕ between the ordinary and extraordinary components of the field determines the polarisation state of the light.

If the phase difference ϕ between the two orthogonal components of the field is π (180°), which corresponds to one half of the wavelength ($\lambda/2$) of retardation, then the retarder is referred to as a half wave-plate. If the phase difference ϕ is $\pi/2$ (90°), this corresponds to the quarter of the wavelength ($\lambda/4$) of retardation and is referred to as a quarter wave-plate [42, 43].

2.4.7. Electro-optic effects

When an external electric field is applied to a material, the refractive index of the material is changed, which alters the optical properties of the material. When an electric field is applied, it alters the movement of electrons in the material, and, therefore, a change in optical properties is observed. Hence isotropic materials can become birefringent. Once the electric field is applied, the refractive index of the material can be calculated as

$$n' = n + a_1 E + a_2 E^2 + \dots$$

Here, a_1 and a_2 are the linear and second order electro-optic coefficients respectively. Higher order values of electric field (E) are very small and can be neglected. The variation of refractive index due to the first term E is called the Pockels effect and due to the second term E^2 is called the Kerr effect in equation 2.37.

Electro-optic effects can be used for controlling the phase, frequency, amplitude or polarisation of the modulated beam in electro-optic modulators. The polarisation modulation is achieved by controlling the signal on the element using the electro-optic effect, which can modulate the input beam of light emanating from the laser diode. This can be achieved up to gigahertz (GHz) rates [44].

2.4.8. Carrier induced effects

The refractive index of a quantum well material can be changed by a variation in carrier concentration. This occurs, when interactions between the carriers change the absorption band edge of the material [45]. The main factors which change the refractive index of the material involving carrier injection are band filling, band edge shrinkage and free carrier absorption.

In band filling, which is also known as Burstein-Moss effect, the absorption for photon energies is reduced slightly above the nominal band-gap of the semiconductor material. This effect can be observed by doping the semiconductors [46], due to which, the lower states of the conduction band in n-type of the material and higher states in the valance band in p-type of the material are filled. Therefore, a greater energy than the nominal band-gap energy is required when optically exciting electrons from the valance band to the conduction band. Resultantly, the absorption co-efficient is decreased above the nominal band-gap. This band filling effect occurs due to the free carriers; therefore, injection should be equivalent to doping, except that injection will result in band filling effects from both the electrons and holes [45]. The refractive index

change due to carrier injection is largest for the photon energies near the band-gap of the material as compared to energies far above or below the nominal band-gap.

Band-gap shrinkage (re-normalization) occurs when the injected carriers occupy the states at the bottom of the conduction band and at the top of the valence band. When this concentration is quite high, the electron and the hole wave functions overlap each other in the conduction band and the valence band, respectively. Resultantly, a gas of interacting particles is formed. These electrons in the conduction band and holes in the valence band repel each other due to the Coulombic force. Hence, reducing the band-gap energy, and further change in the absorption coefficient and refractive index [46]. The band-gap shrinkage is determined by the free carrier density, so it is nearly independent of the impurity concentrations.

Change in the absorption coefficient and refractive index in both band filling and band-gap shrinkage effects is mainly observed in inter-band effects. However, a free carrier can also absorb a photon and move to a higher energy state, intra-band. This phenomenon is known as free carrier absorption (plasma effect) [46]. In this effect, the change in refractive index is always negative, hence it will add to band filling for energies below the material band-gap.

The above stated three mechanisms for carrier induced effects; band filling, band-gap shrinkage and free carrier absorption are independent to each other. However, the total change in the refractive index is the sum of all three effects.

2.5. Review of the major contributions to polarisation mode converters

In modern communication systems, polarisation handling is of immense importance as there are a number of devices which are totally polarisation sensitive. The polarisation conversion is a key element in polarisation multiplexing, polarisation based filtering and polarisation diversity [47]. PMCs provide the basis to manipulate and control the polarisation states of light in

integrated optical devices and circuits. Both active and passive components have an ability to integrate PMCs to overcome this. In semiconductor optoelectronic systems, an exchange of power between polarisation states, due to bends, tappers, and junctions, can occur. Therefore, careful appropriate designs are needed to eliminate or to minimize any detrimental polarisation effects.

Photonic integrated circuits must be polarisation insensitive especially at the point when the signals are entering from the optical fibres, because these circuits are used as detectors, multiplexers or digital cross connects. In the last few years, many PMCs have been realised and demonstrated; on GaAs/AlGaAs, InP/InGaAsP, silicon on insulator (SOI) and InGaAsP based quantum well structures. Based upon the design parameters, PMCs can be active or passive in nature. PMCs are referred to as active if controlled by an external influence (current or voltage) or otherwise, referred to as passive PMCs. Passive PMCs can be realised using different approaches and can be categorised according to their functionality, which is illustrated in Figure 2.16.

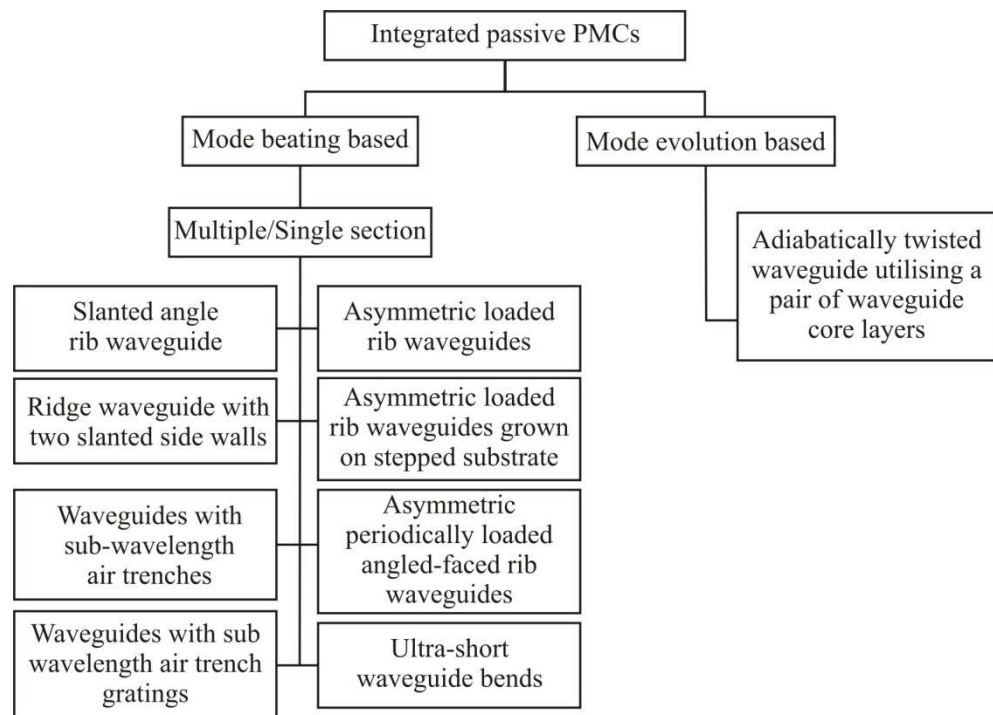


Figure 2.16: Different approaches to the realization of PMCs.

Shani et al. [48] realised the first PMC in 1991 by employing an asymmetric periodically loaded rib waveguide. These asymmetric loaded rib waveguides create perturbation in the optical axis of the waveguide and causes polarisation to rotate. In his experiments, TE-TM conversion was obtained in a 3.7 mm long waveguide with 2-3 dB excess loss and with 80% rotation. A schematic picture of periodic asymmetric rib waveguide is shown in Figure 2.17. Huang [49] in 1992 demonstrated theoretically that full polarisation rotation can be attained due to the phase matching of the TE and TM modes through the asymmetric periodic loading of the waveguides. Further F. J. Mustieles and Gustavsson also presented their work on asymmetrically loaded waveguides [50, 51]. Based on the asymmetrically loaded rib waveguide design, Obayya et al. proposed a new improved design for a short and low loss PMC [52]. He obtained 98% of polarisation mode conversion with a $0.74 \mu\text{m}$ long device with 0.13 dB insertion loss at a wavelength of $1.5 \mu\text{m}$. He used the full vector beam propagation method based on the finite element method.

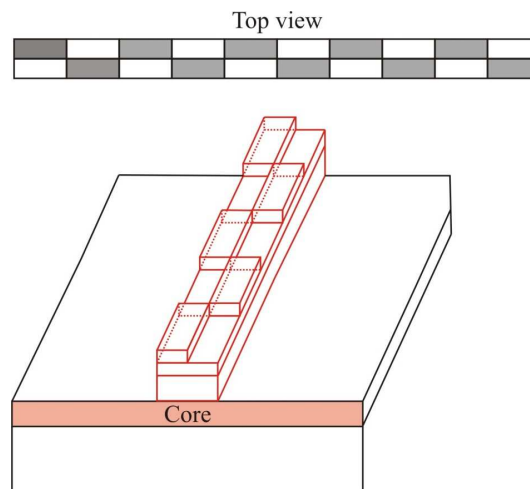


Figure 2.17: A schematic diagram of the periodic asymmetric rib waveguide.

H. Heidrich [53] realised the passive PMC based on the periodically tilted and shifted waveguides on InP/InGaAsP stepped substrate structure. In order to achieve a rotation of the optical waveguide axis relative to the surface of the substrate, modification is made in the surface of the substrate underneath the core area. A schematic of this technique is shown in Figure 2.18. Using this technique,

a 45° rotator is realised with 3 dB loss. However, due to the critical formation of stepped substrate, it is very difficult to integrate with other optical components on the same chip.

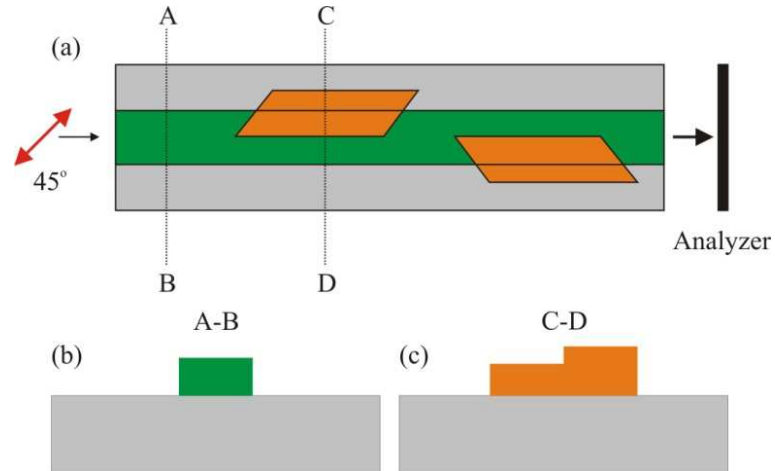


Figure 2.18: (a) A schematic diagram of top view of the passive 45° PMC based on tilted rib waveguides (b) cross section of the feeding waveguide (A-B) and (c) cross section of the converter section (C-D).

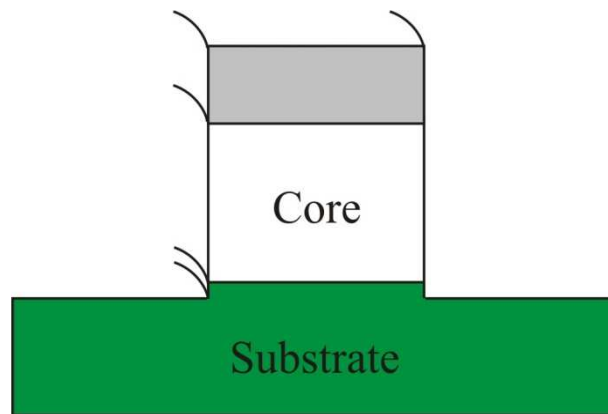


Figure 2.19: A schematic diagram of a deep etched bended waveguide structure used for the polarisation conversion.

PMCs have also been fabricated using integrated and ultrashort bends [54]. A schematic diagram of deep etched bended ridge waveguide structure used for the polarisation conversion is shown in Figure 2.19. The device fabricated with this structure has attained 85 % and 45 % polarisation conversions with excess loss of 2.7 dB and 0.4 dB with device dimensions of $975 \times 83 \mu\text{m}$ and 760×86

μm , respectively. Van der Tol [55] proposed PMC with a series of asymmetric loaded waveguides and with angled facets. This design was a modification of the previously stated asymmetrical ridge waveguide structures. This design consisted of long device lengths as multiple sections are required to achieve the significant polarisation conversion. This also showed excess losses on the interfaces of multiple coupling sections in the device. In addition to design parameters, fabrication is also a key challenge in these devices, as monolithic integration is quite demanding.

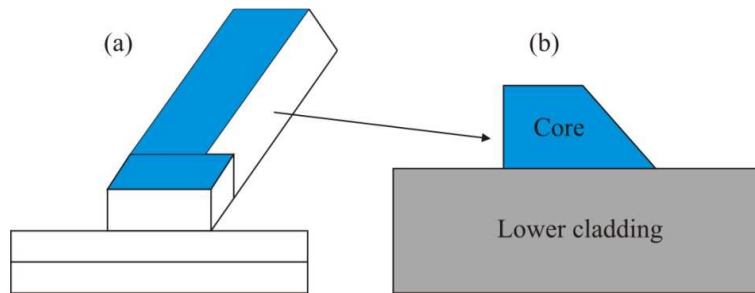


Figure 2.20: (a) A schematic diagram of a single section passive PMC with angled facet waveguide structure and (b) the cross-sectional profile of the device.

Huang et al. [56] designed and fabricated a single section PMC with one slanted and one straight wall as alternative to the periodically asymmetric loaded rib waveguides. During fabrication, he achieved a straight wall using the dry etch technique and slanted wall with the wet chemical etching procedure. This type of device requires an accurate re-masking alignment between the two etch process steps. There are also optical losses due to mode size mis-matching at the convertor section interface with the symmetric waveguide section. This device was realised on GaAs/AlGaAs with the device length of $720\ \mu\text{m}$ and with 96 % rotation. El-Refaei et al. [57, 58] demonstrated these type of devices theoretically and experimentally. He obtained polarisation conversion of 99.68 % with the device length of $226\ \mu\text{m}$ at a wavelength of $1550\ \text{nm}$.

Reactive ion etching (RIE) lag phenomenon [59] was also used to realise different etch depths in the same asymmetric waveguides. In this phenomenon, aspect ratio dependent etching is performed, where, as the aspect ratio of the

feature increases, the depth of an etched feature becomes proportional to the width. Here, small features are etched slowly in comparison to large features [60]. Holmes et al. [61-65] realised such a device with efficiencies of greater than 96 %. This device had low loss, with 150 μm conversion length. The fabrication of the structure of this type of device was vastly simplified, as only one step was required for the dry etch process. Due to this, fabrication errors can be minimized. A schematic diagram of the cross-section profile of this device structure is shown in Figure 2.21. Kim S.H. et al. [66] later demonstrated a single trench PMC using this technique. He attained 95 % polarisation conversion with a 210 μm long device. PMCs based on sub-wavelength air trench gratings are realised by Kotlyar et al. [67]. This design was based on the principle that an incident linear polarised mode is forced to convert into two orthogonal components; one of which becomes polarised in the direction of the etched air trench, whereas the other becomes orthogonal to it. The polarised component in the direction of air trench imparts lower refractive index, resultantly moves with higher phase velocity than the other component. These devices are quite short as high form birefringence is introduced by air trenches.

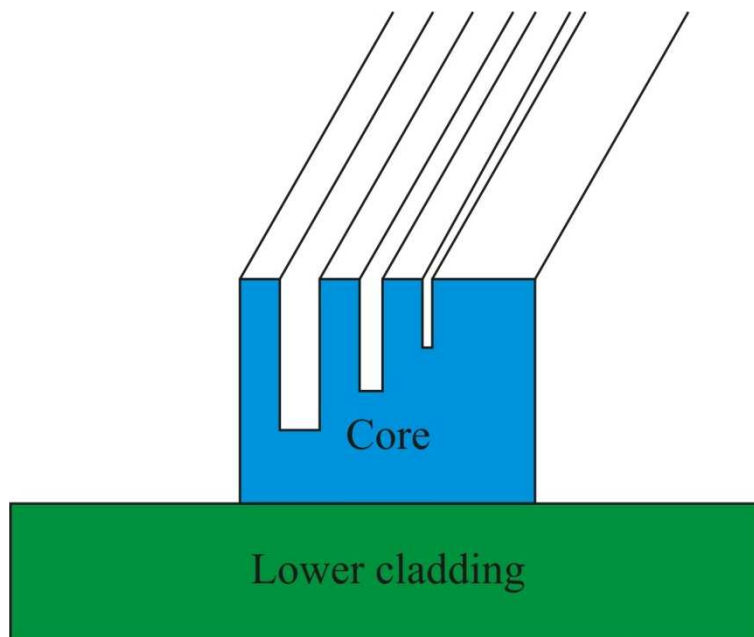


Figure 2.21: A schematic diagram of cross-section profile of RIE Lag structure.

A passive PMC has been designed and fabricated with both side walls tilted [62, 68-70] in the same direction with RIE as well as with chemically assisted ion beam etching (CAIBE) [71] techniques. A schematic diagram of cross-sectional profile of tilted waveguide facet in both directions of this device is shown in Figure 2.22. Here, a polarisation conversion of greater than 80 % is attained for a convertor length of 20 μm at the operation wavelength of 867 nm.

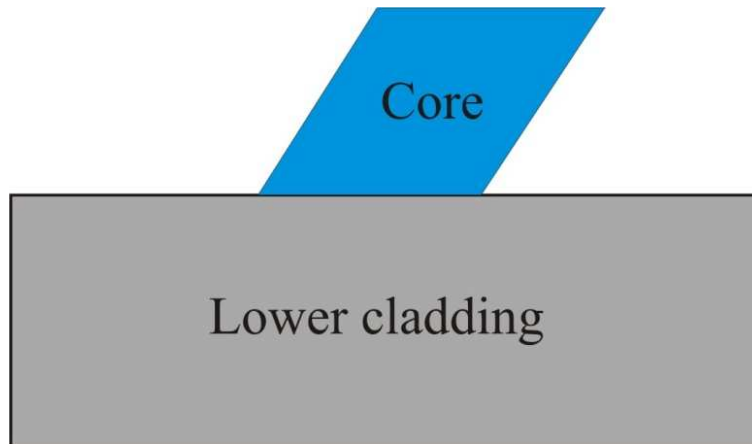


Figure 2.22: A schematic diagram of cross-sectional profile of tilted waveguide facet in both directions.

In this work, the RIE lag technique is used for the realisation of the PMCs, which was used by Holmes et al. (as discussed earlier). Here, input and output sections of waveguides, along with PMC sections are fabricated at the same time using a single mask process. Due to this, re-alignment and re-masking issues of the device at each subsequent etch step are eliminated, which were the key problems of previously designed and realised PMCs. Therefore, the risks of potential fabrication errors are reduced. Furthermore, smooth transitions from the symmetric to anti-symmetric waveguides are addressed in this technique, thereby resolved the mode mis-matching issue between the modes. Low insertion losses and single etch capability of this structure is also advantageous. Moreover, the complexity and time consuming factors to produce such devices are significantly reduced. Also we use a re-mask single trench process to realise integrated devices.

2.6. Conclusions

In the first section of this chapter, a review of semiconductor materials including bulk, quantum well and strained quantum well materials, are described. The effect of direct and indirect band-gap materials for realisation of devices and the effect of heavy and light hole to obtain polarisation insensitive devices are explained. In the next section, SOAs, which most aptly demonstrate the requirement for polarisation control in integrated optical circuits and PICs, are introduced. Thereon, polarisation mode convertor theory, including Maxwell's equations and plane waves, is presented. Polarisation induced by change in refractive index by birefringence and due to induced carriers is explained. In the last section, a review of major contributions in realising PMCs is given. An overview on the device parameters of realised devices using a slanted angle rib waveguide approach is given in Table 2.1.

Table 2.1: An overview of proposed and realised passive PMCs using a slanted angle rib waveguide.

Author name	Year	Material	Polarisation conversion	Convertor length	Losses
Tzolov et al. [72]	1996	InP/InGaAsP	92-93%	250 μm	Coupling loss=2.5 dB
Huang et al. [49]	2000	GaAs/AlGaAs	96 %	720 μm	Propagation loss=1.25 dB
Rahman et al. [73]	2001	GaAs/AlGaAs	>99%	320 μm	Insertion loss =0.4 dB
El-Rafai et al. [57]	2003	InP/InGaAsP	> 99.98 %	226 μm	N/A
Groen et al. [74]	2003	InP/InGaAsP	>80 %	150 μm	Insertion loss =2dB

El-Rafai et al. [58]	2004	InP/InGaAsP	N/A	330 μm	excess loss = 0.02 dB
Zhu et al. [75]	2004	InP/InGaAsP	95-99 %	120 μm	Excess loss <2dB
Khalique et al. [76, 77]	2004/ 2005	InP/InGaAsP	>95 %	125 μm	Excess loss <1dB
Augustin et al. [47]	2007	InP/InGaAsP	97 %	131 μm	Excess loss = 2.5 dB

In this research work, the RIE lag technique is used for the realisation of the PMCs. This technique was advantageous from other techniques as a single mask process is required, so re-alignment and re-masking issues of the device at each subsequent etch step are eliminated, which were the key problems of previously designed and realised PMCs. Furthermore, smooth transitions from the symmetric to anti-symmetric waveguides are addressed, thereby resolved the mode mis-matching issue between the modes. Low insertion losses and single etch capability of this structure is also advantageous.

2.7. References

1. Smith, R.A., *Semiconductors, 2nd Edition*. 1979, London: Cambridge University Press.
2. Kittel, C., *Introduction to Solid State Physics*. 1976, New York: Wiley.
3. Ashcroft, N.W. and N.D. Mermin, *Solid State Physics*. 1976, Philadelphia: Holt, Rinehart Winston, Saunders College.
4. Parker, G.J., *Introductory Semiconductor device Physics*. 1994, UK: Prentics Hall International, ISBN 0-13-143777-1.
5. Streetman, B.G., *Solid State Electronic Devices*. 1980: Prentice Hall, Englewood Cliffs, NJ.
6. Pierret, R.F., *Semiconductor Fundamentals*. 1983: Vol. 1 in Pierret R. F. and Neudeck G. W. Eds., Modular Series on Solid State Devices, Addison-Wesley, Reading, MA.
7. Kroemer, H., *A proposed class of hetero-junction injection lasers*. Proceedings of the IEEE, 1963. **51**(12): p. 1782-1783.
8. Chuang, S.L., *Physics of Optoelectronic Devices*. 1995, New York: Wiley Interscience.
9. Tsang, W.T., *Volume Ed., Lightwave Communications Technology*. 1985, New York: in Willardson R. K. and Beer A. C. Eds., Semiconductor and Semimetals, Academic.
10. Osbourn, G.C., *InxGal-xAs-InyGal-yAs strained-layer superlattices: A proposal for useful, new electronic materials*. Physical Review B, 1983. **27**(8): p. 5126.
11. Osbourn, G.C., *InAsSb strained-layer superlattices for long wavelength detector applications*. Journal of Vacuum Science & Technology B: Microelectronics and Nanometer Structures, 1984. **2**(2): p. 176-178.

12. Yablonovitch, E. and E.O. Kane, *Band structure engineering of semiconductor lasers for optical communications*. Lightwave Technology, Journal of, 1988. **6**(8): p. 1292-1299.
13. Pearsall, T.P., *Volume Ed., Strained-layer superlattices:Physics*. 1990, New York: in Willardson R. K. and Beer A. C. Eds., *Semiconductor and Semimetals*, Academic.
14. Zory, P.S., *Quantum Well Lasers*. 1993, New York: Academic.
15. Connelly, M.J., *Semiconductor Optical Amplifiers*. 2002: Kluwer Academic Publishers, The Netherlands, ISBN 0-7923-7657-9.
16. Newkirk, M.A., et al., *1.5 μm multiquantum-well semiconductor optical amplifier with tensile and compressively strained wells for polarization-independent gain*. Photonics Technology Letters, IEEE, 1993. **5**(4): p. 406-408.
17. Silver, M., et al., *Design and ASE characteristics of 1550-nm polarization-insensitive semiconductor optical amplifiers containing tensile and compressive wells*. Quantum Electronics, IEEE Journal of, 2000. **36**(1): p. 118-122.
18. Osbourn, G., *Strained-layer superlattices: A brief review*. Quantum Electronics, IEEE Journal of, 1986. **22**(9): p. 1677-1681.
19. Schirber, J.E., I.J. Fritz, and L.R. Dawson, *Light-hole conduction in InGaAs/GaAs strained-layer superlattices*. Applied Physics Letters, 1985. **46**(2): p. 187-189.
20. Reilly, E.P.O., *Valence band engineering in strained-layer structures*. Semiconductor Science and Technology, 1989. **4**(3): p. 121-137.
21. Lancefield, D., et al., *Pressure dependence of light-hole transport in strained InGaAs/GaAs*. Surface Science, 1990. **229**(1-3): p. 122-125.

22. Krijn, M.P.C.M., et al., *Improved performance of compressively as well as tensile strained quantum-well lasers*. Applied Physics Letters, 1992. **61**(15): p. 1772-1774.
23. Silver, M. and E.P. O'Reilly, *Gain and radiative current density in InGaAs/InGaAsP lasers with electrostatically confined electron states*. Quantum Electronics, IEEE Journal of, 1994. **30**(2): p. 547-553.
24. Bakonyi, Z., et al., *High-gain quantum-dot semiconductor optical amplifier for 1300 nm*. Quantum Electronics, IEEE Journal of, 2003. **39**(11): p. 1409-1414.
25. Zeidler, G. and D. Schicketanz, *Use of laser amplifiers in a glass-fibre communications system*. Radio and Electronic Engineer, 1973. **43**(11): p. 675-682.
26. Personick, S.D., *Applications for quantum amplifiers in simple digital optical communication systems*. The Bell Systems Technical Journal, 1973. **52**(1): p. 117-133.
27. Yamamoto, Y., *Characteristics of AlGaAs Fabry-Perot cavity type laser amplifiers*. Quantum Electronics, IEEE Journal of, 1980. **16**(10): p. 1047-1052.
28. Mukai, T., Y. Yamamoto, and T. Kimura, *S/N and Error Rate Performance in AlGaAs Semiconductor Laser Preamplifier and Linear Repeater Systems*. Microwave Theory and Techniques, IEEE Transactions on, 1982. **30**(10): p. 1548-1556.
29. Simon, J., *GaInAsP semiconductor laser amplifiers for single-mode fiber communications*. Lightwave Technology, Journal of, 1987. **5**(9): p. 1286-1295.
30. Olsson, N.A., et al., *Polarisation-independent optical amplifier with buried facets*. Electronics Letters, 1989. **25**(16): p. 1048-1049.
31. Agrawal, G.P., *Fiber-Optic Communication Systems*. 1992, New York: Wiley.

32. Deguet, C., et al., *Homogeneous buried ridge stripe semiconductor optical amplifier with near polarization independence*. Proceedings, European Conference on Optical Communication, 1999: p. 26-30.
33. Mersali, B., et al., *1.55 μm high-gain polarisation-insensitive semiconductor travelling wave amplifier with low driving current*. Electronics Letters, 1990. **26**(2): p. 124-125.
34. Doussiere, P., et al., *1.55 μm polarisation independent semiconductor optical amplifier with 25 dB fiber to fiber gain*. Photonics Technology Letters, IEEE, 1994. **6**(2): p. 170-172.
35. Tishinin, D., et al., *1.3- μm polarization insensitive amplifiers with integrated-mode transformers*. Photonics Technology Letters, IEEE, 1997. **9**(10): p. 1337-1339.
36. Holtmann, C., et al., *Polarization independent bulk active region semiconductor optical amplifiers for 1.3 μm wavelengths*. Photonics Technology Letters, IEEE, 1996. **8**(3): p. 343-345.
37. Magari, K., M. Okamoto, and Y. Noguchi, *1.55 μm polarization-insensitive high-gain tensile-strained-barrier MQW optical amplifier*. Photonics Technology Letters, IEEE, 1991. **3**(11): p. 998-1000.
38. Joma, M., et al., *Polarization insensitive semiconductor laser amplifiers with tensile strained InGaAsP/InGaAsP multiple quantum well structure*. Applied Physics Letters, 1993. **62**(2): p. 121-122.
39. Godefroy, A., et al., *1.55- μm polarization-insensitive optical amplifier with strain-balanced superlattice active layer*. Photonics Technology Letters, IEEE, 1995. **7**(5): p. 473-475.
40. Syms, R.R.A. and J.R. Cozens, *Optical guided waves and devices*. 1992, London, UK: McGraw Hill, ISBN 0-07-707425-4.
41. Chen, C.C., *Foundation for guided-wave optics*. 2006: 1st edition, John Wiley & Sons, Hoboken, New Jersey, USA, ISBN: 978-0-7503-0646-1.

42. Kasap, S.O., *Optoelectronics and Photonics: principles and practices*. 2001, New Gersey: Prentice Hall, ISBN 0-321-19046-7.
43. Hobbs and C.D. Philip, *Building electro-optical systems:making it all*. 2000: Wiley Interscience, John Wiley & Sons, Inc. USA, ISBN 0-471-24681-6.
44. Akbar, J., *High Power Mode Locked Lasers monolithically Integrated with Semiconductor Optical Amplifiers*. 2012, PhD thesis, University of Glasgow: UK.
45. Chan, M.C.Y., P.C.K. Kwok, and E.H. Li, *The effect of carrier-induced change on the optical properties of AlGaAs-GaAs intermixed quantum wells*. Selected Topics in Quantum Electronics, IEEE Journal of, 1998. **4**(4): p. 685-694.
46. Bennett, B.R., R.A. Soref, and J.A. Del Alamo, *Carrier-induced change in refractive index of InP, GaAs and InGaAsP*. Quantum Electronics, IEEE Journal of, 1990. **26**(1): p. 113-122.
47. Augustin, L.M., et al., *Short Polarization Converter Optimized for Active-Passive Integration in InGaAsP-InP*. Photonics Technology Letters, IEEE, 2007. **19**(20): p. 1673-1675.
48. Shani, Y., et al., *Polarization rotation in asymmetric periodic loaded rib waveguides*. Applied Physics Letters, 1991. **59**(11): p. 1278-1280.
49. Huang, W. and Z.M. Mao, *Polarization rotation in periodic loaded rib waveguides*. Lightwave Technology, Journal of, 1992. **10**(12): p. 1825-1831.
50. Mustieles, F.J., E. Ballesteros, and F. Hernandez-Gil, *Multimodal analysis method for the design of passive TE/TM converters in integrated waveguides*. Photonics Technology Letters, IEEE, 1993. **5**(7): p. 809-811.
51. Gustavsson, M., *Analysis of polarization independent optical amplifiers and filters based on polarization rotation in periodically asymmetric*

- waveguides*. Quantum Electronics, IEEE Journal of, 1993. **29**(4): p. 1168-1178.
52. Obayya, S.S.A., B.M.A. Rahman, and H.A. El-Mikati, *Vector beam propagation analysis of polarization conversion in periodically loaded waveguides*. Photonics Technology Letters, IEEE, 2000. **12**(10): p. 1346-1348.
53. Heidrich, H., et al., *Passive mode converter with a periodically tilted InP/GaInAsP rib waveguide*. Photonics Technology Letters, IEEE, 1992. **4**(1): p. 34-36.
54. Dam, C.v., et al., *Novel compact polarization converters based on ultra short bends*. Photonics Technology Letters, IEEE, 1996. **8**(10): p. 1346-1348.
55. van der Tol, J.J.G.M., et al., *A new short and low-loss passive polarization converter on InP*. Photonics Technology Letters, IEEE, 1995. **7**(1): p. 32-34.
56. Huang, Z., et al., *Realization of a compact and single-mode optical passive polarization converter*. Photonics Technology Letters, IEEE, 2000. **12**(3): p. 317-319.
57. El-Refaei, H. and D. Yevick, *An optimized InGaAsP/InP polarization converter employing asymmetric rib waveguides*. Lightwave Technology, Journal of, 2003. **21**(6): p. 1544-1548.
58. El-Refaei, H., D. Yevick, and T. Jones, *Slanted-Rib Waveguide InGaAsP-InP Polarization Converters*. J. Lightwave Technol., 2004. **22**(5): p. 1352.
59. Hedlund, C., et al., *Microloading effect in reactive ion etching*. Journal of Vacuum Science & Technology A: Vacuum, Surfaces, and Films, 1994. **12**(4): p. 1962-1965.
60. Gottscho, R.A., C.W. Jurgensen, and D.J. Vitkavage, *Microscopic uniformity in plasma etching*. Journal of Vacuum Science & Technology B: Microelectronics and Nanometer Structures, 1992. **10**(5): p. 2133-2147.

61. Holmes, B., D.C. Hutchings, and J.J. Bregenzner, *Experiments towards the realisation of a monolithically-integrated optical isolator incorporating quasi-phase matched magneto-optical effects*, in *MRS Fall Meeting : Materials research society*. 2004, Materials Research Society: Boston, USA.
62. Holmes, B.M., J.J. Bregenzner, and D.C. Hutchings. *Novel fabrication techniques for the realisation of passive waveguide polarisation converters*. in *Lasers and Electro-Optics, 2005. (CLEO). Conference on*. 2005.
63. Holmes, B.M. and D.C. Hutchings, *Realization of novel low-loss monolithically integrated passive waveguide mode converters*. *Photonics Technology Letters, IEEE*, 2006. **18**(1): p. 43-45.
64. Holmes, B.M. and D.C. Hutchings. *High efficiency and low loss fully integrated passive waveguide mode converters*. in *Lasers and Electro-Optics, 2006 and 2006 Quantum Electronics and Laser Science Conference. CLEO/QELS 2006. Conference on*. 2006.
65. Holmes, B.M., J.J. Bregenzner, and D.C. Hutchings. *Enabling Technologies for the Monolithic Integration of Semiconductor Lasers and Waveguide Optical Isolators*. in *Lasers and Electro-Optics, 2007. CLEO 2007. Conference on*. 2007.
66. Kim, S.-H., et al., *Single-trench waveguide TE-TM mode converter*. *Opt. Express*, 2009. **17**(14): p. 11267-11273.
67. Kotlyar, M., et al., *Compact polarization converter in InP-based material*. *Opt. Express*, 2005. **13**(13): p. 5040-5045.
68. Bregenzner, J.J., et al. *Realization of a single-section passive polarization converter using a single-step etch process*. in *Lasers and Electro-Optics Society, 2004. LEOS 2004. The 17th Annual Meeting of the IEEE*. 2004.
69. Bregenzner, J.J., et al. *Polarisation Mode Converter Monolithically Integrated within a Semiconductor Laser*. in *Conference on Lasers and*

- Electro-Optics/Quantum Electronics and Laser Science Conference and Photonic Applications Systems Technologies*. 2008: Optical Society of America.
70. Bregenzer, J.J., et al., *Compact Polarization Mode Converter Monolithically Integrated Within a Semiconductor Laser*. *Lightwave Technology, Journal of*, 2009. **27**(14): p. 2732-2736.
 71. Hagberg, M., B. Jonsson, and A.G. Larsson, *Investigation of chemically assisted ion beam etching for the fabrication of vertical, ultrahigh quality facets in GaAs*. *Journal of Vacuum Science & Technology B: Microelectronics and Nanometer Structures*, 1994. **12**(2): p. 555-566.
 72. Tzolov, V.P. and M. Fontaine, *A passive polarization converter free of longitudinally-periodic structure*. *Optics Communications*, 1996. **127**(1996): p. 7-13.
 73. Rahman, B.M.A., et al., *Design and characterization of compact single-section passive polarization rotator*. *Lightwave Technology, Journal of*, 2001. **19**(4): p. 512-519.
 74. Groen, F.H., Y.C. Zhu., and d. J.J.G.M. Van, Tol., . *Compact polarization convertor on InP/InGaAsP using an asymmetrical waveguide in proceedings of the 11th European Conference on Integrated Optics 2003 (ECIO'03), Prague, Chech Republic. pp. 141-144*. 2003.
 75. Zhu, Y.C., et al. *Ultrashort polarization convertor on InP/InGaAsP in proceedings of the 9th Annual Symposium of the IEEE Laser & Electro-Optics Society (LEOS), Belgium. pp. 115-118*. 2004.
 76. Khalique, U., et al. *Polarization convertor on InP/InGaAsP fabricated with optical reduction wafer stepper in proceedings of the 9th Annual Symposium of the IEEE Laser & Electro-Optics Society (LEOS), Belgium. pp. 131-135*. 2004.
 77. Khalique, U., et al. *Ultrashort polarization convertor on InP/InGaAsP fabricated by optical lithography in proceedings of OSA Topical Meetings:*

Integrated Photonics Research and Applications Nanophotonics for Information Systems 2005 (IPRA 2005), USA pp. 1-3. 2004.

Chapter 3

Device fabrication

3.1. Introduction

Advanced technologies are required to realise modern integrated optoelectronic components and circuits. Active and passive semiconductor based optoelectronic devices are realised using different fabrication techniques, etching, deposition and lithographic processes. Passive devices covered in this work generally require one lithographic process and one etch, whilst fabrication of integrated devices for active functionality require multiple lithographic and etch/deposition processes for high precision and accuracy of the realised devices. A technique with RIE lag was used in this research work to attain the polarisation mode conversion. Whilst in integrated devices, multiple etch processes were used to achieve shallow etched laser section and deep etched PMC section. Mostly contact-optical lithography and electron-beam (e-beam) lithography methods are used for device realisation. The e-beam lithography technique was used due to the nano-scale patterns required in the design which need high resolution and rapid prototyping capabilities. This chapter describes optical and e-beam lithography methods and fabrication steps starting from cleaning of the wafer, through dry etching and metallisation lift off techniques.

3.2. Lithography

Optical lithography is a process to transfer a pre-paid mask pattern on to a semiconductor wafer, which subsequently is used as a mask to transfer the pattern within the material via etch processing or lift off process. Crucial steps in the fabrication process flow are the transfer of the etch pattern, metallisation lift-off and accurate alignment of the mask with the previous pattern. Contact optical lithography is the most common and quickest method to transfer the pattern onto the substrate and has the capability to produce patterns required for micrometer scale lasers. This process is mainly used for commercial production of devices in industry (large scale). It is also used in the research environment where the same mask is required for the fabrication of the devices time after time. Other lithographic techniques, like e-beam lithography, are more suitable for a research oriented environment, where various sizes of design patterns are required to fabricate a complete device. Due to the maskless pattern transfer process, e-beam lithography is considered as a flexible technique. It also provides very high resolution pattern transfer, with feature sizes of the order of 10 nm readily achievable.

The devices fabricated in this work had small features, which were sub-micrometer, some reaching nanometres, therefore the e-beam lithography (EBL) technique was used to pattern the design onto the substrate. A Vistec Vector Beam 6 (VB6) e-beam tool, which is a state of the art EBL machine, located in the James Watt Nano Fabrication Center (JWNC), University of Glasgow, was used for patterning the features on the structures investigated.

The patterns to be written using EBL, were designed in a computer aided design (CAD) package L-Edit[®]. It has its own internal format, and when transferred to the next stage of the design process, patterns are saved in the GDSII format. It can then become compatible to be processed with the e-beam writer. Here, a computer aided transcription system (CATS) file is generated (which the VB6 tool understands). This software fractures the regions to be exposed in small areas called trapezia, which corresponds to each position of exposure of the

distance between the two lattice points, referred as resolution [1]. The e-beam scans this grid horizontally, row by row, and exposes only dots which are separated by a fixed distance. This fixed distance is called beam step size (BSS), and is the integer multiple of the resolution. This integer (multiplier) is known as variable resolution unit (VRU). The e-beam has a finite width and is called spot size, which depends upon the diameter of the aperture and on the beam current. Therefore, the pattern becomes a discrete set of exposed pixels. The BSS should be a fraction of the minimum feature size (MFS) to be written, therefore, it is suggested to be equal to $MFS/5$ [1, 2]. A schematic illustration of the e-beam writing procedure and parameters are shown in Figure 3.1.

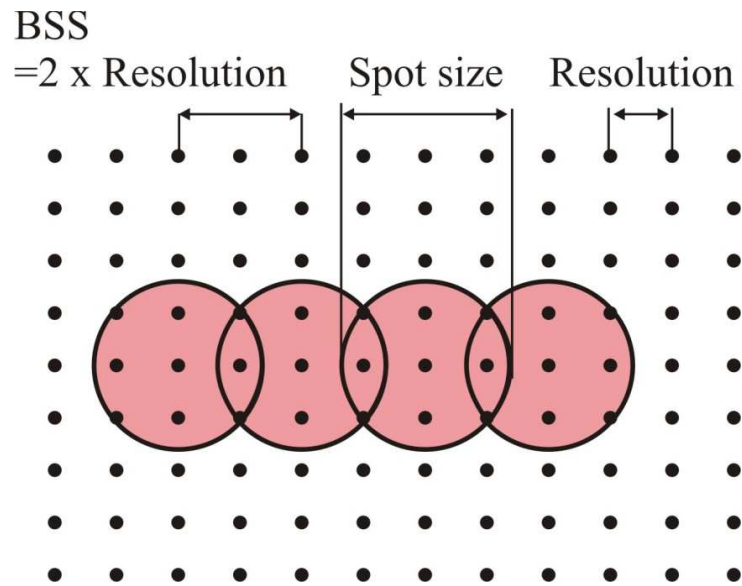


Figure 3.1: A schematic illustration of e-beam writing procedure.

Finally, the Belle software was used to submit the pattern to the VB6 tool. The beam current, spot size, VRU and the necessary exposure dose settings (the required charge per unit area ($\mu C/cm^2$) to expose the resist) was defined here.

Thereon, the fabrication process started with the preparation of the surface of the substrate for deposition of a layer of photosensitive or electro-sensitive material (photoresist). These resists are further explained in detail in the subsequent section.

3.3. Electron-beam lithography resists

EBL resists are radiation sensitive compounds. These are classified into two types, positive and negative, depending upon their response to the electron exposure. Poly-Methyl Methacrylate (PMMA) is used as a positive e-beam resist whereas Hydrogen Silsesquioxane (HSQ) is used as a negative e-beam resist. Chemical composition of the exposed part of the positive resist is changed and it becomes soluble in developer solution, whereas the exposed part of the negative resist becomes insoluble in the developer solution. Figure 3.2 shows the exposure mechanism of both the resists.

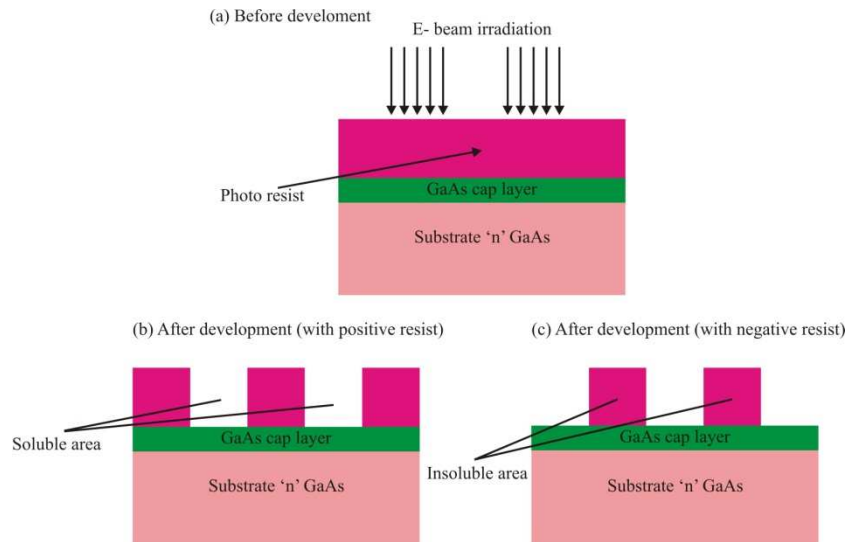


Figure 3.2: Schematic diagrams of exposure (a) before development (b) after development (positive resist) and (c) negative resist.

Parameters including sensitivity and contrast define the EBL resist structure. Sensitivity is the energy required to retain the complete thickness of the exposed region after development, whereas, contrast is a selectivity between exposed and un-exposed regions. EBL resists ideally should have high sensitivity, which allow the possibility of a faster exposure process and high contrast, to achieve vertical profiles after the development.

In this work, PMMA, which is a very high resolution positive tone resist, was used in all the lithographic steps, except for the waveguide definition, for

which HSQ was used. Layer uniformity over the wafer was achieved by spinning a dual layer of PMMA (as pin holes are eliminated which are formed during the first spin). This first spin was with 15 % of 2010 molecular weight PMMA which gives a 1.2 μm thick layer, and second spin was with 4 % of 2041 molecular weight PMMA which gives a 110 nm thick layer. Higher molecular weight (less active) PMMA was used as the top layer. This prevents the sidewalls of the resist to be coated during metal evaporation due to overlap and so the lift off process becomes easier. A schematic diagram of this process is shown in Figure 3.3.

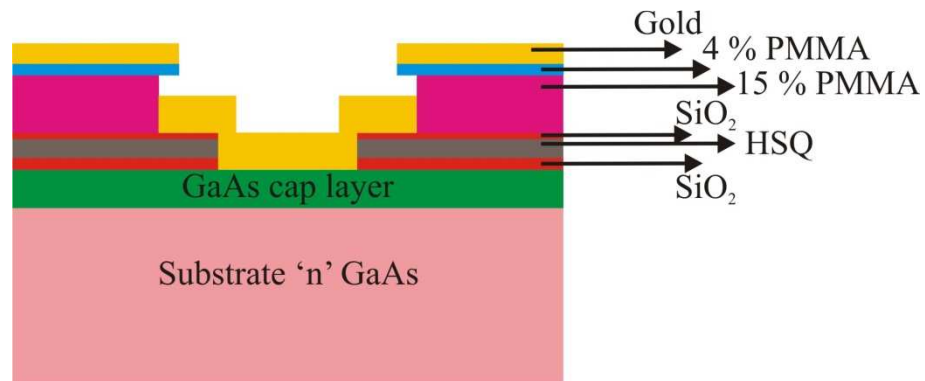


Figure 3.3: A schematic diagram of lift off process.

Generally, PMMA has a poor etching resistance in required chlorine based dry etch processes. The usual etch selectivity between the resist and the SiO_2 or Si_3N_4 mask in fluorine based plasma is around 1:2 (i.e. resist is etched twice than the mask material) [3]. Therefore, a thick layer of resist is required to etch the dielectric material (SiO_2) (i.e. 1 μm thick resist layer for 300 nm dielectric layer). There is also the requirement of an additional layer of SiO_2 if the waveguide is defined using PMMA. The inclusion of additional layer increases the number of fabrication steps, resultantly, there is more chance of imperfections during fabrication.

Throughout this work, the negative tone e-beam resist, HSQ was used to define the waveguide structures onto the substrate. The benefit of using this resist is that, it forms a SiO_2 pattern after development, which is further used as a hard mask for subsequent etching. Therefore, it avoids the deposition of an additional etch mask and additional fabrication steps (etch and resist removal) [4]. A

schematic diagram of the process steps for PMMA and HSQ is shown in Figure 3.4.

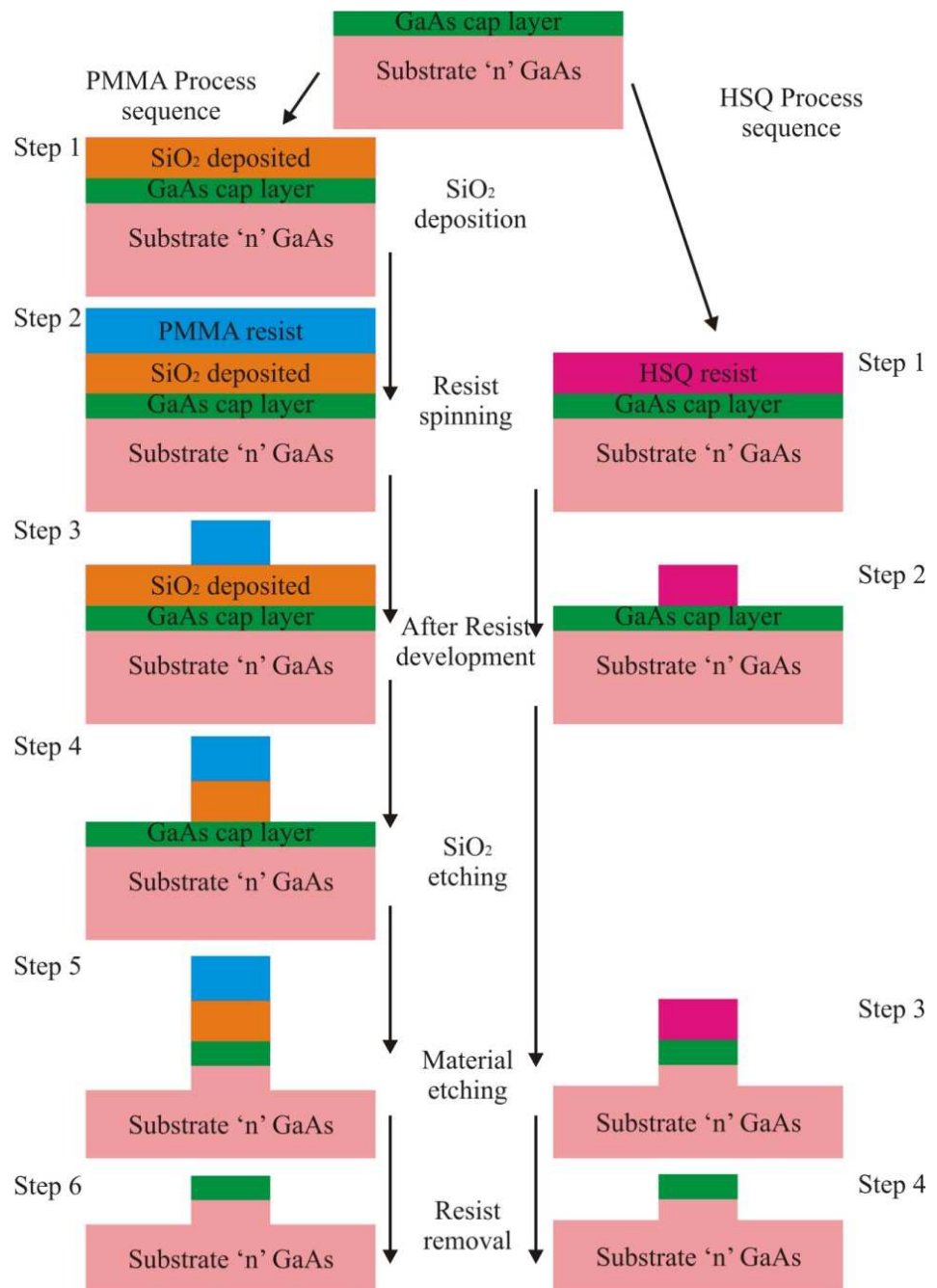


Figure 3.4: A schematic diagram for definition of wave-guiding structure using PMMA (on left) and HSQ (on right) process steps.

Furthermore, HSQ protects the waveguide structures during the definition of the waveguides, and smoother sidewalls are achieved. These smooth side walls

help in reducing the waveguide losses. This loss reduction technique has been demonstrated in the Silicon on insulator (SOI) waveguides [5].

3.3.1. Proximity correction

Electrons from the e-beam, incident upon the surface, propagating in the material, collide in-elastically with neighbouring electrons and the atoms of the lattice, and therefore transfer their energy into the material. This causes the primary electrons to change their direction and energy level. As a result, a well focused, few nanometre, e-beam spot will spread. These electrons scatter in the resist layer and also within the substrate underneath the resist layer. This exposes the part of the resist layer around each of the exposed features. Figure 3.5 shows simulated trajectories of one hundred (100 KeV energy) electrons in InP material with a 1 μm thick HSQ resist layer on the top [3]. The electrons scattering within the resist layer and substrate are clearly visible. Furthermore, the electrons scattering back to the HSQ resist layer and leaving the surface can be seen. Electrons passing through the resist-substrate interface, which do not return to the resist layer, are called forward scattered electrons. Electrons which return towards the resist and affect the exposure process are called back scattered electrons. These back scattered electrons affect the region where they pass and as an outcome, the electron beam irradiation affects the surrounding area, and the exposure region is widened. Additionally, the corners of a desired pattern get rounded and the gap spaces between the features are modified. Therefore, to achieve the optimal resolution throughout the pattern, especially for narrow spaced features, these electrons scattering effects must be minimised to get the required dimensions of the features. By applying the proximity corrections in EBL, during fracturing of the pattern adjusts the dose of each pattern, resultantly minimising the proximity effects. These effects can also be minimised with optimised mask design, and e-beam exposure parameters such as acceleration voltage, spot size, beam step size and exposure dose. Further, these can be minimised using thin resist coatings for small features.

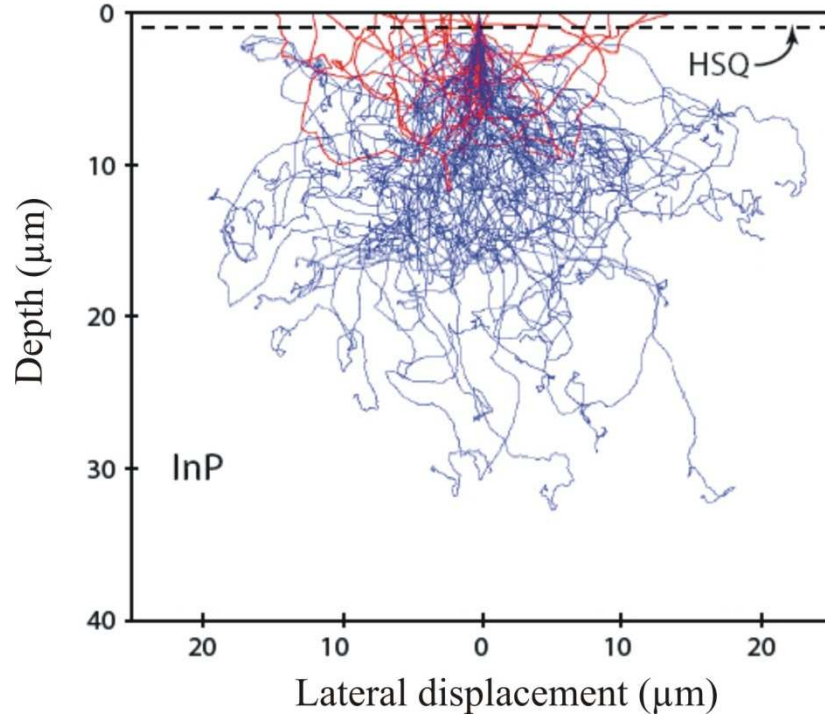


Figure 3.5: Simulated trajectories of one hundred (100KeV energy) electrons through 1 μ m HSQ and 40 μ m InP [3].

3.4. Dry etching

PMCs are designed using various techniques, which mainly depend upon the realisation of asymmetric profile waveguides, in order to increase the birefringence of the waveguide. Asymmetric waveguide profiles can be formed by various methods, one of which is the combination of crystallographic wet etch and dry etch processing. This results in a ridge waveguide consisting of one sloped and one straight sidewall. The alignment in these two steps is a major drawback. The magnitude of the angle of the sloped sidewall in wet etch process is determined by the crystallographic structure of the material [6, 7]. It is, therefore, desirable to fabricate a single section asymmetric waveguide cross-section profile using a single etch process. In this work, a reactive ion etch (RIE) [8-12] process was used for etching the material and the RIE lag technique (i.e. the aspect ratio dependent etching, as described earlier) was employed to achieve the desired trench depth for a single section PMC with a single dry etch method.

3.4.1. Principle

Dry etching techniques, such as RIE, remove undesired material from the sample surface using physical and chemical interactions of highly ionized, low pressure gas, resulting a plasma containing positive ions and free electrons. This technique provides anisotropic profiles and good selectivity between the mask layer and the material to be etched, enabling smaller, well defined features on the sample [12, 13].

The machine used for the RIE of the GaAs/AlGaAs semiconductors was a System 100, manufactured by Oxford instruments [14]. This machine consists of an integrated loadlock chamber, with the main chamber evacuated by a Leybold turbomolecular pump to a base pressure of $<10 \mu\text{Torr}$. The radio frequency (RF) signal generator is coupled to the bottom electrode of a parallel plate reactor. The height and the diameter of the chamber are 135 mm and 370 mm, respectively. The sample is placed in the etch chamber (loaded through a gate) on the lower electrode. A typical diagram of this is shown in Figure 3.6.

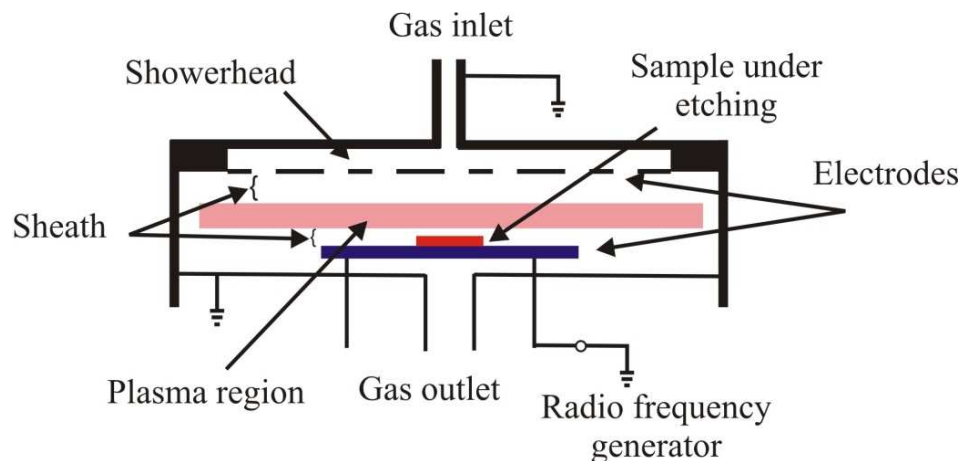


Figure 3.6: A schematic diagram of a parallel plate type RIE machine.

The RF generator drives a current through a low pressured gas between the two electrodes. The plasma is formed due to the discharge which is an ionized gas of freely moving charged particles (positive ions and electrons). These reactive ions are accelerated across the plasma in the vicinity of the substrate in the direction of the electric field. The reactive species contained in the plasma are

diffused perpendicularly onto the surface of the sample [9], which further absorbed and react chemically with the material to be etched. Here, the electrical charge distribution always remains perpendicular to the surface of the sample, due to which smooth etching was achieved. Thereon, the by-products produced during the chemical reactions are pumped away from the sample surface. The etching rate depends upon the plasma density and can be controlled by controlling the ion bombardment. The parameters used for the RIE process are given in Table 3.1.

Table 3.1: The RIE process parameters for System 100 machine at room temperature.

Parameter	Value
Process gas	SiCl ₄
Forward RF power	250 Watt
Process pressure	5 m Torr
Gas flow	13 sccm

Different etch depths were obtained when samples were etched for different times, also different layers were etched at different rates, therefore, to get the desired etch depth, a laser reflectometry technique was used for calibrating etching. This technique uses an input optical beam which is directed perpendicular to the sample area to be etched and collects the reflected beam. This reflected beam, which is received in the form of a wave, is recorded and plotted as a function of time. When the epitaxial layers are etched and the input beam enters into the substrate, the reflectivity of the sample is changed. This change in reflectivity depends upon the thickness and refractive index structure of the layers. The obtained waveform can be used to extinct the etch rate for the specific layer of the material, which can then be used to etch the original devices to the required depth. The simulation result to get the desired etch depth on the under test GaAs/AlGaAs material (layer structure with refractive indices and doping concentrations, given in Table 3.2) is shown in Figure 3.7. Here, the reflectance as

a function of the etch depth (cap layer to substrate) can be seen. Matlab© software was used for these simulation results.

Table 3.2: Layer structure of the GaAs/AlGaAs material.

Layer	Material	Thickness nm)	Refractive index	Doping concentration
8	GaAs	100	3.631	p (1×10^{19})
7	$\text{Al}_{0.30}\text{Ga}_{0.70}\text{As}$	1000	3.381	p (2×10^{17})
6	$\text{Al}_{0.15}\text{Ga}_{0.85}\text{As}$	210	3.498	Un-doped
5	GaAs	5	3.631	Un-doped
4	$\text{Al}_{0.20}\text{Ga}_{0.80}\text{As}$	10	3.455	Un-doped
3	GaAs	5	3.631	Un-doped
2	$\text{Al}_{0.15}\text{Ga}_{0.85}\text{As}$	210	3.498	Un-doped
1	$\text{Al}_{0.30}\text{Ga}_{0.70}\text{As}$	1200	3.381	n (1×10^{17})
n-GaAs Substrate				

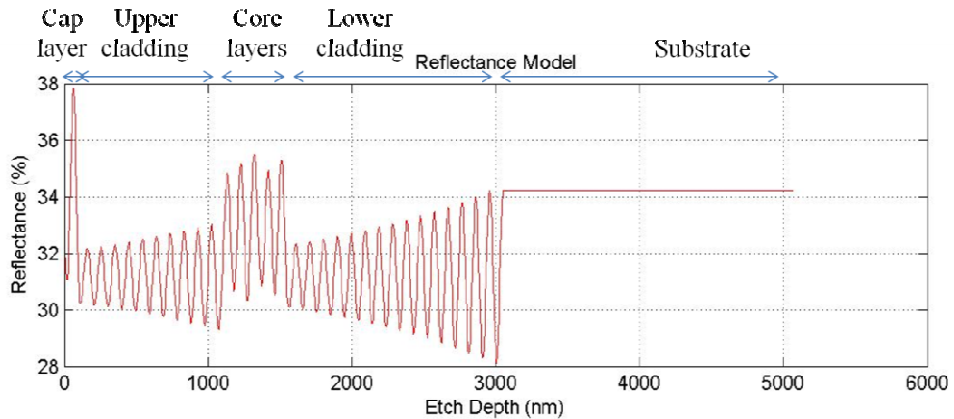


Figure 3.7: Simulation results by Matlab software for etch depth.

Throughout this work, it was required to etch the material through the core, at a desired etch depth of $\sim 1.8 \mu\text{m}$. Therefore, during the etching process on the System 100 machine, ion bombardment was stopped when the beam monitor crossed two cycles in lower cladding of the material. This can be observed clearly from the real time graph obtained using the laser reflectometry method which is shown in Figure 3.8.

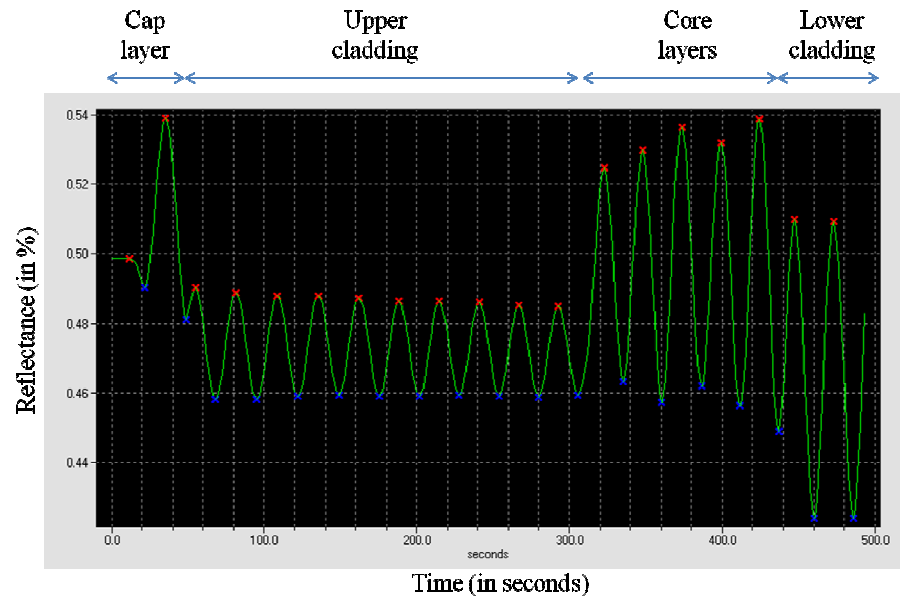


Figure 3.8: Real time etch depth obtained by laser reflectometry method.

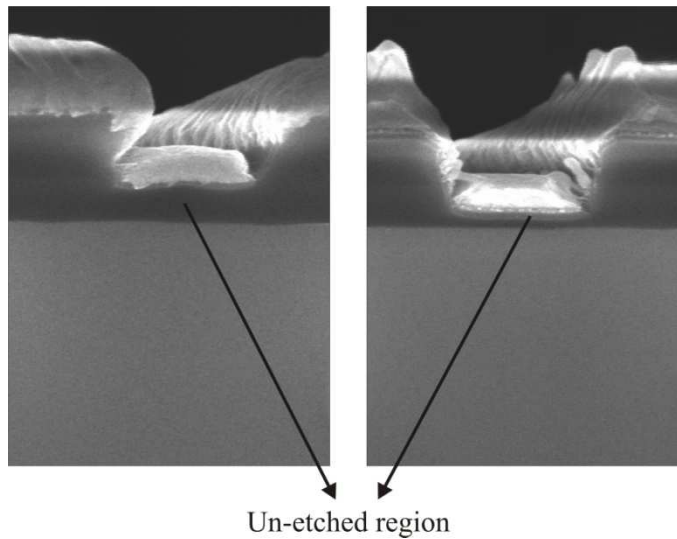


Figure 3.9: An un-etched area due to residual SiO_2 .

Dry etching was also required for defining the patterns into the SiO_2 dielectric barrier layer films. If contact windows in the SiO_2 films are not properly opened, current cannot flow across the device. This problem is observed, when the device is not properly etched at the developed area, and some SiO_2 remains. This residual SiO_2 prevents current flow to the device, which leads to a non-functional device. This is illustrated in SEM picture, shown in Figure 3.9. In order to overcome this problem, the etch rate was properly optimised for SiO_2 etching. The

sample was then properly developed, and etched for a longer time, to ensure full removal of SiO₂.

For this SiO₂ removal, the machine used was an 80 Plus RIE, also manufactured by Oxford instruments, with CHF₃ and Ar gases. The etch rate for this machine was measured at 30 nm/min, therefore, an etching time of 20 minutes was used for etching 600 nm thick SiO₂ film. This included an over etch (about 15 %) to overcome possible variations in oxide thickness. The standard parameters used for this machine are given in Table 3.3.

Table 3.3: The RIE process parameters for an 80 Plus RIE machine at room temperature.

Parameter	Value
Process gas	CHF ₃ / Ar
Forward RF power	200 Watt
Process pressure	30 m Torr
Gas flow	25 sccm / 18 sccm

3.5. Overview of the fabrication process

The fabrication process of semiconductor lasers involves a number of critical processes. It needs considerate handling of the fragile substrate and requires ultra clean environments. The main processing steps are summarised in the block diagram of Figure 3.15. These processing steps are the standard procedure for fabricating semiconductor devices [13, 15, 16]. However, layer thickness, etching recipes and e-beam doses can be different for different devices. All the fabrication work mentioned in this research, was carried out in the James Watt Nano Fabrication Centre (JWNC) except for a few steps like sample cleaving, thinning and mounting. The JWNC has a 750 m² cleanroom which is designed for interdisciplinary nanofabrication activities to be conducted with minimum cross contamination of processes. This cleanroom also contains a class

10 room, hosting the VB6 lithography tool, ten rooms of class 1000, and four rooms of class 10000.

3.5.1. Sample preparation and cleaning

The fabrication process starts with the cleaving of the wafer to the desired dimensions. As the cleaving was carried out in a semi-clean environment, it was pre-requisite to then clean the substrate before it undergoes fabrication. The solvent cleaning method was used for cleaning the substrate, where the substrate was placed in small beakers and then put in an ultra-sonic bath. This ultra-sonic assisted solvent cleaning involves soaking the sample in acetone for 5 minutes, then 5 minutes in Isopropanol (IPA) and 5 minutes in reverse osmosis (RO) water, before the remaining layer of water was blown dry from the sample using the gaseous dry nitrogen (N_2) gun. Sample boxes were also cleaned to avoid any possible contamination. In addition to that, in each step of fabrication and inspection, cleanliness was maintained. Prior to resist spinning, the cleaned sample was placed on a hot plate at 90 °C for 5 minutes to dehydrate the substrate. This helps in increasing the resist adhesion to the surface of the substrate. This dehydration step is very important for small features on devices.

3.5.2. Registration markers

There are multiple lithographic processes involved in the fabrication of semiconductor lasers. These multiple lithographic processes require defining sets of markers for the accurate alignment of previous and successive patterns to one another on the substrate.

The e-beam lithographic method was employed in this work so the registration and alignment techniques defined for the VB6 machine, were followed. Complete information about the alignment functionality of this e-beam tool (which is the Vistec Vector Beam 6 (VB6)), is available in the operator's manual [17]. An alignment cross was defined on the sample's surface, which the e-beam recognises through a sequential search assisted by its internal algorithm. After cross recognition, the system searches and identifies the global markers

which had already been specified in the e-beam job submission process. The e-beam then performs the alignment with $<0.1 \mu\text{m}$ precision. The optical microscope pictures of the big cross marker (before and after e-beam job submission and written) and global markers obtained after the lift-off process are shown in Figure 3.10 and Figure 3.11, respectively.

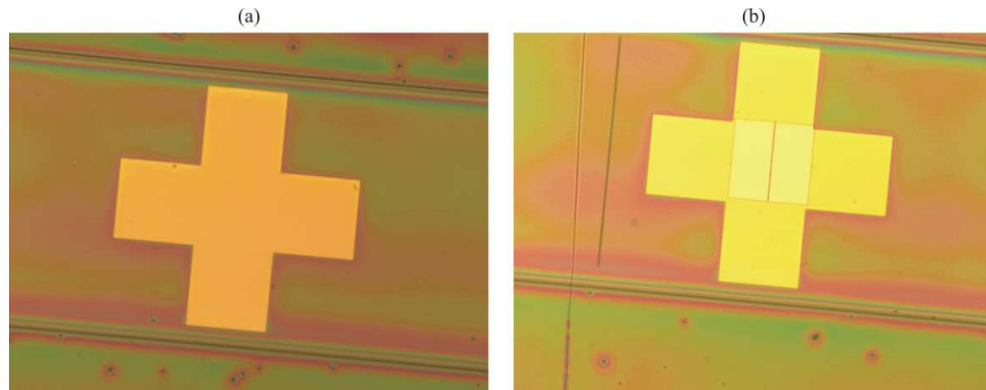


Figure 3.10: Cross markers (a) before e-beam job submission (b) after e-beam job written.

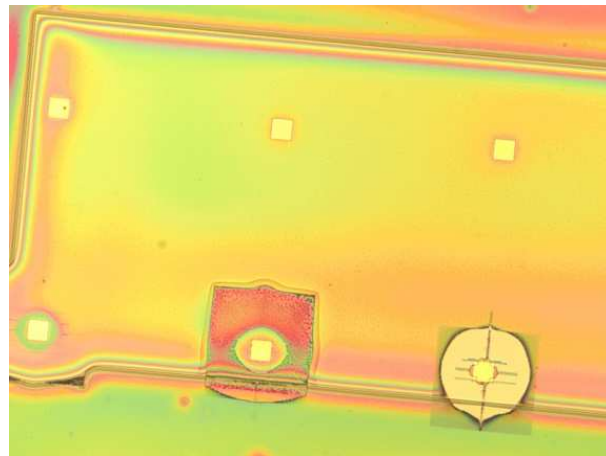


Figure 3.11: Global markers of $20 \mu\text{m} \times 20 \mu\text{m}$ dimensions after alignment.

3.5.3. Waveguide definition

A critical step in the fabrication of a semiconductor laser, is the definition of the waveguide structure. The negative tone resist HSQ (as described earlier) was used for the waveguide patterning in a single step mask fabrication. The process uses 100 % HSQ for spinning, followed by a 15 minute bake on a hot

plate at 90 °C to remove solvent. The substrate, with resist layer, was then exposed to the e-beam and finally the pattern developed in 25 % Tetra-Methyl Ammonium Hydroxide (TMAH) solution. The waveguides are etched to result in a height of $\sim 1.8 \mu\text{m}$ (as described in the previous section using the laser reflectometer). After etching, the sample was cleaned ready for the next fabrication step.

3.5.4. Cap layer removal

The cap layer is highly doped, therefore, to avoid any current leakage from one section of the device to the other; it is beneficial to keep isolation between the metal contacts of adjacent sections. In order to do this, the cap layer of 100 nm GaAs was removed from some areas using the System 100 machine with a SiCl_4 chemistry. Laser reflectometry was also used for this purpose. A real time trace obtained during the cap layer removal is shown in Figure 3.12.

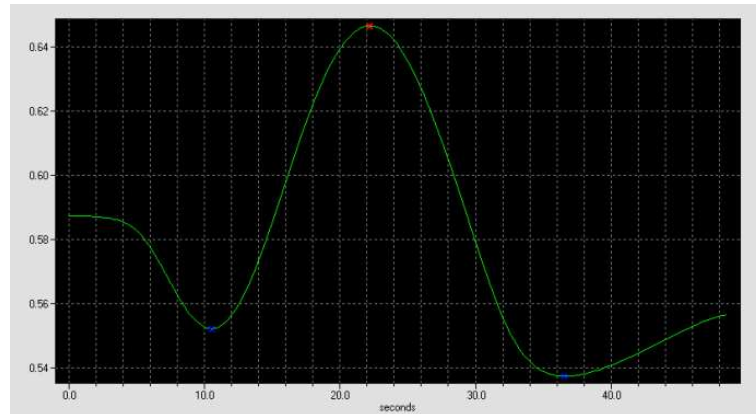


Figure 3.12: A real time trace obtained during the cap layer removal by laser reflectometer.

3.5.5. Planarization

The metal evaporation onto the sample is a highly directional process; therefore, a thin film of metal is very precisely deposited on the wafer, on the top surface. However, the vertical walls of the waveguides are not completely covered by metal when using this process. Due to this non-uniform metal coverage over the walls, the side and top of the waveguides do not have the smooth continuous

metal deposition at all places. During application of higher current injections, the thinner contacts become unstable and devices show uncertain behaviour. This can also be seen when probes are placed on the metal contacts during measurement, and can stop current flowing in the device. SEM pictures with broken metal contacts are shown in Figure 3.13.

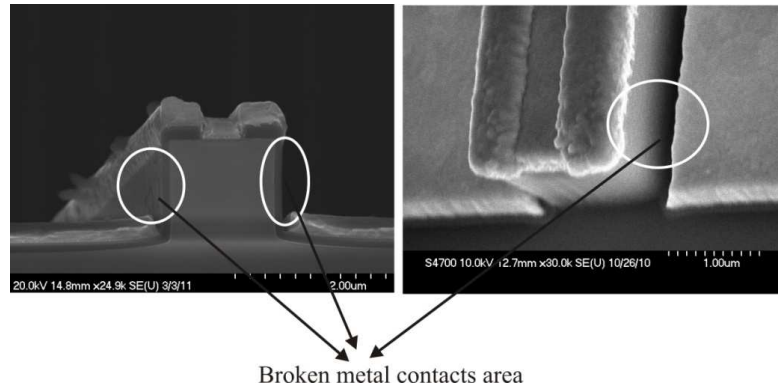


Figure 3.13: SEM pictures showing the broken metal contacts.

Therefore, a planarization technique was used for the smooth and certain operation of the device, in which, HSQ was spun on top of 200 nm plasma enhanced chemical vapour deposited (PECVD) SiO_2 , and was then baked in an oven at 180 °C for 90 minutes. The hot baked HSQ acts as an insulator on the sample. This HSQ has less thickness in the open areas of the sample and gradually increases as it approaches to the waveguides. However, a very thin layer of HSQ remains on the top of the waveguides due to the low surface area. Finally, a layer of 100 nm of PECVD SiO_2 was used in order to achieve better adhesion for the metal contacts. SEM picture of the planarization process is shown in Figure 3.14.

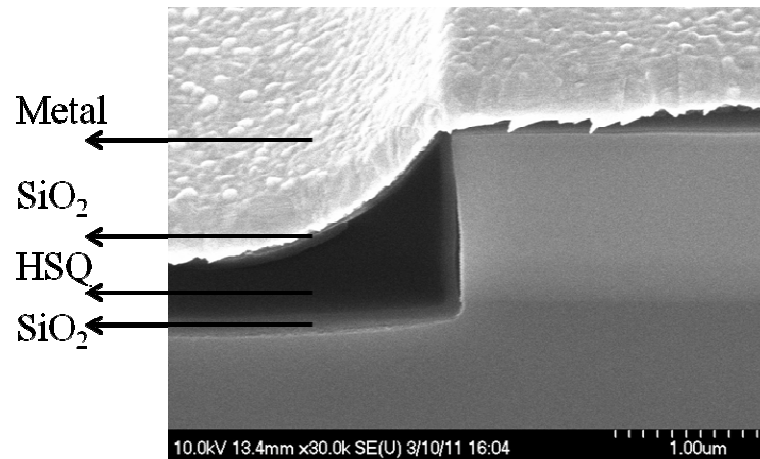


Figure 3.14: SEM picture of planarization.

3.5.6. Current injection window

After the planarization, the most important step is to open the current injection windows on top of the waveguides. If these are not properly opened, there will be no current flow across the device, and the device will behave passively. The samples were prepared for e-beam lithography by spinning a bi-layer, 15 % of 2010 molecular weight PMMA and 4 % of 2041 molecular weight PMMA, and baking at 180 °C for 30 minutes and 90 minutes, respectively. After exposure and development, the samples were cleaned using a short Oxygen ash for the removal of any leftover resist. PMMA is known to leave a thin (~nm's) residual layer. The current injection windows were then opened by RIE, using a CHF₃/Ar chemistry, for 20 minutes including a 15 % overetch. The remaining PMMA was then removed using an O₂ plasma clean.

3.5.7. Contact metallisation

The final patterning job submitted to the e-beam was for the definition of the p-contact layer. A bi-layer of 15 % of 2010 molecular weight PMMA and 4 % of 2041 molecular weight PMMA was used, and then baked at 180 °C for 30 minutes and 90 minutes, respectively. After exposure and development, the sample surface was de-oxidised in a HCl: H₂O solution in the ratio of 1:5. This process was carried out immediately before metal deposition to remove the

oxidised surface that forms on the semiconductor surface overtime. P-contact metallisation was performed in the e-beam assisted, metal evaporator (Plassys machine) with 30 nm Titanium (Ti), 33 nm Platinum (Pt) and 240 nm Gold (Au). Ti is a reactive metal and oxidises readily, therefore, it is used as an adhesion layer with SiO₂ layer, which is used as isolation. Pt is used as a diffusion barrier and prevents Au penetrating into the semiconductor material. Au is used as a conducting layer. Excess metal was then removed using a lift-off process by placing the substrate in a beaker of acetone placed in a hot water bath at 50 °C, for 60 minutes, followed by cleaning of the sample.

3.5.8. Mechanical thinning

The GaAs/AlGaAs material used in this work has a thickness of 354 µm. In semiconductor laser devices, it is necessary to thin these devices to a thickness of about 225 µm. This is desirable in order to reduce the series resistance between the p-side and n-side contacts. The process of mechanical thinning was employed for this purpose. First, the sample was mounted on the glass slide (with p-side down) using photo resist S1818 and baking it in an oven at 90 °C for 60 minutes for better adhesion to the glass. Then the sample mounted glass slide was glued on to a metal rod (using wax) and gently sliding the rod in a figure of 8 pattern on a thick glass plate, using a mixture of water and Aluminium Oxide (Al₂O₃) powder, until the thickness becomes ~225 µm. After achieving this thickness, the sample was removed from the metal rod and put into opticlear to remove the wax from the material, and, the sample was then cleaned in acetone and IPA solutions.

3.5.9. N-contact metallisation and annealing

The creation of the n-contact was achieved using the same procedure as for the p-contact. First, the sample was mounted on the glass slide (with the p-side down) with the thinned surface on the upside. 14 nm Gold (Au), 14 nm Germanium (Ge), 14 nm Gold (Au), 11 nm Nickel (Ni) and 240 nm Gold (Au) were then evaporated with an e-beam assisted, Plassys, machine. Here, the Au/Ge alloy is used because Ge is a group IV element and can be used for doping the

GaAs. It can be diffused into the area immediately under the contact upon annealing, and dopes the GaAs degeneratively n-type. A layer of Ni is used to improve the surface morphology post annealing, as it does not form a eutectic with the contact metals at temperatures below the alloying temperature [13]. After this, the sample was removed from the glass slide by placing it in the acetone solution in a hot water bath and cleaning the sample with nitrogen blow.

Finally, the sample was placed in the rapid thermal annealer (RTA) for annealing the metal contacts at 360 °C for 60 seconds to form ohmic contacts, which allows the current to flow into and out of the devices with low resistance.

3.5.10. Cleaving and mounting

The last step of the fabrication was cleaving the sample to the desired dimensions and mounting onto brass bars with the help of silver conductive epoxy. This conductive epoxy gives better adhesion and conductivity for characterisation and further measurements.

3.6. Conclusions

In the first section of this chapter, the optical and e-beam lithographic processes are discussed. The resists used for patterning the mask are presented. Furthermore, the background and the basic principle of dry etch technique is explained. In this research work, RIE lag technique was used to attain the polarisation mode conversion by changing the optical axis of the waveguide. Then the overview of the fabrication steps starting from the cleaning of the wafer to the realisation of devices and lift-off techniques are briefly explained. The process flow diagram for fabrication of the devices is given in Figure 3.15.

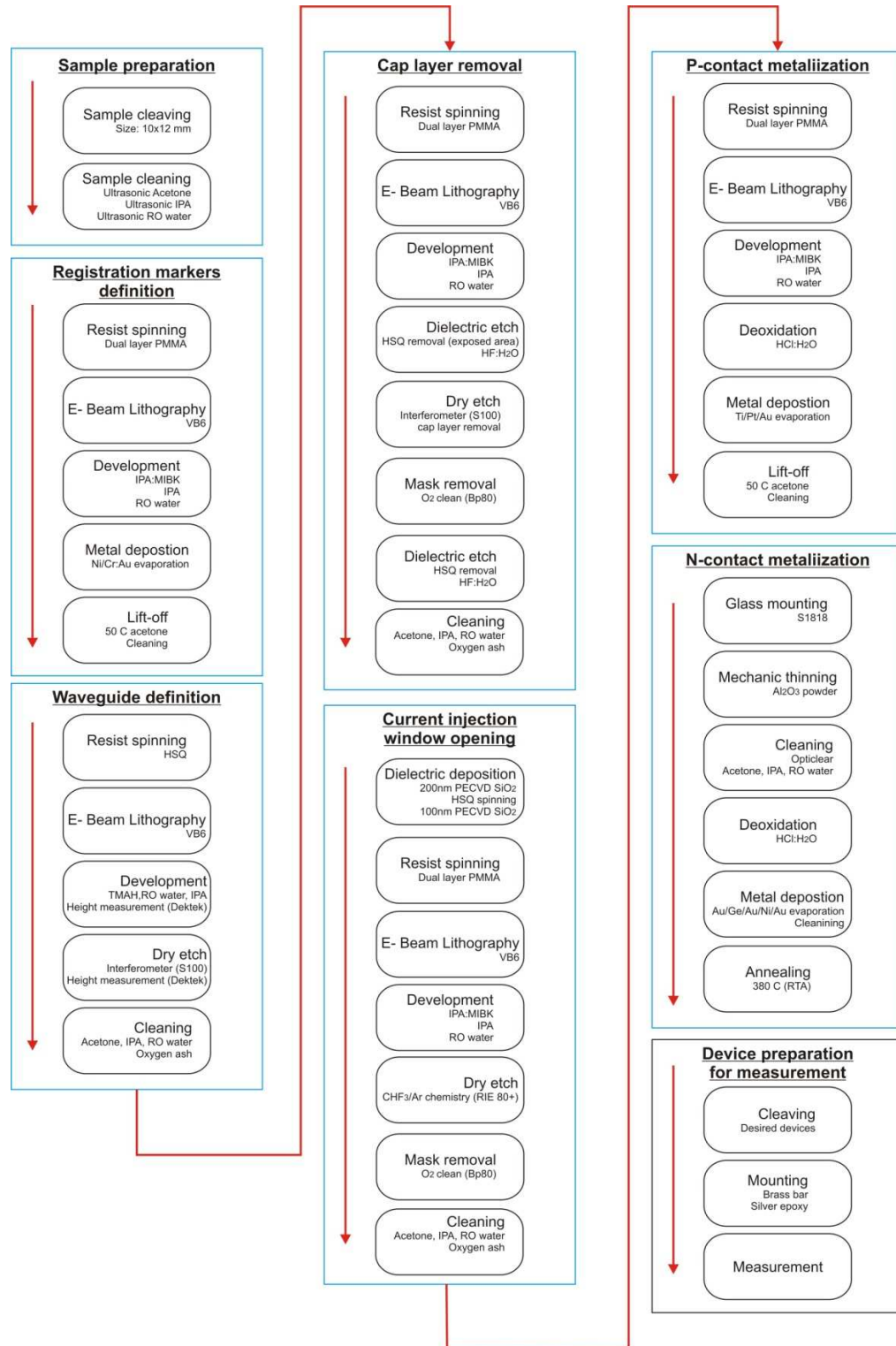


Figure 3.15: Fabrication of semiconductor lasers process flow diagram.

3.7. References

1. *Introduction to Electron beam Lithography*, www.elec.gla.ac.uk/jwnc/pages/Ebeam_Docs/ebeam-lith-1a.pdf.
2. Samarelli, A., *Micro ring resonators in silicon-on-insulator*. 2011, PhD thesis, University of Glasgow: UK.
3. Mezosi, G., *Semiconductor ring lasers for all-optical signal processing*. 2010, PhD thesis, University of Glasgow: UK.
4. Namatsu, H., et al., *Nano-patterning of a hydrogen silsesquioxane resist with reduced linewidth fluctuations*. *Microelectronic Engineering*, 1998. **41-42**(0): p. 331-334.
5. Gnan, M., et al., *Fabrication of low-loss photonic wires in silicon-on-insulator using hydrogen silsesquioxane electron-beam resist*. *Electronics Letters*, 2008. **44**(2): p. 115-116.
6. Howes, M.J. and M.D. V., *Gallium Arsenide*. 1985: John Wiley & Sons, New York, ISBN 0-471-90048-6.
7. Kern, D.P., et al., *Practical aspects of microfabrication in the 100 nm regime*. *Journal of Vacuum Science & Technology B: Microelectronics and Nanometer Structures*, 1983. **1**(4): p. 1096-1100.
8. Coburn, J.W. and H.F. Winters, *Plasma etching-A discussion of mechanisms*. *Journal of Vacuum Science and Technology*, 1979. **16**(2): p. 391-403.
9. Lieberman, M.A. and A.J. Lichtenberg, *Principles of plasma discharges and materials processing*. 1994: John Wiley & Sons, New York, ISBN 0-471-00577-0.
10. May, G.S. and S.M. Sze, *Fundamentals of semiconductor fabrication*. 2004: John Wiley & Sons, NJ, ISBN 0-471-23279-3.
11. Wilkinson, C.D.W. and M. Rahman, *Dry etching and sputtering*. *Philosophical Transactions of the Royal Society of London. Series A:*

- Mathematical, Physical and Engineering Sciences, 2004. **362**(1814): p. 125-138.
12. Williams, R., *Modern GaAs processing techniques*. 1990: Artech House, Inc, Norwood, MA, USA. ISBN 0-89006-343-5.
 13. McMaster, S., *Monolithically integrated mode-locked ring lasers and Mach-Zehnder interferometers in AlGaInAs*. 2010, PhD thesis, University of Glasgow: UK.
 14. *Oxford Instruments, www.oxford-instruments.com*.
 15. Furst, S., *Monolithic integration of semiconductor ring lasers*. 2008, PhD thesis, University of Glasgow: UK.
 16. Younas, U., *Monolithic integration for non linear optical frequency conversion in semiconductor waveguides*. 2010, PhD thesis, University of Glasgow: UK.
 17. *L. M. L. Ltd, Leica Vector Beam series- Vector beam operator manual 2005*.

Chapter 4

Design and characterisation of a semiconductor laser

4.1. Introduction

This chapter describes the material properties of GaAs/AlGaAs and its characterisation, which was designed to emit at a wavelength of 850 nm. This material was subsequently used to fabricate laser devices with integrated polarisation mode convertors (described in chapter 5). The epitaxial layer structures of these materials, which have active functionality, are discussed. Transmission line measurements (TLMs) used to assess the performance of the p-type ohmic contacts, are explained. Furthermore, Fabry-Perot Laser (FPL) design, optimisation, realisation and characterisation are presented. Finally, the simulations and characterisation of far field patterns generated by the FPLs are discussed.

4.2. Material structure

The devices fabricated and presented in this thesis are based on GaAs/AlGaAs and InP/AlGaInAs epitaxial layer structures. The material described in this chapter is GaAs/AlGaAs emitting at a wavelength of 850 nm.

InP/AlGaInAs material structure emitting at a wavelength of 1550 nm is described in the subsequent chapter. The preliminary work is based on the GaAs/AlGaAs wafer structure, given in Table 3.2, for the fabrication and realisation of the devices. This wafer contains double quantum well, hetero-structure layers which are lattice matched to an n- doped GaAs wafer. Layers of 1200 nm and 1000 nm of $\text{Al}_{0.30}\text{Ga}_{0.70}\text{As}$ are used as lower and upper cladding layers, respectively, whereas, 440 nm $\text{GaAs}/\text{Al}_{0.15}\text{Ga}_{0.85}\text{As}$ is used as a core layer. The core layer consists of two GaAs quantum well layers of 5 nm each with barrier $\text{Al}_{0.20}\text{Ga}_{0.80}\text{As}$ of 10 nm, for confinement of the electrons and holes in the core. Also, there are two 210 nm layers of $\text{Al}_{0.15}\text{Ga}_{0.85}\text{As}$ on the upper and lower sides. The quantum well layers are sandwiched between two $\text{Al}_{0.15}\text{Ga}_{0.85}\text{As}$ layers. A highly p-doped layer of 100 nm GaAs is used as a contact layer on top of the wafer. The complete epitaxial layer structure of the wafer with doping concentrations and the refractive indices, is given in Table 3.2. The refractive indices at a wavelength of 850 nm (1.459 eV) and at a temperature of 25 °C (298.15 °K) were used [1-3].

Table 4.1: Layer structure of the GaAs/AlGaAs active functionality material used for the preliminary work.

Layer	Material	Thickness (nm)	Refractive index	Doping concentration
8	GaAs	100	3.631	p (1×10^{19})
7	$\text{Al}_{0.30}\text{Ga}_{0.70}\text{As}$	1000	3.381	p (2×10^{17})
6	$\text{Al}_{0.15}\text{Ga}_{0.85}\text{As}$	210	3.498	Un-doped
5	GaAs	5	3.631	Un-doped
4	$\text{Al}_{0.20}\text{Ga}_{0.80}\text{As}$	10	3.455	Un-doped
3	GaAs	5	3.631	Un-doped
2	$\text{Al}_{0.15}\text{Ga}_{0.85}\text{As}$	210	3.498	Un-doped
1	$\text{Al}_{0.30}\text{Ga}_{0.70}\text{As}$	1200	3.381	n (1×10^{17})
n-GaAs Substrate				

Thereon, the second wafer used for fabrication and realisation of devices, consists of GaAs and AlGaAs material. This material was designed for a wavelength of 867 nm by B. M. Holmes at the University of Glasgow. This wafer contains double quantum well GaAs/AlGaAs separate confinement heterostructure (SCH), which was lattice matched to an n-doped GaAs substrate. The active region consists of two 9 nm quantum well layers with a barrier layer of 10 nm $\text{Al}_{0.20}\text{Ga}_{0.80}\text{As}$. These are sandwiched between two 211 nm thick $\text{Al}_{0.20}\text{Ga}_{0.80}\text{As}$ layers on the upper and lower sides. This helps for better confinement of electrons and holes in the active region. Two layers of 1500 nm and 1000 nm of $\text{Al}_{0.40}\text{Ga}_{0.60}\text{As}$ are used as lower and upper claddings. These are n and p-doped, respectively. Whereas, a highly p-doped 100 nm GaAs cap layer is used for contact purpose. In this structure, a high refractive index layer of GaAs is used as a core layer for the effective guidance of the input source. The epitaxial layer structure of this wafer with doping concentrations and the refractive indices, is given in Table 4.2. This wafer was grown using metal organic chemical vapour deposition (MOCVD) at the EPSRC National Centre for III-V Technologies at the University of Sheffield, Sheffield, United Kingdom.

Table 4.2: Layer structure of the GaAs/AlGaAs double quantum well material.

Layer	Material	Thickness (nm)	Refractive index	Doping concentration
8	GaAs	100	3.631	p (2×10^{18})
7	$\text{Al}_{0.40}\text{Ga}_{0.60}\text{As}$	1000	3.315	p (5×10^{17})
6	$\text{Al}_{0.20}\text{Ga}_{0.80}\text{As}$	211	3.455	Un-doped
5	GaAs	9	3.631	Un-doped
4	$\text{Al}_{0.20}\text{Ga}_{0.80}\text{As}$	10	3.455	Un-doped
3	GaAs	9	3.631	Un-doped
2	$\text{Al}_{0.20}\text{Ga}_{0.80}\text{As}$	211	3.455	Un-doped
1	$\text{Al}_{0.40}\text{Ga}_{0.60}\text{As}$	1500	3.315	n (5×10^{17})
n-GaAs Substrate				

4.3. Basic material testing

The easiest and quickest methods to identify the basic material properties, such as material gain and electrical properties are the fabrication of broad area lasers and TLM measurements. These methods also help in design, optimisation and process development. The devices required to carry out these tests can be fabricated using a simple photolithography technique. In this work, the TLM method was carried out first to identify the contact resistance of the material, and is described in the subsequent section.

4.3.1. Transmission line measurement

TLM is a well known method for the identification of the specific contact resistance of any ohmic contact. This information helps in the selection of materials used for a thin film (ohmic contact), which subsequently affects the device performance.

The TLM in this work, was performed on the wafer structure shown in Table 4.2. The contact resistances were taken on the p-side (top side) of the material in all the measurements. The geometrical details of the mask used for the contact pads are shown in Figure 4.1. The details of the fabrication process steps are given in Annex I.

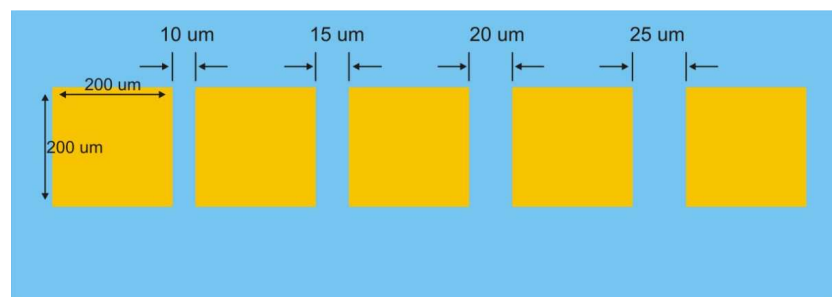


Figure 4.1: A schematic diagram of the mask used for the contact pads.

There are multiple mesas in the sample which were used for the TLM, each mesa has 5 contact pads with $200\ \mu\text{m} \times 200\ \mu\text{m}$ dimension. These contact pads have $25\ \mu\text{m}$, $20\ \mu\text{m}$, $15\ \mu\text{m}$ and $10\ \mu\text{m}$ gaps between them (Figure 4.1).

However the actual gaps obtained after photolithography were 25 μm , 21 μm , 16 μm and 10 μm , which were measured using an optical microscope.

A schematic diagram of the TLM measurement setup is shown in Figure 4.2. The four probe method was used because it can eliminate surrounding resistances, which are produced by the probes. Two probes were brought into contact with each pads, with one designated for the voltage and the other for the current. The measurements were carried out by applying the bias voltage across the contact pads and by measuring the current flow from one contact to the other as shown in a schematic of the measurement setup (Figure 4.2). Here, V_a and V_b are the bias voltages and I_a and I_b are the current flows across the contact pads. Resistance between the two contacts was measured by the automated script on the four probe station. This process was repeated for measuring the four resistances for the four different gaps in a single mesa section. This was performed on the multiple mesa sections across the sample to obtain a graph of the resistances versus gap length. The resistances are then plotted against their respective gaps between the contact pads as shown in Figure 4.3.

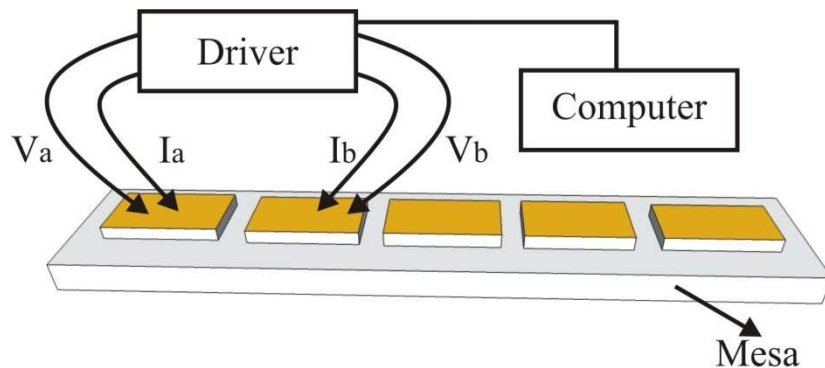


Figure 4.2: A schematic diagram of the four probe measurement setup.

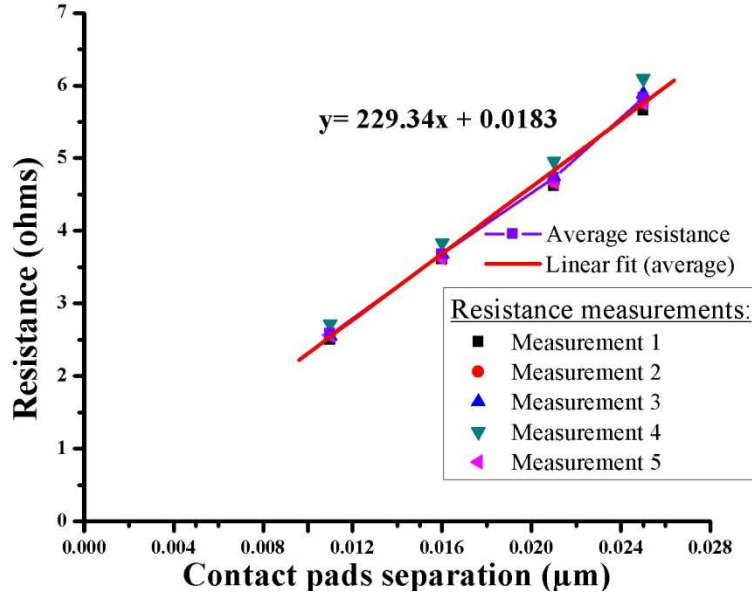


Figure 4.3: The measured resistances as a function of contact pads separations.

The linear fit to this scatter gives information about the contact resistance and ultimately the specific contact resistance. This is calculated using the equation 4.1 [4].

$$L_T = \frac{R_c}{R_s / W}$$

4.1

where L_T is the transfer length, R_c is the contact resistance, R_s is the sheet resistance and W is the width of the contact pad.

The specific contact resistance is measured using equation 4.2.

$$\rho_c = R_s L_T^2$$

4.2

L_T , R_c , R_s , and ρ_c are found to be 3.997×10^{-5} mm, $9.166 \times 10^{-3} \Omega$, 183Ω and $2.932 \times 10^{-7} \Omega \text{mm}^2$ respectively.

Here, the specific contact resistance (ρ_c) is found to be $2.932 \times 10^{-7} \Omega \text{mm}^2$ which is less than the ideal $1 \times 10^{-1} \Omega \text{mm}^2$ [4]. This low specific contact resistance indicates low series resistance between the contacts.

4.3.2. Ridge waveguide lasers

Optical confinement in the vertical direction is obtained by the higher refractive index in the core region than the surrounding layers during the growth of the material, whereas, in the horizontal direction, it is achieved by the presence of the ridge. Lasing action is achieved by the cavity formed between the two cleaved facets resulting in edge emission. The ridge width and etch depth is designed to ensure single mode behaviour. This ridge width should be narrow in dimensions and can be deep or shallow etched.

4.3.2.1. Design and optimisation

Commercial mode solving software [5] was used for optimising the etch depth and the width of the ridge waveguide lasers. This mode solver software determines the effective refractive index ' n ', and propagation constant ' β ', at a particular wavelength with different geometries of the waveguides. Numerical techniques based on finite difference and finite elements are used for the mode solving. In this work, a finite element method (FEM) based on a scalar wave equation solver was used to investigate the ridge waveguide structures. The layer structure shown in Table 4.2 was used to optimise the depth and width of the ridge waveguide for single mode operation. Shallow and deep etched device structures were used to obtain laser and PMC sections, respectively.

In shallow etched devices, only the upper cladding layer was etched, whereas, in deep etched devices, both, the upper cladding layer and the core layer were etched. There is lower optical confinement and hence lower scattering losses in shallow etched devices as compared to the deep etched devices. The shallow etched devices were preferred in this work for semiconductor lasers, due to their lower sidewall scattering losses and to obtain high lasing power. This also avoids side wall recombination (non-radiative) and oxidation of quantum wells. The deep etched devices, where scattering losses are higher due to the optical mode's interaction with the side walls of the ridges, were used to fabricate polarisation mode convertors, where RIE lag was required to introduce asymmetry and alter

the optical axis of the waveguide. Also, it was not possible to achieve necessary asymmetric birefringence in shallow etched devices. More detailed analysis of these structures is given in chapter 7. Schematic diagrams illustrating the deep and shallow etched ridge waveguides are shown in Figure 4.4. The ridge waveguides were based on a design with etch depth of $1.95\ \mu\text{m}$ (for the deep etched waveguide) and etch depth of $0.95\ \mu\text{m}$ (for the shallow etched waveguide). Here, zero order mode operation was verified at a wavelength of $850\ \text{nm}$ for each device.

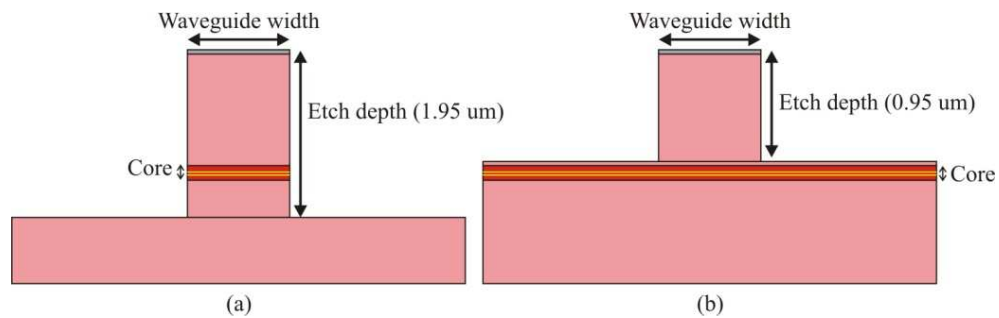


Figure 4.4: Schematic diagrams of (a) deep etched and (b) shallow etched devices.

The mode solving technique was used to determine the correct width and depth of the waveguide. First, the effective modal index values for the first three TE modes with varying widths of the waveguide for shallow and deep etched devices were calculated, which is shown in Figure 4.5. It was observed that increasing the width of the waveguide, the effective refractive index also increases. This is due to the increased confinement factor in wide waveguides, which results in improved laser action. This is also attributable to lower scattering losses in shallow etched waveguides. However, beyond a certain width, the laser design will support more than one mode. The design should therefore, be as wide as possible without resulting in double mode operation [6].

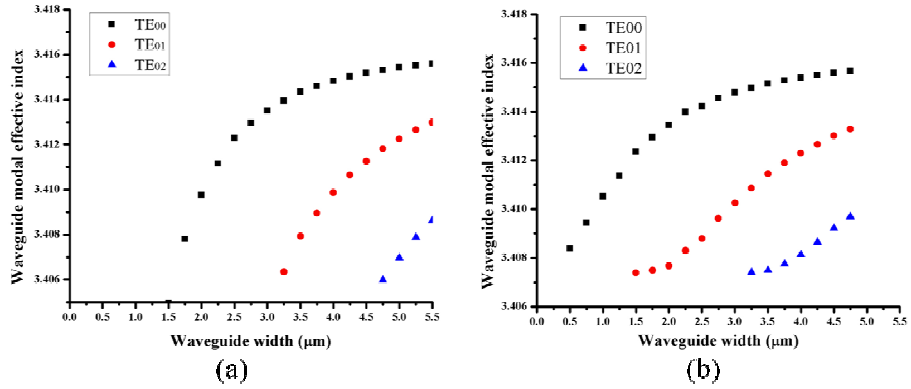


Figure 4.5: Simulated waveguide modal effective index of fundamental, 1st and 2nd order TE polarised modes as a function of the waveguide width for (a) deep etched and (b) shallow etched ridge waveguide structures.

The first order mode cutoff is at 3 μm and 1.5 μm for deep and shallow etched waveguides, respectively. This width is preferable for single mode operation as the losses increase for the zero order mode with decrease in the waveguide width. Therefore, in order to keep the zero order mode, 3.0 μm wide devices were fabricated for characterisation, which provide a single mode operation with high optical confinement. The simulated modal profile of a 3 μm wide ridge waveguide structures at the depth of 1.95 μm (into the waveguide core) and 0.95 μm (above the core), where a single mode operation was obtained, is shown in Figure 4.6.

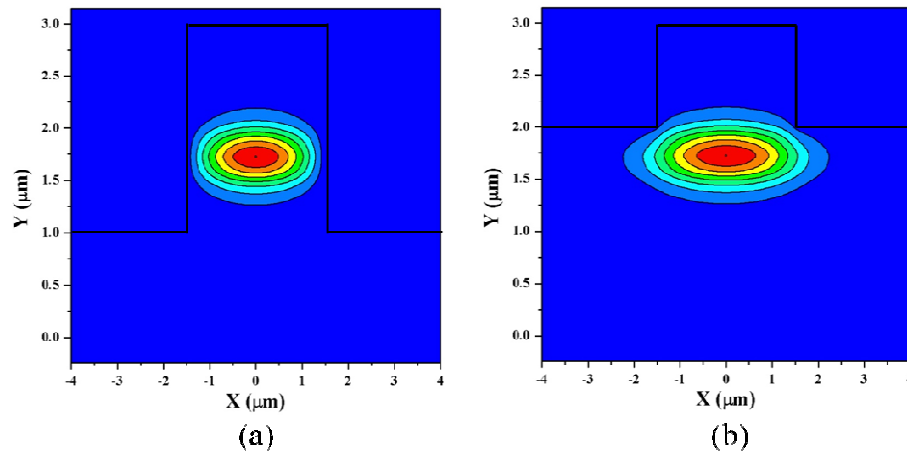


Figure 4.6: Simulated modal profiles of a fundamental mode of (a) deep and (b) shallow etched ridge waveguide structures with 3 μm wide ridge waveguides.

4.3.2.2. Device fabrication

The fabrication of ridge waveguide lasers involves multiple steps as described in chapter 3. The complete fabrication process steps for the ridge waveguide lasers are given in Annex II.

4.3.2.3. Device characterisation

Shallow etched devices were fabricated with 3 μm width. They were then cleaved into lengths of 0.5 mm, 0.8 mm and 1.0 mm. All devices were measured while the samples were kept controlled to 20 $^{\circ}\text{C}$, maintained with a thermoelectric cooler (TEC). A direct current sweep was used to measure the power emitted from the devices. A silicon detector was used to detect the emitted light. The emitted power (light) was measured as a function of applied current for several device lengths. It is observed that with an increase in the length of the cavity with fixed width of the waveguide, the threshold current increases. This is shown in Figure 4.7.

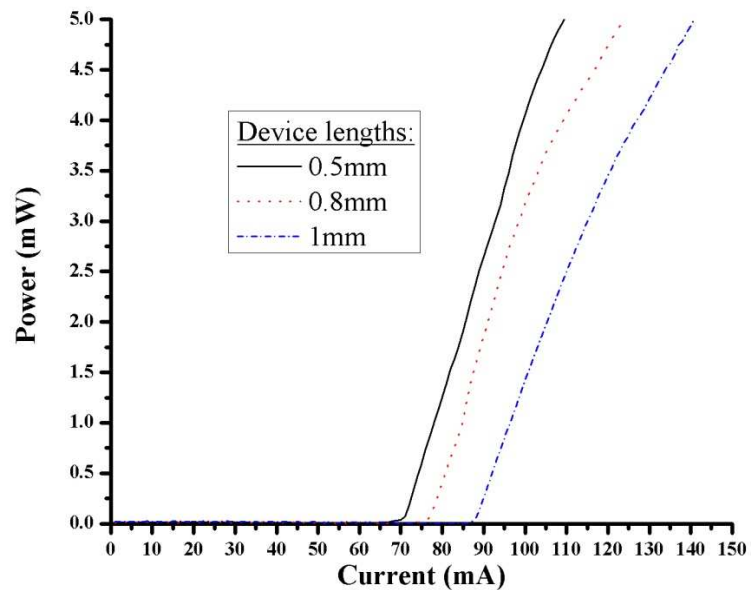


Figure 4.7: Power as a function of applied current for 3 μm wide and various cavity length ridge waveguide lasers.

4.3.2.4. Calculation of material parameters

The quality of the laser material being used can be assessed by the calculation of basic material parameters including; differential quantum efficiency (η_d), internal quantum efficiency (η_i), internal loss (α_i), threshold current density (J_{th}), infinite threshold current density (J_∞) and the modal optical gain (g_m).

Using the L-I curves in Figure 4.7, the threshold current (I_{th}) of the device is determined, and from the slope of the curve, the differential quantum efficiency is calculated using the relation given in equation 4.3.

$$\eta_d = \frac{q}{h\nu} \frac{dP}{dI}$$

4.3

where q is the charge of an electron, h is the Planks constant, ν is the optical frequency of the laser light.

From equation 4.3, η_d is calculated for each device length and then $1/\eta_d$ as a function of cavity length (L) is plotted which is shown in Figure 4.8, and gives a linear relationship. This intersects the y-axis at the value of $1/\eta_d$. From this intercept, and slope of the fitted line, internal quantum efficiency (η_i) is calculated.

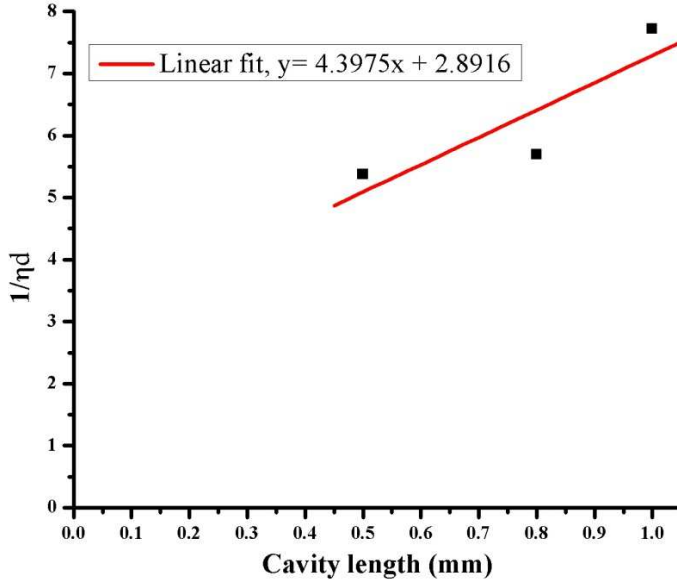


Figure 4.8: A plot of inverse differential quantum efficiency as a function of the cavity length.

Internal loss (α_i) is calculated by substituting η_i into equation 4.4 [7] for each cavity length.

$$\frac{1}{\eta_d} = \frac{1}{\eta_i} + \frac{\alpha_i}{\eta_i \ln \frac{1}{R}} L$$

4.4

where L is the cavity length of the device and R is the mean Fresnel reflectivity of the two cleaved facets which is ~ 0.3 .

In this case, η_i is found to be 34 % and α_i with 0.5 mm, 0.8 mm and 1 mm long devices, is found to be 19/cm, 13.5/cm and 18.5/cm, respectively.

The threshold current density is calculated using equation 4.5.

$$J_{th} = \frac{I_{th}}{Area}$$

4.5

This gives threshold current densities of 4.7 KA/cm², 3.2 KA/cm² and 2.9 KA/cm² for 0.5 mm, 0.8 mm and 1 mm long and 3 μm wide devices, respectively.

The infinite threshold current density (J_{∞}) is calculated by plotting a graph between $\ln J_{th}$ and $1/L$, which is shown in Figure 4.9. From slope of the line and using equation 4.6, J_{∞} is calculated, which is found to be 1763.75 A/cm².

$$\ln J_{th} = \frac{L_0}{L} + \ln J_{\infty}$$

4.6

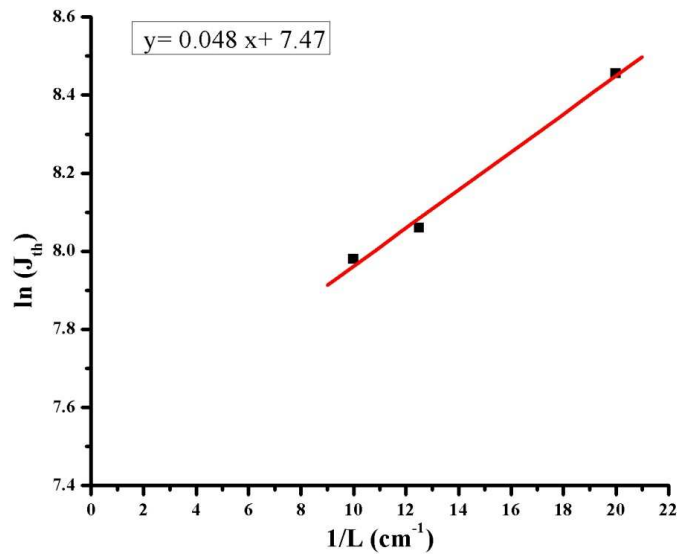


Figure 4.9: A plot of $\ln J_{th}$ as a function of $1/L$.

The modal optical gain is calculated using equation 4.7

$$n_w \Gamma g_{th} = \alpha_i + \frac{1}{L} \ln \frac{1}{R}$$

4.7

where n_w is the number of quantum wells, Γ is the optical confinement factor of one well, g_{th} is the material gain per quantum well at threshold. The product $n_w \Gamma g_{th}$ is called the modal gain (g_m). Here, modal gain of 40.47/cm, 25.23/cm and 22.03/cm was calculated for 0.5 mm, 0.8 mm and 1 mm long and 3

μm wide devices, respectively. This decrease in modal gain with increase in the device length is due to the higher threshold current for longer devices.

4.3.2.5. Temperature characteristics

The semiconductor lasers are temperature sensitive. As the sample temperature increases, the lasing threshold of the devices increases. This can be observed from the L-I curves of $3\ \mu\text{m}$ wide and $1\ \text{mm}$ long lasers at various temperatures, shown in Figure 4.10. This increase in lasing threshold is due to increase in the transparency carrier density with temperature, which in turn decreases the gain of the device. This is because the injected carriers spread over a large range in energy [7]. The losses also increase with a rise in temperature; which are most likely due to the thermionic emissions, in which carriers cross their potential energy barrier, resulting in higher threshold current.

The characteristic temperature (T_0) of the material which describes the temperature dependence of the threshold current is evaluated by plotting the natural log of threshold current (I_{th}) as a function of operating temperature. This is shown in Figure 4.11. The values of the threshold current and the operating temperatures are taken from the measured data (shown in Figure 4.10). By applying a linear fit to the measured data and using the equation 4.8 [8, 9], the characteristic temperature is found to be $97\ \text{°K}$, which is less than earlier reported values [10]. This lower T_0 is attributed to poor quality growth of the material as compared to the commercially growth material, and to design of the material.

$$I_{th} = I_{th0} \exp\left(\frac{T}{T_0}\right)$$

4.8

where I_{th} is the threshold current, I_{th0} is the threshold current at $0\ \text{°K}$ which is known as the characteristic current, T is the operating temperature in °Kelvin and T_0 is the characteristic temperature of the material.

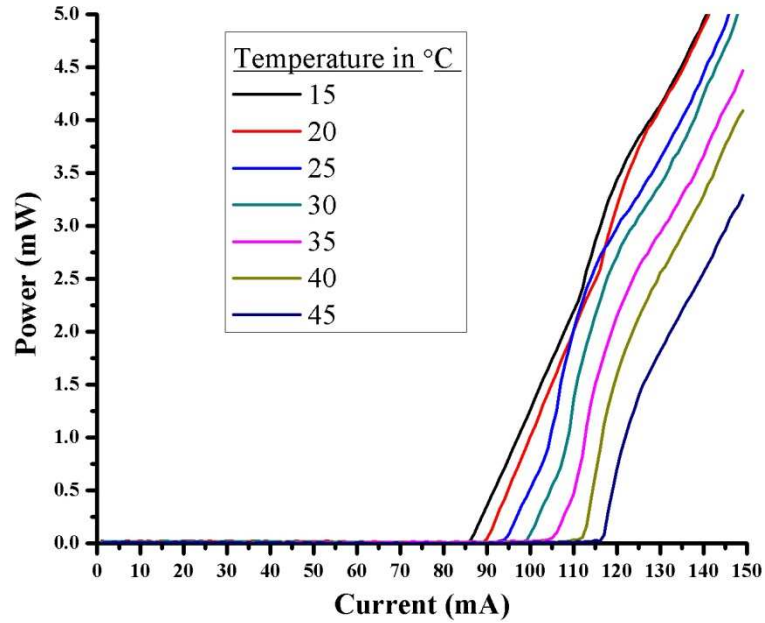


Figure 4.10: A plot of emitted power as a function of current at various temperatures.

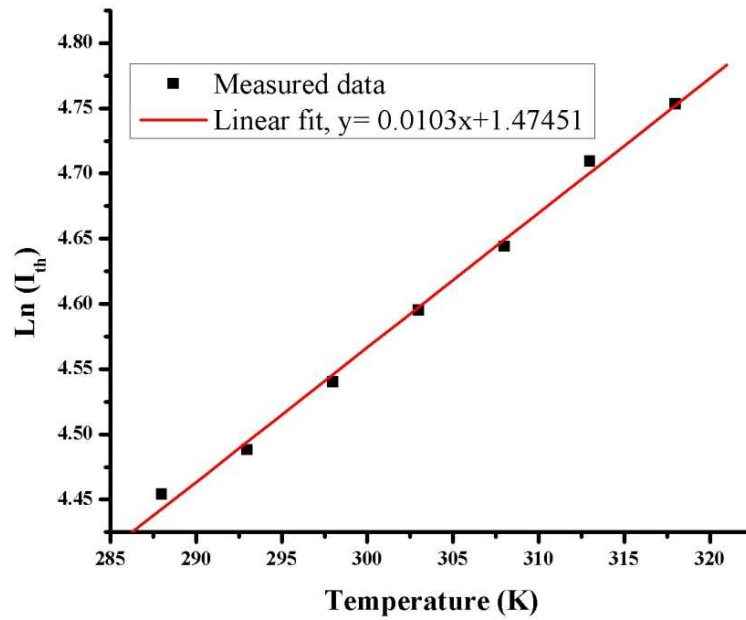


Figure 4.11: A graph of natural log of threshold current as a function of temperature.

4.3.2.6. Spectrum analysis

The optical spectrum was obtained for a 0.5 mm long, 3 μm wide shallow etched waveguide laser. The light was coupled into optical fibre using a microscope objective lens and was measured using the optical spectrum analyser (OSA). A schematic diagram of the optical spectrum measurement setup is shown in Figure 4.12.

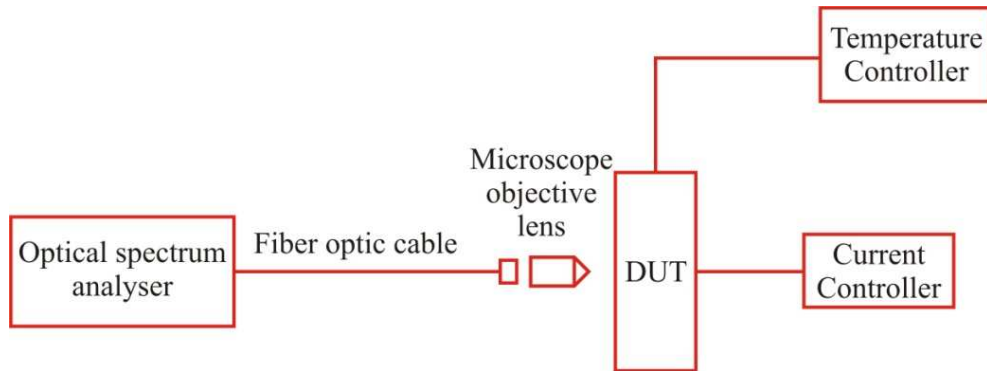


Figure 4.12: A schematic diagram of optical spectrum measurement setup.

The threshold current for this device was 70.5 mA (as shown in Figure 4.7). However, the first peak was observed for 80 mA current at a wavelength of 870 nm. This spectrum is shown in Figure 4.13. There is a change of 20 nm in wavelength between the laser excitation and the designed output wavelength of 850 nm. This difference is likely due to the growth defects or current injection effects i.e. heat. A red shift in peak wavelength was also observed when measured with higher CW current injection. A plot in Figure 4.14 clearly shows the peak wavelength shift with increasing current. Here, with 120 mA change in current, a red shift of 27 nm in peak wavelength was observed as compared to the first peak at a wavelength of 870 nm. This red shift in wavelength is due to the existence of localized heating in the intrinsic core of the material, produced due to the presence of carrier traps in the core which produce hindrance for carrier transportation in the core medium from the surrounding layers.

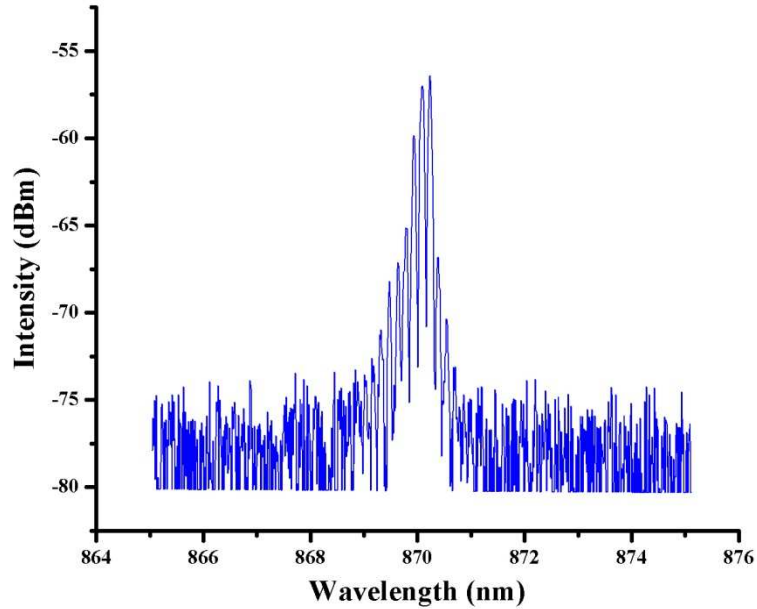


Figure 4.13: Spectrum showing the excitation wavelength of 870 nm for 0.5 mm long and 3 μm wide ridge waveguide laser at 80 mA.

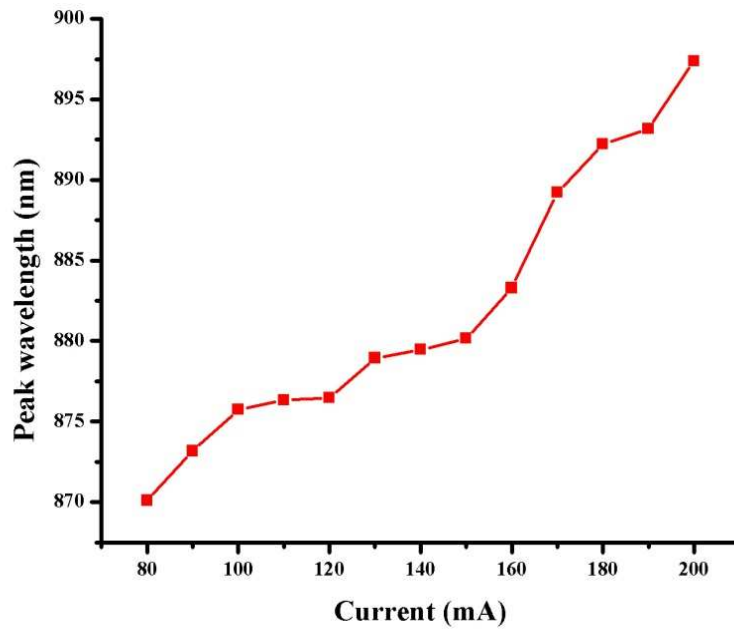


Figure 4.14: A plot of observed peak wavelength with increase in the current.

4.3.2.7. Far field pattern analysis

The far field pattern is important in determining the coupling efficiency and coupling tolerance between a semiconductor laser and a single mode fibre

[11]. Simulation of the far field patterns was performed for a $3\ \mu\text{m}$ wide, $0.8\ \text{mm}$ long and shallow etched device using 3-D BPM. The obtained simulation results are shown in Figure 4.15.

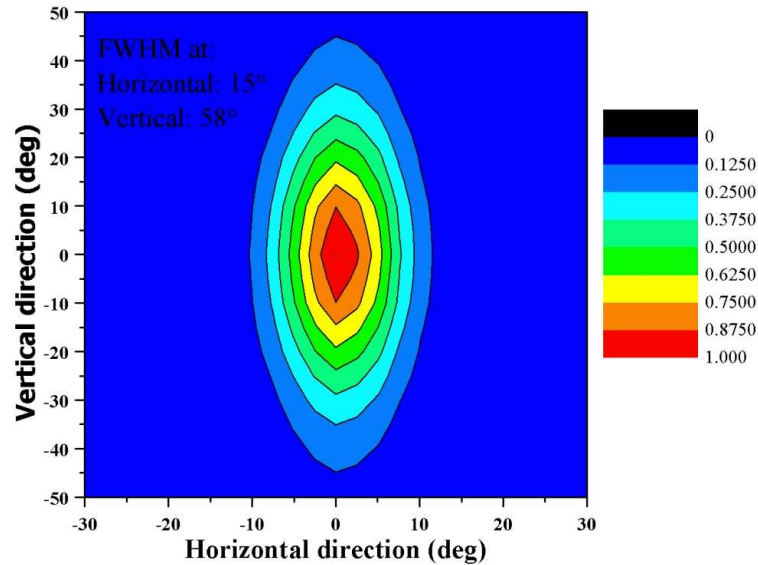


Figure 4.15: Far field simulation of a $3\ \mu\text{m}$ wide shallow etched waveguide structure.

The simulation results show the divergence angle in the horizontal direction is 15° , whereas in the vertical direction is 58° . Thereafter, the fabricated devices were measured for far field patterns at a distance of $5\ \text{mm}$ away from the device facet using the measurement setup shown in Figure 4.16. The devices were mounted on a TEC with the temperature controlled to 20°C and were placed in front of the rotating slit of the goniometric radiometer. The emitted light from the devices was collected and the beam intensity as a function of angular position was measured.

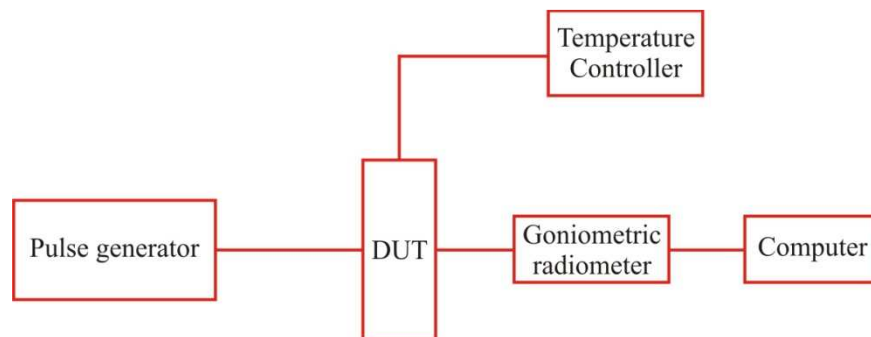


Figure 4.16: A schematic picture of far field patterns measurement setup.

Results were obtained for far field patterns in the horizontal and vertical directions at different currents with full width half maximum (FWHM) measured, and are shown in Figure 4.17.

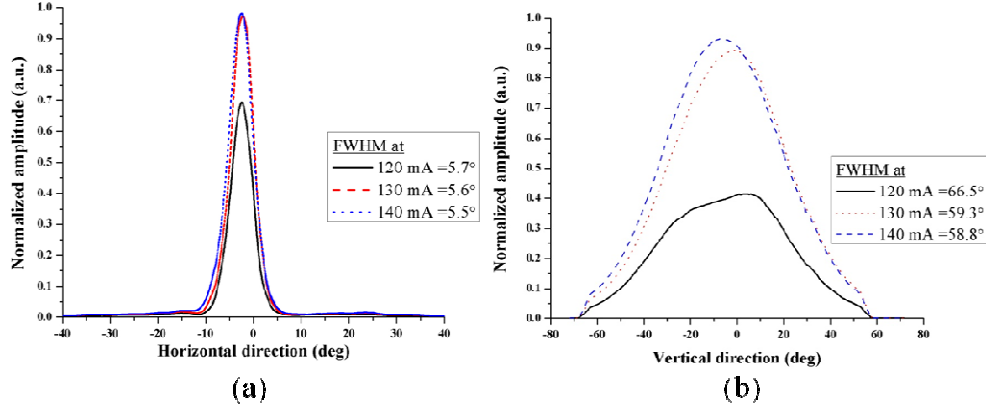


Figure 4.17: The measured far field patterns in (a) horizontal and (b) vertical directions.

The measured divergence angle in horizontal direction was around 5.6° , whilst in the vertical direction, it was around 59.3° at 130 mA current. Compared to the simulated results, the divergence angle in horizontal direction is reduced, likely due to fabrication errors (most likely being an under etched sample), whereas the divergence angle is consistent with the modelling in vertical direction. Furthermore, these results are consistent with the simulated single mode (Figure 4.6 (b)) results, where, the horizontal and vertical spread of mode is entirely opposite to the far field pattern, as would be expected.

4.4. Conclusions

GaAs/AlGaAs material system emitting at a wavelength of 850 nm, with its epitaxial layers is discussed. The methods for material characterisation including TLM and ridge waveguide lasers are presented. Here, TLM method was used for identification of the specific contact resistance of the ohmic contact. It was found to be $2.932 \times 10^{-7} \Omega \text{mm}^2$ which is less than the ideal $1 \times 10^{-1} \Omega \text{mm}^2$. This showed that there was low series resistance between the contacts. Thereafter, the ridge waveguide lasers design, fabrication and characterisation are discussed. The

evaluation of the emitted power with current characteristics of different lengths was used for determination of the most common material properties. These include internal quantum efficiency (η_i), internal loss (α_i), threshold current density (J_{th}) and the modal optical gain (g_m) of the material. Here, η_i was found to be 34 % which is very low from the typical values of 60-80 % for good quality material. Furthermore, the internal losses were also found to be very high which showed that the material is highly resistive. The characteristic temperature was calculated for this material and found to be 97 °K which is less than already measured values. The measured parameters showed that the material is poor to use in devices with active functionality, but it is still worthwhile to make passive devices. The characterisation of above parameters is important to analyse the material quality, so that it can be used for further fabrication of the devices.

In the subsequent section, the optical spectrum was measured for shallow etched fabricated devices. A red shift in wavelength of 20 nm was found between the excitation wavelength and the designed output wavelength of 850 nm. Furthermore, with the injection of current, a red shift in peak wavelength was found. This red shift in wavelength is due to the growth defects and localized thermal effects.

In the last section of this chapter, measurements for far field patterns were carried out. It was found that there was more spread of light in the vertical direction than the horizontal direction. There were also inconsistent results (measured) for far field patterns as compared to the simulated results in the horizontal direction, whilst consistent in the vertical directions. This is most likely due to fabrication errors (being an under etched sample).

4.5. References

1. Palik, E.D., *Handbook of optical constants of solids*. 1991: Academic Press.
2. www.luxpop.com.
3. Gehrsitz, S., et al., *The refractive index of $Al_xGa_{1-x}As$ below the band gap: Accurate determination and empirical modeling*. Journal of Applied Physics, 2000. **87**(11): p. 7825-7837.
4. Chen, K.X., et al., *Four-point TLM measurement for specific contact resistance assessment*. <http://www.ecse.rpi.edu/~schubert/Course-Teaching-modules/A38-Four-point-TLM-measurement.pdf>.
5. RSoft Design Group Inc, www.rsoftdesign.com.
6. Furst, S., *Monolithic integration of semiconductor ring lasers*. 2008, PhD thesis, University of Glasgow: UK.
7. Coldren, L.A. and S.W. Corzine, *Diode lasers and photonic integrated circuits*. 1995: Willey - Interscience.
8. Bhattacharya, P., *Semiconductor optoelectronic devices*. 1996: Upper Saddle river, Prentice Hall Inc., NJ, USA.
9. Pankove, J., *Temperature dependence of emission efficiency and lasing threshold in laser diodes*. Quantum Electronics, IEEE Journal of, 1968. **4**(4): p. 119-122.
10. Wang, Y., et al., *AllInGaAs/AlGaAs/GaAs strained quantum well lasers with high characteristic temperature*. Chin. Opt. Lett., 2007. **5**(S1): p. S143-S144.
11. Akbar, J., *High Power Mode Locked Lasers monolithically Integrated with Semiconductor Optical Amplifiers*. 2012, PhD thesis, University of Glasgow: UK.

Chapter 5

Design and characterisation of polarisation mode convertor on GaAs/AlGaAs material

5.1. Introduction

Numerous polarisation mode convertors (PMCs) and polarisation insensitive devices have been demonstrated on various III-V material systems, including GaAs/AlGaAs, InP/InGaAsP and silicon on insulator (SOI). These PMCs reported in literature are of various designs and are based on the principles of mode evolution [1, 2] and mode beating. These include longitudinal periodically loaded waveguide sections [3], longitudinal waveguide bends [4], single ridge waveguide sections with a sloped side walls [5-8] and sub wavelength air trenches [9-11].

This chapter explains the basic structure and design of the PMC with its principle of operation, which is based on etched slot devices (Figure 5.1). Further, the design and optimisation of PMCs with a semiconductor laser are described.

The modelling was carried out to optimise the optical axis and the length of the PMC. The characterisation of the fabricated devices is also discussed.

5.2. Principle of the etched slot polarisation mode convertor

A schematic design of PMC with a sub-wavelength air trench is shown in Figure 5.1. Here w , h , t and d represent the width of the waveguide, the trench depth, thickness of the trench and position of the trench from the waveguide edge, respectively. The PMC is highly affected by these dimensions, and is described in the subsequent section.

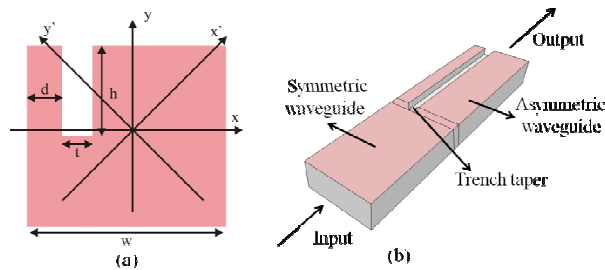


Figure 5.1: (a) A schematic design of a single trench PMC and (b) the symmetric and asymmetric waveguide sections.

The RIE was employed to fabricate the waveguide with sub-wavelength air trenches, resulting in an ability to attain controllable asymmetric waveguide profiles. Therefore, the PMCs were fabricated with deep etching, as it helps to attain the etched slot as well as strong mode confinement. The asymmetric cross section enables the optical axis of the waveguide to be changed relative to the wafer normal as shown in Figure 5.1 (a), where x' and y' axes are changed to 45° from their respective x and y axes. When a TE (or TM) mode enters into the asymmetric waveguide section (PMC section) from the symmetric waveguide (Figure 5.1 (b)), two eigen modes, which are orthogonally polarised to each other, are excited. As a result, the non-dominant field components of these modes are increased, and the modes become hybrid in nature. These modes propagate at different propagation constants, β_1 and β_2 , and for a fully hybridised mode with

optical axis of 45° , results in a polarisation rotation of 90° (100 %) at the half beat length, $L\pi$. Here, $L\pi = \pi/\Delta\beta$ where $\Delta\beta = \beta_1 - \beta_2$ and is the difference between the propagation constants of two fundamental modes. When the optical axis changes to 22.5° or 67.5° , the polarisation is rotated to 45° (50 %) and the length of the convertor is reduced to $L\pi/2$.

5.3. Modelling and design of the polarisation mode convertor

Commercial beamprop software [12] was used to model and design the symmetric and asymmetric waveguide structures (PMC structure) on the material system presented in Table 4.2. The asymmetric waveguide structures can be obtained using a sub-wavelength air trench in the PMC section with deep etching. For simulations, a ridge waveguide with $1.24 \mu\text{m}$ width, which gives single mode operation (as described in Chapter 4) was used as an input waveguide, whereas different trench geometries, were used to design the PMC. This includes one, two and three trenches with different widths, at distinct positions from the waveguide edge, and with various depths. The appropriate conversion was obtained with one trench geometry (Figure 5.1 (a)). However, the conversion can also be obtained using two and three trenches in the waveguides, but these were difficult to realise. Therefore, a single trench design was further pursued, as it was comparatively easier to achieve than two and three trench geometries. The efficacy of the waveguide for polarisation conversion was set by adjusting different trench widths (t), trench positions from the waveguide edge (d), and the trench depths (h). The losses associated with PMCs are not taken into account, due to the software limitations.

The polarisation conversion (PC) efficiency was obtained using the expression in Equation 5.1.

$$PC = \frac{P_{TM}}{(P_{TE} + P_{TM})} \times 100\%$$

5.1

The geometrical dimensions (as stated earlier) affect the polarisation conversion efficiency. Polarisation conversion efficiency changes with changes in dimensions, such as the trench width (t), the trench depth (h) or the trench position from the waveguide edge (d). The trench position from the waveguide edge was determined by the mechanical stability of the remaining pillar (d). This was set by my previous fabrication experience (during this research work) to be 140 nm, as small (d) results in damaging the pillars on the waveguide edges side.

Simulations were carried out for optimisation of the PMC by changing the trench width, the trench depth, and at the position of the trench from the waveguide edge of 140 nm. It was found that 50 % and 100 % polarisation rotations were obtained at trench depths of 1.25 and 1.33 μm , respectively, for a 230 nm trench width with a 140 nm trench position from the waveguide edge. A plot of polarisation mode conversion as a function of the trench depth for different trench widths at constant trench position from the waveguide edge is shown in Figure 5.2.

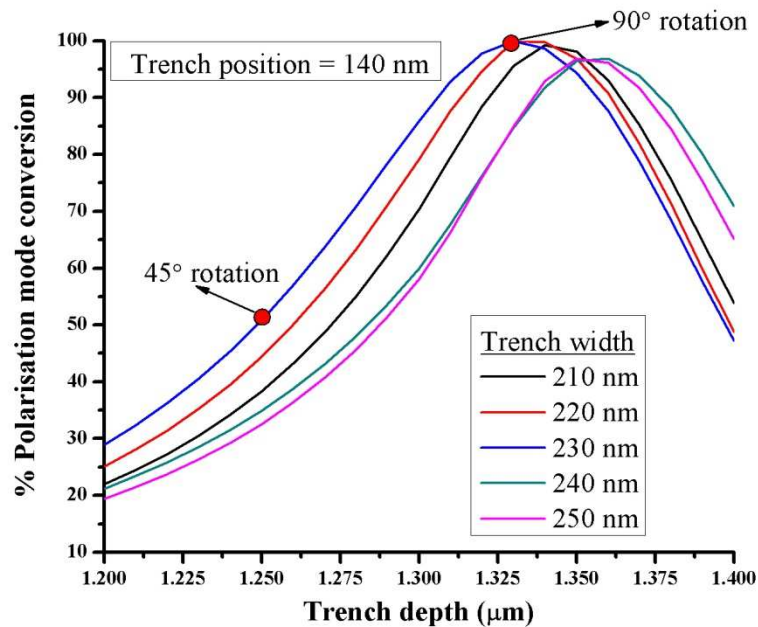


Figure 5.2: A plot of % polarisation mode conversion as a function of the trench depth for different trench widths at constant trench position (140 nm) from the waveguide edge.

Thereafter, using the optimum trench width (230 nm) and the trench depth (1.25 μm) for 50 % polarisation rotation, and position of the trench from the waveguide edge was varied from 120 to 170 nm. The optimum polarisation conversion was obtained at a position of 140 nm. A plot of % polarisation mode conversion as a function of the propagation direction at various trench positions from the waveguide edge, at constant trench width (230 nm) and trench depth (1.25 μm) is shown in Figure 5.3.

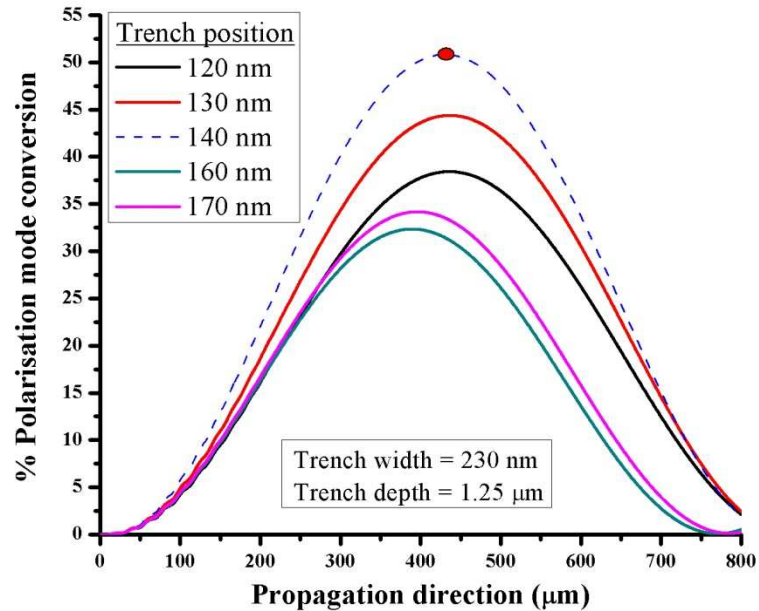


Figure 5.3: A plot of % polarisation mode conversion as a function of the propagation direction at various trench positions from the waveguide edge, at constant trench width (230 nm) and trench depth (1.25 μm).

The optimised values for the trench width (230 nm), the trench depth (1.25 and 1.33 μm) and position of the trench (140 nm) from the waveguide edge for 45° (50 %) and 90° (100 %) rotations, respectively, were used for further simulations. The polarisation mode conversion efficiency of 50.8 % was obtained at the convertor length of 415 μm and the trench depth of 1.25 μm . The width of the PMC section was 1.24 μm and this PMC includes a 230 nm wide trench at a position of 140 nm from the waveguide edge, as optimised above. The polarisation mode conversion as a function of the propagation direction is shown in Figure 5.4.

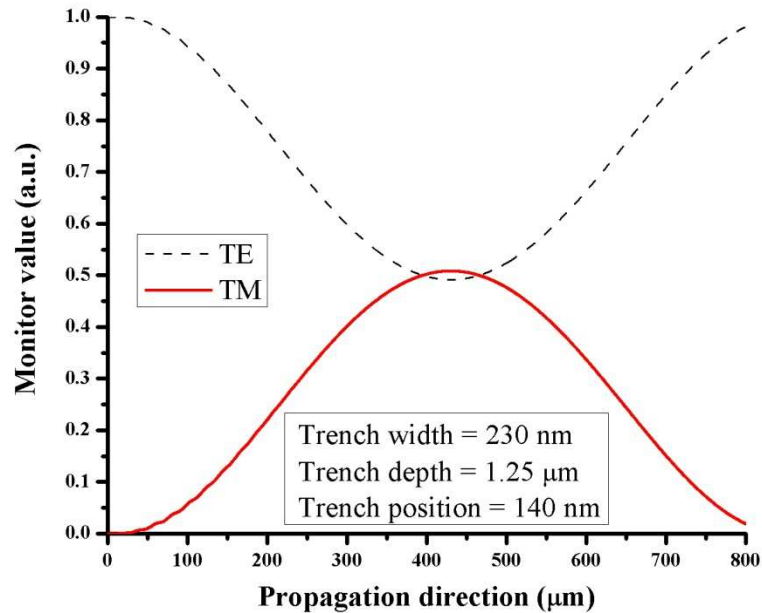


Figure 5.4: The TE to TM mode conversion as a function of the propagation direction for 45° (50 %) rotation.

Using the optimised dimensions for the trench width (230 nm), the trench depth (1.33 μm) and position of the trench from the waveguide edge (140 nm) for 90° (100 %) rotation, the polarisation mode conversion efficiency of 99.9 % was obtained at the convertor length of 665 μm. The polarisation mode conversion as a function of the propagation direction is shown in Figure 5.5. The polarisation mode conversion depends upon the trench depth as shown in Figure 5.4 and Figure 5.5, which identifies that changing the trench depth from 1.25 to 1.33 μm at optimised dimensions of the trench width (230 nm) and the position of the trench from the waveguide edge (140 nm), causes ~50 % difference in polarisation mode conversion, which is due to change in the optical axis of the PMC. In this work, only devices of 50 % rotation were fabricated due to the difficulties associated with etching a deep, narrow trench.

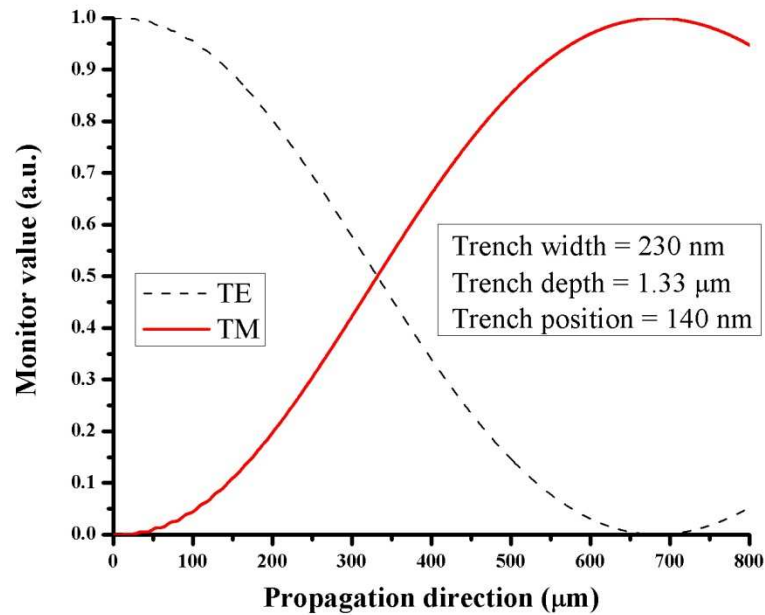


Figure 5.5: The TE to TM mode conversion as a function of the propagation direction for 90° (100 %) rotation.

5.4. Optimisation of the trench depth in realised devices

The trench depth and the trench width are interdependence to each other as shown in SEM images in Figure 5.6. In order to attain the desired etch depth of 1.25 μm for 50 % polarisation rotation, the various devices were fabricated to optimise the trench depth relative to the trench width. The trench width of 500 nm to achieve 1.25 μm trench depth, was optimised. In fabrication, less etching was advantageous to attain 50 % polarisation rotation due to various factors including etch rate, trench widening due to non vertical etching, and pillars breakage due to ions reflections, which results in mesa formation. Over-etching also causes mask erosion.

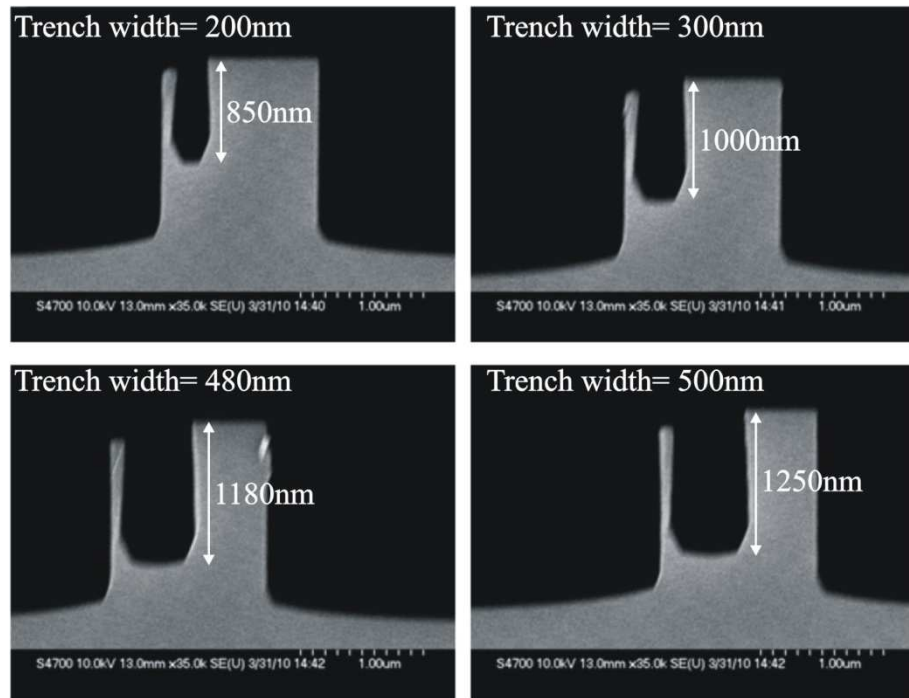


Figure 5.6: SEMs of trench widths relative to the trench depths.

5.5. Device structure with a single PMC

The device structure shown in Figure 5.7 was devised for realisation of devices based on GaAs/AlGaAs material. This structure consists of a single PMC with input and output waveguide sections.

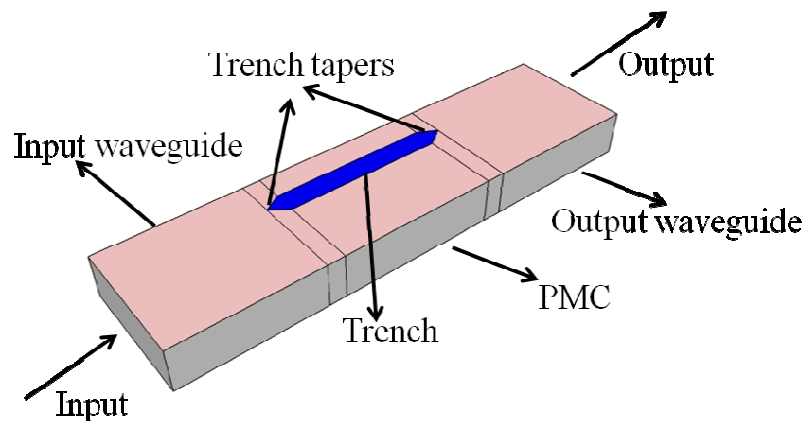


Figure 5.7: A schematic diagram of the device with a single PMC.

In this structure, the dimensions optimised for the PMC including the waveguide width and position of the trench from the waveguide edge, except the trench width, were used. A 500 nm wide trench was used instead of optimised trench width (230 nm, as was in initial design) to attain the trench depth of 1.25 μm for 22.5° rotation in optical axis (as explained previously, Figure 5.6). This was due to the fact that, with optimised trench width, the desired trench depth could not be achieved. A single PMC was placed between 500 μm long input and output waveguide sections. The width of the symmetric waveguide and PMC sections was kept 1.24 μm . The PMC comprises a 500 nm wide trench at position of 140 nm from the waveguide edge. Various PMCs with lengths ranging from 350 to 600 μm , with a step of 50 μm , were fabricated. Tapers of 5 μm length, were provided on each corner of the trench of PMC for smooth etching from the input and output waveguide sections to the convertor section. These tapers provide deep to shallow etching in the slot due to the RIE lag effect, which in turn provides smooth transitions of modes in the device. The devices were deep etched through the waveguide core to achieve asymmetric waveguides (PMC sections).

5.5.1. Device fabrication

Passive PMCs were fabricated and optimised using e-beam lithography. The trench pattern was formed using direct write e-beam and standard etch process as described in chapter 3. The fabrication steps required to realise the passive PMCs are given in Annex III. Precise control over the trench depth in the PMC sections is critical, and was achieved using a reflectometric etch monitoring technique (as described previously). The devices were fabricated using reactive ion etching with ridge depths of 1.45 μm to 1.50 μm , measured for the different samples using a Dektak Profilometer. The cross-section of the fabricated PMC is shown in Figure 5.8. The defined waveguide width, the trench width and position of the trench from the waveguide edge in the PMC were 1.24 μm , 500 nm and 140 nm, respectively. However, the achieved results after fabrication for the waveguide width, the trench depth and position of the trench from the

waveguide edge were $1.27\ \mu\text{m}$, $610\ \text{nm}$ and $100\ \text{nm}$, respectively. The obtained trench depth was $1.18\ \mu\text{m}$.

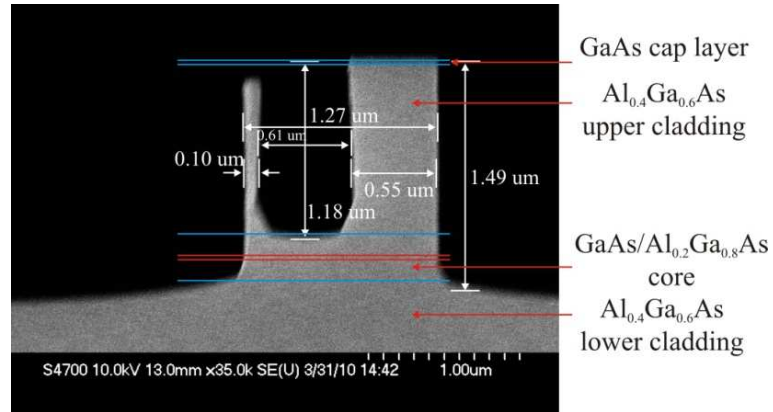


Figure 5.8: SEM picture of the cross section of the passive PMC.

5.5.2. Passive device measurements

The fabricated devices were measured and characterised using the setup shown in Figure 5.9. In this setup, $1064\ \text{nm}$ radiation was provided using the diode pumped solid state neodymium-doped yttrium aluminium garnet (Nd:YAG) laser. A $1064\ \text{nm}$ laser beam was used to avoid any type of absorption losses. An optical chopper was used along with a lock-in amplifier. Microscope objective lenses of $40\times$ were used for coupling the beam through the device. A polarising beam splitter ensured only TE polarised radiation from the Nd:YAG laser was injected into the device. An analyser was used at the output to separate the TE and TM polarised radiations. The TE and TM components were then separately detected using a photo-detector lock-in amplifier.

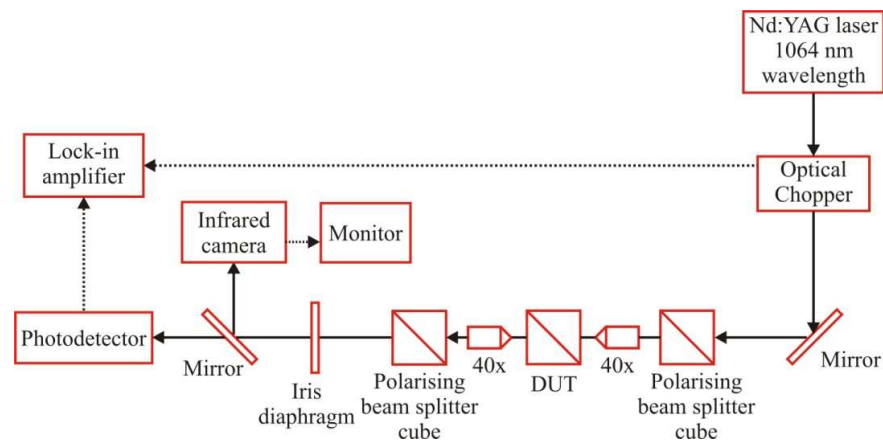


Figure 5.9: A schematic diagram of the device measurement setup with Nd:YAG solid state laser, emitting at 1064 nm.

The TM purity was found to be depend on the PMC length as shown in Figure 5.10. Conversion efficiency varied from 5 to 40.5 %, and maximum conversion efficiency, i.e. 40.5 % was obtained at the convertor length of 400 μm with a 1064 nm wavelength laser beam. The simulated TM purity was in the range of 30.7 to 50.8 % for PMC lengths of 400 to 600 μm with maximum conversion efficiency i.e. 50.8 % at the length of 415 μm at 850 nm wavelength (Figure 5.4). As expected, this lower conversion efficiency for the fabricated devices as compared to the initial simulated results was due to the dimensions of the fabricated PMCs, and due to the wavelength change of injected signal. The % TM purity was obtained at the optimised dimensions of the device, which were 1.24 μm , 230 nm, 1.25 μm and 140 nm (in simulations), whereas, experimentally measured devices had 1.27 μm , 610 nm, 1.18 μm and 100 nm for the PMC width, the trench width, the trench depth and position of the trench from the waveguide edge, respectively. Furthermore, the wavelength was also changed from 850 nm to 1064 nm. Thereon, the experimentally measured dimensions were used to simulate the devices. This yielded a conversion efficiency of 57.3 % at the convertor length of 400 μm with 1064 nm wavelength. The later simulation results (Figure 5.10) are nearly comparable with the experimentally obtained results, and have a similar trend in terms of polarisation mode conversion versus convertor length.

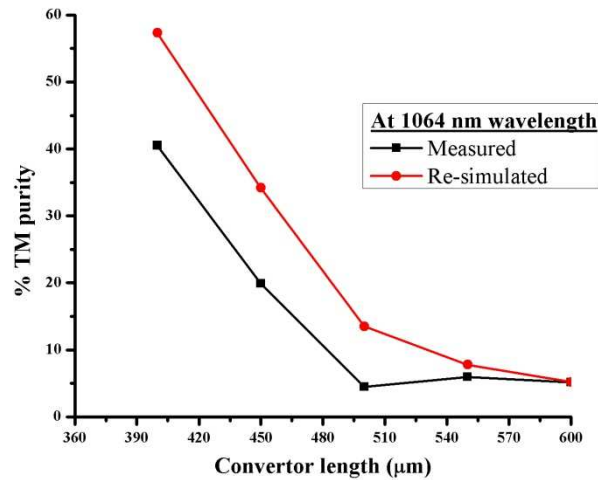


Figure 5.10: The % TM purity as a function of the PMC length (experimentally measured and re-simulated).

5.6. Device structure with back to back PMCs

The devices fabricated with a single PMC (as described earlier) were intended to give 50 % polarisation rotation. The use of two PMCs, and attaching them back to back, is a method to achieve further rotation to the optical axis. The first PMC yields 50 % rotation in the signal, and the second PMC gives further change of 50 % rotation, resulting in 100 % polarisation mode conversion, in total. This device structure is shown in Figure 5.11.

In this structure, two gain sections, with widths ranging from 1.23 to 1.35 μm , and the length of 800 μm , were used on both the longitudinal sides with two PMCs, lengths of each ranging from 300 to 500 μm . These PMCs were sandwiched back to back in the gain sections, and were electrically pumped. Taper waveguides of 5 μm length, were used at the corners of each trench of the PMC to ensure smooth dry etching from the gain sections to the convertor sections, which in turn provides smooth transmission of optical modes in the integrated device. These devices were deep etched through the core, while trenches in the convertor sections were obtained with RIE lag. Trenches of varying widths, ranging from 500 to 540 nm in convertor sections were defined at

positions of 140 nm from the waveguide edge in numerous devices. The wafer shown in (Table 4.2) was used to fabricate these devices.

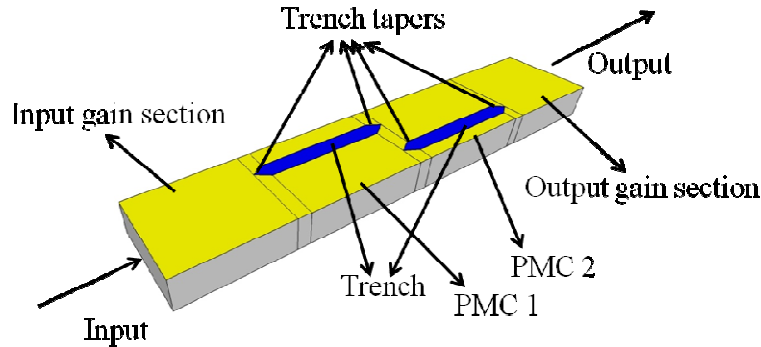


Figure 5.11: A schematic diagram of the device, with back to back PMCs.

5.6.1. Modelling and design of devices with back to back PMCs

Using the optimised dimensions, the back to back PMCs were modelled. The waveguide width of $1.24\ \mu\text{m}$, the trench depth of $1.25\ \mu\text{m}$ and the trench width of $230\ \text{nm}$ at position of $140\ \text{nm}$ from the waveguide edge, which were optimised to attain 45° (50 %) rotation (Figure 5.4), was routed. Simulations were carried out using the beamprop software based on the beam propagation method (BPM). In simulations, the device structure with two PMCs, placed back to back between two symmetric waveguide sections, was used as shown in Figure 5.11. The polarisation conversion efficiency of 99.5 % was obtained from the combination of two PMCs at the convertor length of $840\ \mu\text{m}$. The % polarisation mode conversion as a function of the convertor length is shown in Figure 5.12. Here, the first PMC yields 50 % polarisation mode conversion as the optical axis is rotated at 22.5° (in first PMC), and further 50 % rotation was achieved in the second PMC as mode continues to rotate (in second PMC), resulting in 100 % polarisation mode conversion in total.

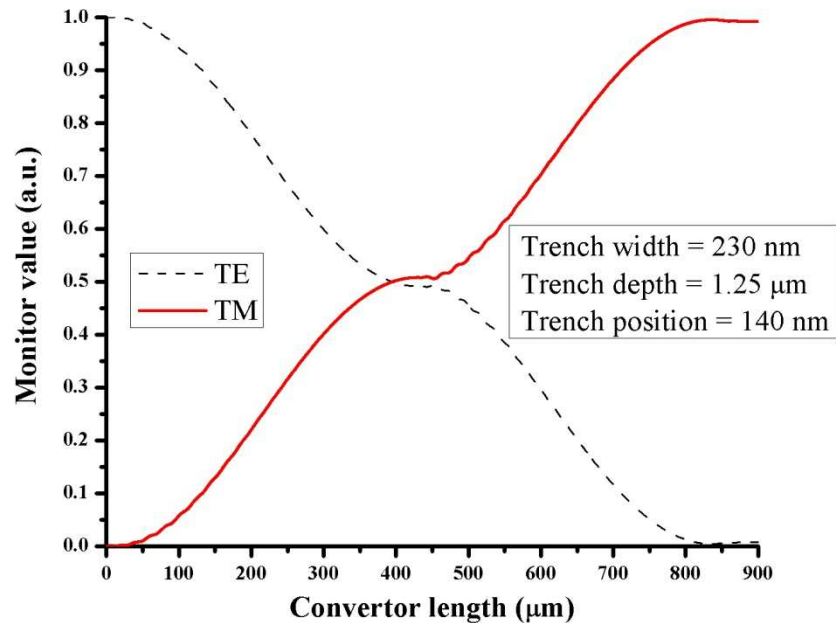


Figure 5.12: The TE to TM mode conversion as a function of the propagation direction for PMCs, attached back to back.

5.6.2. Fabricated device

The fabrication process to realise the integrated devices is given in Annex IV. Figure 5.13 shows the cross section of a realised PMC. This PMC is integrated with a semiconductor laser. A waveguide width of $1.34 \mu\text{m}$, a trench width of 500 nm (as optimised for the realised devices) and position of the trench from the waveguide edge at 140 nm , were designed for fabrication. The waveguide width was kept little bit higher from the optimised values to compensate any fabrication errors during fabrication. The obtained results after the fabrication were $1.34 \mu\text{m}$, 710 nm and 130 nm for the waveguide width, the trench width and position of the trench from the waveguide edge, respectively. The trench depth was found to be $1.18 \mu\text{m}$. All three sections of the integrated devices were electrically pumped.

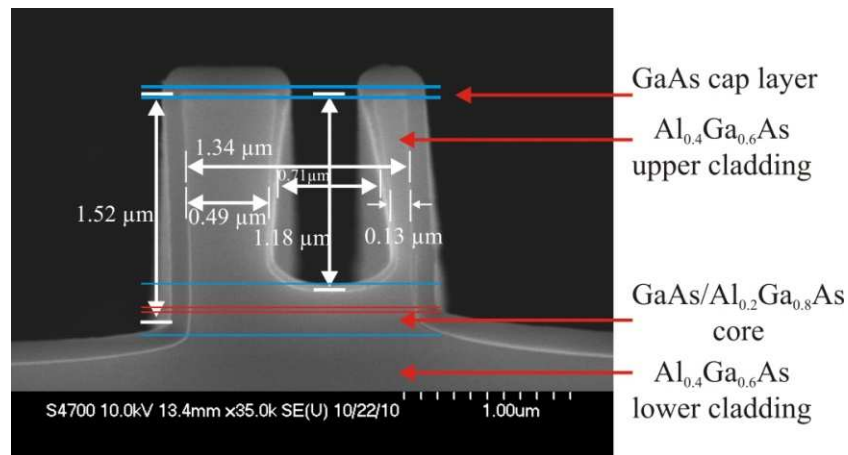


Figure 5.13: SEM picture of cross-section profile of the PMC.

5.6.3. Passive measurements with back to back PMCs

The fabricated devices were measured and characterised using the measurement setup shown in Figure 5.9.

A plot of the % TM purity as a function of the convertor length is shown in Figure 5.14. Conversion efficiency was found vary with length, i.e. from 14.2 to 64.4 %, and maximum conversion efficiency, i.e. 64.4 % was obtained at the convertor length of 760 μm with a 1064 nm wavelength of injected laser beam. The simulated TM purity was in the range from 85 to 99.5 % for PMC lengths ranging from 680 to 840 μm with maximum conversion efficiency, i.e. 99.5 % at the length of 840 μm with 850 nm wavelength. This shows lower conversion efficiency as compared to the initial simulated results. These incomparable results were due to dimensions of the fabricated PMCs, and due to the wavelength change of simulated and experimentally obtained results. The % TM purity was obtained at optimised dimensions of the device which were 1.24 μm , 230 nm, 1.25 μm and 140 nm (in simulations), whereas, experimentally measured devices had 1.34 μm , 710 nm, 1.18 μm and 130 nm for the PMC width, the trench width, the trench depth and position of the trench from the waveguide edge, respectively. The experimentally measured dimensions and wavelength of 1064 nm of injected laser beam were further used to simulate the devices. This yielded a conversion

efficiency of 49.7 % at the convertor length of 760 μm . The re-simulation results (Figure 5.14) compare well with the experimentally obtained results.

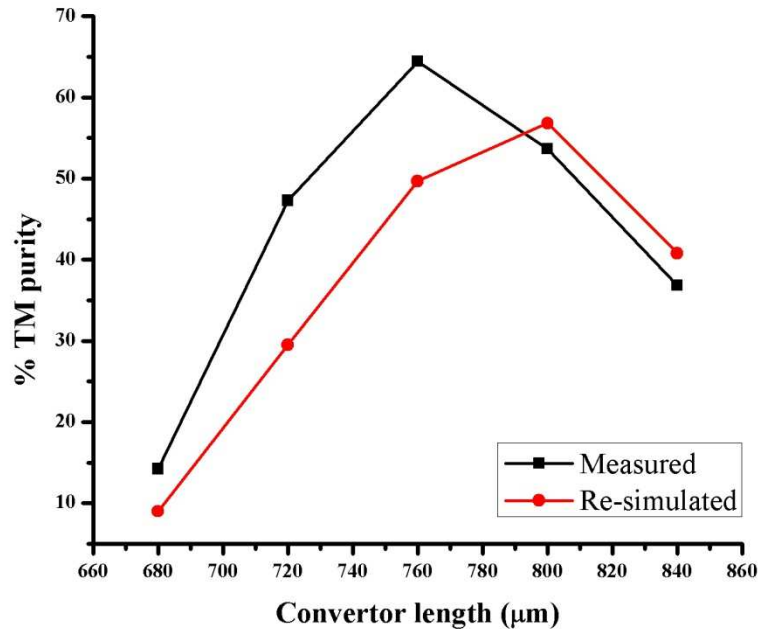


Figure 5.14: A plot showing experimentally measured and re-simulated results of the % TM purity as a function of the convertor length (attached back to back).

5.6.4. Active PMC measurements

The devices consisting of back to back PMCs were measured using the experimentally arrangement shown in Figure 5.15. An optical chopper was used to modulate the lasers and a lock-in amplifier was used for detection of the corresponding signal. A 40x Microscope objective lens was used for coupling the beam from the device using end fire technique [13]. A polarising beam splitter cube was used to get the TE polarised radiation from the injected laser beam, whereas an analyser was used to separate the TE and TM polarised radiation, subsequent to the fabricated device.

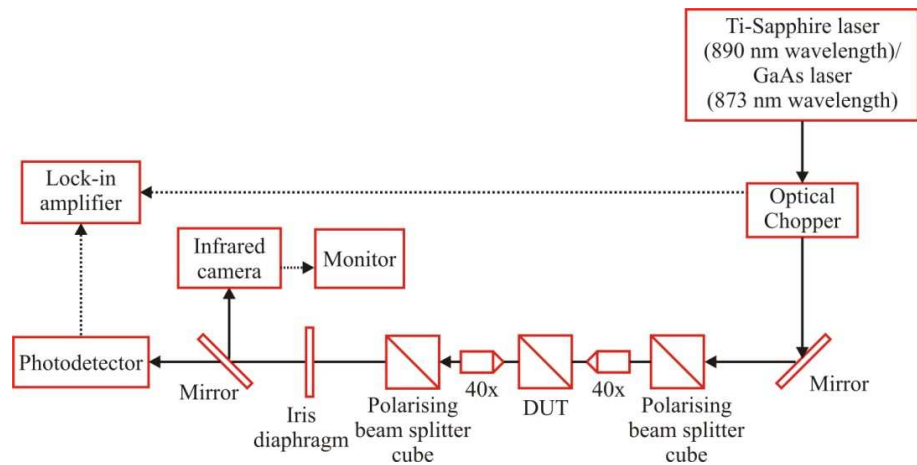


Figure 5.15: A schematic of the device measurement setup with Ti-Sapphire and GaAs laser.

Initially, the input signal was provided using a fabricated Fabry-Perot laser (GaAs, FPL). CW current was injected to different sections of the integrated devices with the intention of amplification of the input optical signal. It was found that no amplification occurred in the integrated devices. These measurements were performed with six fabricated samples, with almost 200 devices, in total. These devices were subsequently tested using the Ti-Sapphire laser (as shown in Figure 5.15) but there was neither lasing nor amplification in all of the fabricated integrated devices. This was assumed to be most probably due to un-even growth of the wafer. The behaviour of some of these fabricated devices was observed by taking V-I curves, which is given in the subsequent section.

5.6.5. Voltage-Current characteristics

The voltage-current (V-I) curves were obtained for different sections of the integrated devices. The V-I curves of a device show the device resistance. It was found that the PMC section and the other sections exhibit a very high resistance ~ 120 ohms for 50 mA injection current. The device resistance should be normally $\sim 6-8 \Omega$ and the switch on voltage should be ~ 1.4 V. The V-I curves of three sections of an integrated device are shown in Figure 5.16, which show the higher voltage (higher resistance) in all the sections. The high series resistance of

the device suggests that the epitaxial layers did not have the specified doping profile leading to high series resistance.

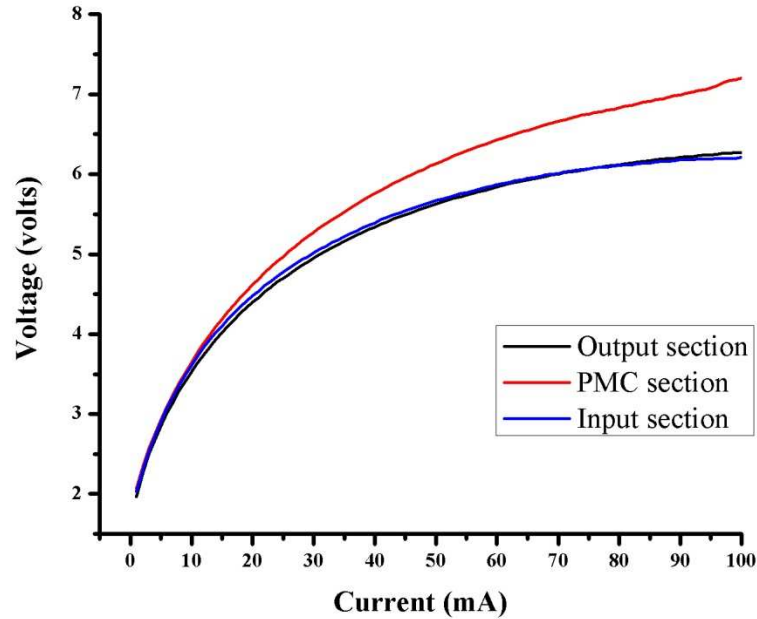


Figure 5.16: Voltage-current curves for three sections of an integrated device.

Output power of these devices was measured for input gain section biased at 80 mA, PMC section biased at 25 mA, while the current at the output gain section was varied from 0 to 100 mA. A plot of measured power as a function of the output gain current is shown in Figure 5.17. The measured output power was very low, i.e. in micro-watts, which is due to high series resistance (as explained earlier).

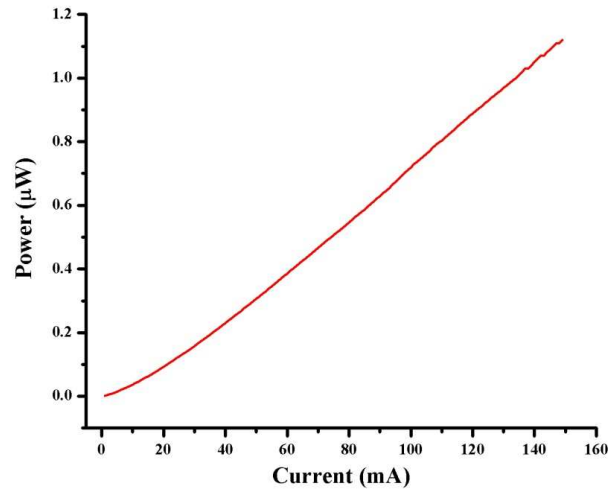


Figure 5.17: A plot of output power as a function of the current on the output gain section of an integrated device.

5.7. Device structure with deep to shallow etching

Integrated devices were fabricated with shallow etched gain sections along with deep etched PMC sections. This was to investigate the poor performance of the previous samples was due to the deep etched gain sections. Tapers between deep and shallow etched sections were used to reduce optical losses. The device structure of these devices is shown Figure 5.18.

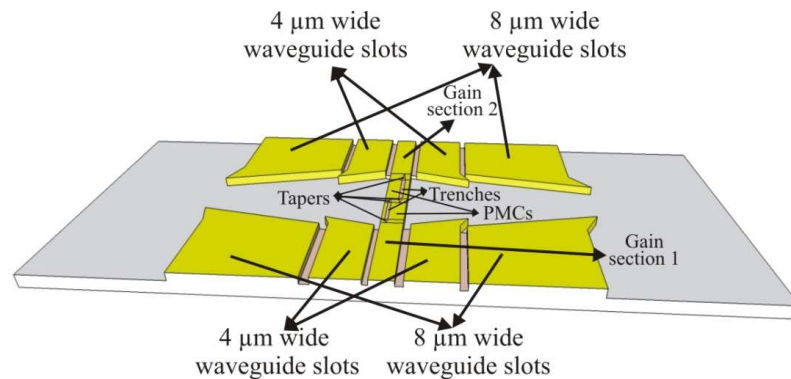


Figure 5.18: A schematic diagram of the deep and shallow etched sections.

In this structure, two gain sections, each ranging from 1.23 to 1.35 μm wide and 800 μm long, were used on both the longitudinal sides with two PMCs of lengths ranging from 300 to 500 μm . These PMCs were sandwiched back to

back in the gain sections. Tapered waveguides of 5 μm length, were used at the corners of each trench of the PMC ensuring smooth dry etching from the gain sections to the convertor sections, which in turn provides smooth transmission of optical modes in the integrated device. Two 4 and 8 μm wide passive waveguides were placed on each side of the two gain sections at position of 300 nm and 800 nm from the waveguide edge respectively. These waveguides confine the carriers in the gain sections by compressing from the sides towards centre and to achieve the shallow gain sections by the RIE lag. A taper waveguide with a length of 100 μm towards the convertor section was used to get smooth shallow to deep etching. The PMC section was deep etched, while the gain sections on both sides were shallow etched. Trenches in the convertor sections were etched to a depth of 1.25 μm by the RIE, in order to attain 45° rotation (as modelled earlier). Trenches of varying widths, ranging from 500 to 540 nm in the convertor sections were defined at position of 140 nm from the waveguide edge. The trench widths of >500 nm instead of the optimised trench width (230 nm) were used to achieve 1.25 μm trench depth (as described earlier).

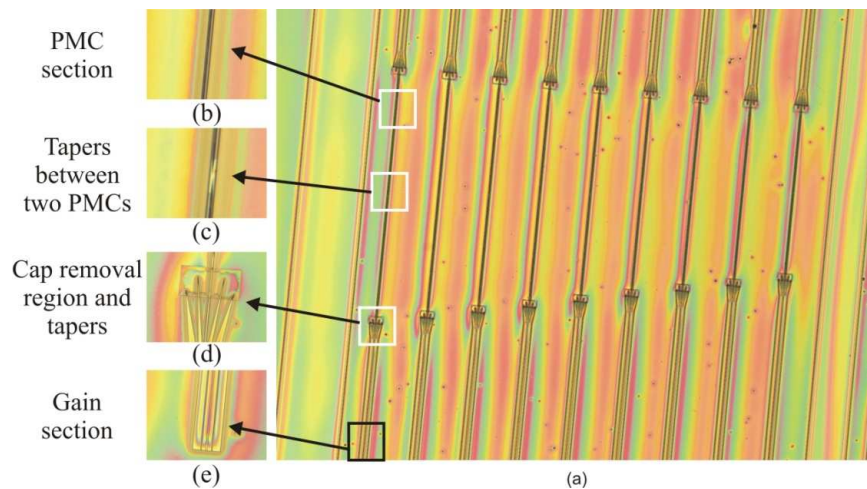


Figure 5.19: (a) An optical microscope image of the fabricated device with a pumped laser section, tapers, cap removal region and PMC sections (b) magnified view of PMC (c) magnified view of tapers used for coupling the two PMCs (d) magnified view of cap removal region and tapers and (e) magnified view of a pumped laser section.

5.7.1. Fabricated device

An optical microscope picture of the fabricated device with a pumped laser section, tapers, and PMC sections is shown in Figure 5.19 (a). Figure 5.19 (b) shows the PMC section, which was used in various dimensions in different devices. The two PMCs were coupled by trench tapers (Figure 5.19 (c)). The heavily doped p-cap layer was removed from the region between different sections of the device for electrical isolation, and the tapers were used to get smooth shallow to deep etching, between the laser section and the PMCs on both sides of the device. This is shown in Figure 5.19 (d). The electrically pumped laser section is given in Figure 5.19 (e). The large passive waveguide slots of 4 and 8 μm widths on both sides of pumped laser sections were provided for confining the injected carriers below the pumped section.

The SEM pictures of cross section of the pumped laser section with passive waveguide slots, and the PMC are shown in Figure 5.20. In Figure 5.20 (b) magnified view of the pumped laser section is shown and Figure 5.20 (c) shows top view and cross sectional profile of the device.

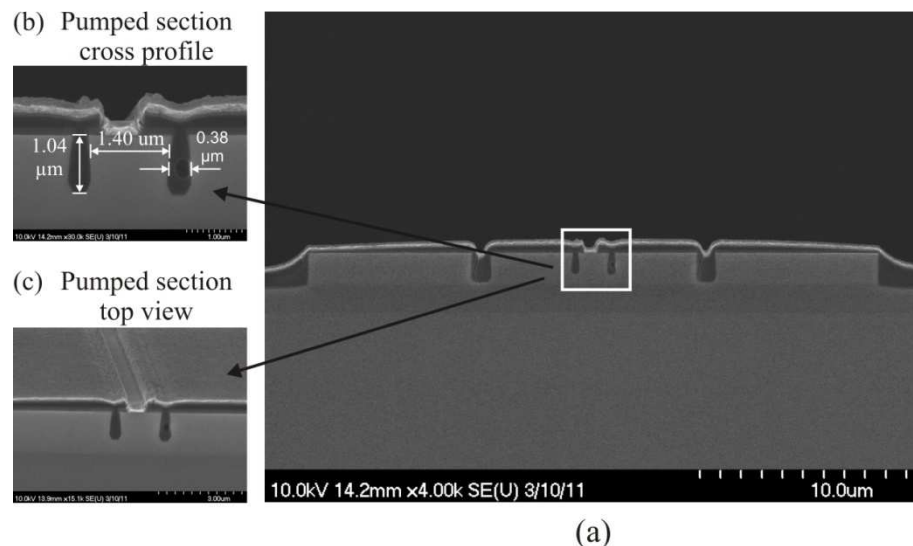


Figure 5.20: (a) SEM picture of cross section of the integrated device including a pumped laser section (b) magnified view of cross section of the pumped laser section and (c) magnified top view of the pumped laser section.

5.7.2. Active PMC measurements

These devices were characterised using the measurement setup shown in Figure 5.15. Unfortunately, the behaviour of these devices was similar to the deep etched devices. There were neither lasing nor optical amplification in all of the fabricated integrated devices.

Some deep and shallow etched devices were cleaved near the start of the PMC section. This was carried out to observe behaviour of the shallow to deep etched sections transitions. These devices were tested using CW and pulsed current setups. It was found that life time of these devices was very short (as immediately, the output power dropped significantly), and all the devices failed when using drive CW current. However, the emission of light was observed under pulsed current measurements. The devices measured with pulse currents were quite stable as compared to the CW currents. It was due to less heating produced during pulsed current injection. The comparison of CW and pulsed current performance of the shallow to deep etched devices is shown in Figure 5.21.

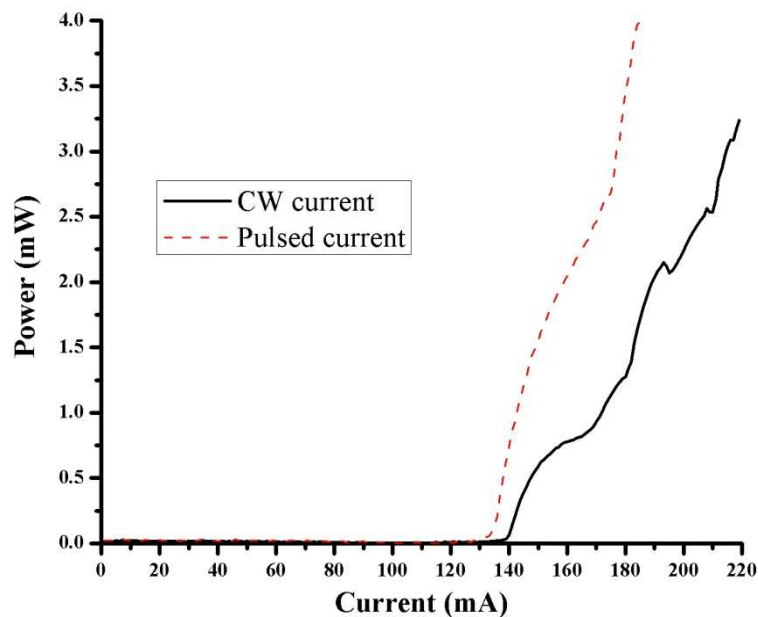


Figure 5.21: Comparison of CW and pulsed current performance of the shallow to deep etched devices.

5.7.3. Power-current characteristics

The power-current (P-I) characteristics of the deep and shallow etched devices, were measured. Most of the devices were not lasing, however some devices showed lasing. Output power of 13.6 mW was obtained at 150 mA injection current. The plot (Figure 5.22) shows that the device is operating in multimode. This is evident that for injection current of around 130 mA, one mode is converted into another, and the device starts lasing again at this current.

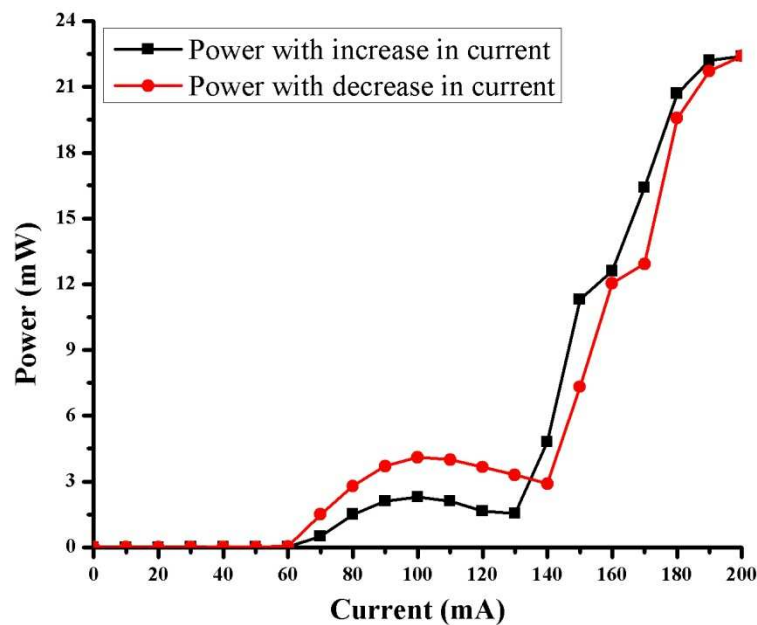


Figure 5.22: Hysteresis of the emitted power as a function of the current.

5.8. Conclusions

This chapter gives the description of the passive PMC, the devices monolithically integrated with a single PMC, and two PMCs, attached back to back, with a semiconductor laser, fabricated with shallow and deep etching. In the first section, the principle of etched slot based PMC is presented. The polarisation mode conversion was obtained by changing the optical axis of the waveguide to the wafer normal. The basic structure, design, modelling and optimisation of the PMC with and without semiconductor lasers are explained. Various PMCs were modelled using different trench depths, trench widths and position of the trench

from the waveguide edge using double hetero-structure, GaAs/AlGaAs material systems. Polarisation mode conversion of 45° (50 %) and 90° (100 %) was obtained at the waveguide width (1.24 μm), the trench width (230 nm), the trench depths (1.25 μm and 1.33 μm) and position of the trench (140 nm) from the waveguide edge, respectively. Simulations were carried out using two PMCs, attached back to back to get 90° (100 %) rotation, which gives 99.5 % polarisation mode conversion at the convertor length of 840 μm (with combination of two PMCs). Fabrication of these devices with SEM pictures is discussed.

The measurements carried out on numerous devices, with passive and active functionality of PMCs, are discussed. The obtained results from the integrated devices for active functionality of deep, shallow, and deep to shallow etched devices, are presented.

Although some polarisation rotation has been demonstrated using these devices, the devices suffered from large amounts of variation between devices and high series resistance, which made a robust analysis of performance versus design difficult. The next chapter addresses these problems by moving to high quality, commercially available epitaxial material.

5.9. References

1. Watts, M.R., *Polarization independant microphotonic circuits*. 2005, PhD thesis, Massachusetts Institute of Technology, USA.
2. Watts, M.R. and H.A. Haus, *Integrated mode-evolution-based polarization rotators*. *Opt. Lett.*, 2005. **30**(2): p. 138-140.
3. Shani, Y., et al., *Polarization rotation in asymmetric periodic loaded rib waveguides*. *Applied Physics Letters*, 1991. **59**(11): p. 1278-1280.
4. Dam, C.v., et al., *Novel compact polarization converters based on ultra short bends*. *Photonics Technology Letters, IEEE*, 1996. **8**(10): p. 1346-1348.
5. Chris, B., et al. *Polarization rotating waveguides in silicon on insulator*. in *Optical Amplifiers and Their Applications/Integrated Photonics Research*. 2004: Optical Society of America.
6. El-Refaei, H., D. Yevick, and T. Jones, *Slanted-rib waveguide InGaAsP-InP polarization converters*. *Lightwave Technology, Journal of*, 2004. **22**(5): p. 1352-1357.
7. Huang, Z., et al., *Realization of a compact and single-mode optical passive polarization converter*. *Photonics Technology Letters, IEEE*, 2000. **12**(3): p. 317-319.
8. Zhu, Y.C., et al. *Single section polarization convertor on InP/InGaAsP using asymmetrical waveguides*. in *Proceedings of the 6th annual symposium of the IEEE Lasers & Electro-Optics Society*. 2001.
9. Holmes, B.M. and D.C. Hutchings, *Realization of novel low-loss monolithically integrated passive waveguide mode converters*. *Photonics Technology Letters, IEEE*, 2006. **18**(1): p. 43-45.
10. Kim, S.-H., et al., *Single-trench waveguide TE-TM mode converter*. *Opt. Express*, 2009. **17**(14): p. 11267-11273.

11. Kotlyar, M., et al., *Compact polarization converter in InP-based material*. Opt. Express, 2005. **13**(13): p. 5040-5045.
12. *RSoft Design Group Inc*, www.rsoftdesign.com.
13. Hunsperger, R.G., *Integrated optics: Theory and Technology*. 1991: Springer, Berlin, Germany, ISBN 0-387-53305-2.

Chapter 6

Design and characterisation of polarisation mode convertor on InP/AlGaInAs material

6.1. Introduction

Devices based on the GaAs/AlGaAs epitaxial material were discussed in the previous chapters. While we demonstrated the basic functionality of polarisation mode convertors, the material quality was not sufficient, which results in poor and variable device performance. Therefore, high quality commercially available material (InP/AlGaInAs) operating at a wavelength of 1550 nm was chosen. This material is suitable for fabrication of the devices operating in a 1530-1565 nm wavelength range. This wavelength range is commonly used for telecommunications devices. This material also provides better performance than other materials operating in this wavelength range, i.e. GaInAsP due to its large conduction band offset and therefore improved temperature performance. The conduction band offset for aluminium quaternary systems ($\Delta E_c = 0.72\Delta E_g$) is larger than the phosphorous quaternary systems

($\Delta E_c = 0.40\Delta E_g$). This results in lower carrier losses due to thermionic emission and therefore a higher characteristic temperature [1, 2]. Furthermore, aluminium layers in the core region have the advantage of selective dry etching, which helps in controlling the etch depth via an Al based etch stop layer.

In this chapter, a brief description of the epitaxial layers, with the band diagram of InP/AlGaInAs material structure, is presented. The integrated device structures, consisting of shallow etched active regions with tapers, and deep etched passive polarisation mode convertors, are discussed. The modelling and optimisation of the integrated devices are also discussed. The characterisation results of the fabricated devices are presented. The polarisation mode conversion is demonstrated. Further, active phase shifting and polarisation modulation at 300 Mbps was demonstrated for the first time.

6.2. Material structure

The devices were fabricated on the commercially available [3, 4] a 1550 nm, p-i-n laser diode structure. The design of the wafer was specified by the supplier. This wafer contains five $\text{Al}_{0.07}\text{Ga}_{0.22}\text{In}_{0.71}\text{As}$ quantum well (QW) layers, and six $\text{Al}_{0.22}\text{Ga}_{0.29}\text{In}_{0.49}\text{As}$ barrier layers. The thicknesses of QW and barrier layers are 6 nm and 10 nm, respectively. The epitaxial layer structure with layer thickness of each layer, and doping concentrations is shown in Table 6.1. The QW and barrier layers are sandwiched between the two 60 nm $\text{Al}_{0.34}\text{Ga}_{0.13}\text{In}_{0.53}\text{As}$ layers, which are graded refractive index separate confinement hetero-structure (GRINSCH) layers. These GRINSCH layers are used for low carrier population in the core and improved optical confinement, as compared to the standard separate confinement hetero-structure (SCH). This also helps in reducing the threshold current density and increase in the differential gain [2, 5]. These layers are further sandwiched between the two wide band-gap $\text{Al}_{0.42}\text{Ga}_{0.05}\text{In}_{0.53}\text{As}$ layers, which prevent electrons and holes escaping from the active region. Two InP layers of 800 nm and 1650 nm thickness are used as lower and upper cladding layers. A 200 nm thick highly doped $\text{Ga}_{0.47}\text{In}_{0.53}\text{As}$ layer is used on the top as a cap and

ohmic contact layer. The quantum well layers are compressive strained with 12000 ppm, whereas, barrier layers are tensile strained with -3000 ppm. All other layers used in this wafer structure are lattice matched to InP. The zinc (Zn) and silicon (Si) are used as p-type and n-type dopants.

Table 6.1: Layer structure of the IQE wafer, part no. IEGNS-13-17

Layer	Material	Thickness (nm)	Doping
16	$\text{Ga}_{0.47}\text{In}_{0.53}\text{As}$	200	$p > (1.5 \times 10^{19})$
15	$\text{Ga}_{0.29}\text{In}_{0.71}\text{As}_{0.62}\text{P}_{0.38}$	50	$p > (3 \times 10^{18})$
14	InP	100	$p > (1.5 \times 10^{18})$
13	InP	1500	$p (1 \times 10^{18})$
12	$\text{Ga}_{0.15}\text{In}_{0.85}\text{As}_{0.33}\text{P}_{0.67}$	20	$p (1 \times 10^{18})$
11	InP	50	$p (7 \times 10^{17})$
10	$\text{Al}_{0.42}\text{Ga}_{0.05}\text{In}_{0.53}\text{As}$	60	$p (4 \times 10^{17})$
9	$\text{Al}_{0.34}\text{Ga}_{0.13}\text{In}_{0.53}\text{As}$	60	Un-doped
8	$\text{Al}_{0.22}\text{Ga}_{0.29}\text{In}_{0.49}\text{As}$	10	Un-doped
7	$\text{Al}_{0.07}\text{Ga}_{0.22}\text{In}_{0.71}\text{As}$	5 x 6	Un-doped
6	$\text{Al}_{0.22}\text{Ga}_{0.29}\text{In}_{0.49}\text{As}$	5 x 10	Un-doped
5	$\text{Al}_{0.34}\text{Ga}_{0.13}\text{In}_{0.53}\text{As}$	60	Un-doped
4	$\text{Al}_{0.42}\text{Ga}_{0.05}\text{In}_{0.53}\text{As}$	60	$n (1 \times 10^{18})$
3	$\text{Al}_{0.40}\text{Ga}_{0.07}\text{In}_{0.53}\text{As}$	10	$n (1 \times 10^{18})$
2	InP	500	$n (1 \times 10^{18})$
1	InP	300	$n (3 \times 10^{18})$
InP-Substrate			

This wafer structure is grown using metal organic chemical vapour deposition (MOCVD). The energy band diagram of this structure is shown in Figure 6.1.

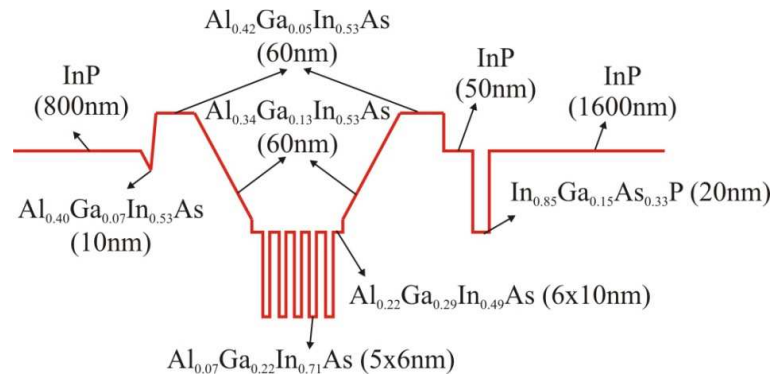


Figure 6.1.: Energy band diagram (conduction band only) of InP/AlGaInAs material system.

6.3. Waveguide design

Optical confinement in the ridge waveguide structures can be achieved in the vertical and horizontal directions. The vertical confinement is achieved due to the higher refractive index of the core region than the surrounding layers. The confinement in the horizontal direction is achieved by definition of a waveguide structure, through etching of the semiconductor material. Deep etched or shallow etched waveguides can be fabricated from the same epitaxial material. A schematic of these is shown in Figure 6.2.

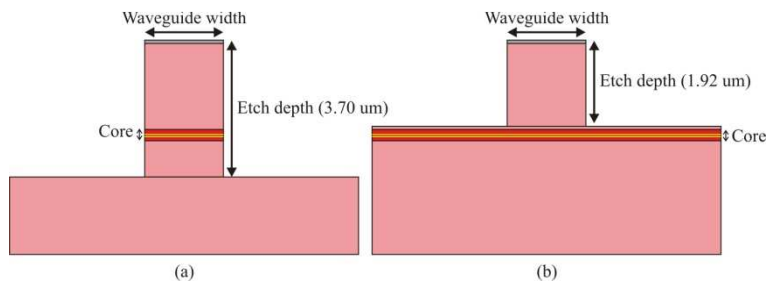


Figure 6.2: Schematic diagrams of (a) deep etched and (b) shallow etched ridge waveguide structures.

In a shallow etched ridge waveguide structure, the lateral confinement is achieved by etching a ridge into the semiconductor material to just above the active region. There is no mechanism for carrier confinement in horizontal direction, which leads to losses due to diffusion and recombination [6]. However, the scattering losses are lower than deeply etched waveguide structures due to the reduced interaction of the optical mode with the sidewalls of the ridge. In a deep etched ridge waveguide structure, stronger optical confinement is achieved due to the large contrast of the refractive index between the waveguide and the surrounding medium, such as air or dielectric. The aluminium containing active region of deep etched waveguide is exposed to the air during fabrication which leads to oxidisation and increase non-radiative recombination losses, which decrease the device performance and life time.

Beamprop software was used to determine the correct width of the waveguide. First, the effective modal index values for the first three TE modes with varying widths of the waveguide for deep and shallow ridge waveguides, were calculated, and are shown in Figure 6.3. These results indicate that the first order cutoff mode is at ridge width of 2.5 μm and 1.5 μm , for deep and shallow etched waveguides, respectively. Whilst any width before the cutoff for the first order mode would be adequate, the losses for deeply etched devices decrease and the confinement factor increases in both structures as the width is increased. It is therefore wise to make the waveguides as wide as possible whilst remaining single mode. A 2.4 μm wide ridge waveguide, with single mode operation was used for shallow etched lasers, in this research. The simulated modal profile of a 2.4 μm wide ridge waveguide structures at the waveguide depth of 3.70 μm (into the waveguide core) and 1.92 μm (above the waveguide core), where a single mode operation was attained, is shown in Figure 6.4.

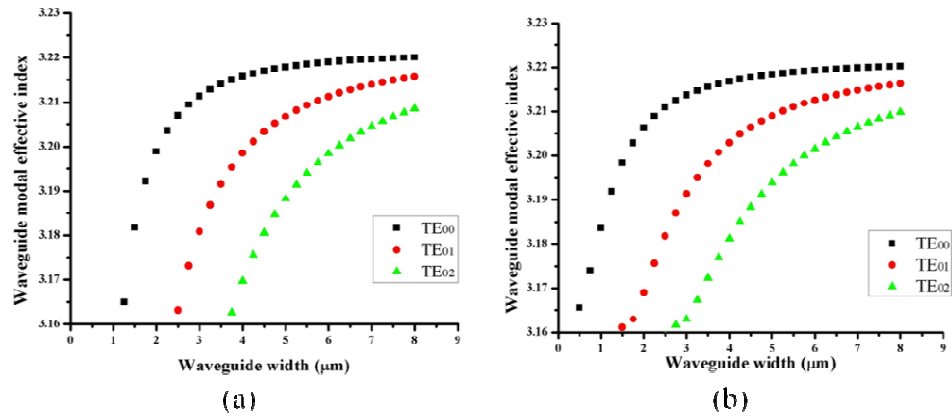


Figure 6.3: Simulated waveguide modal effective refractive index of fundamental, 1st and 2nd order TE polarised modes as a function of the waveguide width for (a) deep etched and (b) shallow etched ridge waveguide structures.

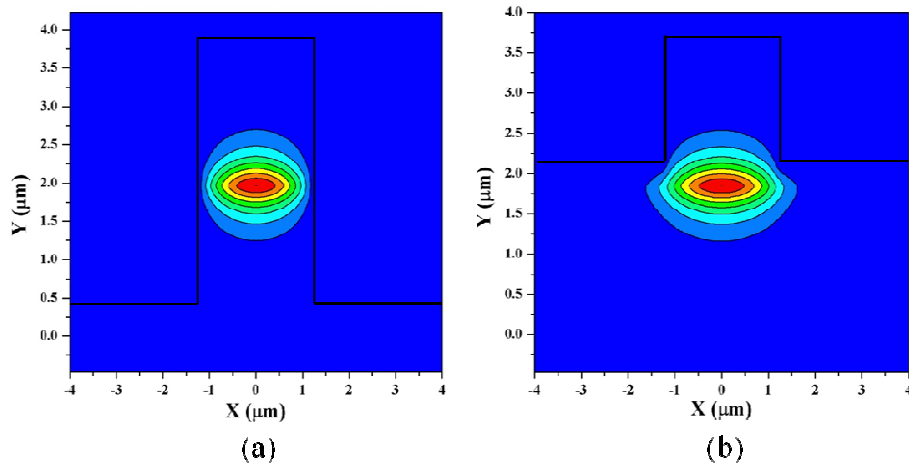


Figure 6.4: Simulated modal profile of a fundamental mode of deep and shallow etched ridge waveguide structures.

6.4. Modelling and design of the device with a single PMC

Commercial beam prop software based on the BPM (as used for earlier devices and described in previous chapters) was used for modelling and design of the PMC with a semiconductor laser.

Initially, using different trench widths, trench depths and position of the trench from the waveguide edge, the trench depth was optimised for 50 % of polarisation mode conversion. It was found to be 1.972 μm deep for the desired polarisation mode conversion of 50 % at the trench width of 600 nm and the trench position of 300 nm from the waveguide edge. The trench position of 300 nm was kept to achieve the vertical pillars. This width also protects them from damaging during dry etching process (as described in Chapter 5). A plot of % polarisation mode conversion as a function of the trench depth is shown in Figure 6.5.

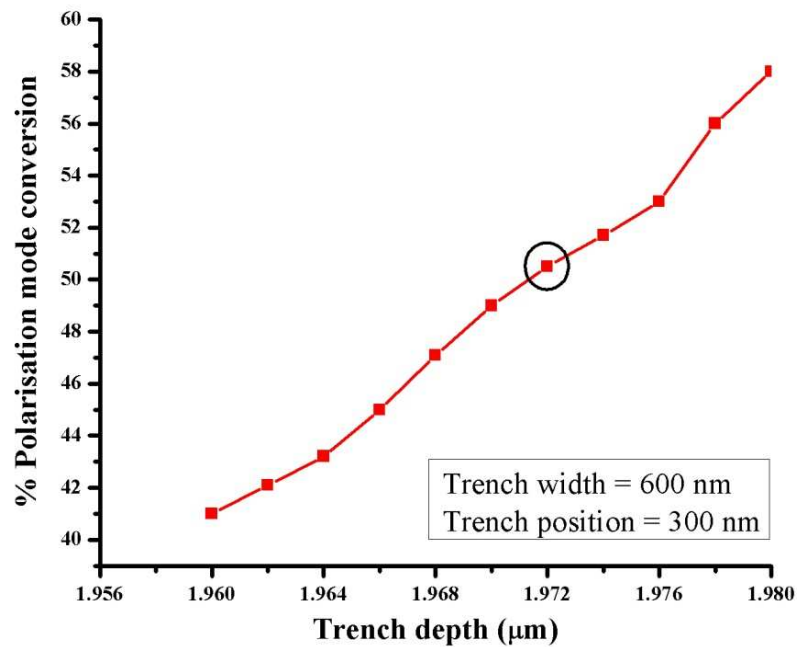


Figure 6.5: Simulated % polarisation mode conversion as a function of the trench depth.

The polarisation mode conversion was also carried out to observe the effect of the trench width, at the optimised trench depth of 1.972 μm and trench position of 300 nm from the waveguide edge (as chosen) for 50 % polarisation mode conversion. A plot of % polarisation mode conversion as a function of the propagation direction at various trench widths is shown in Figure 6.6. This was found that the trench width is tolerant to the polarisation purity i.e. with 20 nm

change in the trench width; there was $\pm 1.75\%$ change in polarisation purity, which is quite stable with little change in the trench width.

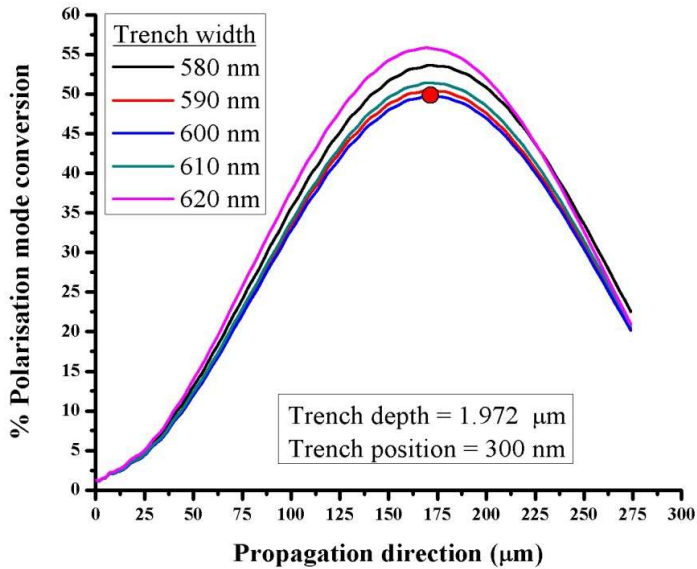


Figure 6.6: A plot of % polarisation mode conversion as a function of the propagation direction at various trench widths.

A trench width of 600 nm and trench depth of 1.972 μm with the position of 300 nm from the waveguide edge, were used in simulations to ascertain the beat length. A plot of polarisation mode conversion efficiency as a function of the propagation direction is shown in Figure 6.7. As expected, the maximum conversion efficiency was 50 % and this occurs at 174 μm length.

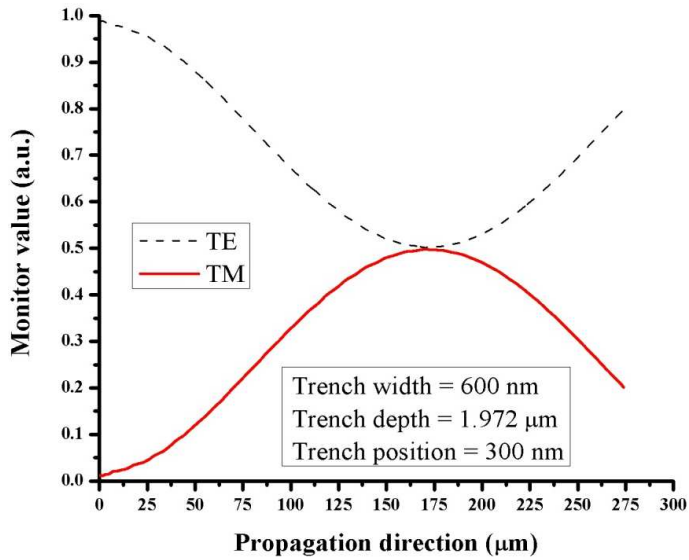


Figure 6.7: The TE to TM mode conversion as a function of the propagation direction.

Additionally, the launched zero order TE mode into the integrated device and modal profiles obtained at the entering point of the PMC, and at the length of 174 μm of the PMC, are shown in Figure 6.8. The tilt of the mode can be observed in PMC which is due to the change in the optical axis of the asymmetric section of the waveguide. This change in optical axis is due to the air trench. The launched mode was obtained at shallow etched waveguide (Figure 6.8 (a)), whereas, modes at the start, and in the PMC section, were attained using deep etched waveguides (Figure 6.8 (b & c)). The structure of the integrated device is further explained in the subsequent section.

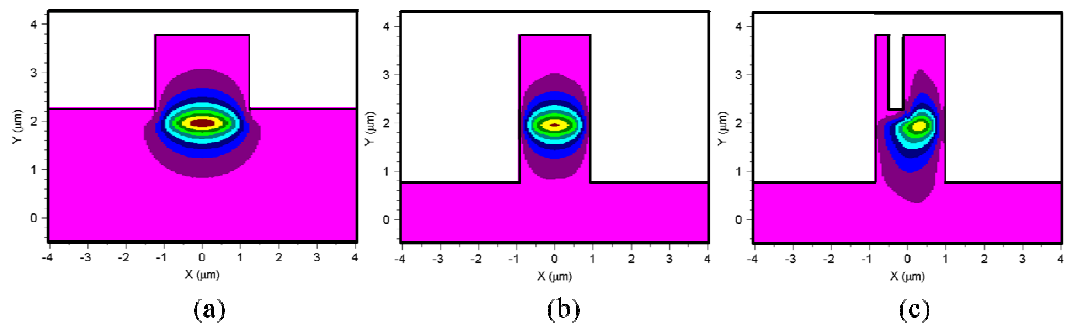


Figure 6.8: Modal profiles at (a) the launched position (b) at start of the PMC and (c) at the length of 174 μm of the PMC.

6.4.1. Device structure with a single PMC

The integrated device structure shown in Figure 6.9 was devised for realisation of the devices on InP/AlGaInAs material using optimised values for the PMC. In this structure, a single PMC was placed between the two gain sections, which consist of a 700 μm long semiconductor laser, a 1000 μm long differential phase shifter (DPS), and a 120 μm long taper section. The width of the laser and DPS sections was 2.4 μm , whereas, the PMC section was 1.8 μm wide. The PMC includes a 600 nm wide trench at position of 300 nm from the waveguide edge, as optimised. Various PMCs with lengths ranging from 100 to 190 μm , with a step of 15 μm , were fabricated. The PMC section, which was 250 μm long for all the devices, was un-pumped. Furthermore, 16.4 μm wide slabs around the gain sections, were placed to obtain the shallow etching (to the top of the waveguide core). Tapers from the laser section to the convertor section, were used to closely match the mode profiles at the interfaces, and minimise the coupling losses. A 373 nm wide deep etched slot was made at the end of the taper section (on the laser side) [7]. This slot provides the reflectivity for lasing action, and means to propagate as a single pass through PMC and DPS sections. Tapers of 4 μm length, were also provided on each corner of the trench of the PMC for provision of smooth etching in the un-pumped section of the device, which in turn provides smooth transition of modes in the integrated device. The devices were shallow etched around the gain sections, whereas, deep etched through the core around convertor sections. Trench depth was obtained to the desired value using RIE lag. The laser cavity was defined between a cleaved facet, and a transverse deep-etched slot prior to the PMC section, with the subsequent exit waveguide set at an angle of 10° to the facet, in order to mitigate against compound cavity effects.

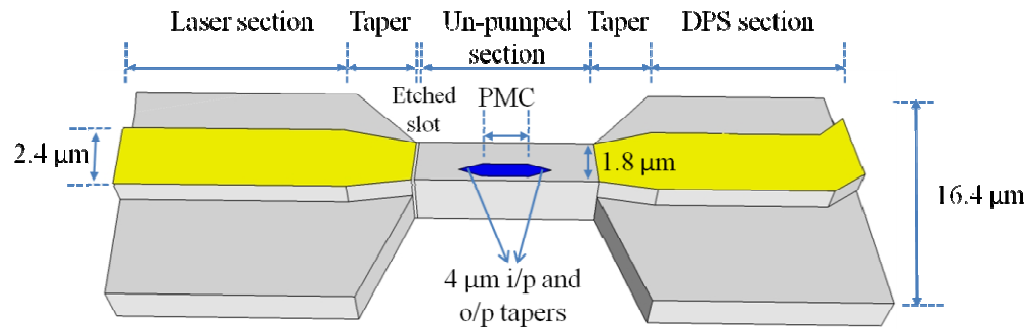


Figure 6.9: A schematic diagram of the integrated device with a single PMC.

6.4.2. PMC fabrication analysis

Previous attempts made, for realisation of active PMCs led to variable and unpredictable behaviour of PMCs and amount of rotation. It was supposed to be probably some stress was induced in the fabricated devices, which can be due to the SiO_2 deposition, HSQ or metallisation during fabrication. As high temperature is needed for these processes, therefore the co-efficient of thermal expansion can be changed after cooling, which can result in stress. Therefore, to isolate the problem, some active PMCs were fabricated, and polarisation rotation was observed at each step of fabrication. Detail of fabrication stages are shown in Figure 6.10.

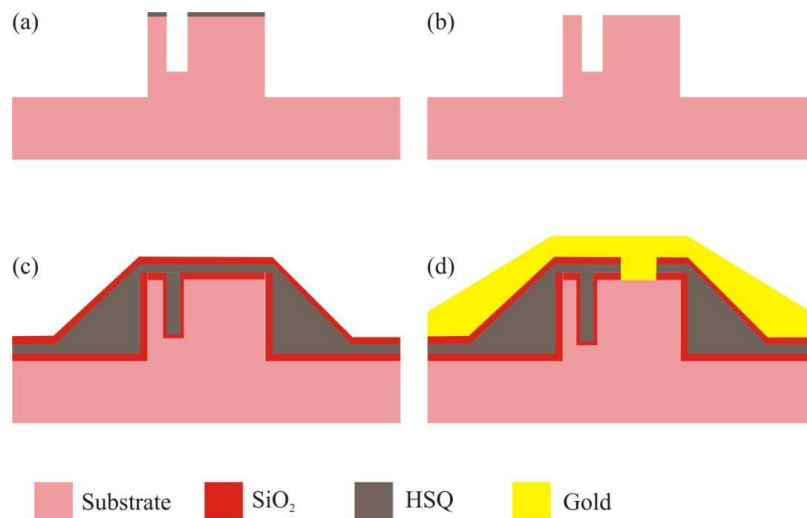


Figure 6.10: Various fabrication stages (a) as fabricated (b) after removal of HSQ (c) after HSQ planarization and (d) after metallisation.

Initially, these PMCs (test chips) were with different convertor lengths ranging from 40 to 300 μm with various widths 2 μm , 2.2 μm and 2.4 μm . These devices were measured passively at different stages of fabrication (as stated above and shown in Figure 6.10), i.e. after etching, after removal of HSQ mask, after HSQ planarization and after metallisation, using the measurement setup shown in Figure 6.11. A tuneable laser was used as an input light source. A TE input at wavelength of 1600 nm (lower than the band-gap energy for passive measurements) was provided using a polarisation maintaining (PM) fibre to reduce the TE optical absorption at the band-edge of the material. The output optical signal was collimated using 20x microscope objective lens onto the detector, which is attached to the high speed oscilloscope. A polarising beam splitter cube was used to examine the ratio of TE and TM polarisation.

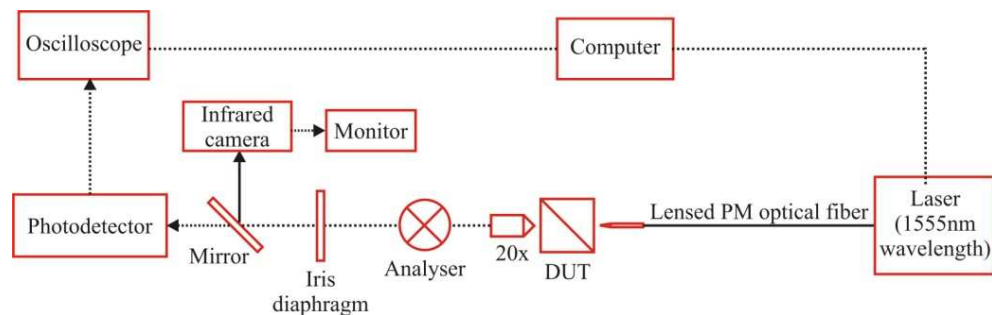


Figure 6.11: A schematic diagram of the device measurement setup with a 1555 nm tuneable laser.

In the fabricated devices with 2.2 μm wide convertors, the % TM purity was found to vary from 4 to 37.5 %, with the maximum conversion efficiency obtained at the convertor lengths ranging from 120 to 160 μm . The data for ‘after etching’, ‘after the removal of HSQ mask’ and ‘after the HSQ planarization’ was consistent with similar trends seen for the three cases with length. Although there is a little bit variation in the experimentally obtained results in terms of TM purity, which is attributed to the fabrication, as these devices are fabricated on different samples. After metallisation the data has changed dramatically. This change seems to be most likely due to the stress induced by the metal or due a heating effect during metallisation. Therefore, the devices further fabricated include

PMCs without metallisation. Although passive PMCs are not advantageous due to extra losses but to remove the stress problem, these are used. A plot of % TM purity as a function of the convertor length with 2.2 μm wide convertor, at different fabrication stages is shown in Figure 6.12.

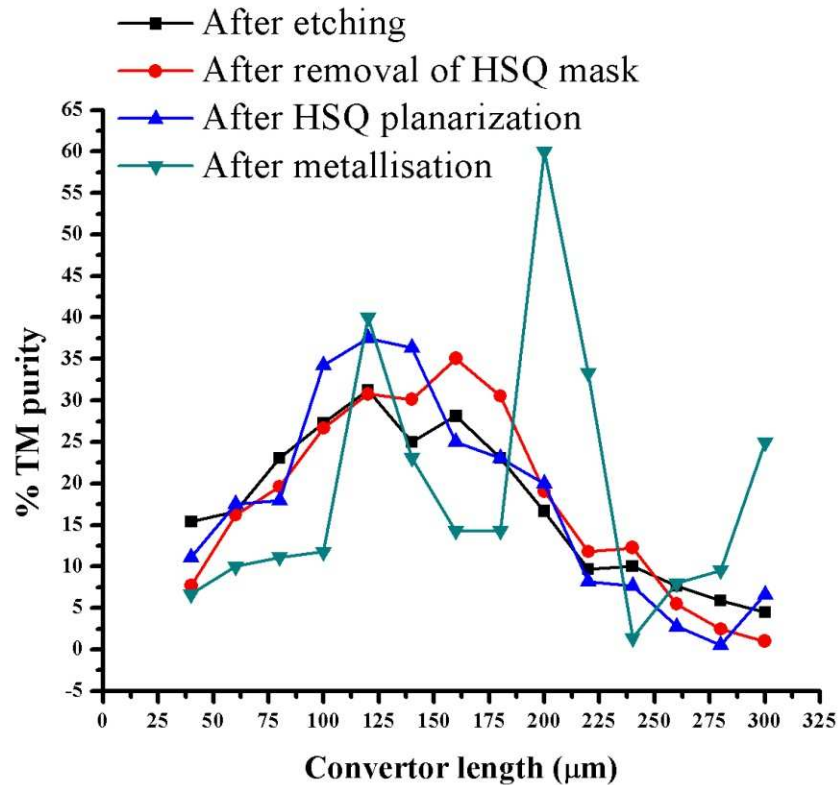


Figure 6.12: A plot of % TM purity as a function of the convertor length at different fabrication stages.

The obtained % TM purity for these devices, measured after planarization, and the simulated results for the convertor lengths of 60 to 220 μm , are shown in Figure 6.13. Here, 23 to 37.5 % TM purity was obtained at the convertor lengths, ranging from 100 to 180 μm , with maximum conversion efficiency at 120 μm length. The simulated TM purity was in range of 30 to 50 % for the PMC lengths of 100 to 174 μm , with maximum conversion efficiency at the length of 174 μm . This difference was due to the trench depth of fabricated devices, as the % TM purity was obtained at the optimised trench depth of 1.972 μm , in simulations, whilst, experimentally measured devices had the trench depth of 1.96 μm .

Furthermore, this difference in measured and simulated purity is most likely due to the fabrication errors, as conversion efficiency is very much sensitive to dimensions of the PMC. Additionally, the devices were simulated at 1550 nm wavelength whereas, measured at 1600 nm wavelength of injected laser beam, to avoid absorption on the band-edge of the material. Thereon, the obtained results of fabrication with trench depth of 1.96 μm with 1600 nm wavelength, were used to re-simulate the devices. This yielded a conversion efficiency of 37.7 % at the convertor length of 120 μm , whereas, a maximum conversion was obtained at the length of 180 μm . The later simulation results (Figure 6.13) were nearly consistent with the experimentally obtained results (at start of convertor lengths). The difference in conversion efficiencies above 140 μm long convertors, was most probably due to fabrication errors.

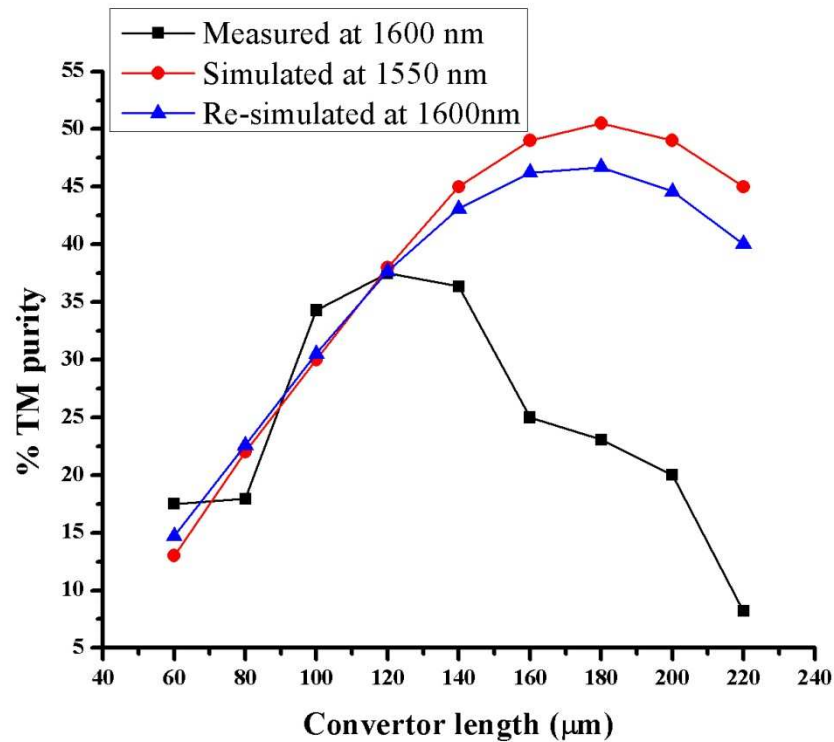


Figure 6.13: The % TM purity as a function of the convertor length (experimentally measured, initially simulated and re-simulated).

6.4.3. Realised device with a single PMC

The integrated devices were fabricated on different chips using standard fabrication procedures. These procedures are described in the previous chapters, in detail. Precise control over trench depth, in the PMC, is critical, and was achieved using an etch-stop layer, together with reflectometric etch monitoring techniques, resulting in the required run-to-run repeatability. The shallow etched laser sections (to the top of the waveguide core) and trenches were fabricated using RIE (as described in Chapter 3) and the etch depth of two individually processed samples were measured - using a Dektak Profilometer - to be $1.912\ \mu\text{m}$ for both the samples. The deep etched sections of the device (into the waveguide core) were fabricated using an inductively coupled plasma (ICP) etching tool, resulting in measured ridge depths of $3.676\ \mu\text{m}$ and $3.665\ \mu\text{m}$ for the two samples. This demonstrates a process repeatability of better than 0.3 %. The SEM image of cross section of a realised PMC in the integrated device is shown in Figure 6.14. The trench depth of $1.96\ \mu\text{m}$ was obtained. The PMC section was kept passive, whereas, both sections on longitudinal sides of the PMC were metallised using standard contact metallisation technique.

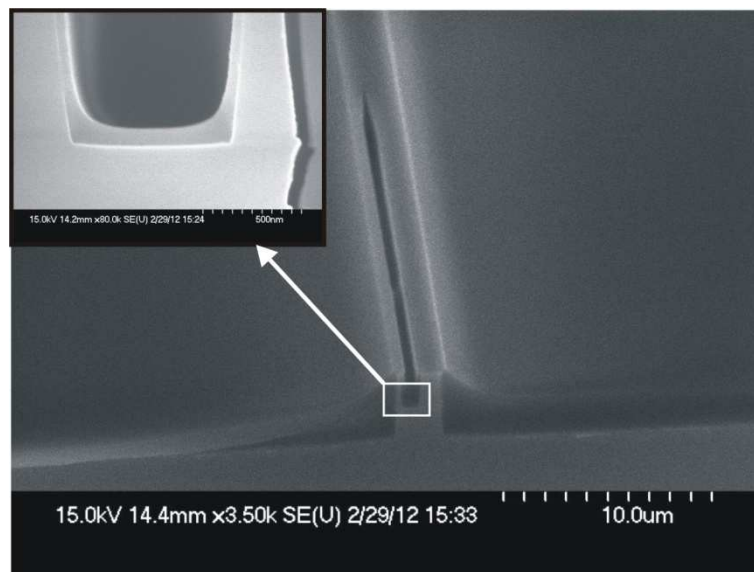


Figure 6.14: SEM image of cross section profile of the PMC used with a semiconductor laser (a magnified view is given in the inset).

6.4.4. Light current characteristics

Light-current (L-I) characteristics of the integrated device were measured using a photodetector at a wavelength of 1550 nm. L-I curves were obtained separately for the TE and TM polarised lights from both sides of the device, i.e. at the semiconductor laser facet and on the angled facet of the DPS side. The device was mounted on a TEC controlled copper with temperature at 20 °C. A constant (CW) current of 10 mA was applied on the DPS section, whereas, the current on the semiconductor laser section was changed from 0 to 150 mA. In order to separate the TE and TM components of light, a polarising beam splitter cube was used. First, L-I curves were measured on the laser facet side, which are shown in Figure 6.15. Here, the TE component is dominant compared to the TM, owing to the material design which emits predominantly TE light. The threshold current for TE polarisation state was found to be 20 mA. The measured TM output power was due to the TE leakage, which emanates from the finite extinction ration of the PBS, which is 30 dB. The L-I curves from DPS angled facet side were also taken. Here, the TE and TM polarised L-I curves show an equal impact in terms of the emitted power, but with lower optical output power compared to the optical power obtained at the semiconductor laser facet. This lower power is most likely due to the TE band-edge absorption in the PMC section. A plot of optical out power as a function of the current at the semiconductor laser section is shown in Figure 6.16. A small kink is observed in L-I curve of the TE polarised light at 70 mA, which is supposed to be due to mode hoping.

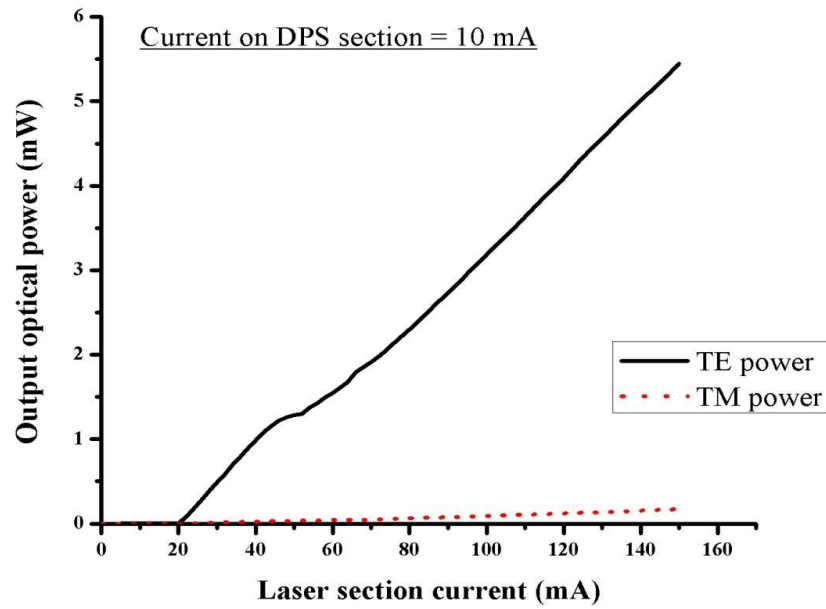


Figure 6.15: L-I curves of the TE and TM polarised light at the laser facet of the integrated device.

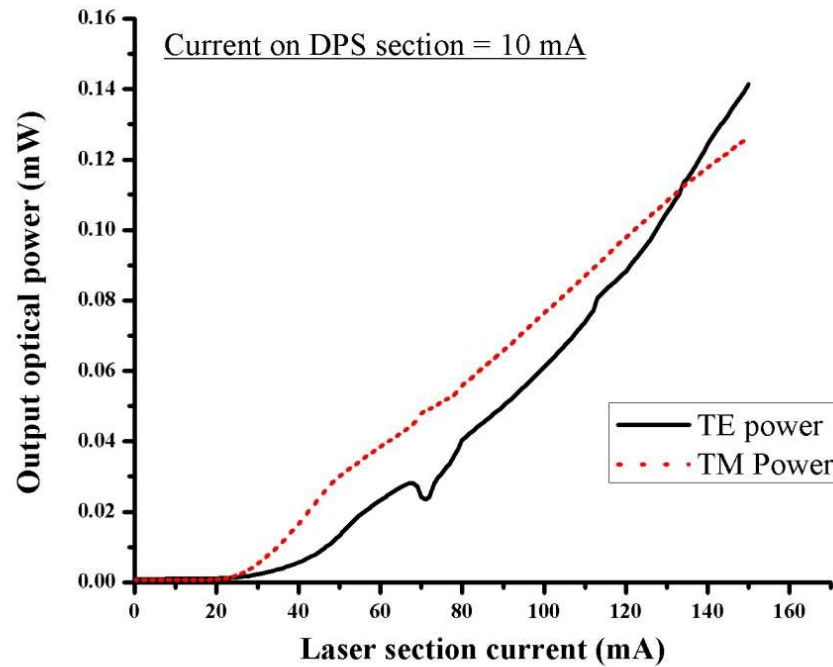


Figure 6.16: L-I curves of the TE and TM polarised light at the DPS angled facet of the integrated device.

6.4.5. Optical spectrum measurements

An optical spectrum was measured for the integrated devices with a single PMC using the measurement setup shown in Chapter 4 (Figure 4.11). It was found that, there is a red shift in peak wavelength of the devices with increase in the injection current. Pictures of the measured optical spectrum at constant currents on laser section, ranging from 40 to 140 mA, and varying currents from 0 to 20 mA on the DPS section, are shown in Figure 6.17. The observed peak wavelength as a function of the current at the laser section with constant current of 20 mA on the DPS section, is also plotted, which is shown in Figure 6.18. The devices start lasing at 1546 nm wavelength and shifts towards higher wavelengths with increase in the current on a laser section. This red shift with increase in the current indicates the existence of localized heating at active region which is temperature dependence of band-gap.

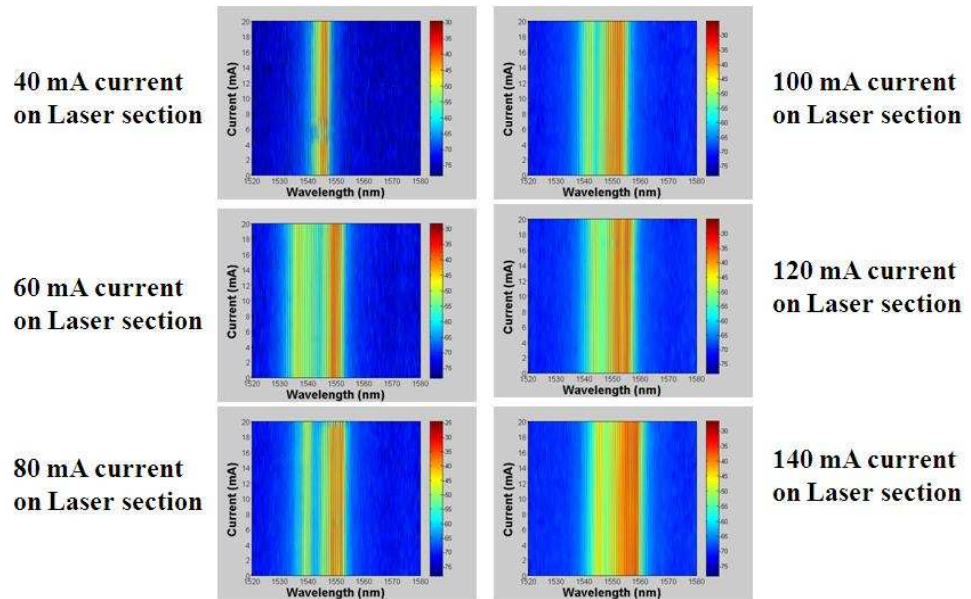


Figure 6.17: Optical spectrums measured at constant currents on the input laser sections, ranging from 40 to 140 mA, with varying currents from 0 to 20 mA on the output gain section.

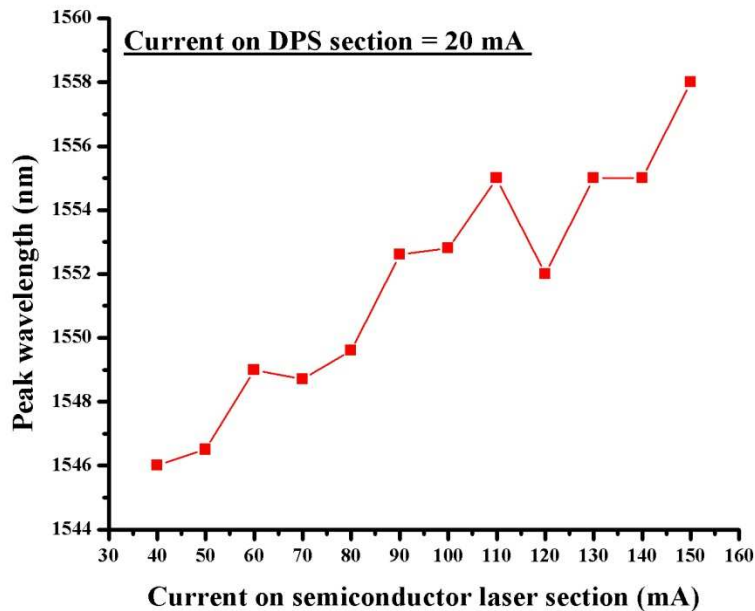


Figure 6.18: A plot of peak wavelength as a function of the current on a laser section, with constant current on the DPS section.

6.4.6. Transparency current measurements

The current at which the semiconductor material becomes transparent and stimulated gain is zero, is referred to as the transparency current (I_{tr}). It is very important to measure I_{tr} for integrated or compound devices, so that, they can be characterised after aging or degradation. We can use this to equalise the stimulated gain and loss in active devices, and to equalise the losses for TE and TM parameters [8]. The Junction-voltage method [9, 10] was used for measuring I_{tr} in this work, in which an input signal was induced for changing the carrier density in the device, due to optical emission/absorption [11]. This results in voltage drop across the p-n junction. The point where absorption becomes equal to the emission, and voltage drops to zero, is called transparency current point. The polarity of the voltage also changes at I_{tr} , therefore, the induced input signal was modulated and lock-in amplification was employed to detect this polarity change sign. An experimental schematic of this setup is shown in Figure 6.19. Here, a tuneable laser with internal modulation of 100 KHz, was used to induce the input signal into the rotator/phase shifter section, which triggers the lock-in amplifier,

and lock-in amplifier was used to detect the null and associated phase in the voltage. A current driver was used to inject the carriers in the device.

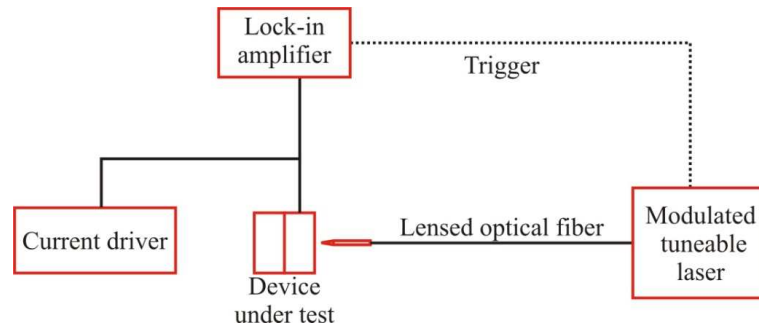


Figure 6.19: A schematic diagram of the transparency current measurement setup.

The transparency current was measured for various fabricated devices of equal lengths, and for different induced input signals having different wavelengths, I_{tr} was found to be similar for all the devices. As an example, the measured I_{tr} was 11.45 mA for a 1550 nm of wavelength. The measured I_{tr} for few devices as a function of the wavelength is shown in Figure 6.20. Here, it can be observed that I_{tr} decreases with increase in the wavelength. This wavelength dependence of I_{tr} is due to the requirement of the lower carriers in the reduced band-gap energy.

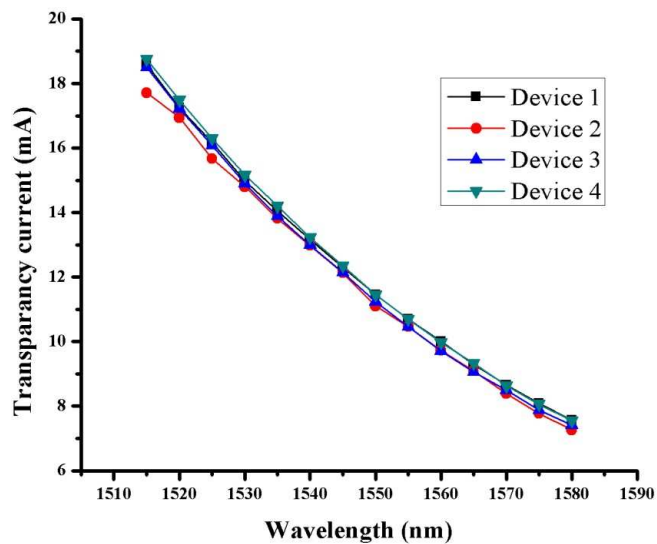


Figure 6.20: Measured transparency current as a function of the wavelength for various fabricated devices.

6.4.7. Active PMC measurements

The fabricated devices (shown in Figure 6.9), were measured using the measurement setup shown in Figure 6.21. These devices were measured with the temperature controlled at 20 °C.

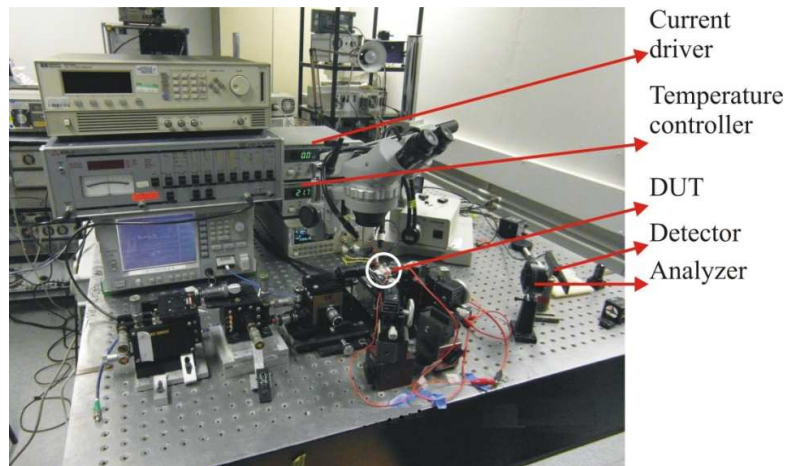


Figure 6.21: A setup used for active PMC measurements.

First, the semiconductor laser sections of these integrated devices were tested, and output powers were measured at the cleaved facet of the laser side at several currents above threshold current. The TE polarisation purity was found to be between 97.5 % and 98 %. Further devices were characterised for the TM purity, and output powers at the angled facets of the devices. Computer automated program was used with CW currents ranging from 80 to 120 mA on the laser section, whereas, varying currents from 0 to 20 mA with a step of 0.2 mA were applied at the DPS section, and the TE and TM polarised output powers of the devices were monitored. At 100 mA drive current, the laser output from the back facet was 3.18 mW, and the TE and TM output powers at the DPS facet were 78 μ W and 98 μ W respectively, with the DPS biased at the transparency current. Assuming 30 % and 40 % reflectivity for the cleaved faced and the slot mirrors of the laser respectively, the total loss of the PMC and DPS combination is of the order of 13 dB. This loss may be attributed to absorption in the unbiased PMC section, diffraction losses in the slot mirror and residual losses at the PMC/DPS

waveguide transition. The TM purity obtained is plotted as a function of the DPS current at each laser injection current for the device with a 100 μm trench length, with the values obtained for transparency current at each of the laser injection currents indicated (Figure 6.22). The injected current changes the effective refractive index of the material, leading to the variation in the operating wavelength. It can also be observed that the % TM purity decreases with increases current on the DPS section. This is consistent with increased TE gain relative to TM, with an increase in the bias current on the DPS section, which is acting an SOA. The value at the DPS transparency condition yields the power fraction in each polarisation mode exiting from the PMC [8]. A range of devices with various trench lengths were characterised in the fashion, and the result closest to that for the desired half beat length 3dB polarisation coupler was the ~40 % TM purity shown for the 100 μm trench length. The wavelength shift with changing bias current has to be taken into account, which results in a change of bias current on the second gain section (DPS section).

The measured results for various trench length devices were analysed, and calculated the % TM purity. It was found that fixing the injection current equal to transparency, polarisation mode conversion of 40.1 %, 39.7 % and 39.2 % were obtained at the convertor length of 100 μm with current injections of 80 mA, 100 mA and 120 mA, respectively. The measured % TM purity as a function of the convertor length of these devices is shown in Figure 6.23.

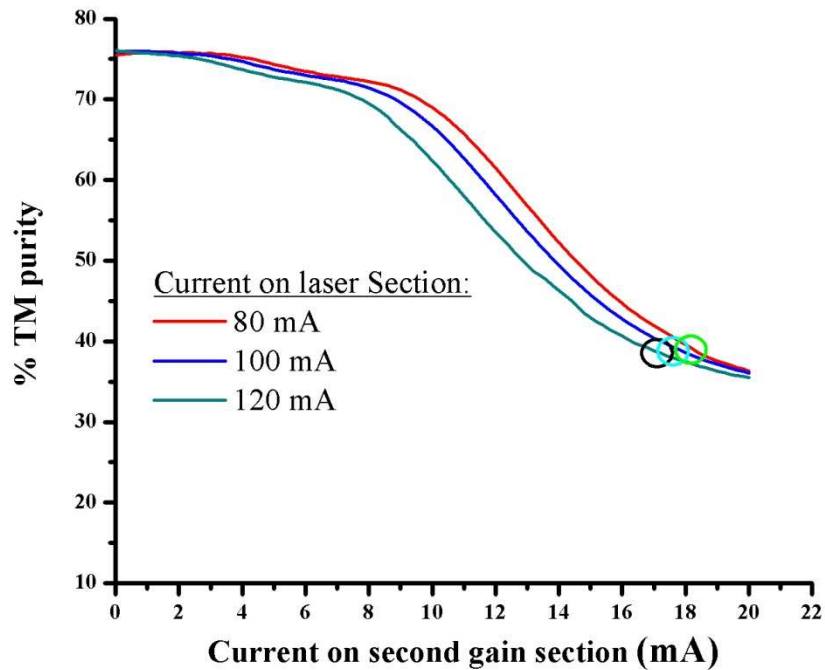


Figure 6.22: The TM purity as a function of the DPS current for a range of laser bias currents in mA. The transparency point for each laser bias is indicated on the graph.

6.4.8. Active polarisation control

Integrated devices which consist of a semiconductor laser monolithically integrated with PMC, followed by an active, differential phase shifter (DPS) (shown in Figure 6.9) were characterised for measuring the active polarisation control. Active polarisation control, which is obtained by injecting the variable current on the DPS section of the device, is advantageous to attain the desired polarisation state, and to change the phase of the applied signal. A constant current of 120 mA was applied on the laser section, and the current on the DPS section was varied in the range of 0 to 6 mA, with a step of 0.2 mA. The optical output power was measured through a polarisation analyser, which was set at $+45^\circ$ and -45° , to the plane of the wafer. The obtained output power as a function of the DPS current is shown in Figure 6.24.

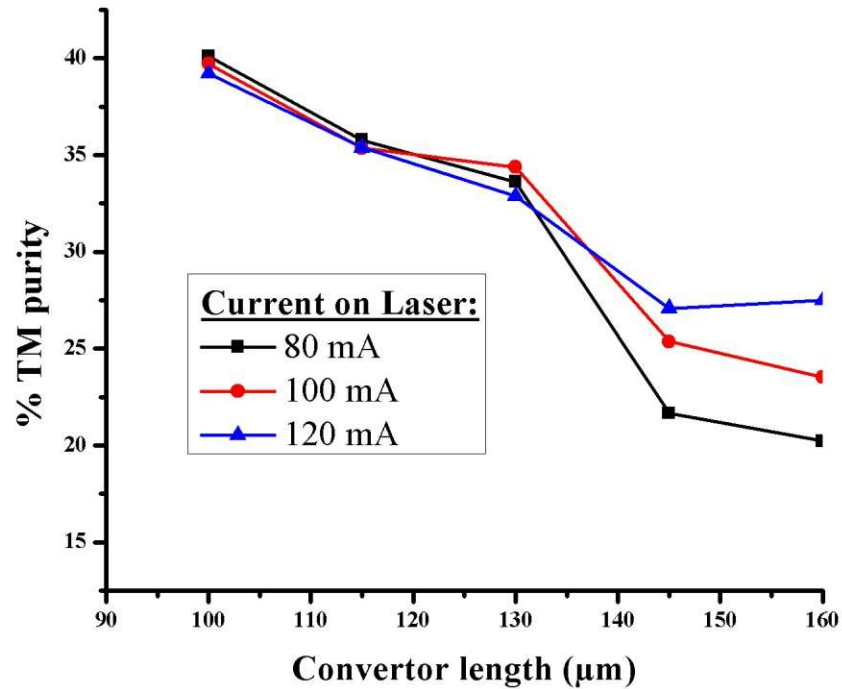


Figure 6.23: The % TM purity as a function of the convertor length for different laser currents.

The output power increases with increasing DPS current. The differential phase shift between the TE and TM modes as the current is varied, results in the observed oscillations as the output polarisation state alternates between linear and elliptical polarisation states. From the number of oscillations, we can deduce that in the range of 0 to 6 mA current on the DPS section, there is a differential phase shift of $9\pi/4$ (slightly larger than 2π) (Figure 6.24). This is due to the % TM purity of ~40 % (as shown earlier) which is less than the ideal (50 % TM purity), therefore 100 % visibility of the depth of the oscillations cannot be observed. Here, the visibility of the oscillations is 88 %.

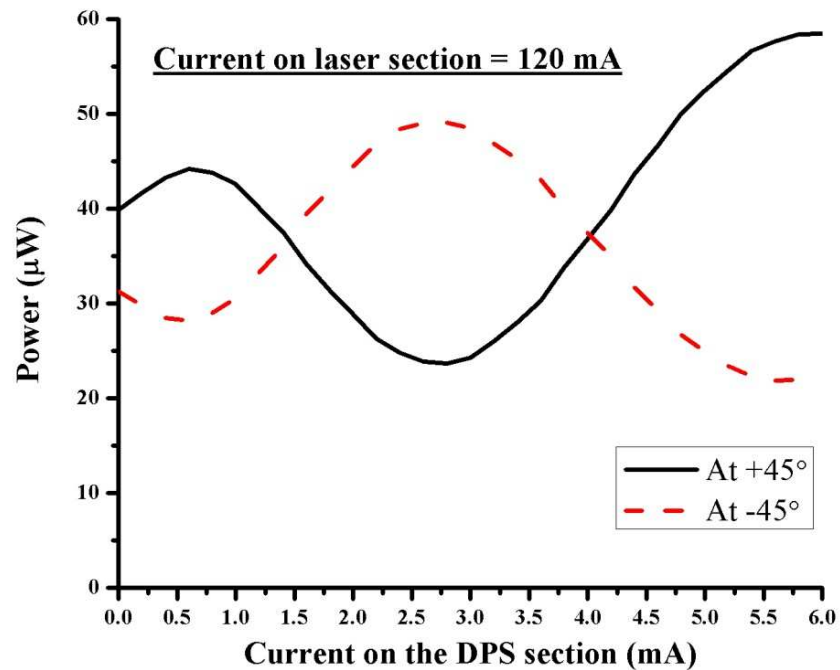


Figure 6.24: Output power as a function of the DPS current for polarisation angles of 45° and -45° .

Thereafter, these measurements were repeated to confirm that behaviour of the devices is due to the current induction, and not to the thermal effects. A quarter wave plate (QWP) was inserted immediately prior to the polarisation analyser, set to $+45^\circ$. The fast axis of the QWP was set parallel to the plane of the wafer to align the TE polarisation. The results obtained with and without QWP are shown in Figure 6.25. It can be observed that with the incorporation of the QWP, the obtained oscillations are in the form similar to the above measured results, but are advanced by a relative phase of $\pi/2$ where the fast axis is aligned with the TE polarisation. It can therefore be deduced that increasing the DPS current decreases the refractive index of the TE polarised mode relative to the TM polarised mode. This result is consistent with a refractive index change due to band filling (carriers injection) affecting the heavy hole/ conduction band resonance (as described in Chapter 2).

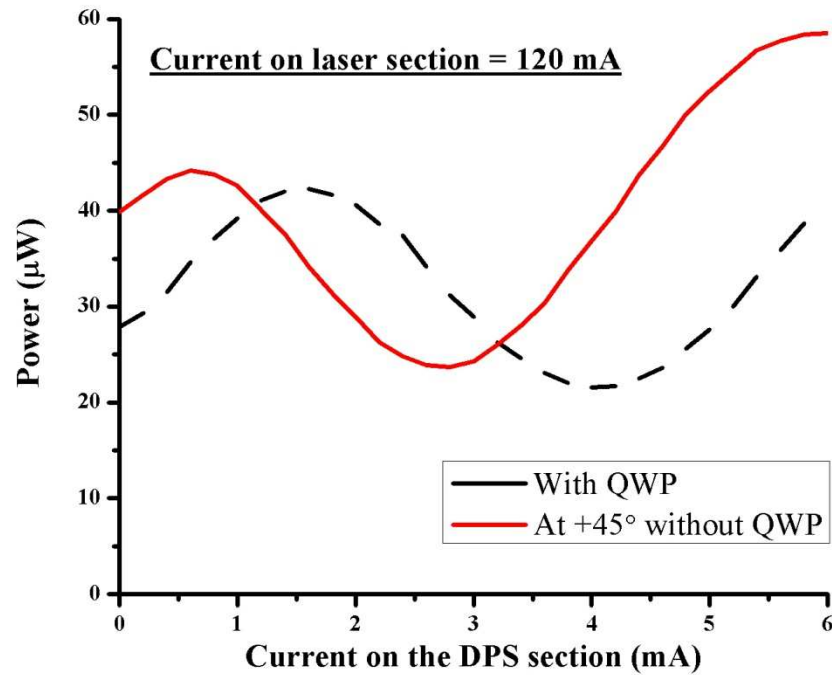


Figure 6.25: Output power as a function of the DPS current with addition of a QWP, with a fast axis aligned in plane of the wafer (TE aligned).

The temporal response of the polarisation state was investigated using the measurement setup shown in Figure 6.26. A modulated signal between 3 mA and 6 mA was provided to the DPS section, using a function generator. The electrical input driving pulse of 8 ns was provided. The output optical pulse was measured on a high speed oscilloscope at output of the polarisation analyser (polariser), set at +45° and using a 2.5 GHz bandwidth, ac coupled photodetector. The polarisation modulation output along with the electrical input driving pulse is shown in Figure 6.27. We can see that the output pulse exhibits significant rise and fall time of 4.8 and 14.6 ns respectively [8]. This is attributed to the electrical driving arrangement used, which consisted of low speed probe connections, designed for use with DC signals. The 3dB bandwidth for DC probes was measured to be 6.4 MHz as shown in Figure 6.28. The carrier life time of this device is expected to be around 500 ps [12]. The high speed modulation can be obtained by employing the quantum confined stark effect with a reverse voltage in these devices.

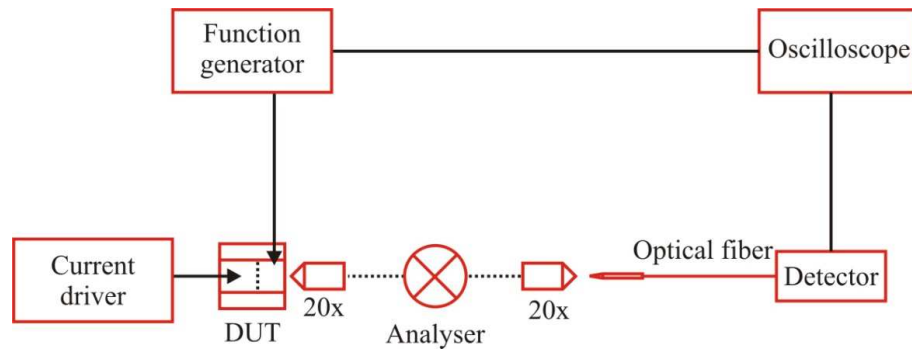


Figure 6.26: A schematic diagram of the measurement setup of temporal response of the polarisation state.

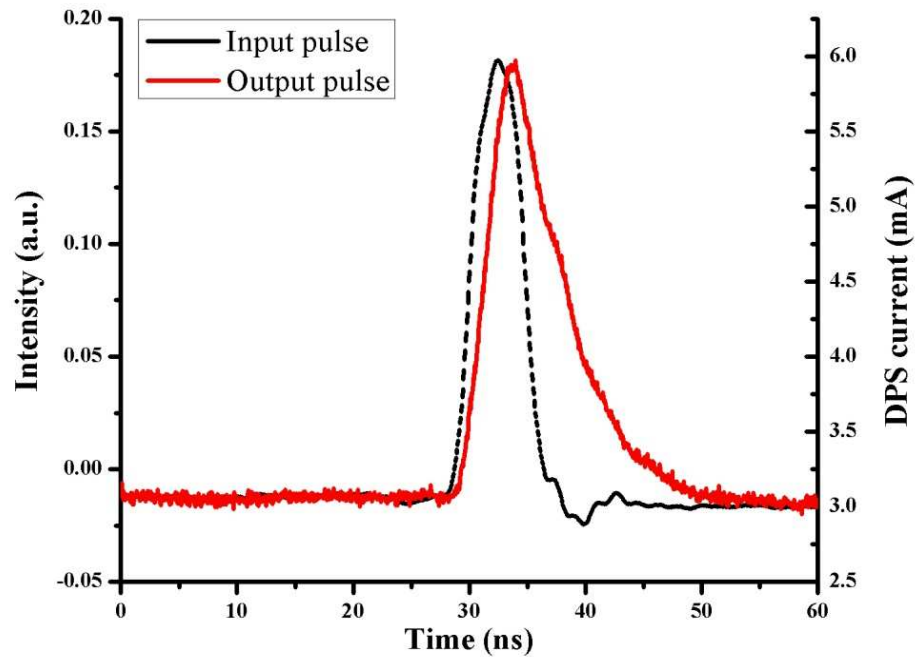


Figure 6.27: Polarisation modulated output measured with 8 ns input driving pulse to the DPS section.

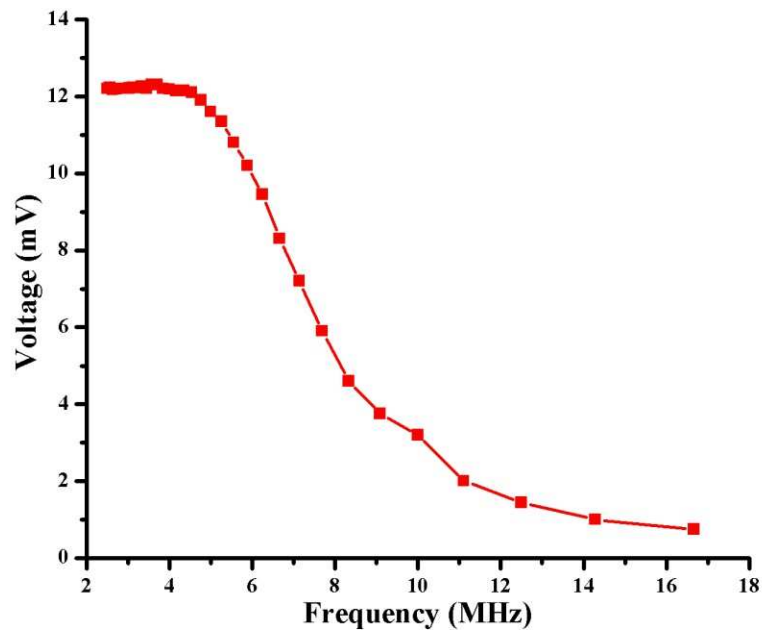


Figure 6.28: A plot of output voltage (response) versus frequency measured with low speed DC probes.

6.4.9. Polarisation modulation measurements with data injection

These devices were also measured to obtain the polarisation switched optical output data. The experimental arrangement used for this is shown in Figure 6.29.

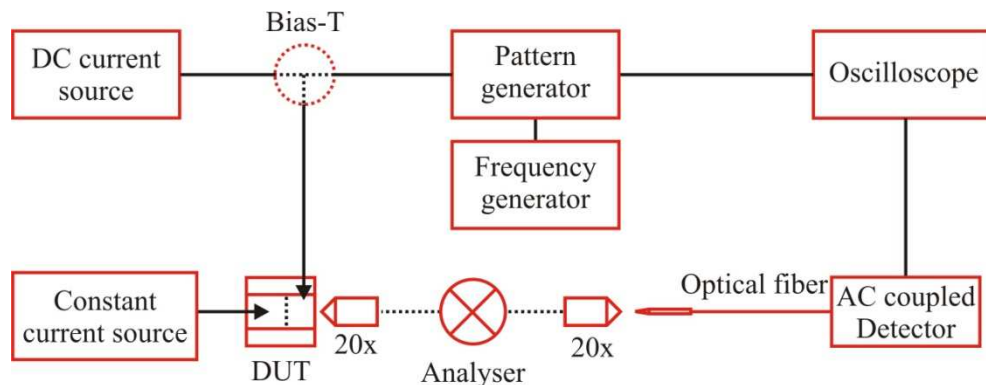


Figure 6.29: A schematic diagram of the measurement setup for measurements of response of polarisation state after inducing binary input data.

A 70 Mbps, 2 V peak to peak signal was combined with a DC bias at 0.7 mA via a bias-T, used to drive the DPS section of the device. A constant current of 120 mA was provided to the laser section. The optical output beam was obtained, and collimated using two 20x microscope objective lenses on the fibre, attached to the 2.5 GHz bandwidth, ac coupled photodetector. A polarisation analyser (polariser) was placed between the two focussing lenses. The optical output power was obtained through the polarisation analyser, set at $+45^\circ$ and -45° to the plane of the wafer. This differential phase shift results in observed polarisation modulation. A comparison with the electrical input driving signal is shown in Figure 6.30, whereas in Figure 6.31, the optical outputs with the analyser at $+45^\circ$ and -45° are shown. As anticipated, the signals are be logical complement of one another. Given the limitations of the existing probe setup (as shown in Figure 6.28) for high speed device driving, the setup was modified using the high speed RF probes, which is explained in the subsequent section.

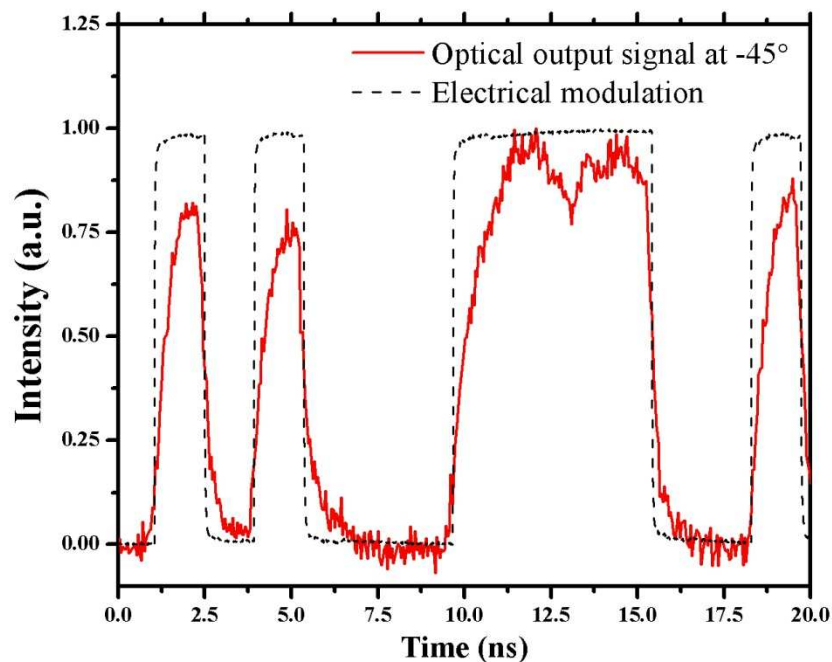


Figure 6.30: Polarisation switched optical output pulse (measured), and induced electrical input binary data.

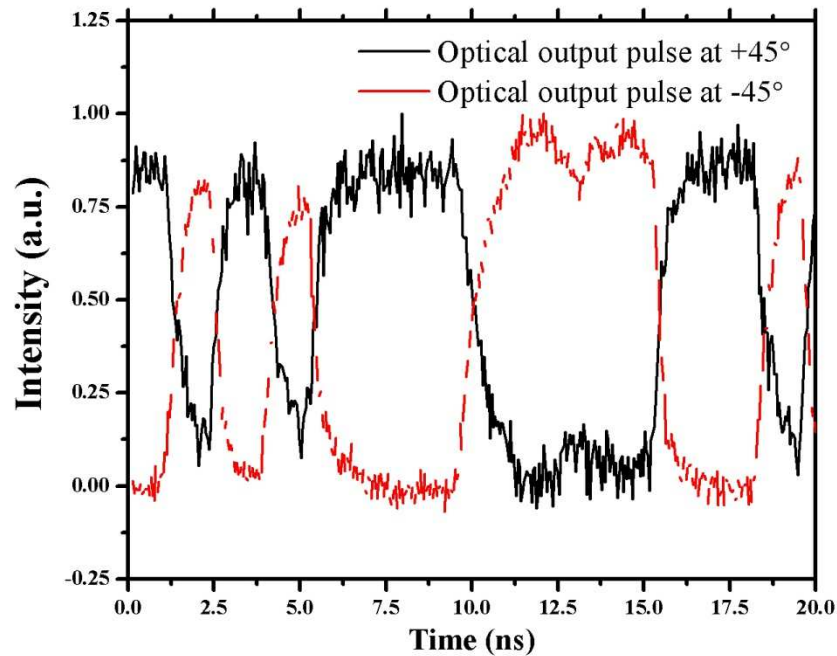


Figure 6.31: Optical output pulses measured for polarisation angles of 45° and -45° (with injection of electrical input binary data).

6.4.10. High speed polarisation modulation measurements

Generally using low speed probe connections, designed for use with DC signals for driving the device, the bandwidth was very low i.e. 6.4 MHz (as described earlier). Therefore, it was investigated that using RF probes; high speed polarisation modulation can be achieved. In order to do this, modification was done to existing arrangement. The device was soldered mounted on the aluminium nitride tile with the impedance matching of 43Ω to make $\sim 50 \Omega$ matched impedance with RF probe. A schematic of this arrangement is shown in Figure 6.32. Normally, the device resistance fall between $4\text{--}7 \Omega$, therefore a 43Ω resistor in series with device, using micro-strip line, was used. This strip line was isolated from the ground plane of the device. The device was positioned perpendicular to the micro-strip line, with the DPS facet facing away from the strip line to provide access for the focusing lense to accumulate the output signal. A gold wire was then made across the end of the strip line (after resistor) to the DPS section of the

device to provide an electrical bridge suitable for RF biasing. The laser section of the device was kept to operate with DC probes to give the input signal to the PMC and DPS section the device.

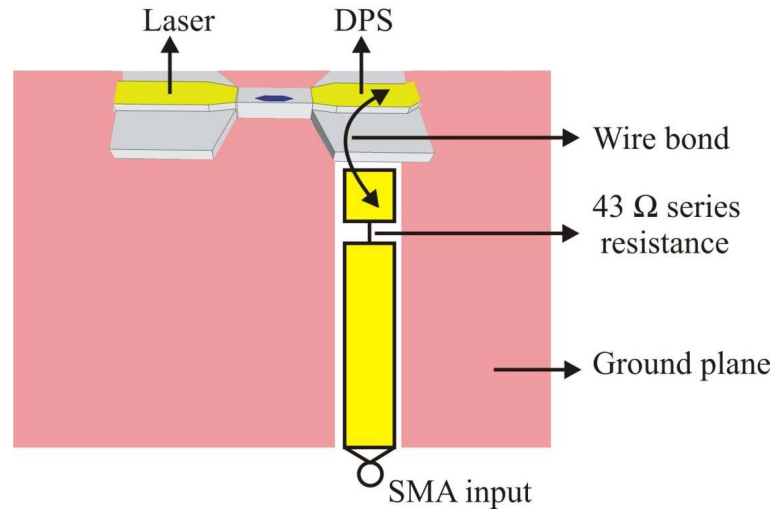


Figure 6.32: A schematic of the wire bonded arrangement of the device to use with RF probes.

Initially, polarisation switching was measured with the voltage bias on DPS section of the device with keeping the constant current of 120 mA on the laser section. This was done due to change in the series resistance of the device. RF probes were used to observe the bias voltage for switching, which was found to be 1.5 Volt. This is the voltage where maximum switching was obtained without amplification of the signal, as DPS section acts as an SOA for higher voltages. At this voltage DC current was 19.8 mA. The optical output power was measured through the polarisation analyser, which was set at $+45^\circ$ and -45° , to the plane of the wafer. The output power as a function of the voltage on the DPS section is shown in Figure 6.33.

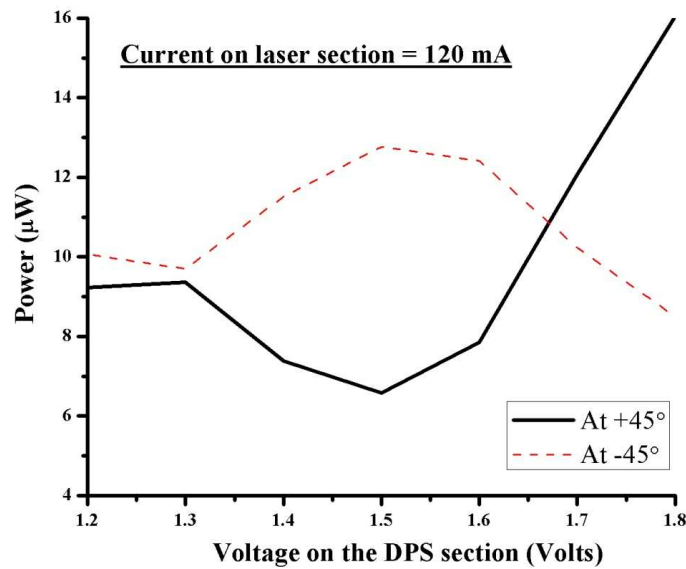


Figure 6.33: Optical output power as a function of the voltage on the DPS section using RF probes for polarisation angles of $+45^\circ$ and -45° .

The high speed polarisation modulation was characterised with the setup explained above, and shown in Figure 6.29. A signal with frequency of 100 to 500 Mbps, with a step of 100 Mbps, was provided. This signal was combined with a DC bias of 19.8 mA, equivalent to 1.5 V via a bias-T used to drive the DPS section of the device. A constant current of 120 mA was provided to the laser section. The data input was 0.5 V. As the voltage source modulation was limited to a minimum of ± 0.25 V, the bias was adjusted to obtain the largest optical modulation whilst checking the polarisation was being modulated, rather than amplification effects. This was confirmed by setting the analyser to 0° and 90° , where no modulation was observed. The eye diagrams with -15 dBm output optical signal from device with frequencies from 100 to 500 Mbps, were obtained through the polarisation analyser, set at $+45^\circ$, -45° , 0° (TE) and 90° (TM). These eye diagrams and output optical signals from 100 to 500 Mbps are shown in Figure 6.34 to Figure 6.38. As anticipated, the output optical signals with polarisation analyser set at $+45^\circ$ and -45° are complement of one another, whereas at 0° (TE) and 90° (TM), there is no signal. A little bit signal at 0° (TE) and 90° (TM) (as shown in Figures) is due to the noise generated by the equipment itself.

We can also see that the signal weakens as we go on the higher bit rates such as at 400 and 500 Mbps. The output optical signals with 300 Mbps obtained at these angles at the same scale are also shown in Figure 6.39. Here, the TE and TM signals are straight lines as anticipated (due to large scale).

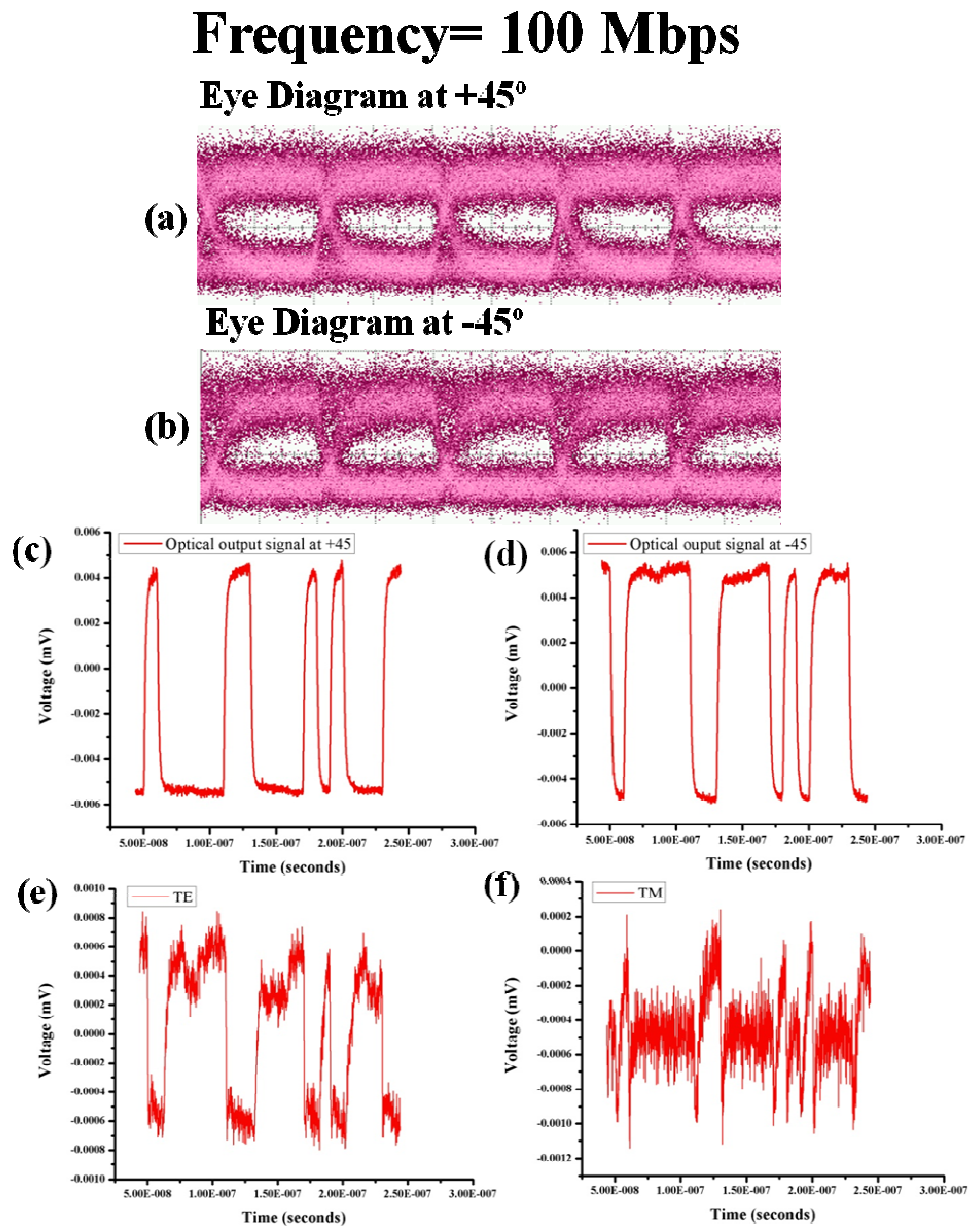


Figure 6.34: Eye diagrams obtained at 45° (b) and -45°, and optical output signals measured for polarisation angles of (c) 45°, (d) -45°, (e) 0° (TE) and (f) 90° (TM) at 100 Mbps.

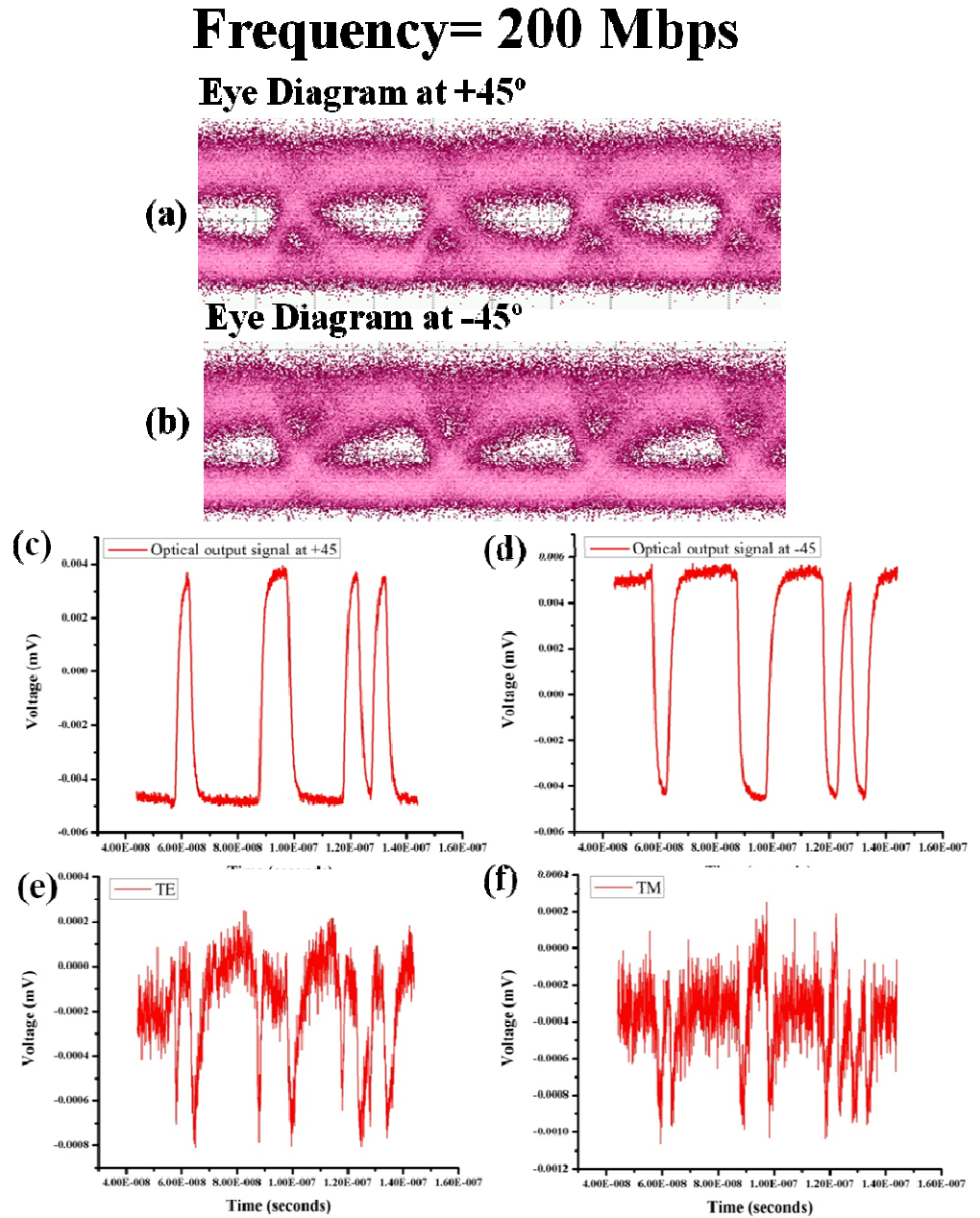


Figure 6.35: Eye diagrams obtained at 45° (a) and -45°, and optical output signals measured for polarisation angles of (c) 45°, (d) -45°, (e) 0° (TE) and (f) 90° (TM) at 200 Mbps.

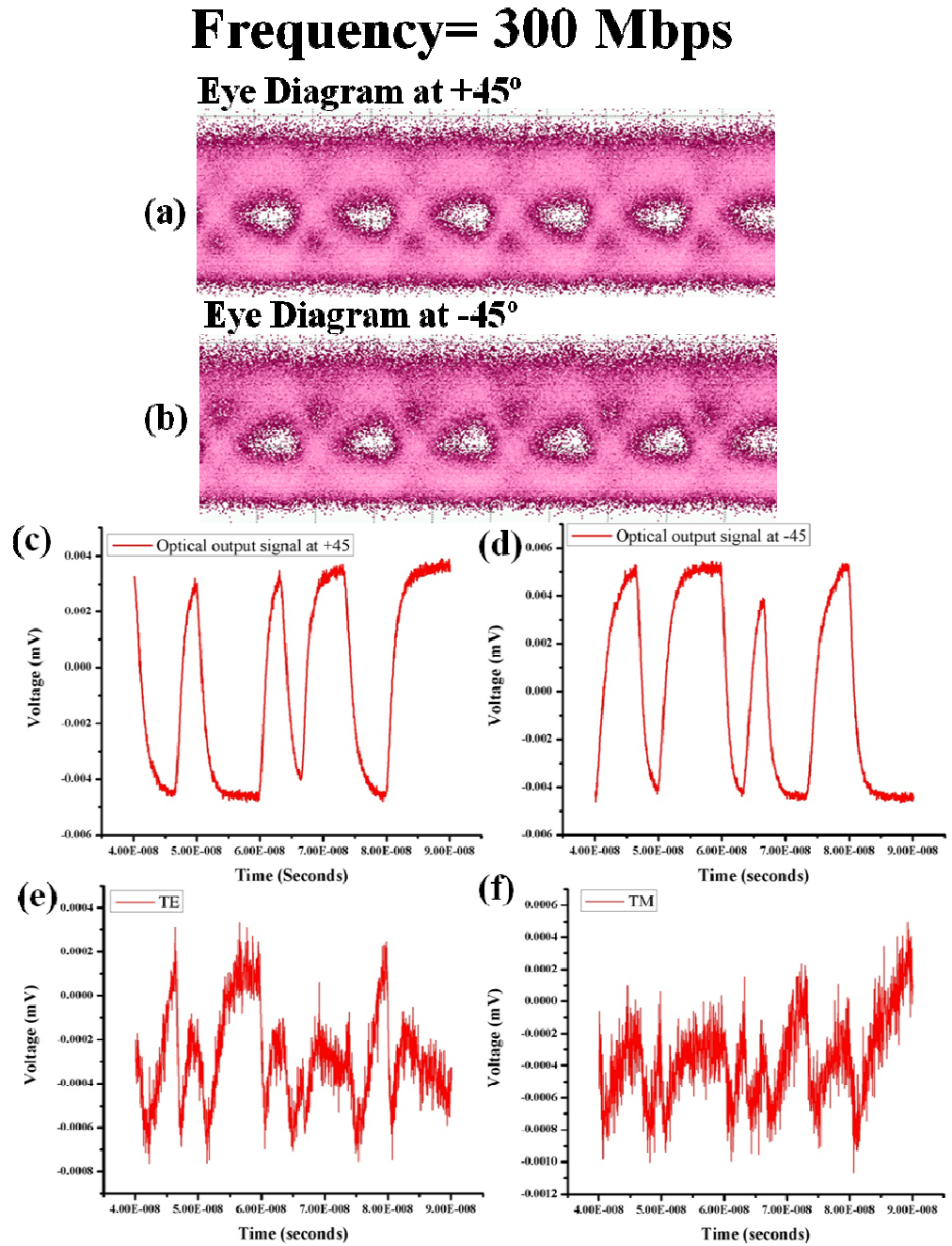
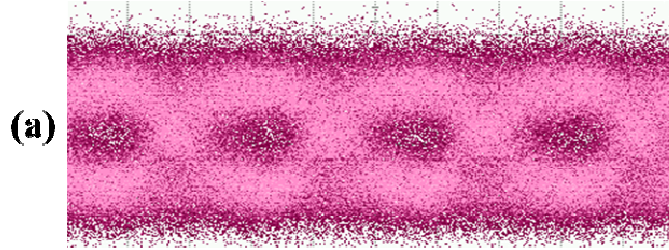


Figure 6.36: Eye diagrams obtained at 45° (b) and -45°, and optical output signals measured for polarisation angles of (c) 45°, (d) -45°, (e) 0° (TE) and (f) 90° (TM) at 300 Mbps.

Frequency= 400 Mbps

Eye Diagram at +45°



Eye Diagram at -45°

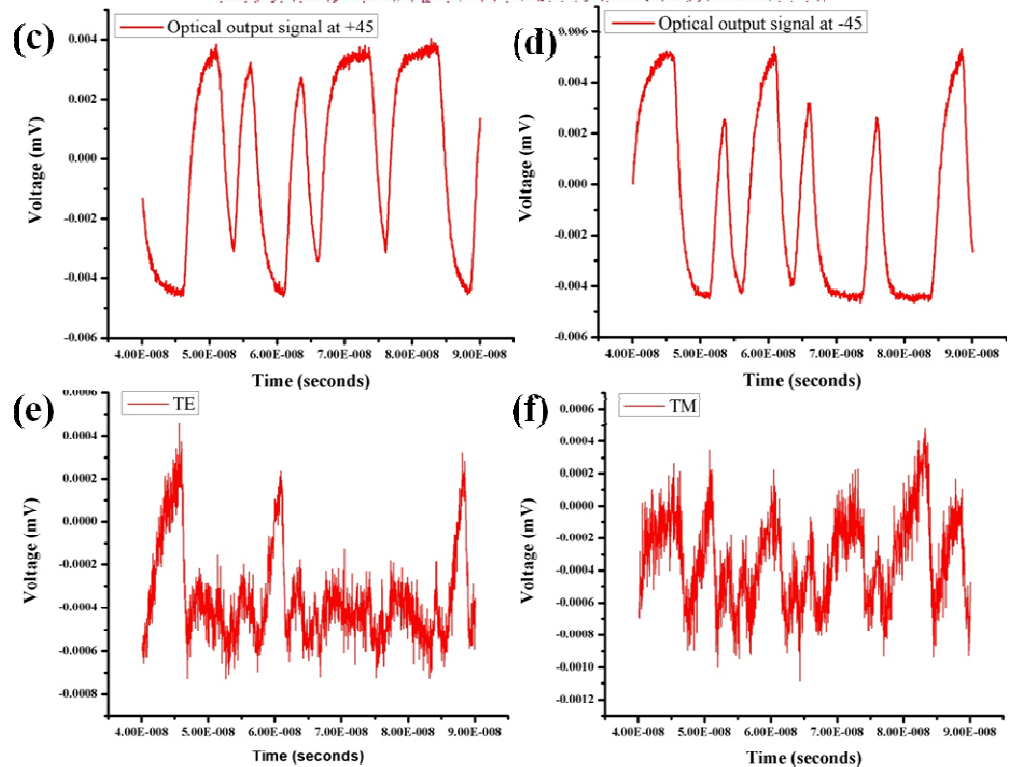
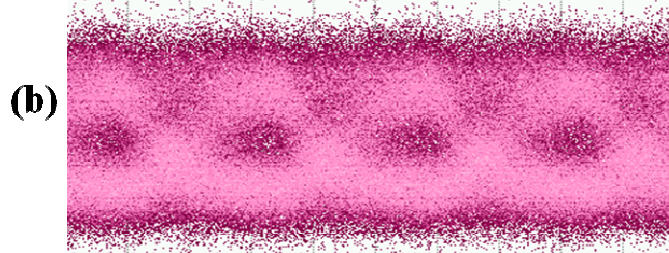


Figure 6.37: Eye diagrams obtained at 45° (b) and -45°, and optical output signals measured for polarisation angles of (c) 45°, (d) -45°, (e) 0° (TE) and (f) 90° (TM) at 400 Mbps.

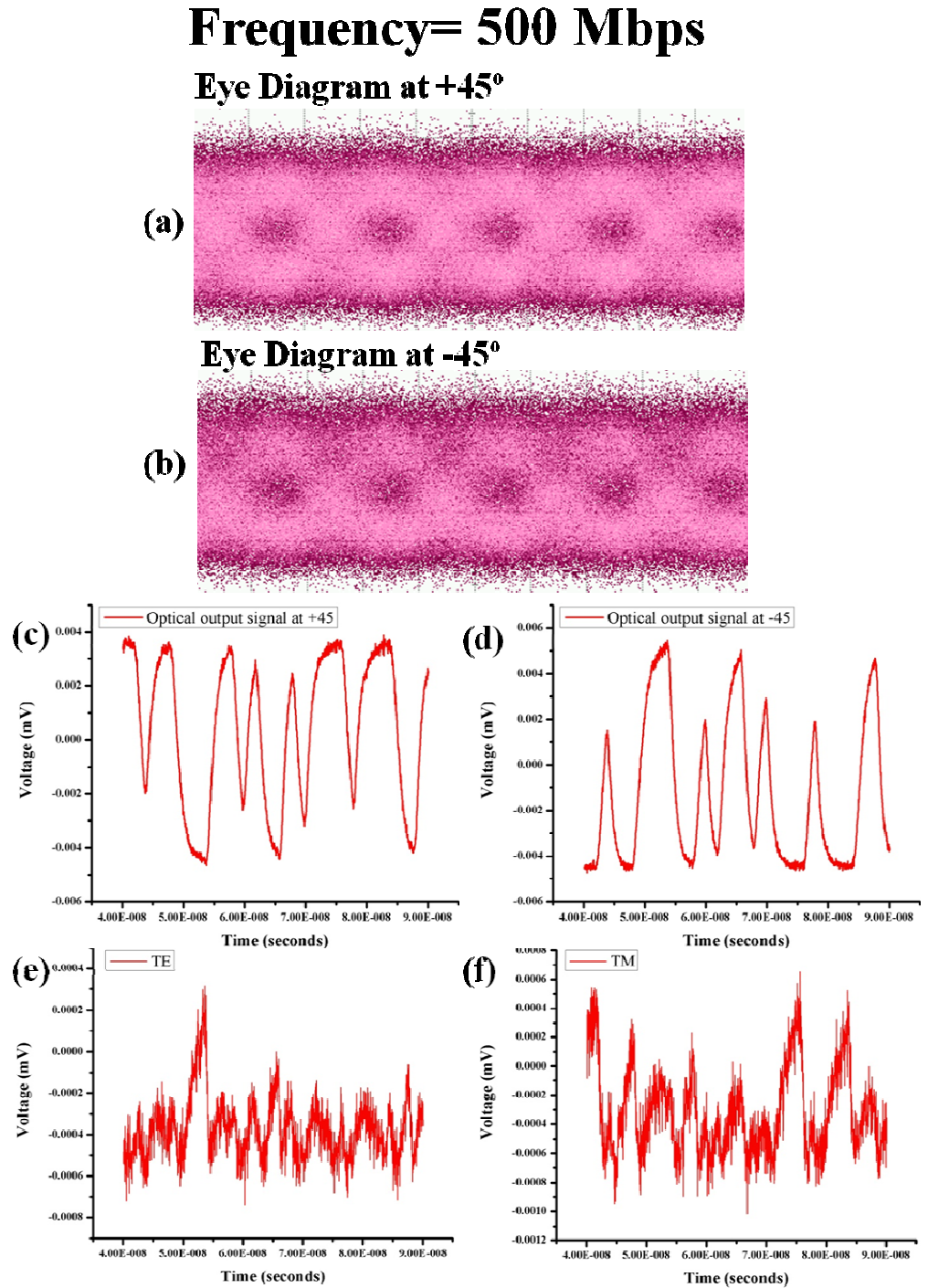


Figure 6.38: Eye diagrams obtained at 45° (a) and -45°, and optical output signals measured for polarisation angles of (c) 45°, (d) -45°, (e) 0° (TE) and (f) 90° (TM) at 500 Mbps.

Frequency= 300 Mbps

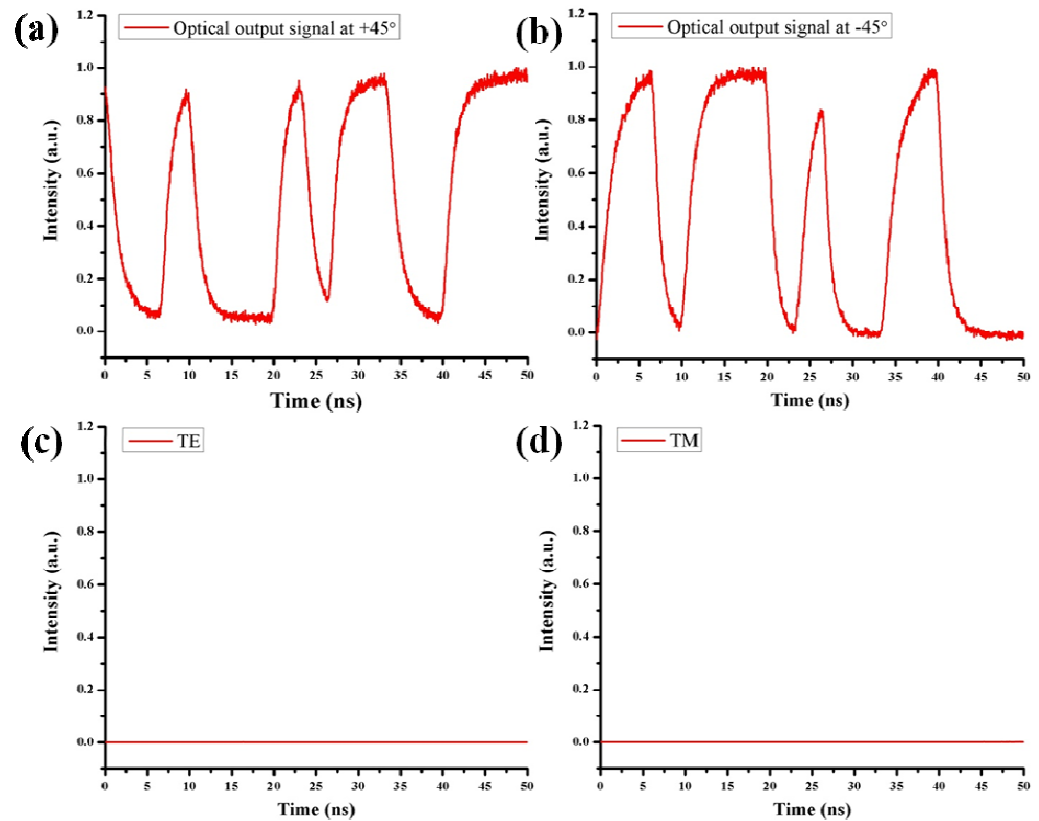


Figure 6.39: Optical output signals measured for polarisation angles of (a) 45° , (b) -45° , (c) 0° (TE) and 90° (TM) at 300 Mbps (on the same scale).

6.5. Integrated devices with back to back PMCs

The concept to attach two PMCs back to back (as described in Chapter 5), was used. The optical axis is rotated at 22.5° after 1st PMC and further 22.5° after 2nd PMC to attain total change in the optical axis for 45° . This change in optical axis yields 100 % polarisation rotation. This change in optical axis is shown in Figure 6.40, where A, B and C are the termination points of the laser, 1st PMC and 2nd PMC. These integrated devices, consisting of a semiconductor laser, two PMCs attached back to back, and a DPS section, are shown in Figure 6.40. This structure with back to back PMCs, instead of using a single PMC, to attain 100 % polarisation rotation is advantageous due to less etching requirement, which is

easily achievable. Further mode matching is easier to achieve. Although it has some disadvantageous such as increase in length of the PMC, and higher losses in the un-pumped section of the PMC. Same dimensions were opted as described in the first structure (Figure 6.9) except lengths of the laser section and the convertor sections. These dimensions were 600 nm trench width with 1.972 μm trench depth, and 300 nm trench position from the waveguide edge. The laser and DPS section widths were 2.4 μm , and PMC section width was 1.8 μm . Here, a 1000 μm long semiconductor laser section, 200 to 380 μm long trenches (in PMC sections) with a step of 30 μm , and a 1050 μm long DPS section, was fabricated. Tapers of 4 μm length were used on each side of the trench for smooth etching and mode matching. These two PMCs helped in obtaining the polarisation mode conversion two times higher as compared to the single PMC devices. The PMC section was 440 μm long and un-pumped for all the devices.

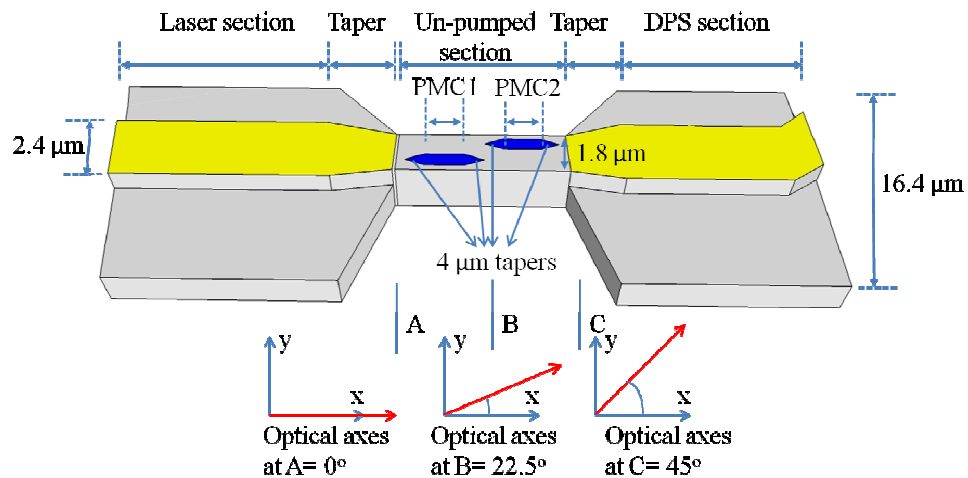


Figure 6.40: A schematic diagram of the integrated device with two back to back PMCs, followed by a DPS section, with change in the optical axis at A, B and C.

6.5.1. Modelling and design of device

The integrated devices with a laser, two back to back PMCs, followed by a DPS section, were simulated using BPM. The simulation parameters used, were same as for the single stage PMC simulations. These parameters were 600 nm trench width with 1.972 μm trench depth, and 300 nm trench position from the

waveguide edge. The width of the laser and DPS section was kept $2.4 \mu\text{m}$, whereas PMC section was $1.8 \mu\text{m}$ wide. A polarisation mode conversion of 99 % was obtained for the convertor length of $366 \mu\text{m}$ (two x $188 \mu\text{m}$ long PMCs), and with $1.972 \mu\text{m}$ deep trench. The TE to TM polarisation mode conversion for a zero order TE mode launched into the convertor section for this device is shown in Figure 6.41. When the TE and TM modes convert to each other at $188 \mu\text{m}$, there is an uneven behaviour of the modes, which might be due to the mode mismatching.

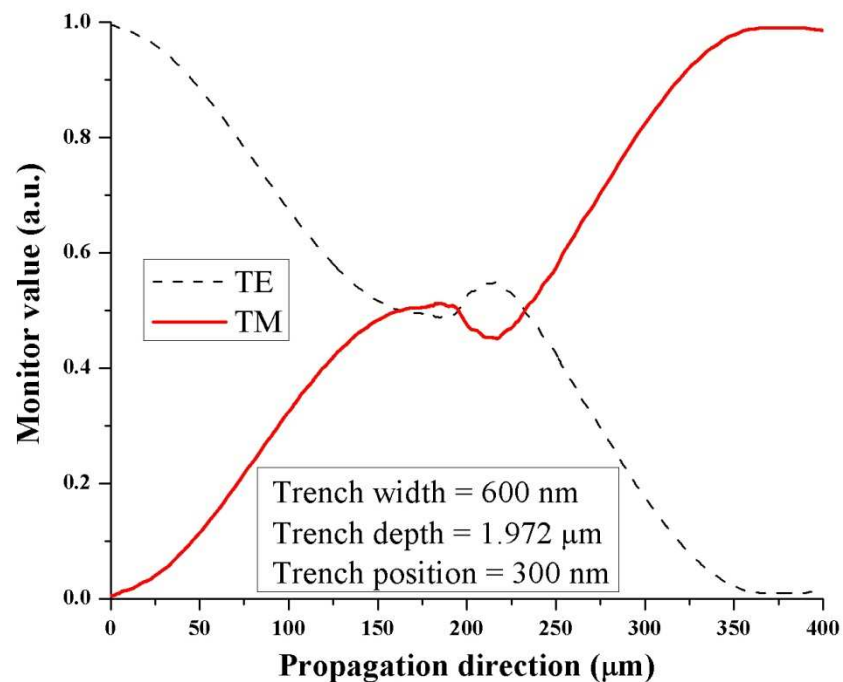


Figure 6.41: The TE to TM mode conversion as a function of the propagation direction for the integrated devices (with back to back PMCs and a DPS section).

Additionally, the modal profiles of the modes propagating in the integrated device at various positions such as at the entering point of 1st PMC, and at termination points of 1st PMC section (at $188 \mu\text{m}$) and 2nd PMC section (at $366 \mu\text{m}$), are shown in Figure 6.42. We can see that there is a tilt of the modes after 1st and 2nd PMCs, which is due to the change in the optical axis of the asymmetric section of the waveguide. This change in optical axis is due to the air trench. These all modes were obtained with deep etched waveguides.

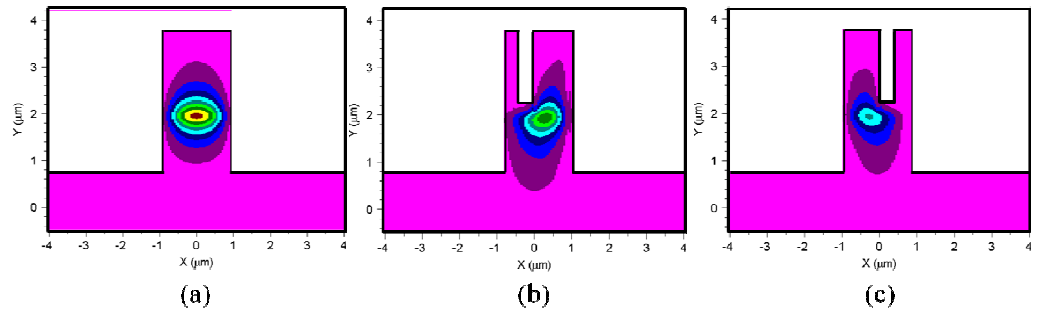


Figure 6.42: Modal profiles (a) at the start of the 1st PMC (b) at the termination point of 1st PMC (188 μm) and (c) at the termination point of 2nd PMC (366 μm).

6.5.2. Device measurements

These integrated devices with back to back PMCs were fabricated on the same chip, on which the integrated devices with a single PMC were fabricated, and described earlier. The measurement setup shown in Figure 6.21 was used to measure the TM purity. In these devices, Polarisation mode conversion efficiencies of 90.7 %, 88.1 % and 86.3 % were obtained for the PMC length of 200 μm with injection currents of 80 mA, 100 mA and 120 mA, respectively. A plot of % TM purity as a function of the PMC length at three laser drive currents is shown in Figure 6.43.

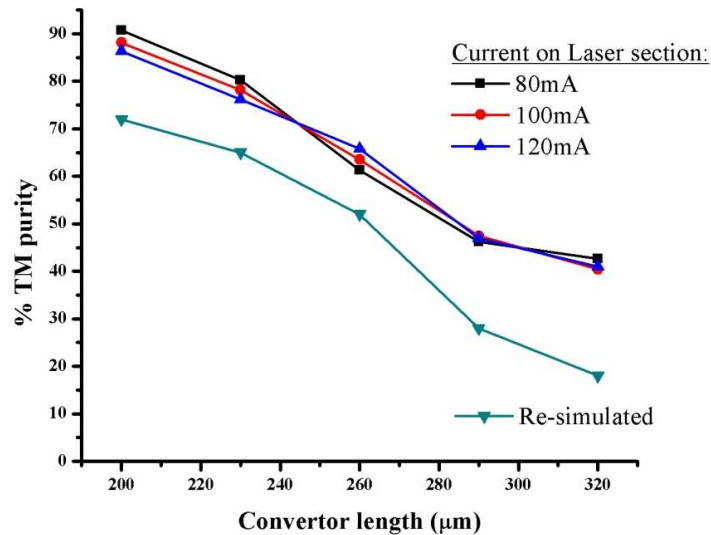


Figure 6.43: A plot of % TM purity (experimentally measured and re-simulated) as a function of the PMC length at three laser drive currents.

Furthermore, the measured results were compared with simulated results, and found that the measured results are not consistent with each other in terms of the convertor lengths. From simulations, conversion efficiency of 99 % was obtained at the convertor length of 366 μm (Figure 6.41), whereas; 86.3 % to 90.7 % conversion efficiencies, were obtained from the realised device with a 200 μm long convertor section. The experimentally obtained results were used to refine the refractive indices and loss coefficients used in the simulations, yielding a conversion efficiency that closely followed the observed trend (as shown in Figure 6.43), albeit with a reduced conversion efficiency due to the effects of preferential absorption of the TE component of polarised light in the un-pumped PMC section [13].

The obtained results of the integrated devices with back to back PMCs were compared with the measured results of the single PMC devices. It is observed that the conversion efficiency is almost double in devices with back to back PMCs as compared to the single PMC devices. This shows the consistency of simulated models with the fabricated devices, with single and back to back PMCs. Comparison of both integrated devices is shown in Figure 6.44.

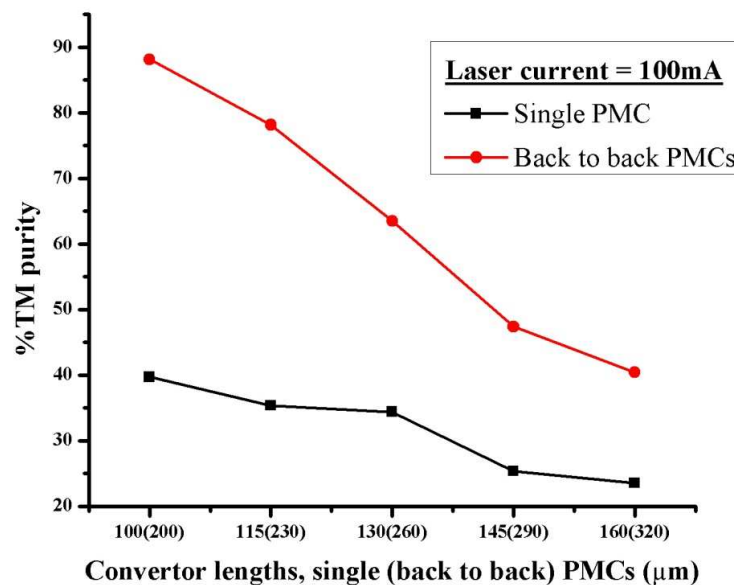


Figure 6.44: Comparison of polarisation mode conversion with single (and back to back) PMCs at 100 mA current on a semiconductor laser section.

6.6. Conclusions

In the first section of this chapter, the description of the quaternary material (InP/AlGaInAs) is provided. This material provides the better research interest than the other phosphorous quaternary material systems, due to the attractive band discontinuity properties. Furthermore, the brief description of the epitaxial layers with the band diagram of InP/AlGaInAs material structure, is presented. Thereon, the structures devised for realisation of the integrated devices using a single PMC, and two PMCs attached back to back, with a laser with their modelling and optimisation, are discussed. The characterisation and measurements including optical spectrum, transparency current and polarisation mode conversion carried out for these devices are given. The polarisation mode conversion efficiencies of 40.1 %, 39.7 % and 39.2 % from 100 μm long convertor, and 90.7 %, 88.1 % and 86.3 % from 200 μm long convertor, with the current injections of 80 mA, 100 mA and 120 mA, respectively, were obtained. Dynamic polarisation control measurements are presented for devices with a single PMC. The investigated temporal response of the polarisation state using a function generator is given, which shows 4.6 ns rise time and 14.6 ns fall time for the electrical input driving pulse of 8 ns duration. The measurements of these devices by applying the electrical input binary data and the optical output signals obtained at $+45^\circ$ and -45° to the plane of the wafer, also presented, which show the consistency with the applied electrical input binary data. The polarisation switching was observed at 300 Mbps using high frequency probes on these devices. This high polarisation switching was obtained by modifying the DC probe arrangement to use with RF probes for driving the DPS section of the device.

6.7. References

1. Higashi, T., et al., *Observation of reduced nonradiative current in 1.3 um AlGaInAs-InP strained MQW lasers*. Photonics Technology Letters, IEEE, 1999. **11**(4): p. 409-411.
2. Camargo Silva, M.T., et al. *1.3 um strained MQW AlGaInAs and InGaAsP ridge-waveguide lasers-a comparative study*. in *Microwave and Optoelectronics Conference, 1999. SBMO/IEEE MTT-S, APS and LEOS - IMOC '99. International*. 1999.
3. IQE Ltd., www.iqep.com.
4. Green, R.P., et al., *Fast saturable absorption and 10 GHz wavelength conversion in Al-quaternary multiple quantum wells*. Opt. Express. **19**(10): p. 9737-9743.
5. Kasukawa, A., et al., *Low threshold current density 1.5 um GaInAs/AlGaInAs graded-index separate-confinement-heterostructure quantum well laser diodes grown by metal organic chemical vapour deposition*. Electronics Letters, 1991. **27**(12): p. 1063-1065.
6. Coldren, L.A. and S.W. Corzine, *Diode lasers and photonic integrated circuits*. 1995: Willey - Interscience.
7. Lianping, H., et al., *160-GHz Passively Mode-Locked AlGaInAs 1.55-um Strained Quantum-Well Compound Cavity Laser*. Photonics Technology Letters, IEEE. **22**(10): p. 727-729.
8. Holmes, B.M., et al., *A semiconductor laser with monolithically integrated dynamic polarization control*. Opt. Express. **20**(18): p. 20545-20550.
9. Vu, L.c., et al., *Electrical diagnostics of the amplifier operation and a feasibility of signal registration on the basis of the voltage saturation effect in junction laser diodes*. Quantum Electronics, IEEE Journal of, 1983. **19**(6): p. 1080-1083.

10. Alping, A., B. Bentland, and S.T. Eng, *100 Mbit/s laser diode terminal with optical gain for fibre-optic local area networks*. Electronics Letters, 1984. **20**(19): p. 794-795.
11. Patterson, F.G., S.P. Dijaili, and R.J. Deri. *Accurate determination of transparency current in packaged semiconductor lasers and semiconductor optical amplifiers*. in *Integrated Photonics Research*. 1995: Optical Society of America.
12. Akbar, J., *High Power Mode Locked Lasers monolithically Integrated with Semiconductor Optical Amplifiers*. 2012, PhD thesis, University of Glasgow: UK.
13. Naeem, M.A., et al. *Passive polarization mode convertor monolithically integrated within a semiconductor laser*. in *Photonics Conference (IPC), 2012 IEEE*.

Chapter 7

Conclusions and future recommendations

7.1. Conclusions

A polarization mode convertor (PMC) integrated monolithically with a semiconductor laser is introduced, which is, theoretically optimised, fabricated and characterised. The integrated devices were realised in a single reactive ion etch (RIE) process, and the RIE lag technique was employed to attain the desired trench depth above the double quantum well (DQW) hetero-structure layers in the polarization mode convertor section. This added trench, makes the asymmetric waveguide section, which helps to alter the optical axis of the waveguide structure.

A DQW, un-strained GaAs/AlGaAs material with active device functionality, was used for optimisation of the trench width, and the depth of the PMC in the integrated devices. The integrated devices were devised, in two ways, i.e. using a single PMC with a semiconductor laser, and using two PMCs attached back to back, with a semiconductor laser. Polarization mode conversion of 40.5 % and 64.4 % was obtained in passive devices with a single PMC, and back to back PMCs, respectively, in the GaAs/AlGaAs material system.

Integrated devices were also fabricated using InP/AlGaInAs strained quantum well material. Polarization mode conversion of ~40 % was obtained for a single PMC with a convertor length of 100 μm , and above 85 % was obtained for a convertor length of 200 μm , using two PMCs, attached back to back, with current injections from 80 to 120 mA on a semiconductor laser section. High speed modulation at 300 Mbps, by applying the input electrical binary data using RF probes, on the differential phase shifter (DPS) section of the integrated device, was also measured using a single PMC with a convertor length of 100 μm .

7.2. Future recommendations

Some suggestions for future work as a follow up to this research are as follows.

- Loss characterisation was not performed in this research work, which should be addressed theoretically and experimentally.
- The devices fabricated for 45° (50 %) polarisation mode conversion, and presented in this research, can be further realised for 90° (100 %) polarisation mode conversion using a single PMC instead of two PMCs attached back to back. This can be achieved by increasing the trench depth in the PMC section. However, an accurate control will be required to achieve the desired trench depth. This will also help in reducing the device length as well.
- The devices with a single PMC, and two PMCs (attaching back to back) can be fabricated with an SOA. Therefore, the integrated devices can be used for polarisation mode conversion, and optical amplification, at the same time.
- High speed modulation in integrated devices ~1GHz can be obtained by employing quantum confined stark effect (QCSE), with a reverse bias voltage on the DPS section.
- Further, improving design of the integrated devices, with two PMCs and two DPSs, a dynamic polarisation controller can be realised. This can be done by increasing the trench length, the width or position of the trench

from the waveguide edge in the PMC for obtaining the % TM purity upto ~100 %. The schematic structure of this type of device is shown in Figure 7.1.

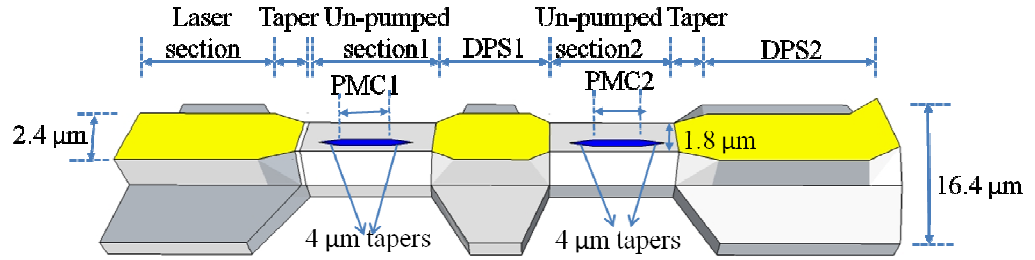


Figure 7.1: A schematic diagram of the integrated device with two single PMCs, and two DPS sections with a semiconductor laser section.

Annex I

Transmission line measurement **fabrication steps**

The steps of the fabrication process for measurement of TLM are given below.

1. Cleave the sample measuring 6 mm x 8 mm in dimension.
2. Clean the sample in ultrasonic bath with acetone, IPA and RO water for 5 minutes each and then blows dry with gaseous nitrogen.
3. Spin coat the sample with photo-resist S1818 (positive resist) at 4000 rpm for 30 seconds. This produces 1.8 μm thick resist layer.
4. Clean backside of the sample with acetone soaked cotton bud and place on the hot plate at 90 °C for 15 minutes.
5. Put the sample in chloro-benzene filled petri dish for 10 minutes. This makes the resist hard enough and the lift off process becomes easier.
6. Blows dry the sample with gaseous nitrogen and place on the hot plate for 5 minutes at 90 °C.
7. Expose the pattern shown in Figure 4.1 in Chapter 4, using photolithography technique.
8. Develop the sample in 1:1 mixture of micro-posit developer and RO water for 75 seconds and then rinse in RO water for 75 seconds. Then blows dry the sample with gaseous nitrogen and inspect the developed pattern under the microscope.
9. Deoxidise the sample with 1:5 HCl: H₂O mixture for 30 seconds and then rinse in RO water for 30 seconds and blows dry with gaseous nitrogen.
10. Evaporate 30 nm Ti, 33 nm Pt and 240 nm Au to make the contact pads using electron-beam assisted Plassys machine.
11. Lift off Ti/Pt/Au layer using acetone in hot water bath at 50 °C for 1 hour.

12. Clean the sample with acetone and RO water for 1 minute each and then blows dry with gaseous nitrogen.
13. Spin coat the sample with photo-resist S1818 (positive resist) at 4000 rpm for 30 seconds.
14. Clean backside of the sample with acetone soaked cotton bud and place on the hot plate at 90 °C for 15 minutes.
15. Expose the pattern using second mask (opposite to already used mask, shown in Figure 4.1 in Chapter 4) using photolithography technique.
16. Develop the sample in 1:1 mixture of micro-posit developer and RO water for 75 seconds and then rinse in RO water for 75 seconds. Blows dry the sample with gaseous nitrogen and inspect the developed pattern under the microscope.
17. Remove any remaining resist on the sample using O₂ ash for 2 minutes.
18. Dry etch the sample to create the mesa structure. System 100 machine was used with SiCl₄ chemistry for 5 minutes. The process was carried out at 5 mTorr pressure, at the flow rate of 13 sccm and 250 watts power. Thereon, the sample was cleaned with usual cleaning process.
19. Anneal the sample in rapid thermal annealer (RTA) for 50 seconds at 360 °C with an initial ramp of 320 °C for 20 seconds. Annealing temperature profile is shown in Figure A-1.

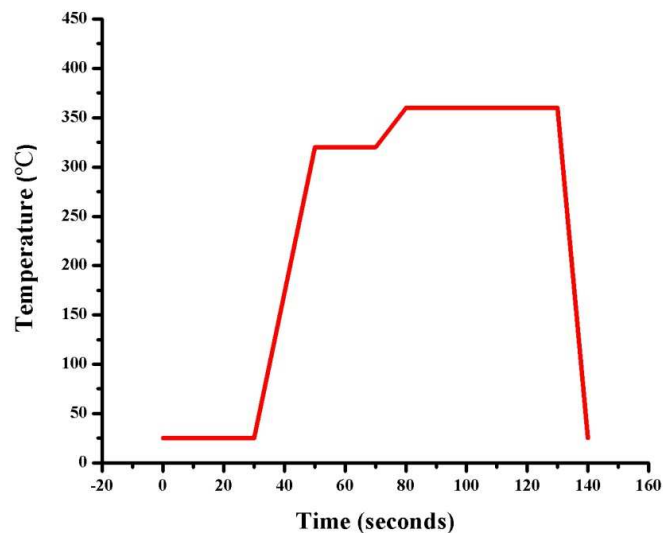


Figure A-1: An annealing temperature profile provided to the sample after mesa definition.

Annex II

Ridge waveguide laser fabrication steps

The fabrication process steps for the ridge waveguide lasers are given below.

Step 1: Creation of e-beam position calibration markers.

1. Cleave the sample measuring 8 mm x 10 mm in dimension.
2. Clean the sample in ultrasonic bath with acetone, IPA and RO water for 5 minutes each and then blows dry with gaseous nitrogen.
3. Spin coat the first e-beam resist layer with lower molecular weight PMMA (positive resist, 15 % of 2010) at 5000 rpm for 60 seconds. This produces 1.2 μm thick resist layer.
4. Clean backside of the sample with acetone soaked cotton bud and place it in the oven at 180 °C for 30 minutes.
5. Spin coat the second e-beam layer with higher molecular weight PMMA (positive resist, 4 % of 2041) at 5000 rpm for 60 seconds. This produces 100 nm thick resist layer.
6. Clean backside of the sample with acetone soaked cotton bud and place it in the oven at 180 °C for 90 minutes.
7. Expose the bi-layer resist coated sample to the position marker pattern with VB6 e-beam writer. VB6 control parameters are, resolution: 1.25 nm, proximity correction file: gaas700-100t.pec, dose: 360 $\mu\text{C}/\text{cm}^2$, spot size: 12 nm and VRU: 8.
8. Develop the exposed position marker pattern using 1:1 IPA:MIBK solution at 23 °C for 30 seconds. Rinse the developed sample in IPA and RO water for 30 seconds and 60 seconds, respectively. Then blows dry with gaseous nitrogen.
9. Metallise the developed sample with 33 nm NiCr: 120 nm Au. This is carried out using e-beam assisted Plassys machine.

10. Lift off NiCr: Au layer using acetone in hot water bath at 50 °C for 1 hour.
11. Clean the sample in acetone, IPA and RO water for 1 minute each and then blows dry with gaseous nitrogen.
12. O₂ ash on asher for 10 minutes at 100 Watt power.

Step 2: Realisation of a ridge waveguide structure.

1. Pre-bake the sample on hot plate for 2 minutes at 90 °C.
2. Spin coat the e-beam resist layer of 100 % HSQ (negative resist) at 5000 rpm for 60 seconds. This produces 360 nm thick resist layer.
3. Clean backside of the sample with acetone soaked cotton bud and place it on the hot plate at 90 °C for 10 minutes.
4. Expose the ridge waveguide structure with VB6 e-beam writer. VB6 control parameters are, resolution: 1.25 nm, proximity correction file: gaas300-100b.pec, proximity minimum: 0.05, proximity grid 0.01, dose: 670 $\mu\text{C}/\text{cm}^2$, spot size: 12 nm and VRU: 8.
5. Expose the protection markers pattern with VB6 e-beam writer. VB6 control parameters are, resolution: 1.25 nm, proximity correction file: gaas300-100b.pec, dose: 640 $\mu\text{C}/\text{cm}^2$, spot size: 33 nm and VRU: 20.
6. Develop the exposed patterns using 25 % TMAH at 23 °C for 30 seconds. Rinse in RO water for 30:30 seconds in two separate beakers and then in IPA solution for 15 seconds. Then blows dry with gaseous nitrogen.
7. Dry etch the developed pattern using System 100 machine to etch 0.95 μm and 1.95 μm for shallow and deep etched waveguides using reflectometer.
8. In order to remove the HSQ from the ridge waveguide structure, process the sample for wet etch with 10:1 ratio of RO water and HF solution for 60 seconds. Rinse in water for 60 seconds and blows dry with gaseous nitrogen.
9. Clean the sample in acetone, IPA and RO water for 1 minute each and blows dry with gaseous nitrogen.
10. O₂ ash on asher for 10 minutes at 100 Watt power.

Step 3: Realisation of a current injection window on the top of the ridge waveguide structure.

1. Deposit the layer of 200 nm SiO₂ (PECVD) to isolate the etched regions and side walls. This isolation acts as passivation layer as well.
2. Spin coat the e-beam resist layer of 100 % HSQ (negative resist) at 5000 rpm for 60 seconds. This produces 360 nm thick resist layer on SiO₂.
3. Clean backside of the sample with acetone soaked cotton bud and place it in the oven at 180 °C for 90 minutes.
4. Deposit the layer of 100 nm SiO₂ (PECVD).
5. Spin coat the first e-beam resist layer with lower molecular weight PMMA (positive resist, 15 % of 2010) at 5000 rpm for 60 seconds. This produces 1.2 µm thick resist layer.
6. Clean backside of the sample with acetone soaked cotton bud and place it in the oven at 180 °C for 30 minutes.
7. Spin coat the second e-beam layer with higher molecular weight PMMA (positive resist, 4 % of 2041) at 5000 rpm for 60 seconds. This produces 100 nm thick resist layer.
8. Clean backside of the sample with acetone soaked cotton bud and place it in the oven at 180 °C for 90 minutes.
9. Expose the current injection window pattern with VB6 e-beam writer. VB6 control parameters are, resolution: 1.25 nm, proximity correction file: iqe_b.pec. proximity minimum: 0.05, proximity grid: 0.01, dose: 360 µC/cm², spot size: 12 nm and VRU: 8.
10. Develop the exposed current injection window pattern using 1:1 IPA:MIBK solution at 23 °C for 30 seconds. Rinse the developed sample in IPA and RO water for 30 seconds and 60 seconds, respectively. Then blows dry with gaseous nitrogen.
11. Process the developed sample with O₂ asher for 1 minute at 100 Watt power to remove any remains of resist after development.

12. Dry etch the sample with RIE 80 plus machine. This will remove the SiO₂ from the exposed regions on the ridge waveguide structure. Dry etch was carried out with CHF₃/Ar chemistry as a reactive gas for 30 minutes.
13. Remove the e-beam resist by an O₂ gas using BP 80 machine for 12 minutes with following recipe, Power: 100 Watt, pressure: 50 mTorr and flow rate: 50 sccm.
14. Clean the sample in acetone for 10 minutes and then rinse with IPA and RO water for 1 minute each and blows dry with gaseous nitrogen.

Step 4: Realisation of p-contact metallisation on current injection window on the top of the ridge waveguide structure.

1. Spin coat the first e-beam resist layer with lower molecular weight PMMA (positive resist, 15 % of 2010) at 5000 rpm for 60 seconds. This produces 1.2 µm thick resist layer.
2. Clean backside of the sample with acetone soaked cotton bud and place it in the oven at 180 °C for 30 minutes.
3. Spin coat the second e-beam layer with higher molecular weight PMMA (positive resist, 4 % of 2041) at 5000 rpm for 60 seconds. This produces 100 nm thick resist layer.
4. Clean backside of the sample with acetone soaked cotton bud and place it in the oven at 180 °C for 90 minutes.
5. Expose the p-contact pattern with VB6 e-beam writer. VB6 control parameters are resolution: 1.25 nm, proximity correction file: gaas700-100t.pec, dose: 370 µC/cm², spot size: 33 nm and VRU: 20.
6. Develop the exposed p-contact pattern using 1:1 IPA:MIBK solution at 23 °C for 30 seconds. Rinse the developed sample in IPA and RO water for 30 seconds and 60 seconds, respectively. Then blows dry with gaseous nitrogen.
7. Deoxidise the sample with 1:5 HCl: H₂O mixture for 30 seconds. Then rinse in RO water for 30 seconds and blows dry with gaseous nitrogen.
8. Evaporate 30 nm Ti, 33 nm Pt and 240 nm Au using electron-beam assisted Plassys machine.

9. Lift off Ti/Pt/Au layer using acetone in hot water bath at 50 °C for 1 hour and clean the sample.
10. Clean the sample in acetone, IPA and RO water for 1 minute each and blows dry with gaseous nitrogen.

Step 5: Realisation of n-contact metallisation on back side of the sample.

1. Spin coat the glass cover-strip with photo-resist S1818 at 2000 rpm for 5 seconds, place p-side of the sample down onto the glass cover-strip. Then put the sample into oven at 90 °C for 60 minutes to stick the resist well with the glass cover-strip.
2. Clear back side of sample with acetone soaked cotton bud.
3. Mount glass cover-strip onto a metal chuck using wax.
4. Process the sample for thinning with aluminium powder (9 µm/ 3 µm granules) with water mix. The sample was thinned to an approximate thickness of 225 µm.
5. Clear off wax from glass cover-strip by putting the sample into opticlear for 10 minutes.
6. Release the sample from glass cover-strip by putting in acetone placed in hot water bath at 50 °C for 30 minutes.
7. Rinse sample with IPA and RO water, blows dry with gaseous nitrogen.
8. Spin coat the glass cover-strip with photo-resist S1818 at 2000 rpm for 5 seconds, place p-side of the sample down onto the glass cover-strip and put it into an oven at 90 °C for 30 minutes.
9. Evaporate 14nm Au, 14nm Ge, 14nm Au, 11nm Ni, and 240nm Au with electron-beam assisted Plassys machine.
10. Release sample from glass cover-strip by putting it into acetone beaker placed in hot water bath at 50 °C for 1 hour.
11. Rinse sample in IPA and RO water for one minute each and then blows dry with gaseous nitrogen.
12. Anneal the sample in RTA at 380 °C for 50 seconds in order to form the ohmic contacts.
13. The sample onwards is scribed and cleaved for testing and measurements.

Annex III

Fabrication steps for realisation of passive polarisation mode convertor

Fabrication process to realise the passive PMC is given below.

1. Cleave the sample measuring 6 mm x 8 mm in dimension.
2. Clean the sample in ultrasonic bath with acetone, IPA and RO water for 5 minutes each and then blows dry with gaseous nitrogen.
3. Pre-bake the sample on hot plate for 2 minutes at 90 °C.
4. Spin coat the e-beam resist layer of 100 % HSQ (negative resist) at 5000 rpm for 60 seconds. This produces 360 nm thick layer of resist.
5. Clean backside of the sample with acetone soaked cotton bud and place it on the hot plate at 90 °C for 10 minutes.
6. Expose the ridge waveguide structure with VB6 e-beam writer. VB6 control parameters are, resolution: 1.25 nm, proximity correction file: gaas300-100b.pec, proximity minimum: 0.05, proximity grid 0.01, dose: 670 $\mu\text{C}/\text{cm}^2$, spot size: 12 nm and VRU: 8.
7. Develop the exposed pattern using 25 % TMAH at 23 °C for 30 seconds. Rinse in RO water for 30:30 seconds in two separate beakers and then in IPA solution for 15 seconds. Then blows dry with gaseous nitrogen.
8. Dry etch the developed pattern using System 100 to etch 1.50 μm using reflectrometer.
9. In order to remove the HSQ from the ridge waveguide structure, process the sample for wet etch with 10:1 ratio of RO water and HF solution for 60 seconds. Rinse in water for 60 seconds and blows dry with gaseous nitrogen.
10. Clean the sample in acetone, IPA and RO water for 1 minute each and blows dry with gaseous nitrogen.
11. Finally the sample was scribed and cleaved for testing and measurements.

A schematic diagram illustrating the fabrication process is shown in Figure A-2.

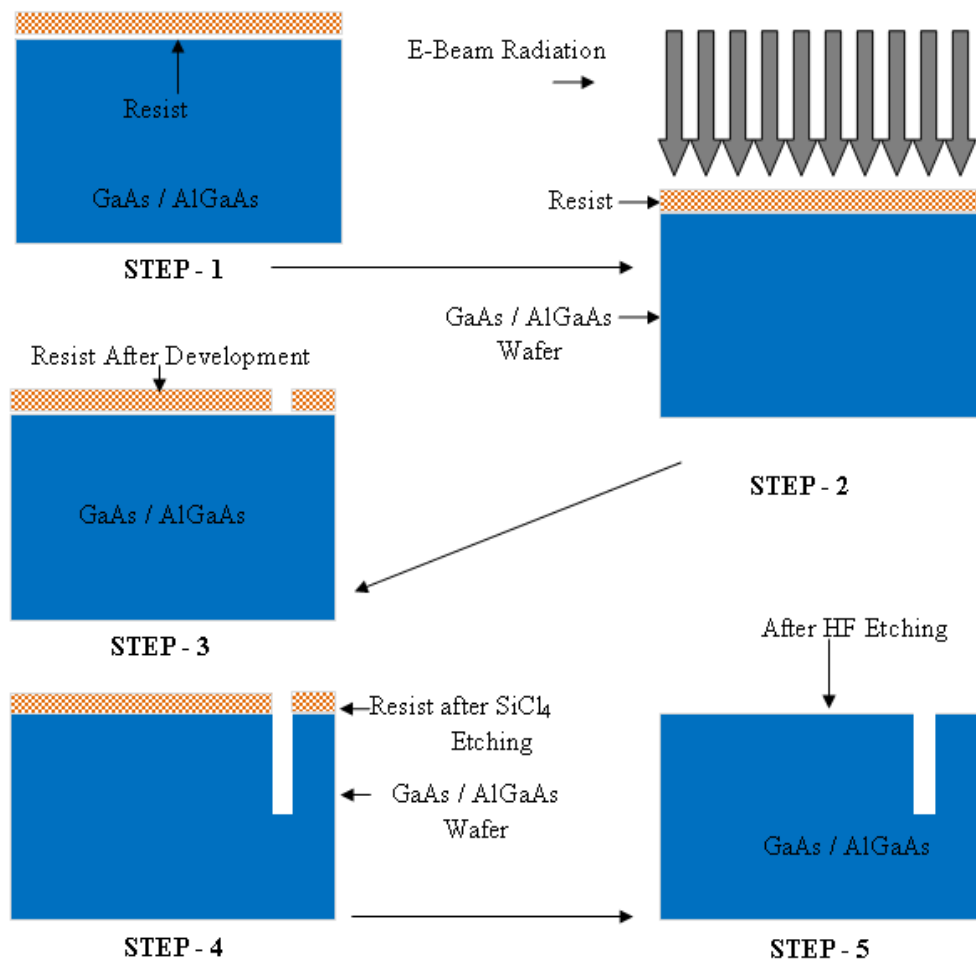


Figure A-2: A schematic diagram of fabrication steps.

Annex IV

Fabrication steps for realisation of polarisation mode convertor with a semiconductor laser

The fabrication steps for realising the PMC with a semiconductor laser are given below.

Step 1: Creation of e-beam position calibration markers.

The electron beam position calibration markers are defined according to the description given in Annex III.

Step 2: Realisation of integrated waveguides structure.

The realisation of integrated waveguides structure is the same excluding step 8 as described for the ridge waveguide structure in the Annex III.

Step 3: Removal of cap layer for isolation of contacts.

1. Spin coat the first e-beam resist layer with lower molecular weight PMMA (positive resist, 15 % of 2010) at 5000 rpm for 60 seconds. This produces 1.2 μm thick resist layer.
2. Clean backside of the sample with acetone soaked cotton bud and place it in the oven at 180 °C for 30 minutes.
3. Spin coat the second e-beam layer with higher molecular weight PMMA (positive resist, 4 % of 2041) at 5000 rpm for 60 seconds. This produces 100 nm thick resist layer.
4. Clean backside of the sample with acetone soaked cotton bud and place it in the oven at 180 °C for 90 minutes.

5. Expose the cap layer pattern with VB6 e-beam writer. VB6 control parameters are, resolution: 1.25 nm, proximity correction file: iqe_b.pec. dose: $270 \mu\text{C}/\text{cm}^2$, spot size: 12 nm and VRU: 8.
6. Expose the reflectometer layer view pattern with VB6 e-beam writer. VB6 control parameters are, resolution: 1.25 nm, proximity correction file: iqe_b.pec. dose: $380 \mu\text{C}/\text{cm}^2$, spot size: 33 nm and VRU: 20.
7. Develop the exposed patterns using 1:1 IPA:MIBK solution at 23 °C for 30 seconds. Rinse the developed sample in IPA and RO water for 30 seconds and 60 seconds, respectively. Then blows dry with gaseous nitrogen.
8. In order to partial remove of the HSQ from the ridge waveguide structure within the cap layer pattern, process the sample for wet etch with 5:1 ratio of RO water and HF solution for 10 seconds. Rinse in water for 60 seconds and blows dry with gaseous nitrogen.
9. Dry etch the developed pattern using System 100 for 45 seconds to etch 100 nm cap layer using reflectometer.
10. Remove the e-beam resist by an O₂ gas using BP 80 machine for 12 minutes with following recipe, Power: 100 Watt, pressure: 50 mTorr and flow rate: 50 sccm.
11. In order to remove the HSQ from the ridge waveguide structure, process the sample for wet etch with 10:1 ratio of RO water and HF solution for 60 seconds. Rinse in water for 60 seconds and blows dry with gaseous nitrogen.
12. Clean the sample in acetone, IPA and RO water for 1 minute each and blows dry with gaseous nitrogen.
13. O₂ ash on asher for 10 minutes at 100 Watt power.

Step 4: Realization of current injection windows on the top of the waveguides structure.

The same steps described in Annex III were carried out for the realisation of current injection windows on the top of the waveguides structure.

Step 5 & 6: Realisation of p-contact and n-contact metallisation.

The steps described in Annex III were performed for the realisation of p-contact metallisation on current injection windows on the top of waveguides structure and the realisation of n-contact metallisation on the back side of the sample.